

# **All-Oxide Thin-Film Varactors**

## **RF Characterization - Modeling - Integration**

Vom Fachbereich Elektrotechnik und Informationstechnik  
der Technischen Universität Darmstadt  
zur Erlangung der Würde eines  
Doktor-Ingenieurs (Dr.-Ing.)  
genehmigte

### **Dissertation**

von

**Dominik Walk, M.Sc.,**  
geboren am 12.06.1989  
in Diez, Deutschland

Referent: Prof. Dr.-Ing. habil. Holger Maune  
Korreferent: Prof. Dr.-Ing. Rolf Jakoby  
Korreferent: Prof. Dr. techn. Stefan J. Rupitsch

Tag der Einreichung: 16. März 2021  
Tag der mündlichen Prüfung: 12. Juli 2021

D17  
Darmstadt 2021

---

Walk, Dominik: "All-Oxide Thin-Film Varactors: RF Characterization - Modeling - Integration"

Darmstadt, Technische Universität Darmstadt,

Jahr der Veröffentlichung der Dissertation auf TUpprints: 2021

URN: urn:nbn:de:tuda-tuprints-192041

Tag der mündlichen Prüfung: 12.07.2021

Veröffentlicht unter CC BY-NC-SA 4.0 International

---

## Erklärungen laut Promotionsordnung

- § 8 Abs. 1 lit. c. PromO** Ich versichere hiermit, dass die elektronische Version meiner Dissertation mit der schriftlichen Version übereinstimmt.
- § 8 Abs. 1 lit. d. PromO** Ich versichere hiermit, dass zu einem vorherigen Zeitpunkt noch keine Promotion versucht wurde.
- § 9 Abs. 1 PromO** Ich versichere hiermit, dass die vorliegende Dissertation selbstständig und nur unter Verwendung der angegebenen Quellen verfasst wurde.
- § 9 Abs. 2 PromO** Die Arbeit hat bisher noch nicht zu Prüfungszwecken gedient.

Darmstadt, 16. März 2020

---

## Copyright Information on Published Papers

During the work on this thesis, several papers were published and presented in notable journals and at conferences, respectively. These are listed in the appendix starting on page 151 and are referred to by consecutive numbers instead of the reference style for external sources by author name and year. My thanks go to the publishers below for the possibility to distribute the scientific content to a wide audience. Parts of the contained results are reused with permission in this monograph.

Some of the papers are copyrighted. If interested in reprinting/reusing copyrighted material, please contact the copyright holders directly.

- [1; 2; 3; 5; 6; 7] with IEEE. ©IEEE 2018 - 2021.
- [4] with AIP APL Materials. Licensed under a Creative Commons Attribution (CC BY) license. Sharing and adaptation is allowed.

# Vorwort

Diese Arbeit ist im Rahmen meiner Tätigkeit als wissenschaftlicher Mitarbeiter am Institut für Mikrowellentechnik und Photonik entstanden. Mit diesem Vorwort möchte ich allen danken, die mich in dieser Arbeit unterstützt haben.

Dr.-Ing – seit kurzem Prof. - Holger Maune, bei dem die Übernahme des Referats meiner Arbeit nur der Abschluss einer langen, wertvollen Unterstützung war. Viele Ideen zur Ausrichtung meiner Arbeit konnte ich mit ihm prüfen und erfolgreich vorsortieren, sodass ich diese Arbeit zielstrebig zu Ende führen konnte. Auch in der detaillierteren, praktischen Umsetzung verdanke ich seiner Expertise und Erfahrung viele gute Anregungen.

Prof. Rolf Jakoby, der mir vor der Übernahme des ersten Koreferats am Institut einen sehr guten Rahmen für meine Arbeit gestellt hat. In diesem Rahmen danke ich für die inhaltliche und strategische Unterstützung bei allen wichtigen Anliegen, sowie für den Raum, meine eigenständige Arbeitsweise auszubauen. Darüber hinaus für viele anregende Gespräche, sowohl fachlich als auch manchem thematischen Vertiefen in deutsche Geschichte auf den Betriebsausflügen.

Prof. Stefan J. Rupitsch, der trotz des frisch übernommenen Lehrstuhls in Freiburg das zweite Koreferat meiner Arbeit übernahm und auch schon zuvor bereitwillig verschiedene wissenschaftliche Fragestellungen mit mir diskutierte.

Meine Projekt-Kollegen Dr.-Ing. Patrick Salg und Dr.-Ing. Lukas Zeinar aus der Materialwissenschaft, die die für diese Arbeit notwendigen Dünnschicht-Systeme hergestellt haben. Ich danke dafür und für die Bereitwilligkeit, meine Wünsche dabei bestmöglich zu erfüllen. Weiterhin für das entspannte Zusammenarbeiten, die vielen Käffchen sowie Crash-Kurse in Mawi-Prozesse und -Messmethoden, sodass ich noch weit über den hochfrequenztechnischen Tellerrand hinausschauen konnte.

Prof. Lambert Alff und Dr. Philipp Komissinskiy für die häufige Erläuterung materialwissenschaftlicher Hintergründe, die anregenden Gespräche und Hilfe bei strategischer Ausrichtung unserer gemeinsamen Arbeit.

Dr. Alexey Arzumanov, der meine Proben sogar auch mal sonntags ätzte und ein besonderes Talent hat, schwierig zu findende Literaturdaten mit genau den benötigten Informationen aufzutreiben.

## VORWORT

---

Silke Schober, die mich vor allem zu Beginn der Promotion mit viel Geduld in alle notwendigen Reinraumprozesse eingewiesen hat. Darüber hinaus leistete sie viel Unterstützung bei der praktischen Arbeit der Probenherstellung und -charakterisierung.

Peter Kießlich und Andreas Semrad, die bei allen Fertigungswünschen stets bereitwillig mit Rat und Tat zur Seite standen.

Außerdem allen weiteren Kollegen am IMP, die auf dem gleichen Flur für Ihre Promotion gearbeitet haben. Darunter besonders mein Büronachbar Dr.-Ing. Daniel Kienemund: Ich erinnere mich dankbar an viele wertvolle Gespräche über's Fach und auch darüber hinaus. Diese haben meine Kreativität immer wieder angeregt, mich in den zähen Phasen ermutigt und häufig einen notwendigen Perspektivwechsel ermöglicht. Außerdem Alejandro Jimenez für viele hochfrequenztechnische Gespräche – auch über das eigene Thema hinaus, einfach weil's Spaß macht.

Ebenso hatte ich außerhalb der Universität viele Unterstützer. Ihnen allen voran danke ich meiner wundervollen Frau Alena, die immer an mich glaubt und praktisch unterstützt hat, wo sie konnte. Für viele Gespräche, in denen sie immer motiviert zugehört und nachgefragt hat, obwohl sie inhaltlich dann doch nicht so viel verstand. :-) Und außerdem für die Zuversicht und seelische Unterstützung – zum Beispiel in dem offen-warmherzigen Lächeln zur Begrüßung an so manchem späten Abend, obwohl sie mich eigentlich früher erwartet hatte.

Meinen Eltern, die seit meiner Kindheit in liebevoller Hingabe so viel in mich investierten, mich prägten und dadurch am Fundament gearbeitet haben, auf dem diese Dissertation zum Erfolg werden konnte.

Meiner weiteren Familie und allen Freunden, die mich im Hintergrund mit Fragen und Interesse unterstützt, mir zwischendurch den auch mal nötigen Abstand zur Arbeit ermöglichen und die Vielseitigkeit bedienten, die mein Geist braucht.

Mein größter Dank und mein Lob gebühren aber dem himmlischen Vater, der mich mit der Kreativität, der Strukturiertheit und der Beharrlichkeit ausgestattet hat, die so eine Promotion erfordert.

Darmstadt, Juli 2021

Dominik Walk

# Abstract

This work depicts the pioneer steps on investigating the novel all-oxide technology for its application in radio frequency (RF) varactors. The platinum bottom electrode of conventional ferroelectric varactors is replaced with the highly conducting oxide strontium molybdate  $\text{SrMoO}_3$  (SMO). Its structural similarity to the ferroelectric barium strontium titanate  $\text{Ba}_x\text{Sr}_{1-x}\text{TiO}_3$  (BST) helps to overcome the most severe drawbacks of the conventional approach: Increased defect concentration in BST and the formation of an untunable deadlayer at the platinum/BST interface. In all-oxide varactors, BST grows epitaxially on top of the bottom electrode and, hence, an ideal crystal forms instead of the polycrystalline BST on top of platinum.

Due to the scarce preliminary knowledge on the properties of jointly integrated SMO and BST layers, a substantial portion of RF characterization and material parameter extraction is required. The first major result of this work is the frequency extension of a widely used on-wafer test structure for dielectric characterization from lower GHz frequencies up to the self-resonant frequency. This allows for the correct extraction of impedance data in the frequency range of interest and is a crucial prerequisite for comprehensive modeling. Furthermore, RF-characterization-based optimization of the deposition process is key to the fabrication of high-performance varactors with unprecedented SMO and BST thicknesses greater than  $5 \mu\text{m}$  and smaller than  $50 \text{ nm}$ , respectively.

The greatest emphasis is put on highly accurate analytic models. Present models are not sufficiently accurate for thin-film devices with electrodes often thinner than skin depth. By incorporating the significant contribution of the substrate, a novel schematic model is proposed. It reacts to all significant material properties and yields the true RF properties of the varactor, based on predicting reasonably exact impedance data. This high accuracy further allows for the derivation of a bias-dependent model that considers the electromechanic excitation of acoustic waves. The final model tracks the impedance over a wide range of frequency and electric bias field up to  $12 \text{ GHz}$  and  $100 \text{ V}/\mu\text{m}$ , respectively. Based only on a simple RF characterization, this model enables a confident estimation of both electric and mechanic properties of the integrated varactor. On the one hand, this allows for the precise design of high-performing circuits. On the other hand, it helps to evaluate the great potential of all-oxide varactors to overcome a severe frequency limitation

of conventional varactors by reducing the impact of acoustic resonances.

To its end, this work addresses the transfer from material identification and optimization towards an industrial realization of the all-oxide technology. Sample reproducibility and uniformity are evaluated as hitherto insufficient, which is, however, a known drawback of the deployed pulsed laser deposition (PLD). Furthermore, the functional varactor deposition on silicon as an industrially established substrate is demonstrated. Finally, the integrability of the novel all-oxide varactors into circuits is demonstrated in two configurations; as a standalone surface-mount device and via integrated growth in an exemplary phase shifter.

An outstanding performance of all-oxide devices is predicted after two enhancements in future work. Firstly, the transfer to a method other than PLD is recommended to allow larger substrates and reliably yield high-quality materials. Secondly, a significant improvement was demonstrated by doping BST to increase the  $Q$  factor and decrease the acoustic activity. This greatly increases the applicable frequency range beyond the limits of conventional ferroelectric varactors and predicts low loss of all-oxide devices in the full 5G sub-6 GHz range and beyond.

# Kurzfassung

Diese Arbeit beschreibt die ersten Schritte der Erforschung der Vollooxid-Technologie für eine Anwendung in Hochfrequenz- (HF-)Varaktoren. Dabei wird die Platin-Bodenelektrode von herkömmlichen ferroelektrischen Varaktoren mit dem hochleitfähigen Strontium-Molybdän-Oxid (SMO) ersetzt. Dessen strukturelle Ähnlichkeit mit dem ferroelektrischen Barium-Strontium-Titanat (BST) ermöglicht das Überwinden der gravierendsten Nachteile des herkömmlichen Ansatzes: Eine erhöhte Defektkonzentration in BST und das Ausbilden einer unsteuerbaren Grenzschicht am Platin-BST-Übergang. In volloxydischen Varaktoren wächst ein idealer BST-Kristall epitaktisch auf der SMO-Bodenelektrode anstatt des polykristallinen BST auf Platin.

Da zuvor kaum Informationen über integrierte SMO-BST-Schichtsysteme berichtet wurden, ist die HF-Charakterisierung und Materialparameterbestimmung ein wesentlicher Bestandteil dieser Arbeit. Das erste wichtige Ergebnis ist dabei die Erweiterung des Frequenzbereichs einer weit verbreiteten On-Wafer-Teststruktur vom unteren GHz-Bereich bis zu ihrer Selbstresonanzfrequenz. Dies ermöglicht die korrekte Extraktion der Varaktorimpedanz im gesamten gewünschten Frequenzbereich und ist fundamental für eine umfassende Modellierung. Hierdurch konnte der Abscheideprozesses optimiert werden, was entscheidend dazu beitrug, hochperformante Varaktoren herzustellen. Diese zeichnen sich durch die Kombination bisher unerreichter SMO- und BST-Schichtdicken aus, die jeweils dicker als 5 µm und dünner als 50 nm sind.

Der Schwerpunkt dieser Arbeit liegt auf hochgenauen analytischen Modellen. Vorhandene Modelle sind nicht genau genug für Dünnschichtschaltungen mit Elektroden, die dünner als die Skintiefe sind. Ein neues Modell wird vorgestellt, das den signifikanten Beitrag des Substrats berücksichtigt. Es beachtet den Einfluss aller maßgeblichen Materialeigenschaften und erlaubt damit die Extraktion der tatsächlichen HF-Eigenschaften des Varaktors. Die erreichte hohe Genauigkeit ermöglicht die Erweiterung zu einem Modell, das zusätzlich die elektrische Vorspannung mit einbezieht. Letztere führt zu induzierter Piezoelektrizität in BST, wodurch akustische Wellen im Modell berücksichtigt werden müssen. Das elektro-akustische Modell folgt der tatsächlichen Varaktorimpedanz in einem weiten Frequenz- und Vorspannungsbereich bis zu jeweils 12 GHz und 100 V/µm. Dadurch ermöglicht

es die Extraktion von sowohl elektrischen als auch mechanischen Eigenschaften des integrierten Varaktors, die lediglich eine einfache On-Wafer-Messung benötigt. Dies eröffnet einerseits die Möglichkeit einer präzisen Modellierung von hochperformanten Schaltungen. Andererseits ermöglicht es die Evaluierung des Potentials von volloxidischen Varaktoren und deren Optimierung, um die gravierende Frequenzbeschränkung von herkömmlichen Varaktoren durch akustische Resonanzen zu überwinden.

Zum Schluss der Arbeit wird der Transfer hin zur industriellen Realisierung der Volloxid-Technologie thematisiert. Reproduzierbarkeit und Gleichförmigkeit der Proben werden als unzureichend identifiziert, was die potentiellen Nachteile der verwendeten gepulsten Laserabscheidung (engl.: *pulsed laser deposition*, PLD) bestätigt. Weiterhin wird die Abscheidung eines funktionalen Varaktors auf industriell etablierten Silizium-Substraten demonstriert. Schließlich wird die Integrierbarkeit der neuen volloxidischen Varaktoren in Schaltungen gezeigt, und zwar in zwei Konfigurationen; sowohl als ein eigenständiges oberflächenmontierbares Bauteil (engl.: *surface-mount device*) als auch mittels integriertem Wachstum innerhalb eines beispielhaften Phasenschiebers.

Eine herausragende Performanz der volloxidischen Technologie wird nach zwei zukünftigen Entwicklungen ermöglicht. Einerseits ist der Wechsel auf eine andere Abscheidemethode als PLD empfohlen, um reproduzierbar eine hohe Materialqualität auf außerdem größeren Substraten zu erreichen. Daneben zeigt das Dotieren von BST eine signifikante Verbesserung der Materialgüte und eine schwächere akustische Anregung. Dies erweitert den Anwendungsfrequenzbereich erheblich über die Grenzen von herkömmlichen ferroelektrischen Varaktoren hinaus und prognostiziert niedrige Verluste von volloxidischen Geräten bis oberhalb des gesamten 5G sub-6 GHz-Frequenzbereichs.

# Contents

<b>1</b>	<b>Introduction</b>	<b>1</b>
<b>2</b>	<b>Oxide Materials</b>	<b>7</b>
2.1	Functional Barium Strontium Titanate (BST) . . . . .	7
2.1.1	Dielectric Properties . . . . .	9
2.1.2	Microwave Loss Mechanisms . . . . .	14
2.1.3	Induced Piezoelectricity . . . . .	25
2.2	Conducting Strontium Molybdenum Oxide (SMO) . . . . .	28
2.3	Thin-Film Processing . . . . .	31
<b>3</b>	<b>Characterization of All-Oxide Varactors</b>	<b>34</b>
3.1	On-Wafer Testing . . . . .	34
3.2	De-Embedding of Measurement Data . . . . .	39
3.2.1	Determination of True Test Structure Inductance . . . . .	41
3.2.2	Characterization of Negative Measurement Inductance . . . . .	43
3.2.3	Benefits for All-Oxide-Varactor Characterization . . . . .	45
3.3	Characterization Results . . . . .	45
3.3.1	Typical Varactor . . . . .	46
3.3.2	High-Performance Varactor . . . . .	49
3.4	RF-Performance-Driven Material Optimization . . . . .	51
3.4.1	Correlation of Crystallographic and DC/RF Characteristic . .	52
3.4.2	Study on Influence of Laser Fluence . . . . .	55
<b>4</b>	<b>Highly Accurate Analytic Models</b>	<b>58</b>
4.1	Unshielded Substrate Model (USM) . . . . .	61
4.1.1	Extended Schematic Model . . . . .	63
4.1.2	Parameterized Material Variations . . . . .	66
4.1.3	Multivariate Model . . . . .	70
4.1.4	Verification by Measurement . . . . .	73
4.2	Acoustic Unshielded Substrate Model (AUSM) . . . . .	75
4.2.1	Modeling Acoustic Resonances . . . . .	75
4.2.2	Solving the Inverse Problem . . . . .	78

4.2.3	Verification by Measurement . . . . .	81
4.2.4	Identification of Bias-Dependent Properties . . . . .	86
4.2.5	Suppression of Acoustic Resonances . . . . .	89
4.3	Summary on Presented Models . . . . .	93
<b>5</b>	<b>Towards Industrial Realization</b>	<b>95</b>
5.1	Process Stability . . . . .	95
5.2	Transfer to Silicon Substrate . . . . .	100
5.3	Surface-Mount Device . . . . .	102
5.4	Fully Integrated Tunable Circuits . . . . .	109
<b>6</b>	<b>Conclusion &amp; Outlook</b>	<b>114</b>
<b>A</b>	<b>De-Embedding of Excitation Bridge in EM Simulation</b>	<b>120</b>
<b>B</b>	<b>Additional Data to the Analytic Models</b>	<b>124</b>
	<b>Acronyms</b>	<b>131</b>
	<b>Symbols and abbreviations</b>	<b>133</b>
	<b>Bibliography</b>	<b>134</b>
	<b>Own Contributions</b>	<b>151</b>
	<b>Curriculum Vitae</b>	<b>155</b>

# 1 Introduction

In recent days, many fields of innovation rely on a shared key enabler, that is mobile communication. The exchange of sensor information is essential for quickly emerging topics, such as Internet of Things (IoT), smart homes and smart cities or autonomous driving and connected cars. In parts, these are already present but will become much larger contributors to the total data traffic in the future. However, already nowadays, scenarios like mobile video streaming or the concept of mobile work relying on cloud services tremendously increase the data volume per user. Along with the increasing number of connected terminals, this leads to the predicted exponential increase of the mobile transmitted data, see Figure 1.1. This highlights the very strong demand for innovations in the field of mobile RF communications. Currently, this overlaps with the troika of expectations for the novel mobile communication standard 5G, i.e., massive number of terminals, ultra low latency and vast bandwidth increase. Each aspect can roughly be assigned to a different use case and frequency range [Ass17]. As a first one, the IoT will lead to the massive increase of number of terminals and will communicate mostly below 1 GHz. Depending on the application, the latency can be either uncritical or

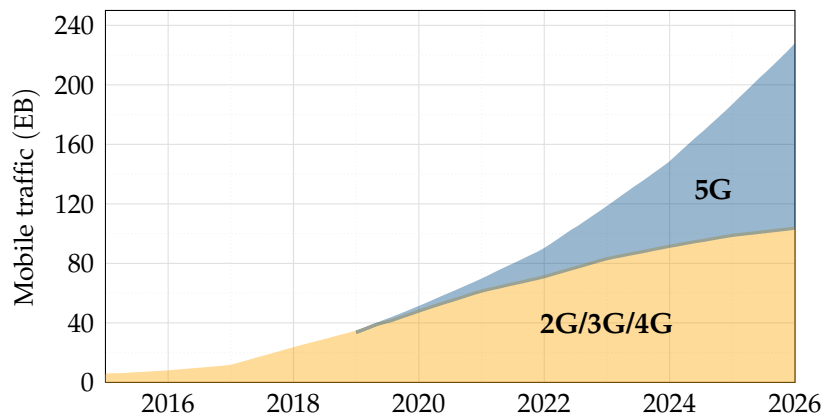


**Figure 1.1:** Total mobile traffic in exabytes (million terabytes) until 2026 predicted by Ericsson in November 2020. [Tel21]

essential as, e.g., for general sensor data or autonomous/assisted driving, respectively. The second use case focuses "classic" mobile communication of the customer who demands an increased coverage and availability of higher data rates. This will be fulfilled in the sub-6 GHz bands and, hence, depicts the closest relation to the previous communication standards up to 4G. Finally, the largest bandwidth increase will be achieved only with millimeter waves at frequencies above 24 GHz (5G-mmWaves). The shorter range of millimeter waves limits the corresponding use cases to, e.g., in-house communication or point-to-point links with high-gain antennas.

This work is motivated by the second use case of mobile communication. To maximize the data rates and number of serviceable terminals, many more frequency bands have been assigned to 5G than were used in former standards [Qua20]. Additionally, bands dedicated to the former standards, particularly 4G, can be used via dynamic spectrum sharing. Thus, the 5G spectrum covers many bands and spans between 800 MHz and 6.4 GHz (USA and South Corea: 7.1 GHz).<sup>1</sup> While this much larger bandwidth greatly increases the theoretical channel capacity, it likewise strongly challenges the technical implementation. In present transceivers, the signal processing is split into a digital part for the baseband signal and the RF frontend. The latter contains the required mixer, amplifiers, filters and antennas to transmit the input analog baseband signal as an electromagnetic (EM) wave and vice versa. Its operation is conventionally fixed by design to certain frequencies (among other properties like the impedance). Hence, each required frequency band must be individually considered in the design process. A multitude of parallel hardware trunks is usually implemented in the RF frontend to provide the different services (e.g. GSM, UMTS, Wifi/Bluetooth, GNSS). Note that each service may contain an unprecedented complexity, especially to communicate on multiple bands. Though already challenging for 4G implementations, this approach gets more and more critical when evolving towards 5G due to the increasing number of bands spread over a wide frequency range. In parallel, the number of required filters increases tremendously as it is discussed in more detail in [Res16]. Additionally, the higher data rates require the incorporation of multiple-input multiple-output (MIMO) with multiple antennas per link [Inc18]. On the other hand, the available printed circuit board (PCB) area remains fixed or even shrinks as, e.g., for modern smartphones with curved displays. In consequence, present 5G RF frontends often serve only a few of all the defined 5G bands [PLC19; Res20]. Letting mobile terminals exploit the full potential of 5G appears as an yet unsolved challenge.

The perspective of an alternative design approach was given by Mitola already in

---

<sup>1</sup>The conventional name "sub-6 GHz" originates from the original declaration. The frequency range has been extended to bands above 6 GHz later-on.

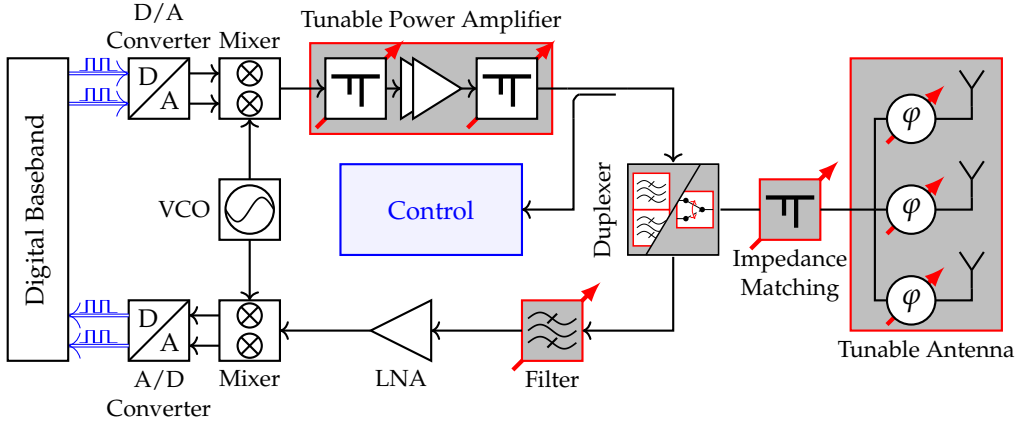


**Figure 1.2:** Schematic of a tunable RF frontend.

1995 [Mit95]: The software-defined radio (SDR). It replaces the previously described hard-wired characteristics of static analog components with an agile implementation. Ideally, no preliminary information about the subsequently used frequency band is necessary during fabrication; the transceiver is capable of software-wise selecting any desired band. This idea is hardly realizable in its ideal form due to limited output power and performance of the analog-to-digital converter (ADC), i.e., sampling rate, speed of memory and dynamic range [Wal08; Gra13]. However, its underlying principle attracts much research focus nonetheless. Since complete flexibility will not be necessary in practice anyways, a huge step towards the idea of SDR can be done by making RF frontends reconfigurable, as shown in Figure 1.2. It resembles the conventional RF frontend in its basic structure, sharing the same type of components like a power amplifier, filter or impedance matching networks. However, the desired agility is implemented by using tunable technologies in these elements. They allow to tune the transmission frequency, such that a multitude of bands can be served by the same RF frontend. Furthermore, there are additional decisive benefits. The partial reflection of the EM signal inside the RF frontend can be minimized by adaptive tuning of the impedance matching networks. Static matching networks can be optimized only for a single pre-defined condition. This conflicts with power-saving implementations of modern modulation schemes or varying environments that impact the antenna impedance. For carrier aggregation, flexible bandwidth allocation will be beneficial, requiring tuning the bandwidth and center frequency of the individual filters. Finally, by tuning the phase shift of each element in an antenna array, beam-forming can be used for spatial multiplexing to use the same frequency band in multiple links and to optimize the link budget by designing high-gain antennas.

There are several ways to introduce tunability in RF networks. They can be grouped into geometric and material tuning principles [Mau20]. In the former case, the performance of a component is tuned with geometrical changes, e.g., for a variable resonating length of a cavity filter. Further examples are micro-electromechanic systems (MEMS) or diodes that deploy micro-mechanical actuation or changes in the depletion zone width, respectively. Diodes score with a high tunability and high speed but suffer from a low linearity. MEMS can be both very linear and low-loss at the cost of a decreased tuning speed, higher required tuning voltage and mechanic fatigue effects. The latter tuning principle relies on functional materials that can change their magnetic or electric susceptibility. These can be used to build tunable inductances and capacitances, respectively.<sup>2</sup> The former often require a large PCB area and electromagnets, which is unattractive for mobile applications due to the high power consumption [Nin+06]. The favorable way to introduce tunability is via varactors, i.e., tunable capacitors, named after their variable reactance. Depending on the frequency, different material classes relying on distinct polarization principles are available. At high frequencies like, e.g., for millimeter waves, many materials using atomic polarization exhibit a severe loss. Instead, a promising approach is to use liquid crystals in the nematic phase, which allow to exploit their anisotropic polarization for a low-loss application up to THz frequencies [Wei+13; Wei17]. However, special care needs to be taken in component design, in particular, to avoid leakage of the liquid crystal. At lower frequencies, other materials are more prominent and easier to integrate. Among them, ferroelectrics are intensely researched due to their generally high tunability and low loss. Furthermore, corresponding devices exhibit a high linearity due to the generally high power-handling capacity of ceramics. The most prominent material for ferroelectric varactors is BST. Depending on the application, BST can be used as a thick bulk ceramic or as a processed thick or thin film [Pre+17; Kie19]. One particular strength of thin films is the lower tuning voltage required for the same tunability at the cost of a reduced linearity that must be compensated by the component design.

This work investigates a novel type of metal-insulator-metal (MIM)<sup>3</sup> varactors based on BST thin films for the application in RF networks for the first time. It was created during an interdisciplinary research project with the partnered Advanced Thin-Film Technology group (ATFT), TU Darmstadt, who was responsible for the deposition

---

<sup>2</sup>Note that more complex tunable components like phase shifters exist that, however, generally rely on the same physical principles. Hence, this discussion confines itself to these two primitives of electric networks.

<sup>3</sup>The MIM configuration describes a layout, where the dielectric is sandwiched between the two electrodes of the capacitor. Its prominent alternative is the interdigitated capacitor (IDC), where both electrodes are deposited adjacent to each other on top of the dielectric.

of the studied thin films.

State-of-the-art varactors deploy electrodes made of metal, e.g., platinum. In this work, the bottom electrode (BE) is replaced with the conducting oxide SMO which brings several advantages. Firstly, other than all metals, SMO and BST share the same crystal structure and a very similar lattice constant. This allows to avoid the defected growth of BST that is common to conventional varactors with metal electrodes. BST can be grown epitaxially, which results in a higher dielectric quality, i.e., lower RF loss and leakage current. Furthermore, an untunable deadlayer between the functional BST and the BE is avoided; ultra-thin dielectric layers of only a few tens of nm can be fabricated. These can be fully tuned at the ion-battery voltage level without the need for DC-DC converters. Since the conductivity of SMO is comparable to or, as a single-crystal, even higher than the one of platinum, no additional ohmic loss is expected from the electrodes. Hence, the benefits of this all-oxide technology are achievable without the typical engineering trade-off between conflicting performance requirements. Finally, another highly valuable property might be the overcoming of a fundamental limitation to frequencies below 2.5 GHz – 3.5 GHz that is inflicted by acoustic resonances. While conventional BST thin-film varactors can only operate below that margin, the all-oxide technology might be able to serve all frequencies used for mobile communication. All these hypotheses are validated within this work.

## Outline

In chapter 2, all required background knowledge on oxide materials is summarized. Starting with ferroelectric BST, the fundamental principles of polarization, loss mechanism and electrostriction-induced piezoelectricity are reviewed. The section on the conducting oxide SMO contains a review of the currently scarce literature information that is relevant for microwave application. However, the interdisciplinary project behind this work yields further insights into the properties of this material. For good reading flow, these results are summarized in that section as well. The chapter is concluded by a description of the deposition process, in particular highlighting the challenge of integrating the reduced SMO into varactors.

Chapter 3 describes the main results with a focus on the characterization which is based on a widely used test structure. However, as of yet, this method is inflicted by a significant frequency limitation due to a difference between the environment of calibration and measurement. The first major result of this work depicts the identification and compensation of that systematic error. In consequence, the applicable frequency range of this method can be extended by one decade or more. Afterwards, typical and high-performance results of all-oxide varactors fabricated

during this work are presented. The chapter ends with discussing the importance of evaluating the microwave impedance data for optimizing the material deposition. Conclusions on the correlation between the crystallographic structure and the RF characteristic are drawn.

The greatest emphasis of this work is put on the novel, highly accurate analytic models derived in chapter 4. Present models consider the BE only by its sheet resistance, i.e., the material's thickness and conductivity. Furthermore, any substrate impact enabled by the typically very thin BEs is neglected. However, these models do not suffice in this work due to the unknown conductivity and small thickness of the integrated SMO films. Hence, the novel model must identify the properties of both the BE and the dielectric layer, i.e., SMO and BST simultaneously. It is derived in two phases. Firstly, only zero-bias data is considered such that there is no acoustic activity and the focus can be put on the thin BE and the substrate. It is shown that the complex impedance characteristic can be tracked reasonably exact by the proposed unshielded substrate model (USM). Secondly, the proven very high accuracy of the acoustic USM allows to investigate the BST properties in an unprecedented level of detail. Both the dielectric and the mechanic properties can be identified with a simple, rapid microwave characterization. Besides material identification, the very high model accuracy up to 12 GHz and electric biasing of 100 V/ $\mu$ m yields it as a powerful tool for network designers.

This thesis closes with investigations towards an industrial realization in chapter 5. The pivotal requirement for building networks or producing varactors on a large scale is precise control of reproducibility and uniformity. Both properties are investigated initially. Afterwards, the results of a varactor deposited on the widely used substrate silicon are presented. This is an important step for the integrability of the all-oxide technology into industrial processes. The next section presents the design of a component for circuit integration that was developed in this work. Its application in an experimental phase shifter prototype is demonstrated as a proof of concept.

## 2 Oxide Materials

Generally, ceramic oxides are widely used dielectric materials in densely-packed capacitors due to their very large dielectric constant and high electrical breakdown strength. Conventionally, these should exhibit a fixed capacitance independent of environmental impacts like, e.g., possibly superimposed supply voltage levels or temperature variations. In this work, this is different as the electric-field dependence of ferroelectric ceramics is engineered to build varactors. Hence, a significant dependence of the capacitance on a DC bias voltage  $C(V_{\text{bias}})$  is desired to allow for designing tunable microwave components. It is, however, an engineering challenge to circumvent or reduce parasitic effects correlated to tuning such as increased losses or self-biasing with large radio frequency (RF) signals and temperature changes. Besides that, oxides are not necessarily dielectrics. The integration of the novel conducting oxide strontium molybdate  $\text{SrMoO}_3$  (SMO) in varactors is investigated in this work. Hence, the motivation for their use and all relevant material properties are discussed in this chapter. Additionally, the thin-film deposition method for these materials is explained such that important aspects for the design of microwave components can be understood.

### 2.1 Functional Barium Strontium Titanate (BST)

Barium strontium titanate  $\text{Ba}_x\text{Sr}_{1-x}\text{TiO}_3$  (BST) is used as functional material for the tunable devices investigated in this work. It is an oxide ceramic from the group of perovskite materials which exhibits ferroelectricity. In this section, the theoretical background of ferroelectric materials is explained. Furthermore, the dielectric and electro-acoustic properties and phenomena are reported with a focus on microwave loss mechanisms.

The term "ferroelectric" refers to the analogue ferromagnetic materials, which retain their magnetic polarization after being exposed to an external magnetic field. Ferroelectric materials exhibit a spontaneous electric polarization after turning off an external electric field. For the ferroelectric phase, the qualitative dependence

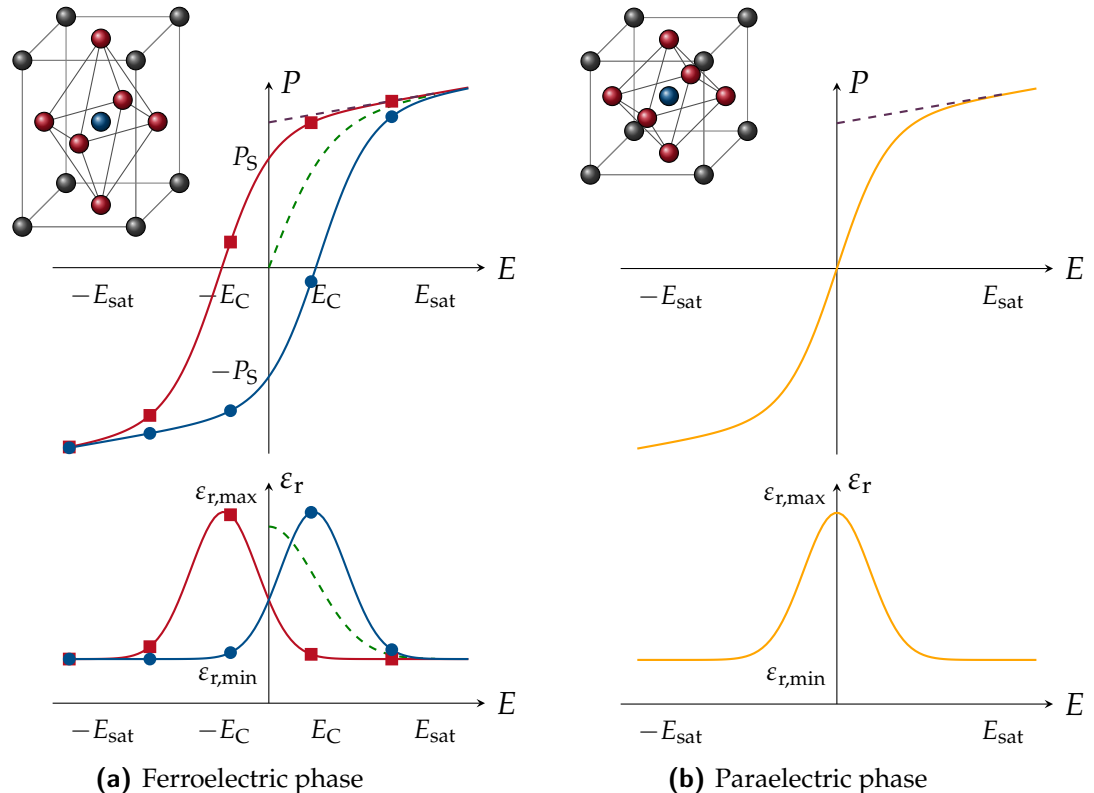


**Figure 2.1:** Electric polarization  $P$  and dielectric permittivity  $\epsilon_r$  versus electric field  $E$  for a ferroelectric material.

of electric polarization and permittivity on the electric field for is shown in Figure 2.1a. Exposed to an electric field of increasing strength, the polarization leaps up until the saturation field strength  $E_{\text{sat}}$  is reached. Above  $E_{\text{sat}}$ , the polarization increases approximately linear and much slower. After removing the applied field, a spontaneous polarization  $P_S$  is retained that is canceled out only after applying the coercitive field strength  $E_C$  with inverted polarity. This phenomena cycles likewise for opposite amplitudes, leading to the observed hysteresis that classifies the material as an ferroelectric [Mar64]. The slope in this graph is known as the electric susceptibility that is defined as [Poz11]

$$\begin{aligned}\chi_e(E) &= \frac{1}{\varepsilon_0} \frac{\partial P(E)}{\partial E} \\ &= \varepsilon_r(E) - 1,\end{aligned}\tag{2.1}$$

which links the polarization to the dielectric permittivity and is scalar only for isotropic problems. While ferroelectricity is a very useful property for memory applications [Uch10], it is strongly disturbing for microwave tunable devices for several reasons. Firstly, the effective polarization, i.e., the capacitance of the varactor has no unique relation to the applied electric field but also depends on the previous state. Hence, complex and most likely iterative biasing would be needed to reach a specific capacitance value. Furthermore, tremendous loss would be caused by the hysteresis during the repeated re-polarization with every oscillation of the RF field. Finally, especially when desiring fast tuning in the  $\mu\text{s}$  or  $\text{ns}$  range, a higher energy consumption would result from elastic loss during perpetually re-biasing [Liu+15]. This memory effect can be removed when deploying ferroelectrics above their Curie temperature  $T_c$ , i.e., in the paraelectric phase. In that case, the spontaneous polarization and hysteresis vanish, yielding a unique dependence of polarization and permittivity on the electric field as can be seen in Figure 2.1b. A very thorough description of the possible orders of phase transition is done in [BZ74, pp.25-32]. This transition can be understood as the freezing of a certain vibrational (soft) mode of the crystal lattice, i.e., the infrared active transverse optical phonon [BZ74, p.13]. In the paraelectric phase, the real part of this phonon's frequency can be derived from the Lyddane-Sachs-Teller relation and the Curie-Weiss law as

$$\Omega_0 = A_{\text{sm}} \sqrt{T - T_0} \quad (\text{for } T > T_0) \quad (2.2)$$

with material-dependent soft-mode temperature constant  $A_{\text{sm}}$ , temperature  $T$  and Curie-Weiss temperature  $T_0$ . Due to the temperature dependence, the frequency becomes zero at  $T_0$ , yielding a permanent deformation of the crystal lattice.

The crystal lattice of perovskite materials consists of  $\text{ABO}_3$  unitcells where the A-site and B-site are at the corner and center, respectively, and the oxygen ions sit on the face centers (compare Figure 2.1). These unitcells are tetragonal and cubic in the ferro- and paraelectric phase, respectively. The tetragonal unitcell in the ferroelectric phase exhibits two minima of the Helmholtz free energy [Smi+03], causing the hysteresis, i.e., a non-unique dependence of the polarization on the applied electric field.

### 2.1.1 Dielectric Properties

The research of ferroelectric-tunable microwave devices often focuses on BST due to its low loss, high tunability and high integrability, e.g., for communication systems up to 10GHz. However, studies have also shown its applicability beyond this

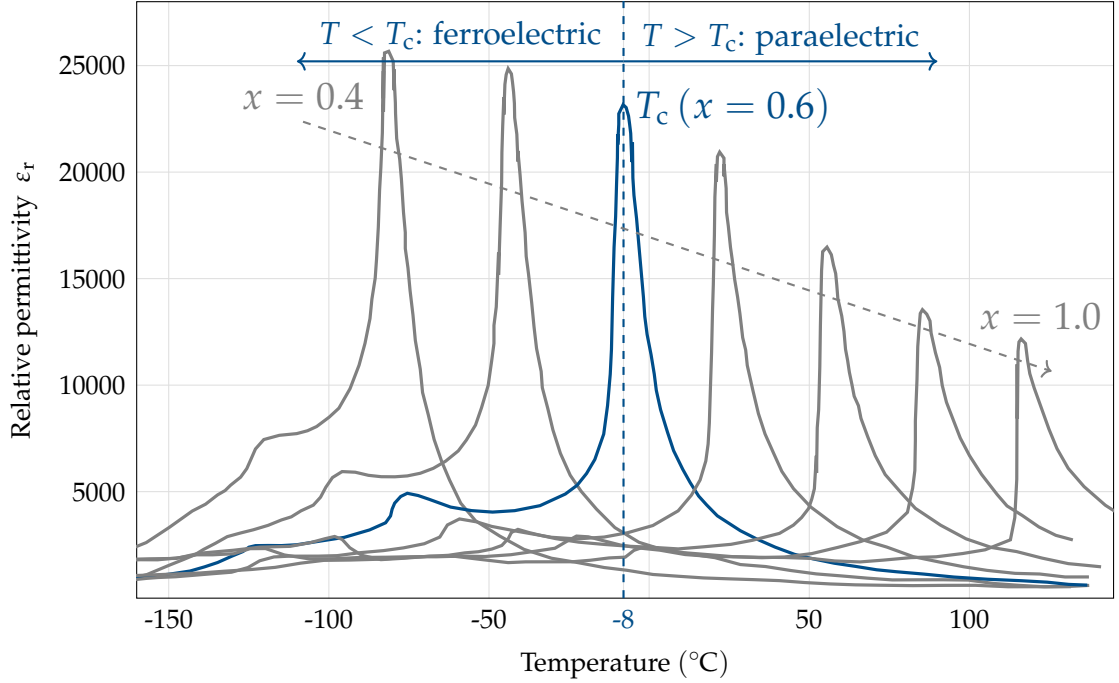


**Figure 2.2:** Relative dielectric constant versus temperature for different Ba/Sr contents  $x = 0.4, 0.5, \dots, 1.0$  in  $\text{Ba}_x\text{Sr}_{1-x}\text{TiO}_3$  bulk ceramics sintered at  $1450^\circ\text{C}$  [Jeo04]. The transition temperature from ferro- to paraelectric phase  $T_c$  depends on  $x$ , the respective domains are highlighted for  $x = 0.6$ .

margin up to 60 GHz [Alt+19]. BST, i.e.,  $\text{Ba}_x\text{Sr}_{1-x}\text{TiO}_3$  emerges from mixing the perovskites  $\text{BaTiO}_3$  and  $\text{SrTiO}_3$ , in which the A-sites are occupied by Ba- and Sr-ions. The complete mixture range from  $0 \leq x \leq 1$  can be produced. The variation of  $x$  allows for precisely balancing the material's loss, permittivity and tunability

$$\tau_\epsilon(E) = \frac{\epsilon(0) - \epsilon(E)}{\epsilon(0)} = 1 - \frac{\epsilon(E)}{\epsilon(0)}. \quad (2.3)$$

In the paraelectric phase and at a given operation temperature, all three properties decrease for a lower barium content. For the metal-insulator-metal (MIM) structures investigated in this work, the material tunability can be assumed equal to the varactor tunability

$$\tau_C(E) = \frac{C(0) - C(E)}{C(0)} = 1 - \frac{C(E)}{C(0)} \stackrel{\text{MIM}}{=} \tau_\epsilon(E) = \tau(E). \quad (2.4)$$

due to the homogeneous field distribution inside the functional material. A typical varactor implementation with inhomogeneous fields is the interdigitated capacitor

(IDC) [Mey+16b].

The dielectric constant of sintered BST is plotted versus temperature for different Ba/Sr contents  $0.4 \leq x \leq 1.0$  in Figure 2.2 [Jeo04]. The phase transition between para- and ferroelectric phase happens at the Curie temperature, and can be identified by the peak permittivity. For lower barium contents ( $x < 0.5$ ), the Curie temperature can be approximated by [VZN02]

$$T_c = 42 + 439.37x - 95.95x^2. \quad (2.5)$$

For the exemplified  $\text{Ba}_{0.6}\text{Sr}_{0.4}\text{TiO}_3$ , Figure 2.2 yields  $T_c = -8^\circ\text{C}$ . Below and above this temperature, this composition is in the ferro- and the paraelectric phase, respectively. The higher the temperature beyond the phase transition, the lower the tunability  $\tau_\varepsilon(E)$ , as the deepness of the Helmholtz free energy minima increases [Smi+03]. The Curie temperature increases for an increasing barium content and, as long as in the paraelectric phase, the permittivity at a fixed temperature increases likewise. However, although these tendencies remain independent of the processing technique, a strong quantitative variation of the material properties can happen during the processing. In macro- and microscopic inclusions, the local barium-strontium ratio or the balance with oxygen or titanium can deviate strongly [Jeo04]. In thin films, mechanical stress can particularly impact the material properties, as will be observed during this work.

The hyperbolic decrease of the permittivity in the paraelectric phase is described by the Curie-Weiss law

$$\varepsilon = \frac{C}{T - T_0}, \quad (2.6)$$

where  $C$  is the material's Curie constant and  $T_0$  is the Curie-Weiss temperature. Despite sometimes confused in previous works,  $T_0$  can deviate from  $T_c$ , depending on the order of the phase transition [Was05; Mau11]. The former can be obtained by plotting the inverse of  $\varepsilon$  versus temperature, which is generally not the temperature of the previously described phase transition [MMK85].

### Tunability model

To predict the performance of tunable microwave devices, models for the varactor tunability are mandatory. Several analytical models have been proposed that are all derived from the Ginzburg-Landau theory, which describes the thermodynamic dependence of the polarization on the electric field and temperature [GS03]. Vendik's model is very detailed and relies on physical parameters like Curie constant, Curie

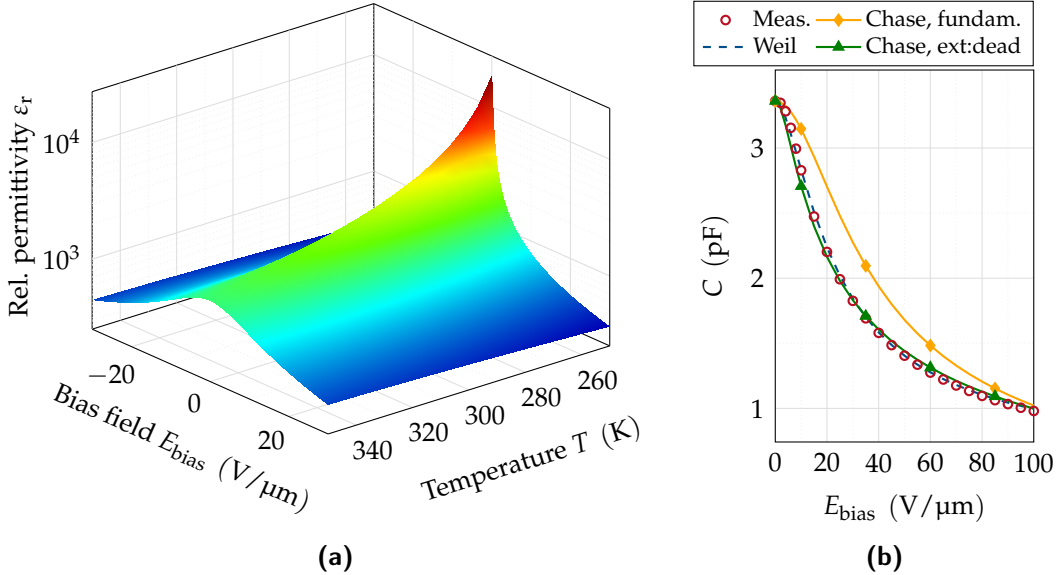


**Figure 2.3:** (a) Modeled relative permittivity for  $\text{Ba}_{0.6}\text{Sr}_{0.4}\text{TiO}_3$  versus electric bias field and temperature according to [VZ97]. (b) Comparison of the modeled capacitance versus bias field by the models of Weil and Chase with respect to an example varactor characterized during this work.

temperature and Debye temperature [VZ97]. As it is sensitive to both electric field and temperature, it can be used to illustrate the decreasing voltage tunability for increasing temperatures in the paraelectric phase. Figure 2.3a shows the calculated material permittivity reported for  $\text{Ba}_{0.6}\text{Sr}_{0.4}\text{TiO}_3$  in [Mau11]. However, although this model relies on physical quantities and is most accurate, it is often hard to apply due to its many degrees of freedom. Especially in thin films, these properties can vary due to mechanical stress and external defects. In practical applications, satisfying results can often be achieved with a simpler model.

The following two are only sensitive to the bias field and refer to a zero-bias capacitance  $C(0)$ . The models refer to the capacitance instead the permittivity, since this property is easily accessible by measurement. Nonetheless, for MIM structures, the same model can be used for both by introducing a scaling factor, compare (2.4). When restraining the polarization to first- and third-order terms, Chase derived with two degrees of freedom for MIM capacitors [CCY05]

$$C(E) = C(0) \left( 2 \cosh \left[ \frac{2}{3} \sinh^{-1} \left( \frac{2E}{E_{0.5}} \right) \right] - 1 \right)^{-1} \quad (2.7)$$

with the unbiased capacitance  $C(0)$  and the electric field strength  $E_{0.5}$  to achieve a tunability of 50 %. This simple model could not be fitted to the varactors in this work as shown in Figure 2.3b. However, Chase suggests several extensions to the fundamental model in (2.7) like the inclusion of charged defects, an untunable fringing capacitance or a dead layer. Incorporating the latter allows a much closer fitting due to the impact of necessary interlayers, compare section 2.3. An even higher accuracy can be expected from further including charged defects, since oxygen vacancies are often observed in the varactors in this work. However, this requires an increased deposition reproducibility as discussed in [CCY05]. In that case, this model can be used for important conclusions on the impact of both deadlayer and charged defects.

On a purely phenomenological basis, Weil defined a model with four degrees of freedom [Wei03]

$$C(E) = C(0) (1 - \tau(E)) \quad (2.8)$$

$$\tau(E) = \tau_{\text{ref}} \cdot (1 + a_1 + a_2) \frac{|E/E_{\text{ref}}|^2}{1 + a_1|E/E_{\text{ref}}| + a_2|E/E_{\text{ref}}|^2} \quad (2.9)$$

with anchor parameters  $E_{\text{ref}}$  and  $\tau_{\text{ref}} = \tau(E_{\text{ref}})$  and the fitting parameters  $a_1$  and  $a_2$  that are non-physical. However, if the physical connection is not needed, this model provides an elegant solution for a highly accurate fitting. In this case, the Weil model tracks the tunability of the example measurement very closely with  $a_1 = 3.2287$  and  $a_2 = 9.4168$ , as obtained by the minimizing root-mean-squared error (RMSE).

The above models all describe the macroscopic behavior; microstructural features are averaged instead of being modeled exactly. More sophisticated models based on a certain distribution order of the feature type (e.g., layered, columnar, spherical) have been described in [Tag+03]. For sintered ceramics, the spherical model usually shows the best structural similarity. For an even higher accuracy, it was incorporated in an electromagnetic (EM) simulation and extended by sintering necks between the spheres in [Gie09]. Further, modeling quaternary ceramics succeeded particularly well in [Wie17] by using a gravity-ordered distribution of spheres with, afterwards, varying sizes to produce partial overlap. However, these models are beneficial only when microstructural features like local doping or defects are present. As, throughout this work, single-crystal BST is grown where, if at all, only ionic defects can be expected, these models are not used here.

### 2.1.2 Microwave Loss Mechanisms

A varactor's microwave loss comprises the finite conductivity of the electrodes and dielectric loss. Regarding the latter, two sub-groups are distinguished: Intrinsic loss that is common to all dielectrics, and extrinsic loss that is related to defects in the lattice introduced, e.g., during manufacturing or engineering the material. The dielectric loss can be described by a complex permittivity

$$\underline{\epsilon} = \epsilon' - j\epsilon'' = \epsilon (1 - j \tan \delta_{\text{diel}}), \quad (2.10)$$

with the material's loss factor  $\tan \delta_{\text{diel}}$  and the shorter notation for the real part of the permittivity  $\epsilon = \epsilon'$ . A very detailed understanding on different loss mechanisms has been developed during the second half of the 20<sup>th</sup> century [CC73; Pop+78; Tag79; Tag81; GT86; GT91; TPS93; Tag+03; Kit05; ATS05; SC12]. However, considering the application in microwave devices, a fundamental discussion of the underlying dielectric loss mechanisms is often not fruitful. This is due to the concurrence of the mechanisms and limited insight into the exact material composition and defect distribution. Nonetheless, an accurate modeling of the overall characteristic versus frequency and temperature is essential as this provides all significant information to designers of components and systems. To derive these models, a fundamental understanding of the significant loss mechanisms is beneficial. Hence, after shortly reviewing the physical origin, their overall frequency and temperature dependence will be described in the following.

#### Intrinsic Loss

In crystals, the intrinsic loss originates from the interaction of the applied EM field with the thermal phonons in the material [Tag+03; Kit05]. Three mechanisms can occur: The three-quantum loss, the four-quantum loss and the quasi-Debye loss. In centrosymmetric crystals, only the former two are relevant, as the latter only occurs in lattices with non-centrosymmetric unitcells [GT86]. If the quasi-Debye loss is enabled by non-centrosymmetry, it can easily be by orders stronger than the other two [ATS05]. In ferroelectric BST in the paraelectric phase, both cases occur, as in the unbiased and biased state the unitcell is centrosymmetric and non-centrosymmetric, respectively. Note that intrinsic mechanisms generally are of minor significance in the lower GHz domain for conventional BST varactors as will be shown in this section. However, for single-crystal BST extrinsic loss contribute less, rendering the fundamental limit given by intrinsic loss more prominent.

Both the three- and the four-quantum mechanism describe the coalescence or the

decay of phonons. For the following derivation, all phonon or photon frequencies refer to angular frequencies. The energy of a quantum with angular frequency  $\omega$  is given by

$$E = \hbar\omega = \frac{\hbar}{2\pi}2\pi f = hf \quad (2.11)$$

with the reduced Planck constant  $\hbar$ . The EM field has a much lower angular frequency  $\omega$  than the thermal frequency of the phonons  $\Omega \gg \omega$  [Tag81]. Nonetheless, the EM quanta and thermal phonons interact with each other as the former causes a transition between different phonon branches, i.e., directions of the phonon wave vector [Tag79]. Pictorially speaking, e.g., in three-quantum coalescence processes, a quantum of the electric field attaches to an acoustic phonon to form another phonon with slightly different properties [GT86]. Thereby, the energy of the EM quantum gets transformed, which is a loss for the microwave signal. In the three-quantum mechanism, the wave vectors and frequencies of the two phonons need to be very similar:

$$\Omega(\vec{k}) \pm \Omega^*(\vec{k}^*) = \omega, \quad \vec{k} \pm \vec{k}^* = 0, \quad (2.12)$$

where  $\{\Omega(\vec{k}), \vec{k}\}$  and  $\{\Omega(\vec{k}^*), \vec{k}^*\}$  describe the angular frequency and wave vector of the initial and resulting phonon, respectively. (2.12) follows from the conservation laws for energy and momentum, as the energy of a phonon or photon depends linearly on its frequency. In the four-quantum mechanism, phonons with much more differing properties can principally contribute. The full wave vector space can be exploited and the mechanism is also much less sensitive to the crystal symmetry [GT91; SC12]:

$$\Omega(\vec{k}) \pm \Omega^*(\vec{k}^*) \pm \Omega^\#(\vec{k}^\#) = \omega, \quad \vec{k} \pm \vec{k}^* \pm \vec{k}^\# = \vec{b}, \quad (2.13)$$

with angular frequency  $\Omega(\vec{k}^\#)$  and wave vector  $\vec{k}^\#$  of the third phonon and  $\vec{b}$  a reciprocal lattice vector. A detailed explanation of the reciprocal lattice and its relation to the direct (physical) lattice can be found in [Kit05]. When adding an electric bias field, the unitcell is not centrosymmetric anymore, enabling the quasi-Debye loss mechanism. It arises from the linear change of the phonon frequency under a small electric field [ATS05]

$$\Omega(\vec{k})_{\text{non-CS}} \propto E. \quad (2.14)$$

Due to that, an oscillating electric field will cause a time modulation of the phonon frequency. After having calculated its impact on the dielectric loss, compare (2.22)

**Table 2.1:** Phonon-related material properties of SrTiO<sub>3</sub> and BaTiO<sub>3</sub>.

	SrTiO <sub>3</sub>	BaTiO <sub>3</sub>	
$A_{\text{sm}}$	$((\text{cm}\sqrt{\text{K}})^{-1})$	5.3	3.5
$T_0$	(K)	35	387
$\Theta_D$	(K)	497	693

below, one can easily recognize its similarity with the (original) Debye loss mechanism [Kao04], depicting it as a relaxation process [CC73; ATS05]. Analogue to the Debye loss, where the dipoles relax in tracking the orientation of the electric field for high frequencies, the phonon distribution function relaxes giving rise to the dielectric loss.

The analytical description of these mechanisms in terms of loss tangent is very complex. In [GT91], a good overview is given that differentiates between different temperature domains and crystal symmetries, and also ordinary dielectrics and ferroelectrics. Especially due to the strong restrictions on the wave vector in the three-quantum mechanism, a strong spread in frequency and temperature dependence has been observed for crystals in general:

$$\tan \delta \propto \omega^n T^m \quad (2.15)$$

with temperature  $T$  and  $n \in [1, 5]$ ,  $m \in [1, 9]$  [Tag+03]. Restricting oneself to displacive ferroelectrics with a centrosymmetric cubic paraelectric phase (like BaTiO<sub>3</sub>, SrTiO<sub>3</sub> or Ba<sub>x</sub>Sr<sub>1-x</sub>TiO<sub>3</sub>), a more concrete characteristic was derived. However, constraints on the EM frequency and the temperature are given by the applied theory. The former must satisfy

$$\omega \ll \Omega_0. \quad (2.16)$$

The soft-mode frequency can be assessed by (2.2) and linear interpolation of the parameters given in Table 2.1. Most BST compositions in the paraelectric phase exhibit a soft-mode frequency in the THz range, e.g., for Ba<sub>0.5</sub>Sr<sub>0.5</sub>TiO<sub>3</sub>, one obtains  $\Omega_0 = 2\pi \cdot 1.25 \text{ THz}$ .<sup>1</sup> Thus, (2.16) does practically not constitute a limitation for microwave frequency analysis. The Ba<sub>x</sub>Sr<sub>1-x</sub>TiO<sub>3</sub> parameters can be assumed to range in-between these two extremes [VZN02]. The temperature must satisfy<sup>2</sup>

$$T \gtrapprox \frac{\hbar\Omega_0}{k_B} \gtrapprox \frac{\hbar\Omega_D}{k_B\sqrt{\chi}} = \frac{\Theta_D}{\sqrt{\chi}} \quad (2.17)$$

<sup>1</sup>The relation of wave number  $1/\lambda$  in cm<sup>-1</sup> and frequency is given by  $f = c \cdot 1/\lambda$  [Lew09].

<sup>2</sup>In the following,  $\gtrapprox$  depicts the equaling of the former expression to the order of magnitude of the latter,  $\gtrsim$  analogue.

with the reduced Planck constant  $\hbar$ , Boltzmann constant  $k_B$ , lattice susceptibility  $\chi$ , Debye frequency  $\Omega_D$  and Debye temperature  $\Theta_D$ . With Table 2.1 and a typical susceptibility of a few hundred, one can easily assess this constraint to be uncritical for typical applications of microwave tunable devices. Thus, regarding this work, the general applicability of the following equations (2.20)–(2.22) can be assumed. All of them contain the correlation factor

$$\xi = \mu\sqrt{\chi}, \quad (2.18)$$

$$\mu = \frac{k_B T}{Mv^2} \quad (2.19)$$

with the parameter of lattice anharmonicity  $\mu \approx 0.01$ , average ion mass  $M$  and average speed of sound  $v$ . Due to the various contributing atoms with varying ion mass and average sound velocity, just the order of the loss factors attributed to the respective mechanisms can be given [GT91]:

$$\tan \delta_{\text{three-quantum}} \sim \xi \frac{\omega \Gamma_0}{\Omega_0^2} \left[ \ln \left( \frac{\Omega_0^2}{\omega^2 + 4\Gamma_0^2} \right) + \frac{\omega}{\Gamma_0} \arctan \left( \frac{\omega}{2\Gamma_0} \right) \right], \quad (2.20)$$

$$\tan \delta_{\text{four-quantum}} \sim \xi \frac{\omega \Gamma_0}{\Omega_0^2}, \quad (2.21)$$

$$\tan \delta_{\text{quasi-Debye}} \sim \xi \frac{\omega \Gamma_0}{\omega^2 + \Gamma_0^2}, \quad (2.22)$$

describe the three-quantum, four-quantum and quasi-Debye loss tangent, respectively, with soft-mode damping  $\Gamma_0 \sim \mu \Omega_D$  and soft-mode frequency  $\Omega_0 \sim \Omega_D / \sqrt{\chi}$ . By replacing  $\xi$ ,  $\Gamma_0$  and  $\Omega_0$ , the general dependence on frequency  $\omega$ , temperature  $T$  and susceptibility  $\chi \approx \epsilon_r$  can be derived:

$$\tan \delta_{\text{three-/four-quantum}} \propto \omega T^2 \chi^{3/2}, \quad (2.23)$$

$$\tan \delta_{\text{quasi-Debye}} \propto \frac{\omega T^2 \sqrt{\chi}}{\omega^2 + \Omega_D^2 / \chi}, \quad (2.24)$$

The non-linear terms in (2.20) introduce an error that, however, becomes significant only for greatly increased frequencies. An order of magnitude estimate of each intrinsic loss mechanism to the overall loss balance versus frequency is shown in Figure 2.4 for a  $\text{Ba}_x\text{Sr}_{1-x}\text{TiO}_3$  crystal [GT91; Tag+03]. As the theory is constrained to  $\omega \ll \Omega_0$ , the high-frequency region is just displayed by tendency. Thus, the quasi-Debye mechanism dominates the overall characteristic. Up to  $\omega_{\text{lin}}$ , all three contributions can well be approximated as proportional to frequency. The wide applicability of this assumption will be shown in the following.

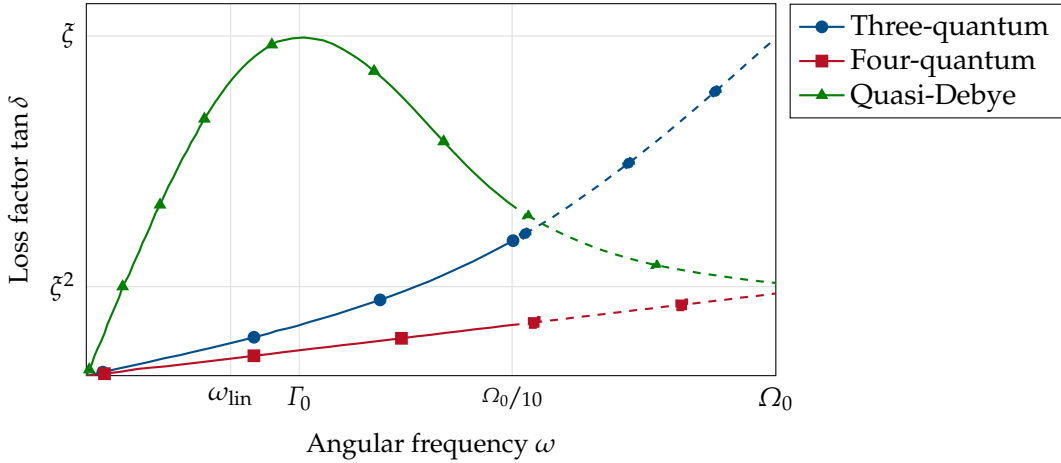


**Figure 2.4:** Order-of-magnitude estimate of the three intrinsic loss mechanisms in displacive ferroelectric crystals in the paraelectric phase versus angular frequency [GT91; Tag+03]. The dashed line above  $\Omega_0/10$  indicates that the estimate is, strictly speaking, only valid for  $\omega \ll \Omega_0$ . Both axes are in logarithmic scale.

This is done for  $\text{Ba}_{0.5}\text{Sr}_{0.5}\text{TiO}_3$  by an analysis based on exemplary material parameters. Therein, a Debye temperature of  $\Theta_D = 595\text{ K}$  was estimated for  $x = 0.5$  by a linear dependence on the relative barium concentration  $x$ . The values for  $x = \{0,1\}$  are listed in Table 2.1. Furthermore, an untuned and tuned susceptibility of 600 and 200 was assumed, respectively, as typical values for thin films often reported [Kim+00; Del+03; Oua+05] and characterized in this work.  $M = 6.9195 \cdot 10^{-26}\text{ kg}$  and  $v = 6 \cdot 10^3\text{ m/s}$  are chosen as a rough estimate by averaging the atom masses of  $\text{Ba}_{0.5}\text{Sr}_{0.5}\text{TiO}_3$  and as an example value from [Kas+73], respectively. However, these two parameters strongly influence the phonon damping  $\Gamma_0$  and the order of magnitude of all three mechanisms. Therefore, they must be validated for each

**Table 2.2:** Intrinsic loss mechanism model parameters of  $\text{Ba}_{0.5}\text{Sr}_{0.5}\text{TiO}_3$ .

	unit	value	source
$\Theta_D$	(K)	595	lin. interp.
$T_{\text{model}}$	(K)	300	
$\chi(0V)$		600	[Kim+00; Del+03; Oua+05]
$\chi(\text{bias})$		200	[Kim+00; Del+03; Oua+05]
$M$	(kg)	$6.92 \cdot 10^{-26}$	avg. ion mass
$v$	(m/s)	$6 \cdot 10^3$	[Kas+73]

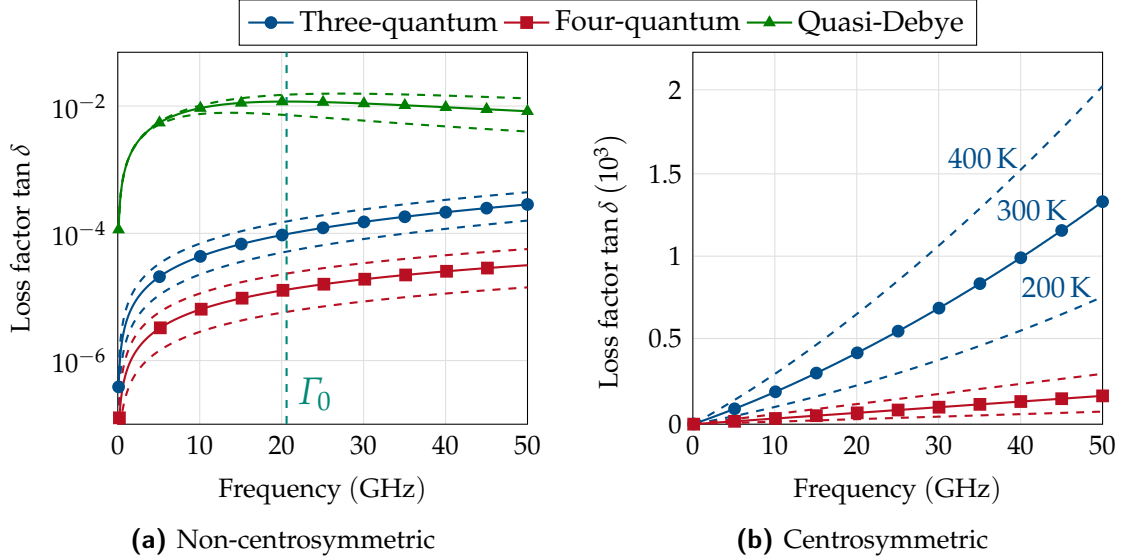


**Figure 2.5:** Assessment of the contribution of each intrinsic mechanism to the overall loss. The solid lines show the characteristic at room temperature (300 K) and the dashed lines the increased and decreased loss for 400 K and 200 K, respectively.

processed material in a concrete case.<sup>3</sup> All parameters are summarized in Table 2.2. In the biased non-centrosymmetric case, Figure 2.5a, the general dominance of the quasi-Debye mechanism is clearly visible. The three- and four-quantum loss can be neglected without noticeable harm to the accuracy. The order-of-magnitude peak estimate yields  $\tan \delta_{\text{quasi-Debye,max}} = 0.012$  at  $\Gamma_0/2\pi = 20.6$  GHz. A direct frequency proportionality can be assumed up to  $\omega_{\text{lin}}/2\pi \approx 6.5$  GHz with an initially just slowly increasing error above that frequency. In the untuned centrosymmetric case, Figure 2.5b, the intrinsic loss contribute stronger than for the tuned case due to the increased susceptibility. Both mechanisms show just a slightly-more-than-linear increase with frequency which can often be neglected [TPS93]. In conclusion, in the range up to 10 GHz, a direct proportionality for the frequency dependence of the intrinsic loss is a valid assumption when, e.g., considering in a schematic model. To illustrate the temperature impact, two dashed lines for every mechanism have been added in Figure 2.5, displaying the deviation of  $\pm 100$  K from room temperature of 300 K, respectively. Intuitively, the loss increase with temperature. Note, that for the dominating quasi-Debye mechanism, the temperature dependence is negligible for frequencies up to 10 GHz. In the centrosymmetric case, the temperature impacts the intrinsic mechanisms stronger. However, the sum of the three- and the four-

<sup>3</sup>In a thin film, strain, locally altered composition and defects can strongly vary the stiffness, which in turn strongly changes the speed of sound  $v$ .

quantum loss is  $2.2 \cdot 10^{-4}$  at 10 GHz and, thus, will likely be negligible compared to extrinsic defects or electrode loss in most cases.

In total, the quasi-Debye loss constitutes the intrinsic limitation for the microwave performance of BST varactors in tunable devices (the impact of defects will be described below). Therefore, a simpler expression was derived for the case of EM frequency smaller than typical damping of phonon contribution to the loss  $\omega \leq \omega_{\text{lin}}$  in Figure 2.4 [Tag+03; ATS05]. Then, the quasi-Debye loss can be described as approximately proportional to the frequency and relative tunability (2.3)

$$\tan \delta_{\text{quasi-Debye}}(E) = \omega A_{\text{QD}} I(E) \tau(E) \quad (2.25)$$

with proportionality factor  $A_{\text{QD}}$  and intensity scaling  $I(E)$  ( $\approx 1$  for weak biasing fields). Different sources estimate different values of  $A_{\text{QD}}$  for  $x = 0.6$ , i.e., 0.1 ps in [ATS05] and 0.7 ps in [Tag+03]. Furthermore,  $A_{\text{QD}}$  can increase by orders of magnitude for a decreased barium content  $x$ . For stronger fields, the change in  $I(E)$  strongly depends on the crystal composition. The two cases  $I(E, x = 0) \gg 1$  and  $I(E, x = 0.6) \leq 1$  were described in [ATS05] with the difference coming from a smaller flexoelectric coupling<sup>4</sup> observed for an increased barium content. The resulting contribution of the quasi-Debye mechanism is shown in Figure 2.6a. Both estimates match well to the order-of-magnitude estimate done in Figure 2.5a.

Note, that in addition to the well-studied intrinsic mechanisms above, a low-frequency relaxation (LFR) was described in [VZN02] phenomenologically based on the experimental data provided in [Ven+77]. To the author's knowledge, the physical explanation of its nature is missing yet. However, the experimental data could be coarsely modeled by understanding the ferroelectric mode as a damped harmonic oscillator with memory [BZ74, pp.118-124]. Therein, the soft mode is damped by the interaction with other modes which is affected by the external EM field. From the response function of the damped-oscillator soft mode, the microwave loss tangent can be derived as

$$\tan \delta_{\text{LFrelax}} \sim \frac{A_{\text{LFR}} \frac{\omega}{\omega_{\text{LFR}}}}{A_{\text{LFR}} + G^{-1} \left( 1 + \left( \frac{\omega}{\omega_{\text{LFR}}} \right)^2 \right)} \quad (2.26)$$

with material-dependent  $A_{\text{LFR}} = 0.005$ , the inverse of the duration of a "collision" with other modes  $1/\tau_{\text{sm}} = \omega_{\text{LFR}}/2\pi = 10 \text{ MHz}$  and  $G^{-1} \approx 0.435$  as a highest-loss

---

<sup>4</sup>Flexoelectricity is a property of all insulators whereby they polarize under the impact of a strain gradient, i.e., when experiencing an inhomogeneous deformation [ZCT13]. Note the difference to piezoelectricity, which relates to the strain itself and can be active under homogeneous strain as well but only for certain materials.

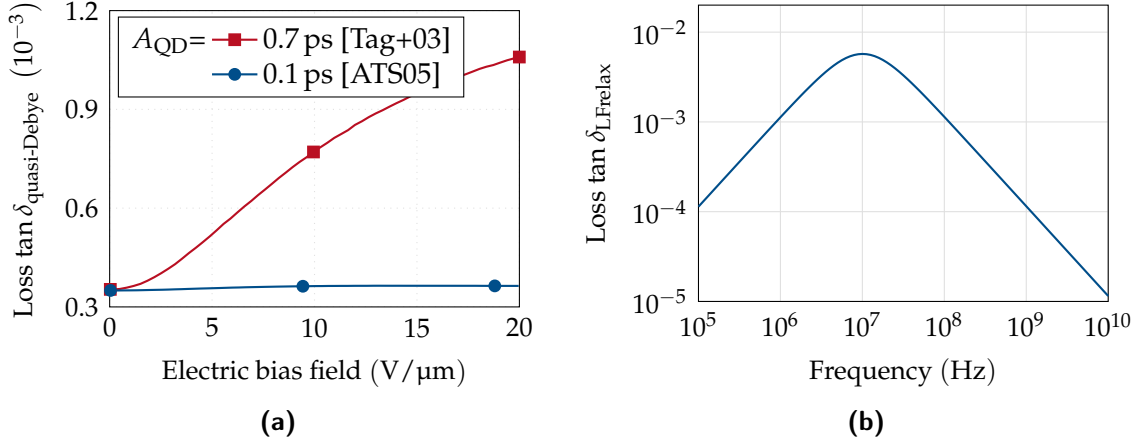


**Figure 2.6:** (a) Simulated field dependence of the quasi-Debye loss versus electric field for single-crystal  $\text{Ba}_{0.6}\text{Sr}_{0.4}\text{TiO}_3$  at 1 GHz and 300 K. In [Tag+03] and [ATS05],  $A_{\text{QD}}$  is estimated as 0.7 ps and 0.1 ps, respectively. (b) Simulated loss contribution by the phenomenological low-frequency relaxation process.

estimate in the absence of a bias field [VZ97]. An order-of-magnitude estimate is shown in Figure 2.6b.  $\tan \delta_{\text{LFrelax}}$  decreases by  $\propto 1/\omega$  above the peak frequency  $\omega_{\text{LFR}}$ , resulting in the order of  $10^{-3}$  and  $10^{-4}$  at 100 MHz and 1 GHz, respectively. Hence, in practical microwave applications, the quasi-Debye loss and extrinsic mechanisms are likely to render this effect negligible.

### Extrinsic Loss

In processed materials, defects and inhomogeneities can introduce additional loss. Especially in the lower GHz domain, these can easily shadow the intrinsic ones, see Figure 2.7a. The limit for real loss factors is given by the intrinsic mechanisms with the margin calculated from the model presented in [VZN02; Men+11]. Data from single crystal measurements confirms the order of magnitude for the modeled data [Bet69]. For comparison, exemplary measurement data from a coplanar waveguide (CPW) thin film characterization is shown, indicating a significant amount of extrinsic loss contribution [Oua+05]. The higher the crystal quality as, e.g., expected in this work for epitaxial BST grown on an oxide electrode, the closer the effective loss approaches the intrinsic loss margin. Three loss sources are distinguished in [Tag+03] that are often observed as significant in processed films: Charged defects, firstly, generate acoustic waves and, secondly, induce additional quasi-Debye loss

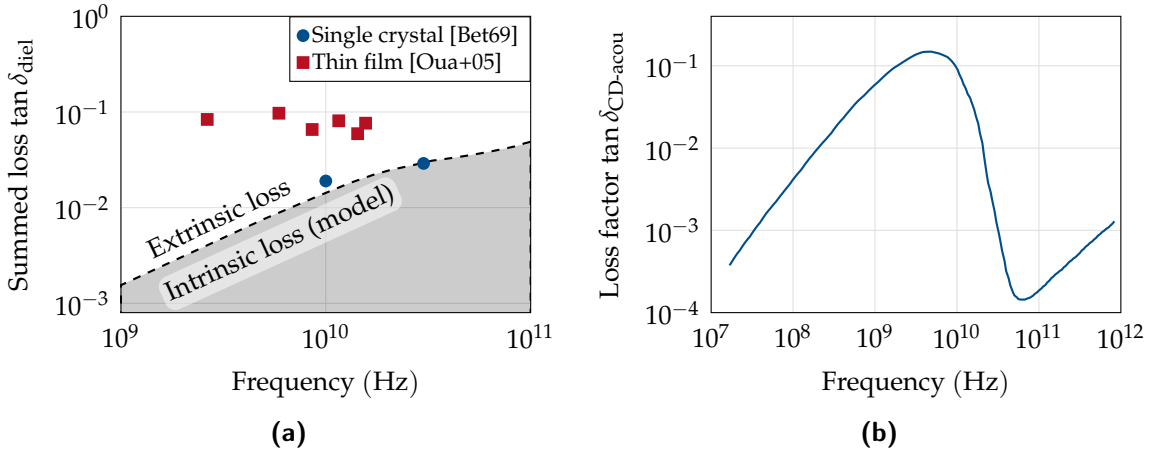


**Figure 2.7:** (a) Comparison of exemplary thin film and single crystal data to intrinsic loss contributions. (b) Loss tangent from charged-defect-induced quasi-Debye mechanism, extracted from calculated complex permittivity based on exemplary defects in [VP71].

due to local polar regions. Thirdly, loss due to universal relaxation occurs. However, this cannot constitute a complete list of all possible extrinsic mechanisms. Several device-dependent impacts can also increase the loss of devices depending on the fabrication due, e.g., to bad interfaces, rough metalization or acoustic resonances. Since the latter are generally significant in all BST varactors (independent of fabrication), they are as well discussed in this section.

Charged defects can introduce a permanent local polarization, which invokes electrostriction similar to an external bias field, see section 2.1.3. Under an RF field, the harmonic movements of the ions excite acoustic waves in the lattice. In terms of quantum mechanics, the energy of one photon is absorbed to excite one acoustic phonon [Gar90]. To rate how disturbing this loss mechanism contributes, [VP71] distinguishes between point, line and two-dimensional defects. For a  $\text{BaTiO}_3$  layer with typical defect concentration, a qualitative analysis of the impact on the complex permittivity was done.<sup>5</sup> The resulting loss tangent in Figure 2.7b was extracted from its plot [VP71] and shows the possible dominance of this mechanism in the microwave frequency range. Of course, this is strongly depending on the actual

<sup>5</sup>The analytical model for the complex permittivity from [VP71] is not given here, as it depends on many material parameters that are often unknown in a processed film since varying strongly from one sample to the other. A more practical model can be found in [Tag+03] that, however, is given without derivation.

defect content. In many publications (as in this work), much lower loss tangents are observed, indicating the given loss tangent being often too pessimistic.

Besides electrostriction, it is expected that these defects also introduce an additional loss of the quasi-Debye type. Comparable to the bias voltage that shifts the unitcell into non-centrosymmetry, defects can also induce a permanent dipole moment. While the presence of this effect can be well-understood principally, an analytical expression for the macroscopic loss tangent is not available. This effect clearly depends on the exact defect structure, which can be strongly inhomogeneous. A dependence on the permittivity with respect to the type of defect (point, line, area) based on their respective polarization is described in [Tag+03]. However, assuming that the external electric field enabling the intrinsic quasi-Debye mechanism is much stronger than the field due to charged defects, a much weaker contribution than in Figure 2.5a is expected.

Experimentally, an universal relaxation law was observed in  $\text{Ba}_x\text{Sr}_{1-x}\text{TiO}_3$  up to 20 GHz [Hor+95; Ban+98]. A widely accepted description is given by the Curie-von Schweidler equations, which are based on Debye-type relaxations of the relaxation current  $J \propto \exp(-t/\tau_{\text{CVS}})$  with distributed relaxation times  $\tau_{\text{CVS}}$  [Was95, pp.233-235]. Therein, this distribution is attributed to a possible variation in the charge transport barrier, e.g., at grain boundaries in the dielectric. In [Fuk+96], the presence of oxygen vacancies were identified as an contributor to this effect that might amplify its significance. Considering only this relaxation mechanism, one can find [Tag+03]

$$\varepsilon_{\text{CVS}} \propto (j\omega)^{n-1} \quad (2.27)$$

However, this relaxation is significant only when observing several decades of frequency, starting from the mHz domain. In [Ban+98], a quasi-constant loss tangent was found with only 4 % quasi-linear increase from 1 mHz to 35 GHz. Fitting the reported data in that work yields  $n = 0.9995$ . For the capacitance, a change of -5 % was observed. Hence, when observing only fewer decades of frequencies, this effect is expected to be invisible. A more detailed discussion of dielectric relaxation mechanisms can be found in [Jon83] and [Fu14].

Finally, loss due to acoustic resonances must be considered in all ferroelectric varactors. Their origin is electrostriction-induced piezoelectricity; the physical background is discussed in more detail in section 2.1.3. They can be easily dominating for the component quality factor, though the conduction loss actually becomes dominating for increasing GHz frequencies, compare the following comparison by the schematic model. In realized devices, acoustic resonances easily degrade the quality factor to  $Q < 10$ , yielding the device unusable, as can be seen, e.g., in section 4.2.3. Though this transduction is inherent for ferroelectric devices, it is sorted

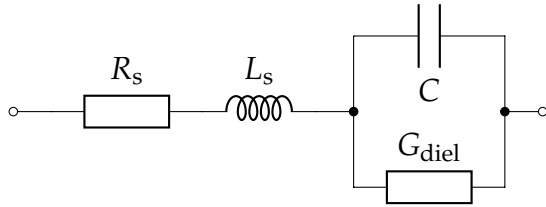


**Figure 2.8:** Schematic of the RLC model with  $G_{\text{diel}}$  representing the dielectric loss.

to the extrinsic loss mechanisms due to the dependence on the device geometry. By choosing small layer thicknesses, the resonator lengths are decreased, which in turn increases the resonating frequencies. However, commonly workable minimum layer thicknesses are about a few 100 nm. This mainly constitutes the common upper frequency limitation of ferroelectric varactors to 2 GHz – 3 GHz. However, oxide electrodes might overcome this limitation by providing a combination of low reflection of acoustic waves due to its structural similarity and little excitation due to thin layers. The success of this approach is presented in section 4.2.5.

In conclusion on all presented loss mechanisms, the degradation due to acoustic resonances is usually dominant. They occur due to bias-induced piezoelectricity as is described in section 2.1.3. From the intrinsic mechanisms, a significant contribution can only be expected by the quasi-Debye loss. Given a sufficiently low extrinsic loss, these mechanisms can be distinguished in integrated layers as the latter is not geometry-dependent.

### Schematic Varactor Model

For integrating all the above loss mechanisms in a macroscopic varactor model, the loss tangents of each mechanism can be summed up:

$$\tan \delta_{\text{diel}} = \sum_m \tan \delta_m \quad (2.28)$$

with  $m$  enumerating all considered mechanisms like, e.g., quasi-Debye, three-/four-quantum, charged defects. However, in a fabricated component, a clear distinction of intrinsic and extrinsic mechanisms will often be impracticable due to the limited insight in integrated films. Furthermore, electrode/connector loss must be considered in components in series to the capacitance. A common schematic model for varactors is the RLC model shown in Figure 2.8. Analytically, it can be described by

$$Z_{\text{var}} = R_s + j\omega L_s + \frac{1}{j\omega \underline{C}}, \quad (2.29)$$

with electrode resistance  $R_s$  and inductance  $L_s$  and complex capacitance  $\underline{C} = C(1 - j \tan \delta_{\text{diel}})$ . Note, that though  $G_{\text{diel}} = \omega C \tan \delta_{\text{diel}}$  can be understood as a parallel resistance, it shows a significant frequency dependence for the typically dominant mechanisms. This model yields for the component's quality factor

$$Q_{\text{var}} = -\frac{\Im\{Z_{\text{var}}\}}{\Re\{Z_{\text{var}}\}} = \frac{1 - \omega^2 L_s C (1 + \tan^2 \delta_{\text{diel}})}{\omega R_s C (1 + \tan^2 \delta_{\text{diel}}) + \tan \delta_{\text{diel}}} \approx \frac{1 - \omega^2 L_s C}{\omega R_s C + \tan \delta_{\text{diel}}}. \quad (2.30)$$

Using  $C = 10 \text{ pF}$  and  $\omega = 2\pi \cdot 1.59 \text{ GHz} = 10^{10} \text{ rad/s}$  as an order-of-magnitude estimate for varactors deployed in microwave frontends, an electrode resistance of  $R_s = 0.01 \Omega$  and a dielectric loss of  $\tan \delta_{\text{diel}} = 0.001$  contribute equally to the overall varactor loss. Hence, in a real component, both effects need to be considered.

### 2.1.3 Induced Piezoelectricity

Piezoelectricity describes the proportional connection of mechanic deformation and attraction/repulsion of electric charges in solid materials with a certain crystallinity. The direct piezoelectric effect describes the impact of external mechanic stress leading to a deformation of the crystal lattice. This shift of ions leads to an altered dipole moment in the unit cell and, hence, excites an overall electric field, causing a charge accumulation on the solid's surface. In the opposite, the converse piezoelectric effect describes the mechanic actuation in ferroelectrics, which causes the acoustic loss in BST varactors. An externally applied electric field interacts with the dipoles in the crystal lattice. Pictorially speaking, it pulls against the ions in the lattice [Jaf58], leading to mechanic stress. If the lattice is sufficiently ordered as in crystals and many ceramics, this deformation adds up across all unit cells, leading to a significant impact on the macroscopic scale. Typically, the material will elongate in the direction of the electric field while it narrows transversally.

The thermodynamic potential in the form of the differential elastic enthalpy<sup>6</sup> is [Mas50; 3]

$$dH_2 = \tilde{\bar{T}}_{ij} d\tilde{\bar{S}}_{ij} - \tilde{\bar{D}}_m d\tilde{\bar{E}}_m + \Theta d\sigma, \quad i,j,m = 1 \text{ to } 3 \quad (2.31)$$

with strain  $\tilde{\bar{S}}$ , stress  $\tilde{\bar{T}}$ , electric displacement  $\tilde{\bar{D}}$ , electric field  $\tilde{\bar{E}}$ , temperature  $\Theta$  and entropy  $\sigma$ . Generally, adiabatic conditions, i.e., no significant heat transfer due to crystal vibrations can be assumed, i.e., which allows to neglect the temperature

---

<sup>6</sup>In this derivation, Einstein's convention is used that interprets repeated indices as summation with respect to that index.

addend. As all ferroelectrics, BST is not intrinsically piezoelectric in the paraelectric phase due to its centrosymmetric unit cells. However, as ferroelectrics generally exhibit a remarkably high permittivity, the impact of electrostriction is significant. Mason has derived the constitutive electromechanical equations for this case in tensor notation by partially differentiating (2.31) to [Mas50]

$$\begin{aligned}\overset{\sim}{S}_{ij} &= -\frac{\partial H_2}{\partial \overset{\sim}{T}_{ij}} = s_{ijkl}^D \overset{\sim}{T}_{kl} + Q_{ES,ijmn} \overset{\sim}{D}_m \overset{\sim}{D}_n \\ \overset{\sim}{E}_m &= \frac{\partial H_2}{\partial \overset{\sim}{D}_m} = \beta_{mn}^T \overset{\sim}{D}_n - 2Q_{ES,ijmn} \overset{\sim}{D}_n \overset{\sim}{T}_{ij},\end{aligned}\quad (2.32)$$

with elastic compliance  $s_{ijkl}$ , electrostriction coefficient  $Q_{ES,ijmn}$  and dielectric impermittivity  $\beta_{mn}$ . The superscripts  $()^D$  and  $()^T$  depict these parameters to be invariable to electric displacement and stress, respectively.<sup>7</sup>

This work is confined to MIM structures, where the bias field is laterally constant and parallel to the RF field, compare Figure 3.1. Anticipating the test structure presented in section 3.1, (2.32) can be greatly simplified due to the very large aspect ratio between the top electrode (TE) diameter and the BST thickness. In this case, boundary and transversal effects at the periphery are negligible and, hence, only fields perpendicular to the films, i.e., in direction 3 must be considered.<sup>8</sup> With these constraints, one obtains

$$\begin{aligned}\overset{\sim}{S} &= s^D \overset{\sim}{T} + Q_{ES} \overset{\sim}{D}^2 \\ \overset{\sim}{E} &= \beta^T \overset{\sim}{D} - 2Q_{ES} \overset{\sim}{D} \overset{\sim}{T},\end{aligned}\quad (2.33)$$

where, from now on, the subscripts of all fields are dropped and all quantities generally refer to the vertical direction (e.g.,  $D_3$ ,  $s_{33}$  or  $T_{33}$ ). Under an applied direct current (DC) bias voltage, piezoelectricity is introduced, since the bias voltage shifts the titanium ion off its center position and, hence, distorts the cubic symmetry. In varactors for microwave applications, the fields can usually be described by the superposition

$$\overset{\sim}{E} = \bar{E} + \tilde{E} = E_{DC} + E, \quad (\overset{\sim}{D}, \overset{\sim}{S}, \overset{\sim}{T} \text{ analogue}) \quad (2.34)$$

with the electric DC bias field  $E_{DC}$  and the RF signal  $E$ . Other than the RF-induced stress  $T$ , the static stress  $T_{DC}$  must be uniform and, hence, vanish due to the boundary conditions. This allows to reformulate (2.33) to the piezoelectric constitutive

<sup>7</sup>Due to the link of mechanic and dielectric fields, the value of the *mechanic* proportionality factor depends on the *electric* field/displacement, and vice versa.

<sup>8</sup>The weak asymmetry introduced by the spot-wise grounding of the on-wafer probe is no conflict since the conductivity of the TE is much higher than the one of the BE.

equations in the strain-voltage form

$$\begin{aligned} S &= s^D T + g_{\text{ind}} D \\ E &= \beta^T D - g_{\text{ind}} T, \end{aligned} \quad (2.35)$$

with the induced piezoelectric coupling coefficient

$$g_{\text{ind}} = 2Q_{\text{ES}} D_{\text{DC}}. \quad (2.36)$$

These equations are fundamental to modeling the material stack as an acoustic resonator in Section 4.2. Then, it's more practical to reformulate the piezoelectric equations (2.35) into the stress-charge form

$$\begin{aligned} T &= c^E S - e_{\text{ind}} E \\ D &= \varepsilon^S E + e_{\text{ind}} S, \end{aligned} \quad (2.37)$$

with induced piezoelectric coefficient  $e_{\text{ind}}$ , elastic stiffness  $c$  and permittivity  $\varepsilon$ . Due to the crystal symmetry<sup>9</sup>, the otherwise sophisticated tensor inversion necessary for calculating the parameters in (2.37) [Mas50] gets simplified to scalar operations, i.e.,

$$c^E = \left[ s^D + g_{\text{ind}}^2 \varepsilon^T \right]^{-1} \quad (2.38)$$

$$e_{\text{ind}} = \varepsilon^T c^E g_{\text{ind}} \quad (2.39)$$

$$\varepsilon^S = \varepsilon^T - e_{\text{ind}}^2 / c^E. \quad (2.40)$$

In conclusion, although BST is not piezoelectric for zero bias, electrostriction leads to an induced piezoelectric effect under bias. In fact, the generally large electrostriction coefficient of ferroelectrics leads to a significant induced piezoelectricity that is enhancing with a stronger bias field. Pictorially speaking, the oscillating electric field pulls on the dipoles via the electrostriction effect and excites acoustic oscillations in the BST crystal lattice.

It is noteworthy that an effective loss is not necessarily observed, as the direct piezoelectric effect simultaneously harvests the energy for EM oscillations. No significant intrinsic loss connected with this transduction has been reported yet. On the contrary, its general insignificance is important for bulk/surface acoustic wave (BAW/SAW) devices. Therein, the low conversion loss enables the design of very-high quality filters with  $Q > 2500$ , e.g., for mobile communication devices [Abb+17]. When, e.g., sandwiched between two electrodes in an MIM configuration, the piezoelectric transduction causes waves in the BST layer with finite thickness that are

---

<sup>9</sup>The crystal structure of BST belongs to the tetragonal class 4mm [Smi+08].

reflected at the electrodes (BAW). Harmonic excitation and repeated reflection of the acoustic waves can, for certain frequencies, cause constructive interference, i.e., acoustic resonances. In BAW/SAW filters, this property is highly valuable as a highly frequency-selective energy transmitter. However, this changes dramatically when using BST in varactors for tunable microwave systems. Instead of double transduction from the electric to the mechanic domain and back, the desired property is the tunable charge separation at the electrodes, i.e., the capacitance. At acoustic resonance frequencies, the RF signal does suffer a tremendous loss while polarizing the ferroelectric due to the self-enhancing mechanic lattice vibrations. This phenomenon was discussed with the other microwave loss mechanisms in section 2.1.2.

Note that mechanical properties like sound velocity and acoustic impedance are dependent on mechanical stress in the film, which in turn is connected to atomic defects. Therefore, a remarkable spread is observed when studying reported data on mechanical (and dielectric) properties; an individual characterization of given thin films is usually necessary.

## 2.2 Conducting Strontium Molybdenum Oxide (SMO)

Oxides, i.e., oxide ceramics are generally not associated with a high conductivity but with good insulating properties. Typically, metals are predominant as conductors due to the outstanding conductivity caused by the ever-present valence electrons in their atomic structure. Nonetheless, oxide conductors are subject to ongoing research due to their potential for highly valuable properties like transparency for, e.g., photovoltaics or electronics in glass, or their atomic structure. The latter is of particular importance for this work.

A general drawback of the conventional approach, i.e., growing BST on top of metals is the different lattice structure. Many pure metals like, e.g., gold or platinum exhibit a face-centered cubic (fcc) lattice structure [Arb97; KDO07], which is very different from the perovskite structure described in section 2.1. Hence, even though the lattice constants can be similar or equal, BST is unlikely to grow epitaxially on metals. This can only be achieved using low-energetic deposition methods like molecular beam epitaxy (MBE) [Mik+12], which are unusable in practice due to slow deposition and high process costs. By using a structurally matching oxide as bottom electrode (BE), a high-quality BST layer is available in MIM configuration even for simpler high-energetic deposition techniques which is important for scalability.

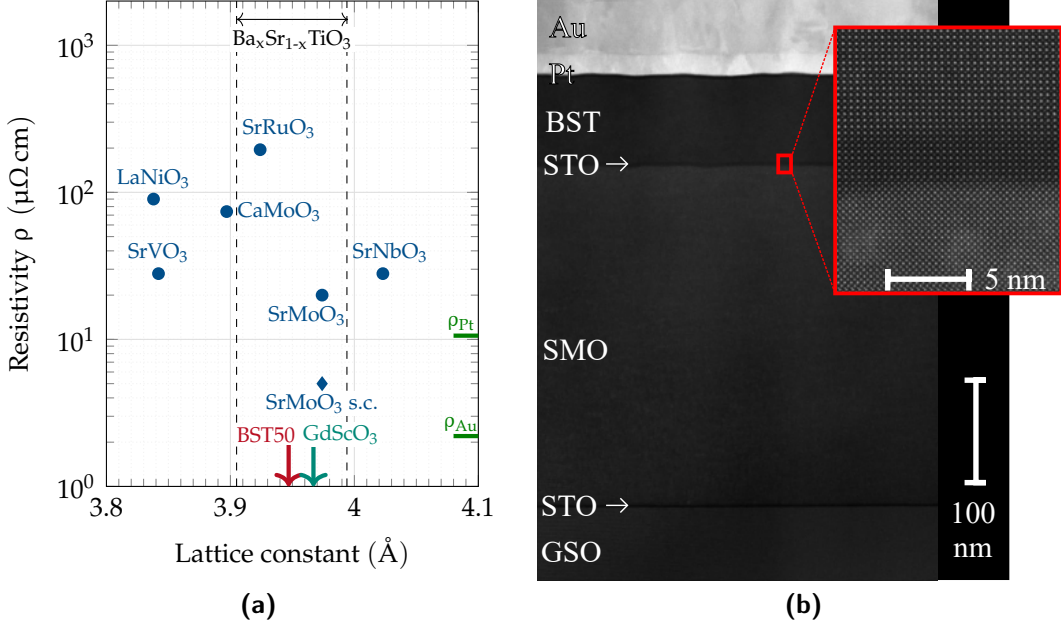


**Figure 2.9:** (a) Comparison of several oxide conductors with respect to their resistivity and in-plane lattice constant to other perovskites and metals [4], (b) TEM image of SMO-BST layer stack with inset showing the atomic interface [2].

The alternative approach used in this work replaces the metal BE with a conducting oxide with perovskite crystal structure. A remarkable conductivity was found for perovskite oxides with certain transition metals at the B site [Mot36; Lee+03; Nag+05]. Some examples with highest conductivity are shown in Figure 2.9a. The perovskite BE candidates are compared with respect to their resistivity and in-plane lattice constant. A deposited BST thin film will exhibit fewer defects if the BE has a similar lattice constant. The optimum electrode material will be, hence, found at the bottom center of the graph with a high conductivity and inside the region between the two dashed lines that represent  $\text{SrTiO}_3$  and  $\text{BaTiO}_3$ . In principle, a lower barium content can adapt to a smaller BE lattice constant. Note, however, that a good room-temperature trade-off between tunability and quality factor is often obtained for  $\text{Ba}_x\text{Sr}_{1-x}\text{TiO}_3$  with  $0.4 \leq x \leq 0.6$ . However, most of the oxide conductors have no sufficient conductivity for the required component quality factors at microwave frequencies [She+10; Kos+12]. Hence, until recently, this coined the general perception of oxide electrodes being not suitable for applications in microwave devices [Bao+08].

Among the reported materials, solely SMO can compete with metals; the resistivities of platinum and gold are shown in the graph. Its very low resistivity results from

an extremely small electron-phonon scattering [Nag+05], whereby its single-crystal value excels even platinum. Furthermore, its lattice constant is very similar to the one of BST. For these reasons, SMO appears as the ideal BE candidate in MIM microwave varactors. However, its integration is challenging due to conflicting thermodynamic requirements, which is described in more detail in section 2.3.

Nonetheless, its feasibility is proven in collaboration with this work and has shown outstanding results in terms of microwave quality factor and tunability. A transmission electron microscopy (TEM) photograph of a complete varactor deposited via pulsed laser deposition (PLD) is shown in Figure 2.9b. Due to the structural matching, all materials exhibit a monocrystalline lattice. Especially remarkable is the lower interface of BST, shown in smaller scale in the inset. Despite the multiple 100 nm thick SMO layer underneath, this interface is sharp to the atomic level. This confirms the possibility to grow monocrystalline BST in an MIM configuration with a highly conducting BE in high-energetic deposition processes. Additionally, two aspects of the similar structure enable another possibly striking benefit, i.e., overcoming the conventional frequency limitation of thin-film microwave varactors. Firstly, unprecedently thin BST films can be grown that excite less acoustic waves. Secondly, by similar acoustic properties of the likewise perovskite electrode, the reflection of acoustic waves can be optimized. The all-oxide technology promises to make ferroelectric varactors applicable in the complete 5G sub-6 GHz bands and beyond.

For this work on varactors, the resistivity for integrated thin-films is of primary importance before the previously reported value for single crystals. Figure 2.10 shows the resistivity-thickness pairs of all suitable varactor-integrated thin films that were characterized in this work. The indicated resistivity is extracted from characterization and analytic modeling as described in chapters 3 and 4. Therein, bad results due to defects in either the TE or the deposited thin films have been excluded. Note that the accuracy of the film thickness and, hence, of the extracted resistivity is limited when no unique information from X-ray diffraction (XRD) is available.<sup>10</sup> Nonetheless, valuable conclusions can be drawn from this evaluation. The high-quality thin-films realized during this work show a resistivity  $\rho_{SMO}$  between 20  $\mu\Omega$  cm and 30  $\mu\Omega$  cm. However, a rather large spread towards higher resistivity values is observed for many samples. This yields the microwave properties being non-reproducible, which is the main obstacle in building microwave components based on the all-oxide technology. The samples are grouped by their

<sup>10</sup>XRD commonly allows to determine the thickness of thin films with sufficient crystal quality, compare section 3.4.1. For thicker films or lower quality, the evaluated reflection high-energy electron diffraction (RHEED) intensity oscillations were extrapolated to an assessed film thickness [4].

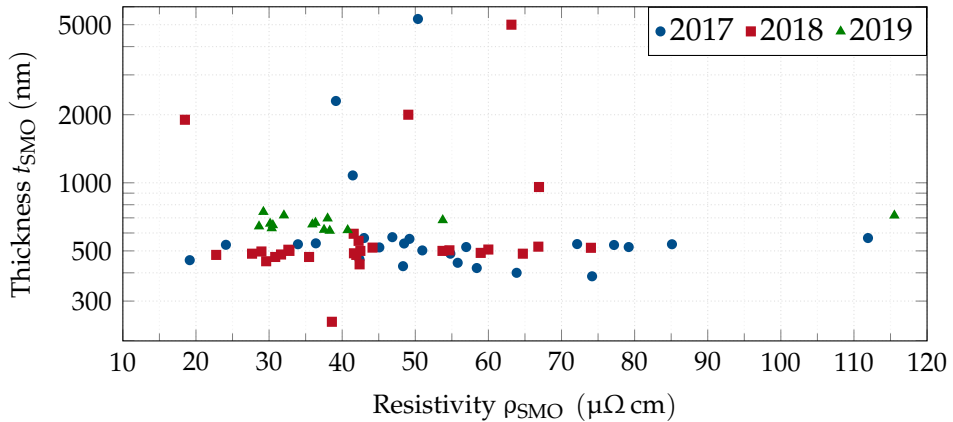


**Figure 2.10:** Thickness-resistivity pairs of integrated SMO films as extracted from modeling the varactor-test-structure characterization data and grouped by year of fabrication.

manufacturing year, revealing the optimization of the deposition process that was supported by this work, compare section 3.4. A trend of reducing spread towards the more recent samples is observed. Hence, the integration of all-oxide components into networks can be approached in the future. Note that the rather low growth rate in PLD required a limited thickness of  $t_{\text{SMO}} \leq 800 \text{ nm}$  for the majority of samples. The formation of defects is also more likely for thicker SMO films, which requires greater care during deposition [Sal20, p.69]. However, pairs of large thickness and low resistivity are present proving the absence of a principle degradation with increasing thickness. This confirms the expected large potential of high-performance devices based on the all-oxide technology.

## 2.3 Thin-Film Processing

The samples studied in this work were fabricated in collaboration with the material scientists from Advanced Thin-Film Technology group (ATFT), TU Darmstadt. Hence, the planar thin-film deposition of the oxides was not part of this work; it will be described only briefly with important aspects for this work. More details can be found in the corresponding dissertations published by Salg [Sal20] and Zeinar [Zei20]. The further processing, i.e., structuring, possible adding of an insulation layer and TE deposition in the clean room was shared between both groups. It is noteworthy that the final material properties can deviate strongly from the

single crystal values. For example, the temperature dependence and maximum permittivity will generally decrease greatly in a processed film. Furthermore, loss and tunability of a thin film significantly depend on the fabrication due to extrinsic defects or a strong impact of artefacts in the microstructure.

Possible deposition mechanisms for oxide thin films are PLD, RF sputtering, MBE, chemical solution deposition (CSD) and metalorganic chemical vapour deposition (MOCVD). They differ in certain key qualities like low-temperature compatibility, throughput and uniformity of composition or film thickness. A detailed description and comparison is given in [Sub+13]. PLD is used throughout this work as it has decisive benefits for scientific considerations despite its limitation to small-scale substrates. The suitability for epitaxial layer-by-layer growth allows to define the interfaces on the atomic level, which is a key for the all-oxide technology. Furthermore, the required targets can be produced in-house and, thus, fast. Different materials can be used, including a very broad stoichiometry range that can precisely be controlled. Though their small size is a drawback for producing large RF networks, it is important to be cost-effective in the lab-scale. The possibility of fast variation of the material composition eases the material optimization to obtain optimum microwave properties. Thirdly, the total fabrication process including pre- and post-processing is very fast, such that a complete cycle of varactor fabrication and RF characterization can be done within 1 – 2 workdays. Two main drawbacks of this deposition method have been observed in this work: the non-uniformity of many fabricated thin films on the one hand and the difficulty to ensure reproducibility on the other. Both are quantified exemplarily for the all-oxide varactors in section 5.1. This is connected to a high sensitivity to a multitude of parameters like, e.g., temperature, ambient atmosphere and pressure, laser energy, where even minor changes impact the deposition process. Especially for an increasing film thickness, a greater care is required for homogeneous film properties. This contributed to the focus on highly accurate modeling of thin electrodes in this work.

A simplified sketch of a PLD system is shown in Figure 2.11a. The plasma plume for the transport of the target materials to the substrate is created by the pulsed laser. The vacuum pump and gas supply allow the precise control of flow and partial pressure of the background gas. Depending on the deposited material, different conditions must be chosen like, e.g., oxygen for BST, argon and hydrogen for SMO and ultra-high vacuum for interlayers [Rad17]. Connected with each part of the system, several parameters must be chosen correctly for a high-quality result. In the scope of this work, e.g., the laser energy density and the oxygen background pressure during the BST deposition have been optimized based on RF characterization, compare section 3.4.

The main challenge for the deposition of this varactor heterostructure are the con-

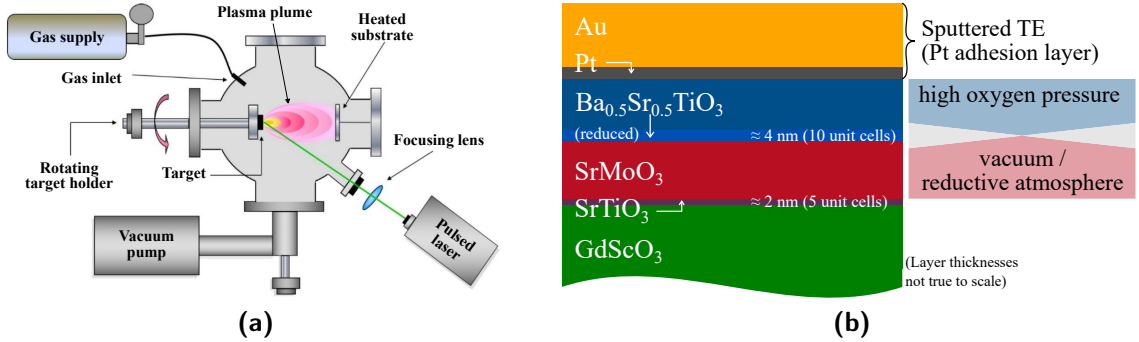


**Figure 2.11:** (a) Sketch of a PLD system [BT20] and (b) all-oxide layer stack with example TE and conflicting thermodynamic requirements of BST/SMO.

flicting thermodynamic requirements for the growth of BST and SMO: They require a high oxygen background pressure and a high vacuum level, respectively. If grown under a too low oxygen pressure, BST will exhibit a strongly degraded quality factor and increased leakage current due to oxygen vacancies [Sch+08]. SMO, on the other hand, is unstable in an oxygen environment and will react into the insulating scheelite SrMoO<sub>4</sub>. This conflict is solved by introducing a very thin interlayer as an oxygen barrier. As candidates, the complete mixing range of Ba<sub>x</sub>Sr<sub>1-x</sub>TiO<sub>3</sub> has been studied, revealing that a higher barium content leads to an earlier oxidization of SMO [Sal20]. The composition with  $x = 0.5$  was chosen, since it is mostly used for the functional BST layer in this work and is an optimum oxygen diffusion barrier. Note that no tunability and a reduced permittivity is expected from that oxygen diffusion barrier. Hence, as this stack constitutes a capacitor with stacked dielectric, the interlayer must be as thin as possible. Only ten unit cells ( $\approx 4$  nm) have proven sufficient in terms of oxygen barrier and can be deposited atomic-layer-wise in PLD. The final layer stack of the varactor heterostructure is shown in Figure 2.11b. It is deposited on a gadolinium scandate (GSO) substrate due to its pseudocubic in-plane lattice constant of the (110)-plane cut, which offers a very low lattice mismatch to the entire heterostructure, see Figure 2.9a. The subsequent SrTiO<sub>3</sub> interlayer above GSO improves the smooth layer-by-layer growth of SMO [Koz+12; Ito+16]. However, due to its very small thickness, it does not impact the varactor impedance significantly.

# 3 Characterization of All-Oxide Varactors

Especially during the early stage of the all-oxide varactor research, a focus on material optimization is required. For being able to accurately extract the material properties of the integrated layers in the varactor structure, a precise characterization scheme is necessary. For this, a widely used on-wafer test structure is adopted in this work. This constitutes a fundamental requirement for the highly accurate models developed later in this work. However, the deployed test structure is frequency-limited due to a breach of the standard-on-wafer CPW calibration environment. To compensate this systematic error, this work derives a de-embedding of this environment breach prior to the actual characterization. By that, the frequency range can be extended up to the self-resonant frequency (SRF) of the investigated test structures. Subsequently, the results of several varactors are discussed. The final section covers the correlation of crystallographic structure and RF performance. An RF-characterization-based material optimization is presented.

## 3.1 On-Wafer Testing

The on-wafer test structure used in this work is inspired by [Ma+98], which describes a well-established method for dielectric characterization of thin films on top of a planar conductive layer. It allows the extraction of the complex permittivity  $\underline{\epsilon}$  from the measurement of test structures with a circular inner pad surrounded by a much larger outer pad, see Figure 3.1. The impact of the outer electrode can be crossed out by comparing two structures with equal outer diameter  $d_{\text{out}}$ . For varying inner pad diameters  $d_{\text{in}1,2}$ , one obtains

$$\underline{Z}_1 - \underline{Z}_2 = \frac{R_s}{2\pi} \ln \left( \frac{d_{\text{in}2}}{d_{\text{in}1}} \right) + \frac{4t_{\text{diel}}}{j\omega\pi\underline{\epsilon}} \left( \frac{1}{d_{\text{in}1}^2} - \frac{1}{d_{\text{in}2}^2} \right), \quad (3.1)$$

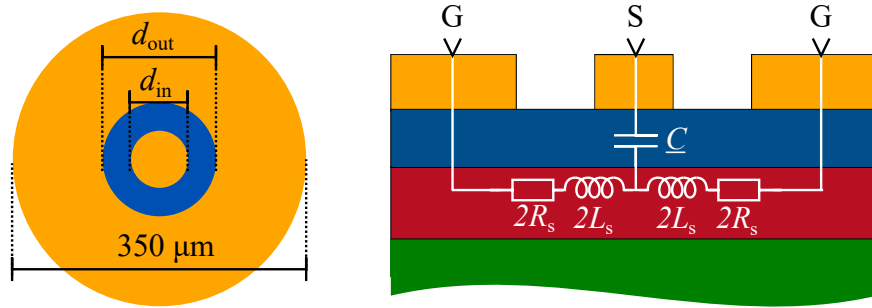


**Figure 3.1:** Circular test structure with all-oxide layers and their respective contribution to the RLC model.

with the angular frequency  $\omega$ , impedance  $Z_{1,2}$  of the two structures, BE sheet resistance  $R_s$  and the thickness  $t_{\text{dielectric}}$  of the dielectric. For thin layers, the skin effect is negligible and the BE sheet resistance is given by

$$R_s = \frac{\sigma_{\text{BE}}}{t_{\text{BE}}} \quad (3.2)$$

with BE conductivity  $\sigma_{\text{BE}}$  and thickness  $t_{\text{BE}}$ . The interpretation of (3.1) is straightforward: The former and the latter term describe the difference of the bottom electrode resistance for radial current flow and of the center pad capacitance, respectively. Note that, among other constraints, this model requires equal dielectric and conductor properties across all measured and compared structures. While the sheet resistance needs to be known in (3.1), the BE thin-film resistivity is as well unknown for the varactors characterized in this work. Nonetheless, theoretically, this parameter can also be identified by measurement if a third test structure with pad diameter  $d_{\text{in}3}$  is added to the pattern of the photo-lithography mask. The deployed varactor test structure mask pattern is shown in Figure 3.2a. It contains four equal quadrants of  $3 \times 3$  varactor geometries with varying inner and outer pad diameters as shown in Table 3.1.

In (3.1), the sheet resistance  $R_s$  needs to be known and has a very large impact on the extracted dielectric loss. Therefore, effects like a bad metal quality or a strong electrode surface roughness can prevent a correct extraction. This is illustrated in Figure 3.2b, where the above method is applied to exemplary 3D-simulated data based on simulations with CST Microwave Studio. The extracted real part of the permittivity  $\epsilon'_r$  and loss factor  $\tan \delta$  are compared to the true data directly exported from CST. In  $\epsilon'_r$ , only the negligence of the electrode's inductance leads to an error that is increasing for higher frequencies; the sheet resistance does not affect the real part of the permittivity. For the extracted loss factor, a significant error is introduced, firstly, by the neglected inductance and, secondly, by a badly assumed sheet

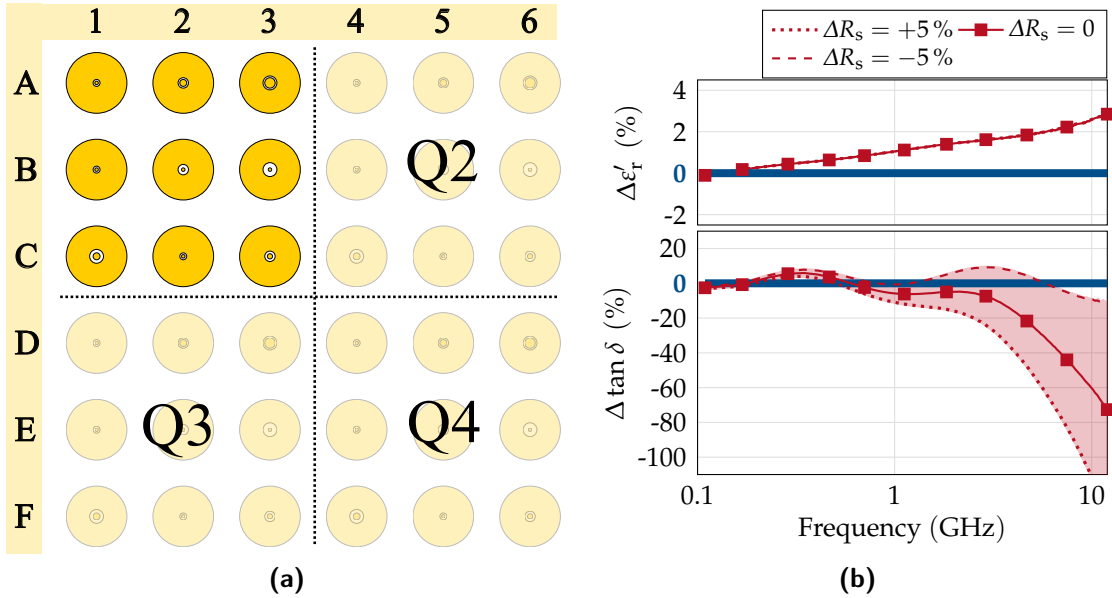


**Figure 3.2:** (a) Varactor test structure pattern. (b) Relative deviation of real part of permittivity and loss factor to the data directly exported by CST as extracted by (3.1). To illustrate the impact of  $R_s$ , the result of the extraction with a slightly varied sheet resistance by 5 % is also shown, with the difference highlighted.

resistance. Already a 5 % deviation from the correct value renders this method's results increasingly unusable above 1 GHz. Additionally, the electromagnetic fields penetrate the substrate significantly when this characterization method is used in combination with a small BE thickness of only a few hundreds of nm up to 1  $\mu\text{m}$ . This impedance variation is not accounted for by the given model relying only on  $R_s$ . For that, a different modeling approach was chosen in this work that considers the substrate separately for highest extraction accuracy, see Section 4.1.

Another issue with the established method is the mere subtraction of impedances of two different structures in (3.1). While this is an elegant way to remove the impact of the outer ring electrode from the analytic model, any structure variation (e.g., by processing errors) will degrade the resulting accuracy. Furthermore, inhomogeneous thin-film (TF) properties lead to errors for the same reason. The latter effect might not be severe generally, i.e., for homogeneous films. However, for the majority of varactors fabricated in this work, a strong fluctuation of material properties across the  $5 \times 5 \text{ mm}^2$  crystal substrates is observed. This conflicts with the constraints for the above analytical evaluation, preventing the direct extraction of the desired material properties. Prior to this work, this leaves the simple, but severely time-consuming sweeping of parameters in a fully-electromagnetic 3D

**Table 3.1:** Varying inner and outer pad diameters as depicted in Figure 3.2a.

	$d_{in}$ ( $\mu\text{m}$ )			$d_{out}$ ( $\mu\text{m}$ )		
	{1, 4}	{2, 5}	{3, 6}	{1, 4}	{2, 5}	{3, 6}
{A, D}	20	40	60	40	60	80
{B, E}	20	20	20	40	60	80
{C, F}	40	20	30	80	40	60

model to fit the measured data as the sole choice to extract material properties from measurements. In contrast, the highly-accurate analytic models derived during this work overcome these limitations due to their schematic nature and can be calculated within seconds. Instead of subtraction of measured impedance data, the material property extraction relies on an analytic extrapolation of a known reference that must be verified just once by a fully-electromagnetic model.

### Characterization Setup

The test structures are commonly contacted with FormFactor Infinity ground-signal-ground (GSG) on-wafer probes with 100  $\mu\text{m}$  pitch. A high automation level of the characterization was developed to cope with the large amount of samples processed in this work. The characterization setup is shown in Figure 3.3. A Matlab script is used to control the RF measurement, the DC source and the semi-automated on-wafer probe station. With that, after calibration, all 36 varactors on one sample can be characterized in all desired bias states automatically within typically 1.5 h to 4 h, depending on the number of bias points and the accuracy parameters like, e.g., IF bandwidth and averaging. Note that two different devices, namely a vector network analyzer (VNA) and an impedance analyzer (ImpA) can be used for recording the microwave impedance. The choice depends on the device under test (DUT) properties that are focused. A large frequency band and accurate leakage current information can be obtained from the 1-port VNA measurement, whereas the ImpA is required for accurate results for DUTs with a large quality factor.<sup>1</sup> Practice has shown that the VNA results are sufficiently accurate for a limited DUT quality factor up to 30–40. During this work, many samples with a rather thin BE thickness of

<sup>1</sup>This is reasoned by the different measurement principles in these devices for extracting the quality factor. The VNA reads the magnitude of the reflection coefficient, which exhibits smaller changes for varactors of increasing quality. The impedance analyzer reads complex voltages and currents, which is less dependent on the DUT but introduces a frequency limitation.

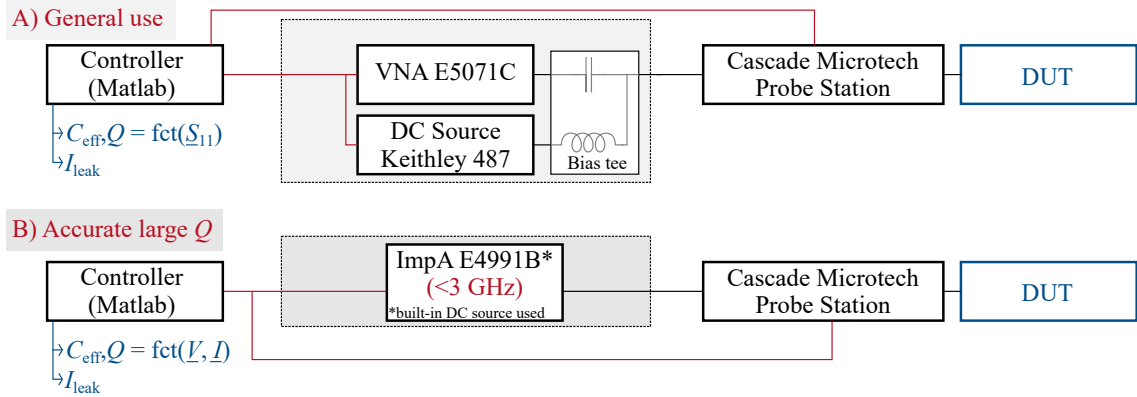


Figure 3.3: Setups for the automated characterization of all 36 test structures

$\approx 500 \mu\text{m}$  are fabricated that lead to quality factors below that limit. Hence, the VNA characterization is commonly used and extended by the ImpA measurement for verification where necessary. The bias voltage is applied to the varactor in-line with the RF signal. For VNA measurements, the RF and DC signal are combined via a bias tee. With the ImpA, the internal DC source is used. As the sole one-port standard, an open-short-load (OSL) calibration is performed with an impedance standard substrate (ISS). Generally, the accuracy of this standard is regarded critical because it shows a strong sensitivity towards the actual position and overtravel of the on-wafer probe on ISS structures. Also, it is known to become less accurate for increasing frequencies. However, reasonable results have been obtained throughout this work that agree for the VNA and ImpA measurements, even despite the manual lateral positioning of the on-wafer probe.

The natural results obtained from the VNA and ImpA are the scattering  $S$  and impedance parameters  $Z$ , respectively. As this is a one-port characterization, the conversion is rather simple,

$$\underline{Z}_{\text{meas}} = Z_0 \frac{1 + \underline{S}_{11}}{1 - \underline{S}_{11}}, \quad (3.3)$$

with the reflection parameter  $\underline{S}_{11}$  and the system's reference impedance  $Z_0$ . When dealing with varactors, the impedance is commonly interpreted as a capacitance  $C_{\text{meas}}$  and quality factor  $Q_{\text{meas}}$ , defined as

$$C_{\text{meas}} = -\frac{1}{\omega \cdot \Im\{\underline{Z}_{\text{meas}}\}} \quad (3.4)$$

$$Q_{\text{meas}} = -\frac{\Im\{\underline{Z}_{\text{meas}}\}}{\Re\{\underline{Z}_{\text{meas}}\}} \quad (3.5)$$

with radial frequency  $\omega = 2\pi f$  and the imaginary and real part of the impedance  $\Im\{\underline{Z}_{\text{meas}}\}$  and  $\Re\{\underline{Z}_{\text{meas}}\}$ , respectively. In this interpretation, the electrode's inductance is neglected and all loss is projected onto a series resistance, i.e., the electrode loss is expected dominant. In redundancy to the information above, the equivalent series resistance (ESR) is, occasionally, also evaluated as a different visualization,

$$\text{ESR} = \Re\{\underline{Z}_{\text{meas}}\}. \quad (3.6)$$

Anticipating the characterization results presented later in this chapter, typical values for electrode resistance  $R_s$  and zero-bias dielectric loss  $\tan \delta_{\text{dielectric}}$  are  $0.2 \Omega - 0.5 \Omega$  and  $0.005 - 0.01$ , respectively. Hence, in comparison to the example calculation for equal loss contributions in section 2.1.2, this is the best model to use in a standard analysis without additional knowledge about the sample. However, especially for lower GHz frequencies, the dielectric loss will show a significant impact on  $Q_{\text{meas}}$  and must not be neglected.

## 3.2 De-Embedding of Measurement Data

Figure 3.4a shows an example for a typical "raw" extracted capacitance and quality factor, respectively, obtained after OSL calibration with the equations from the previous section. The observed decrease of the capacitance with frequency is characteristic for all measurements in this setup, but does not comply with the physical expectations of (2.29). The quality factor appears regular but of course depends on the correctness of the capacitance. This artifact is a widespread problem, as it affects many reported works based on this test structure, for example in [Gev+09; She+10; Gou+18].

### Impairment of On-Wafer Non-CPW Environment

Since the artifact is observed primarily in the capacitance, this indicates a connection to an erroneous reactive part in the extracted impedance. As the inductive contribution of the electrodes is not compensated in this evaluation, it should lead to an increase of  $C_{\text{meas}}$  up to infinity at its SRF.<sup>2</sup> Together with the previously-described difficulty of an imprecise sheet resistance, this negligence is the main reason for

---

<sup>2</sup>If the electrode inductance  $L_{\text{elec}}$  was known and compensated before evaluation, the measured capacitance  $C_{\text{meas}} = -1/\omega (\Im\{\underline{Z}_{\text{meas}}\} - \omega L_{\text{elec}})$  would be quasi-constant with frequency.

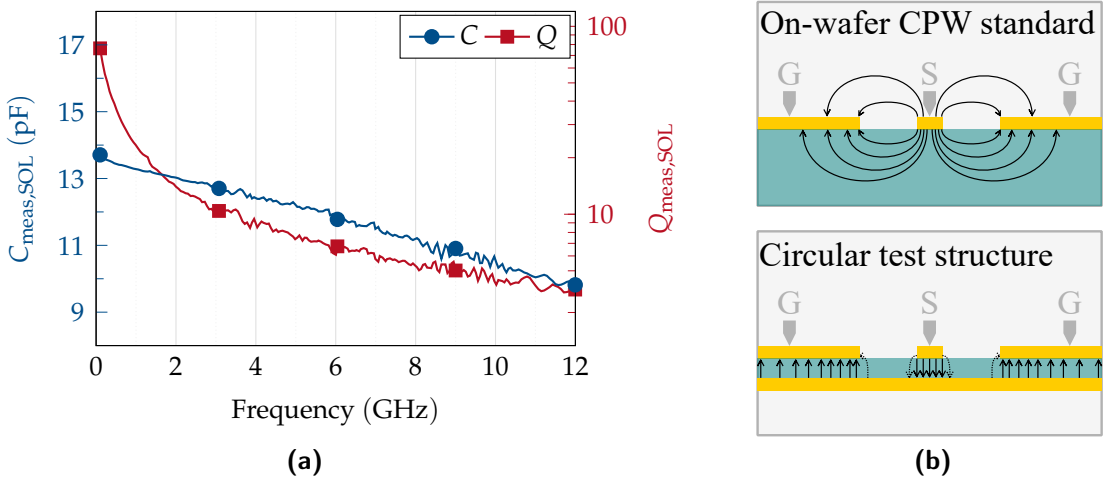


**Figure 3.4:** (a) Example for typical "raw" capacitance and quality factor after OSL calibration, as extracted from (3.4), (3.5). (b) Comparison of electric fields in CPW environment and in cross section through center of circular test structure.

the frequency limitation of this method. However, though the inductive contribution can be small, such that the SRF-induced increase may not be prominent in the observed frequency range, an apparent decrease conflicts with the reasonable dominant contributions. Hence, this does not yet explain the artifact of the decreasing measured capacitance. In a limited frequency range up to a few GHz, a decrease could be explained by resistive effects, e.g., caused by a bad contact of the on-wafer probes or highly-resistive interlayers in the all-oxide layer stack. However, no combination of resistances inside physical constraints leads to a fitting of the observed characteristic. The reason for this artifact might be connected to the breach of the calibration environment, i.e., CPW, when directly probing the circular test structures. The difference is shown in Figure 3.4b, where the electric fields through the cross section of both structures are sketched. Strongly differing field patterns result from the radical difference between ISS and circular structure; the introduction of a close-by BE and the huge contrast of the relative permittivity from 9.6 to a few hundreds for alumina and BST, respectively. Unfortunately, no EM model of the on-wafer probe is available to model the exact field distribution. However, the assumption of a strong impact of the close-by BE is supported by the  $L_{\text{bd}}$  comparison in section 3.2.2. As has been shown above, for the method as described in [Ma+98], these differences do not obstruct a reliable extraction for lower frequencies but lead to a frequency limitation below 5 GHz. In fact, the accuracy decreases already for increasing frequencies below that margin, especially for larger

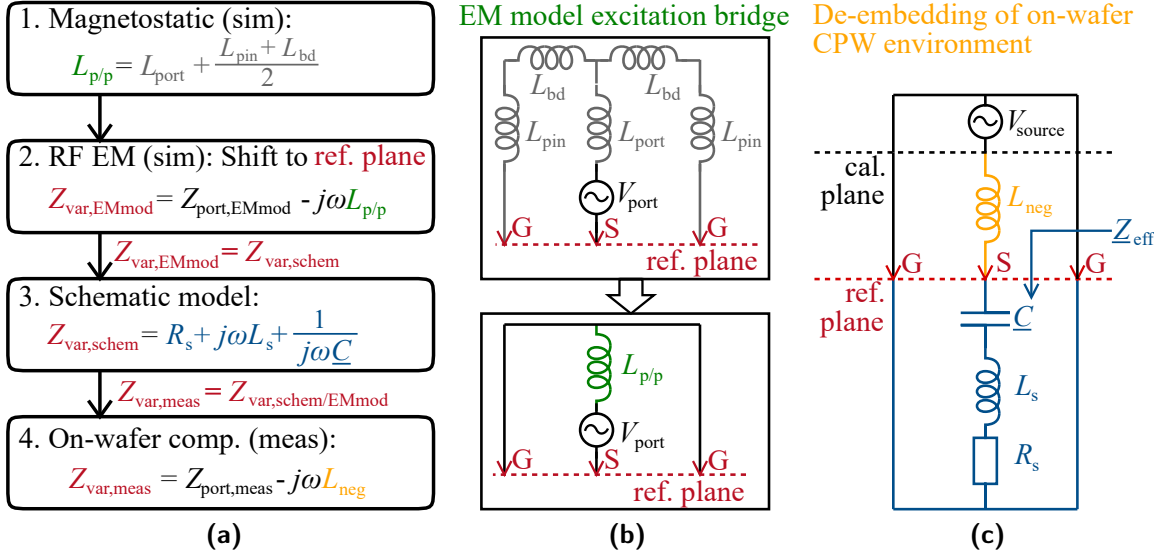


**Figure 3.5:** (a) Flow chart and schematic models to (b) unify the inductance of the excitation bridge and (c) de-embed the on-wafer non-CPW environment.

capacitances with lower SRF. The following sections will show that measurement results are still usable up to the SRF, if phenomenologically modeled as a negative inductance.

### 3.2.1 Determination of True Test Structure Inductance

The inductance inherited by the test structure adds up with the negative measurement inductance. Therefore, it cannot be determined right-away experimentally. To separate these two inductances, the former is firstly determined by schematically fitting the EM model. The flow chart of the complete de-embedding process and the corresponding schematic models are shown in Figure 3.5. Firstly, the inductance of the excitation bridge to stimulate a GSG excitation in the 3D EM model is determined by magnetostatic simulations. Secondly, it is compensated in the EM model to obtain the varactor properties at the simulation reference plane. Then, by schematically fitting the EM model, the varactor's inherent inductance is separated. Finally, by comparing this true inductance with the measured result, the negative measurement inductance can be characterized.

The first two steps refer to the 3D EM model of the varactor as shown in Figure 3.6a. The 100  $\mu\text{m}$  pitch GSG excitation of the on-wafer measurement is modeled by a

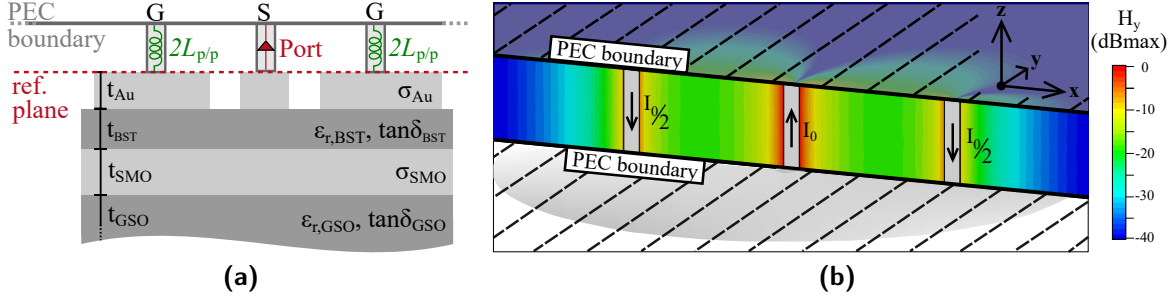


**Figure 3.6:** (a) Cross section of EM model for the circular test structure with PEC pins and port stimulating GSG excitation at the reference plane. (b)  $xz$ -cut plane view of  $H_y$  (tangential field) from magnetostatic simulation for determining  $L_{p/p}$ , the circular electrodes were replaced with PEC boundary.

cylindrical port and perfect electrically conducting (PEC) pins with  $10\text{ }\mu\text{m}$  diameter and  $50\text{ }\mu\text{m}$  length. Those are connected via an PEC boundary, forming an excitation bridge with the total inductance  $L_{p/p}$ . It is determined from a separate magnetostatic simulation. Therein, the circular electrodes and all layers below are replaced with a second PEC boundary. Figure 3.6b shows the y-component of the resulting magnetic field  $H_y$  with indicated current distribution. The additional (lower) PEC boundary must be subtracted to obtain the true inductance of the excitation bridge. Its inductance is obtained from an additional magnetostatic simulation. The detailed description of the magnetostatic simulations and the calculation of the inductance values are given in appendix A.

The resulting inductance of the excitation bridge is

$$L_{p/p} = 38.4\text{ pH.} \quad (3.7)$$

Subtracting the impedance of this inductance from the simulated data shifts the simulation's reference plane to the top electrode layer, the same as for the on-wafer characterization (measurement reference plane). From schematic fitting of the EM simulation, the overall test structure self inductance can then be extracted as circa  $3\text{ pH} - 5\text{ pH}$ , depending on the TE diameters and the BE thickness. Now, by fitting the measured data with a compensating series inductance to this model, the measurement error can be isolated and de-embedded.

### 3.2.2 Characterization of Negative Measurement Inductance

In this study, all functional 33 varactors on one sample are characterized between 100 MHz and 12 GHz, three structures were defect after lithography. The generally recommended over-travel (OT)<sup>3</sup> for the deployed kind of on-wafer probes is 75  $\mu\text{m}$  in order to avoid additional contact resistance and parasitic reactances. However, a reduced OT must be used to avoid damaging the small center pads. Hence, the stability and validity of the extracted impedance must be verified first. The effective capacitance, see (3.4), is used as a sensitive indicator for any change in the reactance. Note that, for calculating the reactance, the phase relation between the transmitted and reflected signal is defining. Thus, even when measuring the highly mismatched capacitances, the high phase accuracy allows for relying on the extracted values. With the deployed semi-automated probing station, the height levels can be precisely controlled. Thereby, the impact of the out-of-specification OT on the measurement results can be investigated. Very smooth layer surfaces are required for comparison, which is ensured in our case by the generally-smooth surface of PLD thin films and sputtered metalizations. In the following, test structures with varied center pad diameters 20  $\mu\text{m}$  – 60  $\mu\text{m}$  and, thus, different capacitances are compared. Each is contacted with different amounts of OT in the range 20  $\mu\text{m}$  – 60  $\mu\text{m}$ .

The small non-planarity of the tips of the probe's pins prevents from measuring without any OT. Even for an exemplary newly opened probe, both ground pins barely contact the electrode's surface at 20  $\mu\text{m}$  OT beyond the signal pin's first contact. After comparing to two more GSG probes with similar offsets, this is deemed as the best possible planarity. When evaluating the results for 20  $\mu\text{m}$  OT, eight of the 33 analyzed varactors on the sample show a series resonance in between 3.5 GHz – 7.5 GHz, all other 25 exhibit a negative trend of  $C_{\text{eff}}$  over frequency. The higher indicated resonance frequencies are close to the expected SRF. However, this resonance is caused by a bad contact due to insufficient OT as proven in the following. Figure 3.7a shows the negative trend for every varactor at 40  $\mu\text{m}$  OT. Many varactors show the same  $C_{\text{eff}}$  characteristic as for 20  $\mu\text{m}$  OT, indicating the same appearing negative series inductance. An increased OT of 60  $\mu\text{m}$  could be applied only to the structures with large center pads (V1-V3). The curves of these are highlighted in Figure 3.7a and show a result stability already at 40  $\mu\text{m}$ .

The compensating inductance

$$L_{\text{neg}} = -5.4 \text{ pH} \pm 0.2 \text{ pH} \quad (3.8)$$

---

<sup>3</sup>OT describes the additional height reduction of the on-wafer probe after the first contact of the pins with the sample.

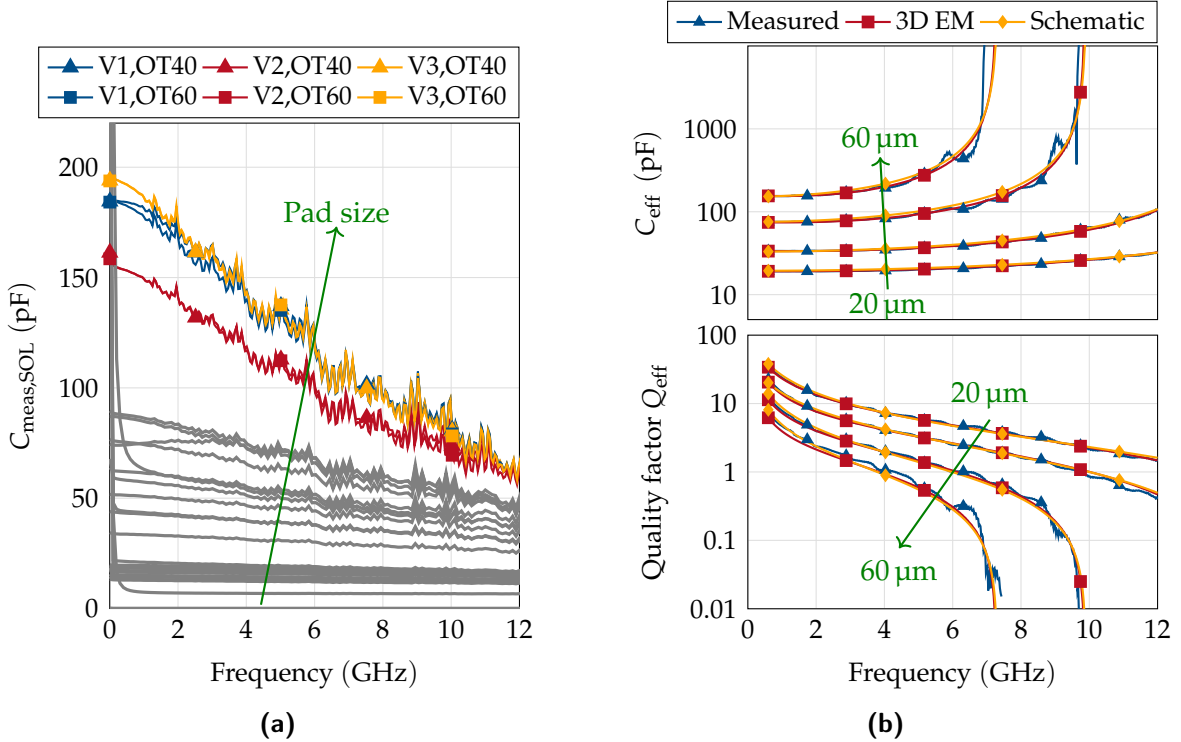


**Figure 3.7:** (a) Uncompensated capacitance for 33 varactors on one sample with  $40 \mu\text{m}$  OT. For three of them, which have a sufficiently-large center electrode, the measurement is repeated with  $60 \mu\text{m}$  OT. (b) Fitting of schematic and EM model to measured data with compensated negative inductance  $L_{\text{neg}} \approx -5.4 \text{ pH}$  for increasing pad diameters  $20, 30, 40, 60 \mu\text{m}$ . The simple schematic models fits more accurately for smaller pad sizes.

leads to a fitting of the EM model, varying only slightly for the different diameters. The fitting result is shown in Figure 3.7b. Hence, the effective varactor properties are defined for the de-embedded impedance

$$Z_{\text{eff}} = Z_{\text{meas}} - j\omega L_{\text{neg}} \quad (3.9)$$

as the effective capacitance and quality factor

$$C_{\text{eff}} = -\frac{1}{\omega \cdot \Im\{Z_{\text{eff}}\}} \text{ and} \quad (3.10)$$

$$Q_{\text{eff}} = -\frac{\Im\{Z_{\text{eff}}\}}{\Re\{Z_{\text{eff}}\}}, \quad (3.11)$$

respectively. During this study, the value in (3.8) was steady for repeated calibrations and exchanged on-wafer probes of the same type and pitch. In later works, compensation inductances of 2 pH – 8 pH were found for different samples. Interestingly, the value of  $L_{\text{neg}}$  is in all cases comparable to the negated inductance calculated for the boundary  $L_{\text{bd}} = 6.3 \text{ pH}$  for equal pitch 100  $\mu\text{m}$  in appendix A. This supports the assumption that the close-by BE might be connected to the physical origin of this appearing negative inductance, compare Figure 3.4b. However, a proof of this is beyond the scope of this work. For now, it is sufficient to extract the value for  $L_{\text{neg}}$  that allows to extend the frequency range in which accurate impedance data for the varactor is obtained. With that, the frequency characteristic of the test structure can be modeled accurately up to the SRF.

### 3.2.3 Benefits for All-Oxide-Varactor Characterization

The wide frequency range is a key enabler for this work bringing many advantages. Firstly, this is especially crucial for investigating the novel electrode material SMO because the electrode's contribution is significant only above a few GHz. Hence, both dielectric and electrode loss can be characterized from a single impedance measurement due to their frequency-specific characteristic. This allows the otherwise-difficult determination of the conductivity of integrated SMO thin films. This is particularly important as stand-alone SMO films are likely to have different properties than integrated ones due to the contradicting thermodynamic constraints during the growth of BST and SMO as discussed in section 2.3. Detailed results will be presented in section 3.3. Secondly, the availability of valid impedance data over a wide frequency range beyond 10 GHz provides the basis for all of the highly accurate models presented in chapter 4. These, in turn, enable the thorough understanding of dominant effects in devices, allow for a rapid characterization of material properties, and provide a strong basis for future device designs.

## 3.3 Characterization Results

By de-embedding the non-CPW environment effects, the characterization of the varactor test structures is possible. Representative results for both a typical varactor and a high-performance sample with optimized thicknesses are reported. The latter will be compared to other works by means of figure of merits for tunable components.

### 3.3.1 Typical Varactor

A large amount of more than 100 samples with each carrying 36 varactors has been characterized throughout this PhD project. These were fabricated during several systematic studies of, e.g., the impact of process parameters or film thicknesses or to analyze the reproducibility. Comparing all of them in general is, hence, not reasonable. Instead, representative results will be presented for the "standard" case that was used as reference for all studies in this work. This reference corresponds to a layer stack with thicknesses  $t_{\text{SMO}}$  and  $t_{\text{BST}}$  in the range 500 nm – 800 nm and 70 nm – 90 nm, respectively. In this domain, the film properties have shown to be the most reproducible. Thicker SMO layers ( $t_{\text{SMO}} > 800 \text{ nm}$ ) are more likely to suffer from hillock formation that disturb the epitaxy and lead to film defects. In thinner BST layers, the film quality is more difficult to ensure because effects on the atomic scale become more dominant: The macroscopic interpretation as a homogeneous thin film is less accurate.

The results shown in Figure 3.8 are obtained from a varactor test structure with  $d_{\text{in}} = 20 \mu\text{m}$ ,  $d_{\text{out}} = 40 \mu\text{m}$  and thicknesses  $t_{\text{SMO}} = 507 \text{ nm}$  and  $t_{\text{BST}} = 91 \text{ nm}$ . The negative measurement inductance has already been compensated. Two points about the change of effective capacitance with frequency in Figure 3.8a are remarkable: Firstly, the initial drop in the lower GHz domain around 3 GHz and, secondly, the apparent decrease with frequency under bias. The former can be connected to substrate effects and the latter to acoustic activity, which is confirmed by the models derived in chapter 4. The capacitive characteristic versus bias field is shown in Figure 3.8b as relative permittivity, approximated by the simple parallel-plate capacitor (PPC) model

$$\epsilon_{r,\text{BST}} = 4C_{\text{eff}}t_{\text{BST}}/\epsilon_0\pi d_{\text{in}}^2. \quad (3.12)$$

A symmetric and strong tunability of  $\tau = 79 \%$  is observed. Below the capacitive data, the quality factor is shown in both plots. Figure 3.8a shows that it decreases with frequency as expected. In agreement with the findings from section 2.1.2, the quality factor does not decrease antiproportional to the frequency due to a significant contribution of dielectric loss. However, with  $Q(5 \text{ GHz})/Q(0.5 \text{ GHz}) = 0.17$  and  $Q(10 \text{ GHz})/Q(1 \text{ GHz}) = 0.12$ , the electrode is clearly the major loss source in the GHz domain for zero-bias.<sup>4</sup> For increasing bias strength, the typical increase of  $Q$  due to the decreased capacitance is not observed. This can be explained by

<sup>4</sup>The possible range of  $Q(10f)/Q(f)$  lies between 0.1 and 1. Neglecting dispersive effects, a purely dielectric loss would result in  $Q(10f)/Q(f) = 1$ . If, in contrast, the electrode resistance  $R_s$  was the sole loss source, this would result in  $Q(10f)/Q(f) = 0.1$  as the quality factor would be determined by  $Q = 1/\omega CR_s$ , compare section 2.1.2.

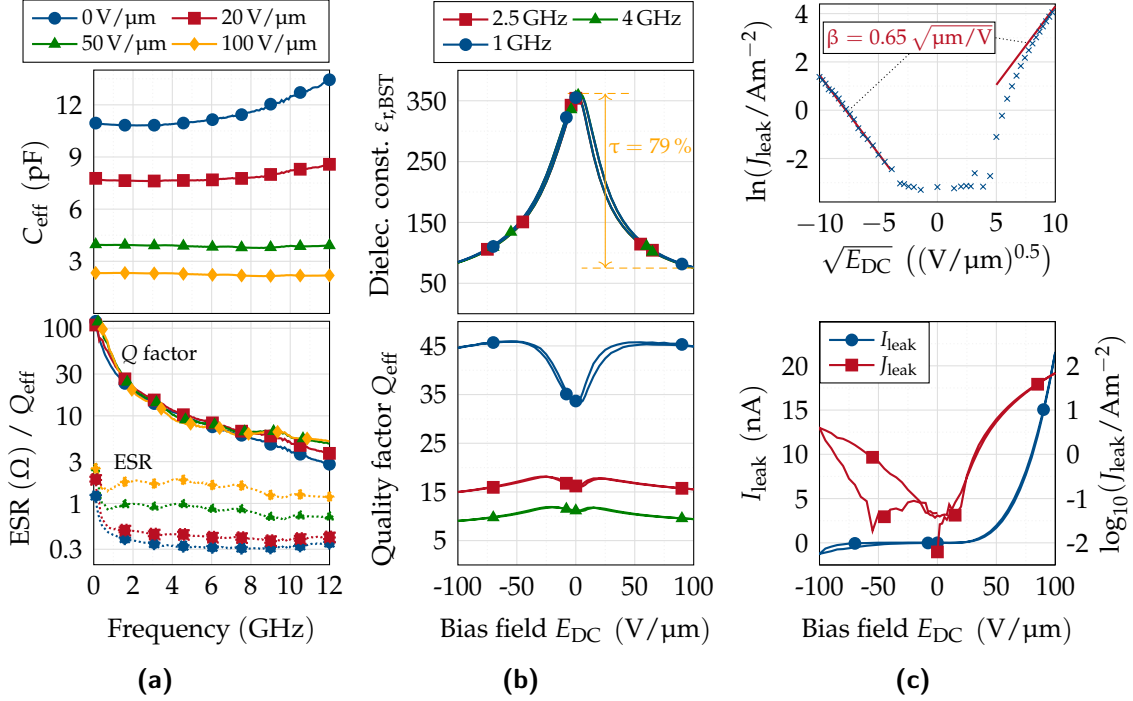


**Figure 3.8:** Representative data of the varactor test structure with inner diameter 20  $\mu\text{m}$ , BST thickness 91 nm and SMO thickness 507 nm. (a) Effective capacitance, quality factor and equivalent series resistance versus frequency for four bias states. (b) Relative permittivity extracted from the simple PPC model and  $Q$  factor versus bias field at three frequencies. (c, bottom) Leakage current in linear and logarithmic scale versus bias field and (c, top) replot of leakage current with different axis indicating Schottky emission as the dominant leakage mechanism.

observing the ESR that increases with bias by up to one order of magnitude. The bias-induced increase is effective for frequencies starting in the lower GHz range. In principle, this could be connected to either a strong quasi-Debye loss mechanism or degrading acoustic activity. The weak but recognizable frequency-selectivity of the ESR indicates the presence of acoustic resonances and, hence, argue for the latter. The analysis in section 4.2.5 clarifies this matter and confirms the strong impact of acoustic activities and the effect of partial resonance suppression in this setup. When plotted versus the bias field in Figure 3.8b, no strong change is observed for this sample in general. At lower frequencies, i.e. 1 GHz, the often observed inverted-bell-shaped characteristic is recorded for weaker bias. For stronger bias fields, it is limited by the acoustic activity which is, in turn, strongly dependent

on the film thicknesses as typical for MIM varactors. Hence, for other samples, especially ones with thinner BST layers, the inverted bell can be more visible. It is noteworthy that acoustic resonances will degrade  $Q_{\text{eff}}$ , in the worst case even below its zero-bias value. This underlines the importance of properly addressing them in the later-on component design.

The leakage current in Figure 3.8c is generally low in the nA domain. This is a very beneficial property, especially for mobile applications, as it enables quasi-powerless tuning. However, it is more than one order of magnitude stronger for a positive polarity in comparison to a negative one. This can be explained by analyzing the dominant leakage mechanism. If the interfacial Schottky emission (SE) is the most limiting mechanism, the leakage current can be described by [Vor+04]

$$J_{\text{SE}} \propto \exp \left[ -\frac{q}{k_B T} \left( \Phi_{\text{SE}} - \sqrt{\frac{q E_{\text{DC}}}{4\pi\epsilon}} \right) \right] \quad (3.13)$$

with electron charge  $q$ , Boltzmann's constant  $k_B$ , temperature  $T$  and the Schottky barrier height  $\Phi_{\text{SE}}$ . Hence, the dominance of SE is indicated if replotted the leakage current as  $\ln(J_{\text{leak}})$  versus  $\sqrt{E_{\text{DC}}}$  yields a linear dependence. This is done in the upper plot of Figure 3.8c and, indeed, the negative half-axis is fitted well by a line with slope  $\beta = 0.65 \sqrt{\mu\text{m}/\text{V}} = 6.5 \cdot 10^{-4} \sqrt{\text{m}/\text{V}}$ . To confirm SE, this slope must correspond to the physical parameters in (3.13). The observed slope leads to an extracted relative permittivity

$$\epsilon_{r,\text{opt}} = \frac{q^3}{4\pi\epsilon_0 (k_B T \beta)^2} = 5.24, \quad (3.14)$$

which is well inside the range of reported optical relative permittivities for BST [Vor+04; Ber+08]. For leakage current considerations, the optical permittivity was found effective for charge transport due to the fast transition times of the electrons [Sim67; JPH05]. Hence, SE is concluded as the dominant mechanism for the negative half-axis. For positive polarities, the same slope is approximated for stronger bias fields and at a higher absolute current level. This difference can be explained by comparing the work functions  $W_{\text{Pt}} \approx 5.5 \text{ eV}$  and  $W_{\text{SMO}} \approx 4.1 \text{ eV}$  [RC99; Rad17]. A band diagram construction of this double junction, not shown, reveals that bias voltages with negative polarities at the TE center pad weaken the barrier on the BE, i.e., between SMO and BST. Hence, the barrier on the TE, i.e., the Pt/BST interface is decisive. Since  $\Phi_{\text{SE},\text{Pt}} = W_{\text{Pt}} - \chi_{\text{BST}}$  [RC99] with electron affinity  $\chi_{\text{BST}} = 3.9 \text{ eV}$  is much larger than  $\Phi_{\text{SE},\text{SMO}}$ , the current must overcome a larger barrier for negative polarity. It is noteworthy in this context that the height of the Schottky barrier depends on the oxidization of BST near the interface [Sch+08]. Since the electron

affinity of BST is close to the work function of SMO and due to the contradicting thermodynamic requirements, a SE-limited current for positive polarities is not necessarily observed for every sample of this kind.

### 3.3.2 High-Performance Varactor

The final goal of this research field is the application of high-performance all-oxide varactors in circuits. In this section, the electrical data for a corresponding varactor is presented. A large microwave quality factor requires low conduction losses, i.e., a preferably thick BE up to at least one skin depth or more. The achievable thickness is, however, limited by the small growth rate in PLD and increasing fluctuations with longer deposition times. Nonetheless, to demonstrate the feasibility, several samples with  $t_{\text{SMO}} \geq 5\,000\,\text{nm}$  were fabricated. Furthermore, one of the pivotal benefits of the all-oxide technology is the possibility to obtain functional layers with thicknesses of only a few 10 nm. This provides a high tunability at very low tuning voltages down to ion-battery voltage levels, yielding the use of DC-DC converters obsolete. The fabrication of these high-performance varactors was enabled by several studies on the deposition process to stabilize optimal material properties, compare section 3.4.

This section summarizes the RF characterization results for a sample with  $t_{\text{BST}} = 50\,\text{nm}$  and  $t_{\text{SMO}} \approx 5\,300\,\text{nm}$  [4]. Note that, in contrast to the description in section 2.3, this sample was fabricated with  $\text{SrTiO}_3$  as oxygen barrier. Note further that the high component quality factor yields VNA data inaccurate due to the worse impedance matching; ImpA results are used that are limited to 3 GHz. The relevant characterization results are summarized in Figure 3.9a. The zero-bias effective relative permittivity  $\epsilon_{r,\text{eff}} = 347$  extracted by (3.12) reveals a high BST crystal quality despite the small layer thickness. Assuming an  $\text{SrTiO}_3$  permittivity between 100 and 150 in a stacked dielectric model with thickness  $\approx 4\,\text{nm}$  leads to the conservative estimate of  $\epsilon_{r,\text{BST}} = 432$  and 388, respectively.<sup>5</sup> A very high tunability of  $\tau(4\,\text{V}/50\,\text{nm}) = 70.5\%$  confirms its high functionality. However, a very high leakage current is recorded up to the current limit of 1 mA at only slightly increased voltage levels. This can be explained by residual oxygen vacancies since a larger part of the BST layer was grown with reduced oxygen pressure to avoid oxidization of the SMO layer [4]. Below in Figure 3.9a, the quality factor is plotted versus frequency for zero bias and 4 V. A zero-bias quality factor of  $Q(1\,\text{GHz}) = 77$  shows the benefit of the thicker BE with respect to Figure 3.8a. However, modeling

---

<sup>5</sup>An even higher permittivity of BST is likely due to a reduced  $\text{SrTiO}_3$  permittivity caused by strain and defects in the thin  $\text{SrTiO}_3$  layer.

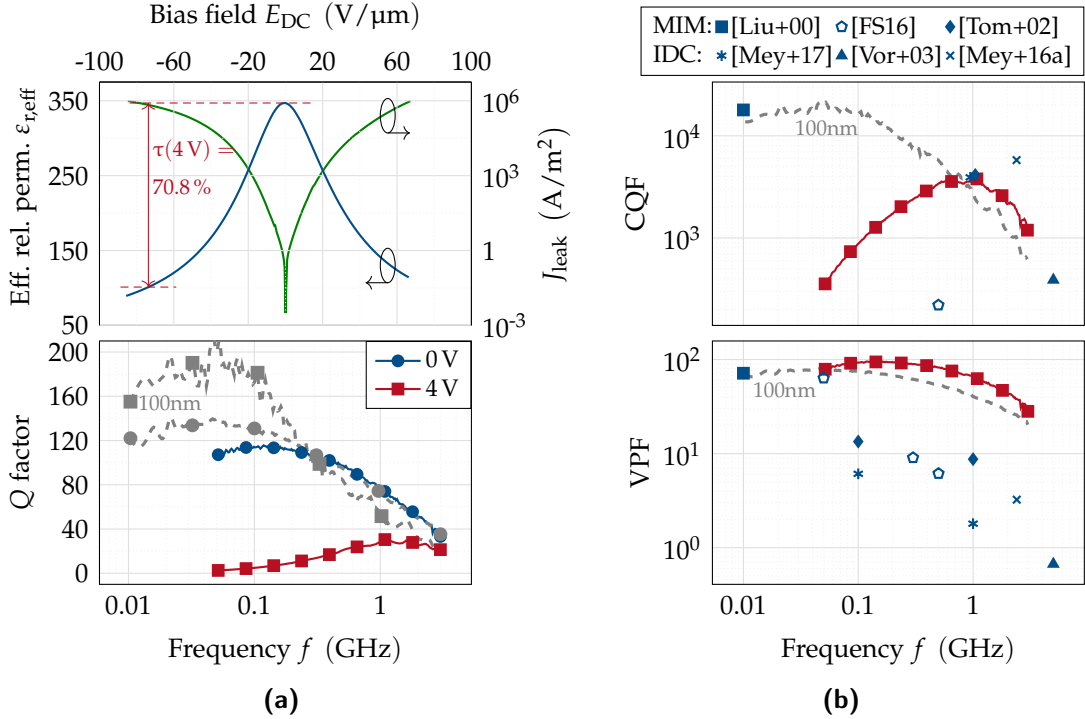


**Figure 3.9:** Characterization results for high-performance varactor with  $t_{\text{SMO}} = 5 \mu\text{m}$  and  $t_{\text{BST}} = 50 \text{ nm}$ . For the Q factor and FoMs, the data of another varactor with the same BE thickness and  $t_{\text{BST}} = 100 \text{ nm}$  is added in gray color. The CQF and VPF are compared to several reported values shown as blue markers.

reveals an increased SMO resistivity of  $\rho_{\text{SMO}} = 50.4 \mu\Omega \text{ cm}$ . Modeling this varactor structure with the lower resistivity values from Figure 2.10 yields  $Q(1 \text{ GHz}) \geq 90$  [5]. Comparing to reported single-crystal resistivity values, a quality factor of up to 100 and higher is conceivable after further material optimization. If biased, a strong decrease of the quality factor is observed, especially for lower frequencies. This degradation can be connected to the huge leakage current by comparing the results for another sample with  $t_{\text{SMO}} \approx 5000 \text{ nm}$  and  $t_{\text{BST}} = 100 \text{ nm}$  shown in gray color in the same plot. The leakage current density of this sample, not shown, is reduced by 3-4 orders of magnitude and does not affect the RF characteristic; the unprecedented decrease for low frequencies is not observed. However, acoustic resonances are more prominent for the thicker BST layer and lead to a decrease under bias for microwave frequencies. Generally and despite the oxygen vacancies, the high quality factor at low frequencies, where the electrode loss does not dominate, reveals the low dielectric loss in BST.

Finally, this varactor gets checked against other works by means of two distinct figures of merit (FoMs) in Figure 3.9b. The first one is the so-called commutation quality factor (CQF) defined by Vendik *et. al.* as [VVK00]

$$\text{CQF}(f) = Q(V_{\text{DC}}, f) Q(0, f) \frac{\tau(V_{\text{DC}})^2}{1 - \tau(V_{\text{DC}})}. \quad (3.15)$$

A competing CQF of 3700 and 1200 is recorded at 1 GHz and 3 GHz, respectively. The condition for general applicability in microwave applications  $\text{CQF} \geq 2000$  [Ven+99] is fulfilled up to 2.4 GHz. However, this FoM does not value the low-voltage tuning and emphasizes the microwave loss as it has been derived for two-state switching devices. Returning to tunable materials, a simple FoM is the product of material tunability  $n = C(0)/C(V_{\text{DC}})$  and quality factor  $Q$  [AGK15]. When dividing this expression by the tuning voltage, one obtains the voltage performance factor (VPF)

$$\text{VPF}(V_{\text{DC}}, f) = \frac{n(V_{\text{DC}})}{V_{\text{DC}}} Q(0 \text{ V}, f), \quad (3.16)$$

which rewards low-voltage tuning. The VPF is suggested in this work to rate technologies in the context of mobile application. The zero-bias quality factor is used instead the biased value to emphasize the technology before the actual varactor implementation.<sup>6</sup> Since none of the reported works tune with such a low voltage level, the all-oxide technology is clearly outstanding.

### 3.4 RF-Performance-Driven Material Optimization

Several studies on the optimization of the deposition process were conducted throughout this work. Especially the growth of BST thin films proved delicate with a high sensitivity towards, e.g., the laser energy density and the oxygen background pressure. A solely crystallographic characterization, however, has been found to fail in predicting the microwave performance. Hence, RF characterization data was evaluated in this work in systematic studies to optimize the deposition parameters. These studies had the goal to stabilize the properties of the resulting thin films at a good performance level which clearly is a fundamental constraint for the design of microwave components. At the same time, they enriched the

---

<sup>6</sup>The geometry dependence of acoustic resonances strongly affects the biased quality factor at microwave frequencies. However, as will be shown in section 4.2.5, the all-oxide technology can overcome the degradation imposed by acoustic resonances by an appropriate component design.

understanding of fundamental effects inside the varactor heterostructure. In this section, the divergence of a high crystal quality from XRD analysis and a low varactor performance is documented firstly. In the following, an example study on the laser fluence is presented, where RF characterization was used to control and optimize the thin-film deposition parameters.

### 3.4.1 Correlation of Crystallographic and DC/RF Characteristic

The most important methods to characterize the crystal structure of thin films are based on X-ray analysis [Ina08], besides other methods using, e.g., electron beams. Generally, prior to the microwave characterization, several measurements based on XRD are conducted to assess the quality of fabricated thin films. However, during this work, it was observed that a high crystallographic film quality does not necessarily yield a good microwave performance. Exemplary results of one study that document this observation are presented in the following. The XRD methods will be sketched only briefly; a more detailed description can be found in [Ina08].

Figure 3.10a shows a  $2\Theta-\Theta$  scan.<sup>7</sup> Here, X-rays are radiated onto the sample under a certain angle  $\omega = \Theta$ , where  $\omega = 0^\circ$  is parallel to the sample surface, and reflected inside the crystal lattice.<sup>8</sup> The reflected X-rays are recorded at an angle  $2\Theta$ , describing the deflection compared to the original beam. Peaks occur when the reflected rays interfere constructively, i.e., when Bragg's law is fulfilled [BB13]:

$$2d \sin \omega = n\lambda \quad (3.17)$$

with distance of lattice planes  $d$ , wavelength of the X-ray  $\lambda$  and an integer  $n$ . The certain angles of the main peaks can be mapped to the reflecting material according to their lattice plane distances. Around these angles, regular repetition of smaller maxima are observed, which are called Laue oscillations. These originate from the stronger reflection at the material interfaces, where each maximum represents a measurable satisfaction of (3.17). Note that, in this case,  $d$  does not correspond to the "bulk" crystal lattice of a material but to the interface to other films. Hence, the Laue oscillations can be used to determine the respective film thickness as described, e.g.,

<sup>7</sup>Inside this section and the context of XRD measurements,  $\Theta$  and  $\omega$  refer to angles in  $^\circ$ , despite the danger of confusion with angular frequency and temperature, which is the common usage in this work. This nomenclature is chosen for an easier comparison to literature for X-ray analysis.

<sup>8</sup>The symmetrical case  $\omega = \Theta$  is used throughout this work. The general asymmetrical case of a  $2\Theta-\omega$  scan uses an variable incident angle of the X-rays  $\omega \neq \Theta$ .

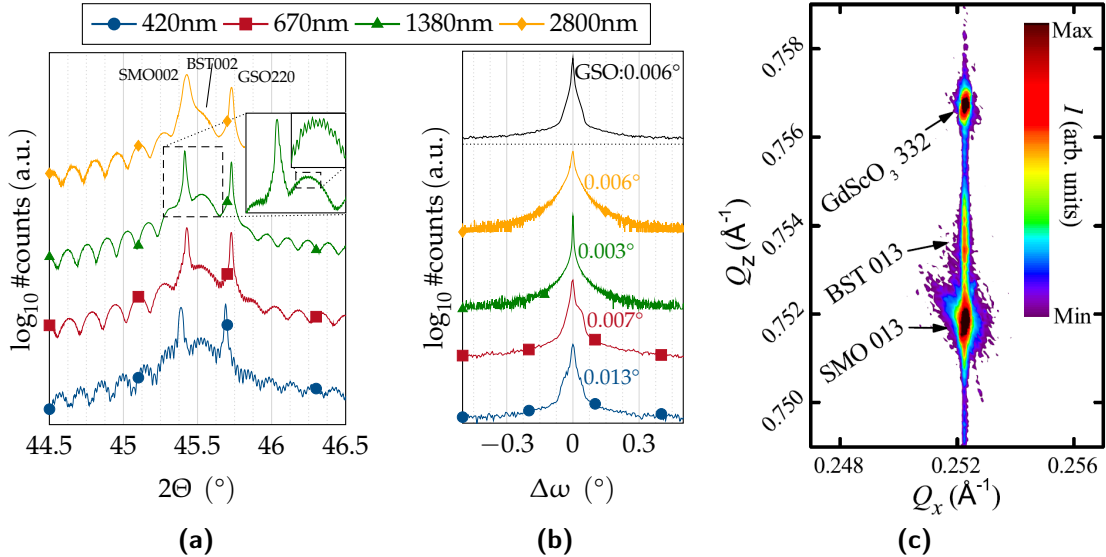


**Figure 3.10:** (a)  $2\Theta$ - $\Theta$  scan of four samples with different SMO thickness. For the sample with 1 380 nm thickness, the inset shows data from high-resolution measurements. (b) Rocking curves around the SMO 002 reflex with FWHM printed next to each line. The data for the epitaxial substrate (GSO 220 reflex) is also shown for comparison. (c) RSM of the sample with thickest SMO layer (2 800 nm).

in [Lin+05]. As intuitively derived from (3.17), a thinner film will cause a larger period of the Laue oscillations. For films with significantly differing thicknesses, multiple oscillations superpose and can often be evaluated in parallel to determine their respective thickness. The similar period of all lines in Figure 3.10a correspond to the likewise similar BST thickness between 61 nm and 70 nm. The oscillation period and strength for SMO decrease with the increasing film thickness as the reflection of the incident rays becomes less angle-dependent. For very thick layers with insignificant Laue oscillations, the thickness is estimated from evaluating the in-situ RHEED measurement.<sup>9</sup> However, for the two samples with thinner SMO, the twofold Laue oscillations can clearly be observed. For the sample "1 380 nm", an additional measurement with a more precise optic configuration, i.e., an analyzer crystal before the detector is able to resolve the Laue oscillations for SMO shown in the inset.

The epitaxy of the fabricated films can be rated by evaluating the rocking curve which is shown in Figure 3.10b. It is obtained by tilting the sample while the respective position of source and detector remains fixed to the angle  $2\Theta$  that corresponds

<sup>9</sup>The number of laser shots required to complete the first layers is counted. The final layer thickness is then estimated by proportional scaling to the number of total shots.

to the main peak of the respective material in Figure 3.10a. The sharper the peak, the less mosaic is the film since fewer tilted lattice planes are present that reflect the rays. This is quantified by the full width at half maximum (FWHM) that is very low for all SMO layers independent of their thickness. In fact, it is comparable to the one of the monocrystalline substrate GSO.

The previous two methods hardly allow an insight into the out-of-plane direction of the sample. This is extended with in-plane information by evaluation of the reciprocal space map (RSM). It can be understood as multiple rocking curve measurements under varying  $2\Theta$  angles inside a carefully chosen range that fulfills two constraints: The contained reflexes must, firstly, lie close to each other in the reciprocal space and, secondly, contain in-plane components. The former yields an adequate measurement time and easier comparison and the latter allows to analyze the in-plane structure. Figure 3.10c shows the RSM of the sample with thickest SMO. This sample is picked for illustration since it is most likely to suffer from relaxation or defect formation. The two axes  $Q_x$  and  $Q_z$  represent the length of the wave vectors in x- (in-plane) and z- (out-of-plane) direction, respectively.<sup>10</sup> From the equal intensity peak in  $Q_x$  it can be seen that all three materials share the same in-plane lattice constant. Thus, the different materials are grown in a locked spacing, following the lattice structure of the substrate GSO. With respect to GSO, BST and SMO exhibit only a small spread of intensity in both x- and z-direction. Hence, a high crystal quality with low mosaicity is indicated for these strained films.

However, this very good crystal quality does not mirror necessarily in good varactor performance. The results shown in Figure 3.11 are obtained from characterizing the samples with the scheme described in section 3.1. The maximum standard deviation of the RF data is sufficiently small for the purpose of this section, i.e., generally smaller than 20 %, such that the average data is considered representative. The relative permittivity is an approximation based on a simple PPC model and extracted from the indicated capacitance. Both, the capacitance and quality factor are evaluated at 1 GHz. In spite of the mutually very high crystal quality, a varying microwave performance is observed that is, however, degraded for all samples. The maximum permittivity ranges from 233 to 410, whereas the peak is offset to bias fields between 0 V/ $\mu$ m and 50 V/ $\mu$ m for the different samples. As expected, the zero-bias quality factor increases with the SMO thickness. However, for increasing bias field strength, a differing characteristic is observed: On the one hand as a monotone increase and on the other hand an eventual decrease after having peaked at interim field strengths. Both the permittivity and quality factor appear very asymmetric with bias. For positive bias fields, the characterization was aborted

---

<sup>10</sup>The inverse  $1/Q$  at the intensity peak yields the lattice constant in the respective direction of each material.

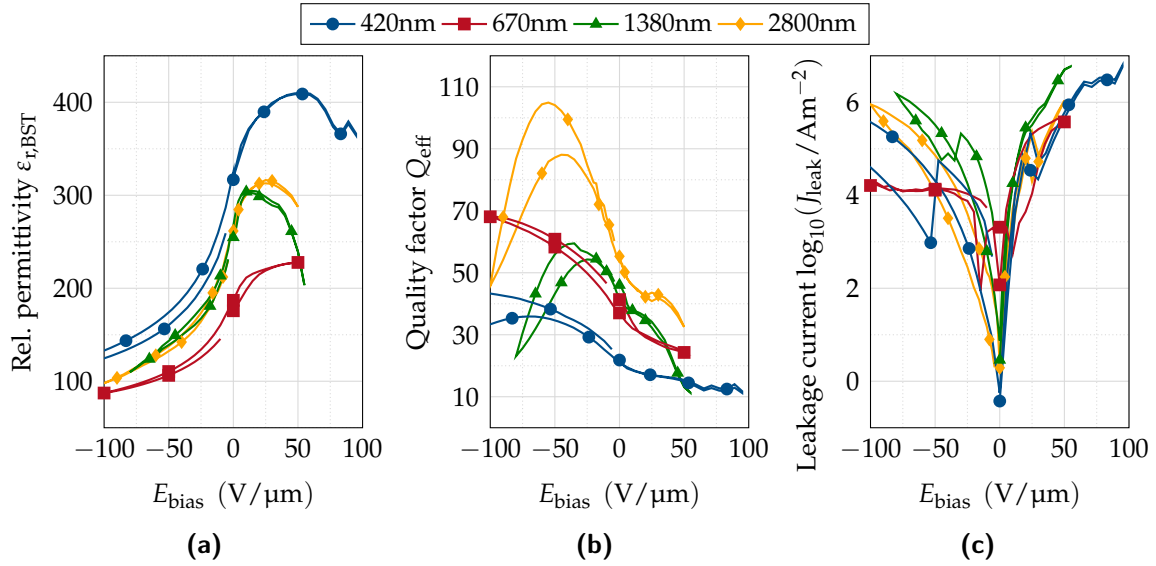


**Figure 3.11:** RF characterization results versus electric bias field  $E_{\text{bias}}$  in terms of (a) BST relative permittivity, (b) overall quality factor and (c) leakage current density. The former two are recorded at 1 GHz. All data represents the mean across all functional dies, the yield was above 85 % in all samples. For the quality factor, only samples with  $d_{\text{in}} = 20 \mu\text{m}$  are considered.

due to a too high leakage current beyond 1 mA. Figure 3.11c shows a very high leakage current density for all samples that is multiple orders of magnitude larger than literature values [Vor+04]. Indeed, the asymmetry of permittivity and quality factor with positive/negative bias fields of equal strength could be connected to the much stronger leakage current for positive polarity. Incidentally, a combination of a degraded Schottky barrier and oxygen vacancies in BST were identified as the source for this malfunction [A13]. The RF-characterization-based material optimization in the following subsection was a key element for these findings. In conclusion of this section, using electrical and microwave characterization of the complete varactor is a decisive tool to optimize deposition processes and materials for microwave components.

### 3.4.2 Study on Influence of Laser Fluence

One pivotal process parameter is the energy density of the pulsed laser (fluence) that ablates the atoms off the target to create the material flux for the film deposition [Nor04]. The exact reproduction of the target stoichiometry in the deposited

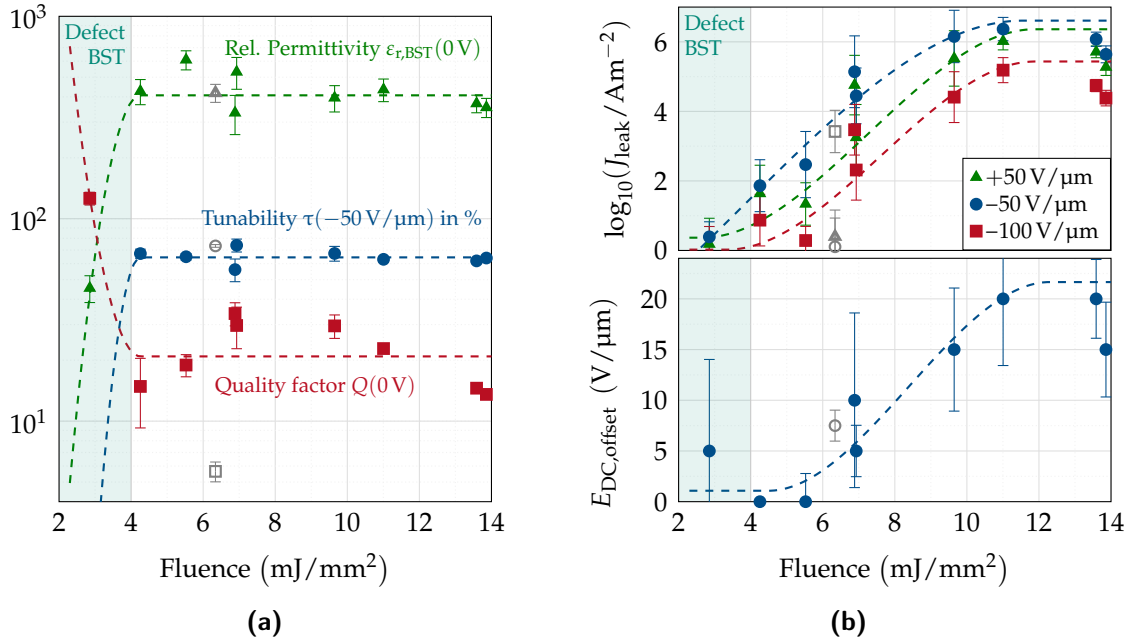


**Figure 3.12:** RF characterization results of study on impact of pulsed laser energy during the BST-film deposition. (a) Zero-bias mean of relative permittivity  $\epsilon_{r,BST}$  and overall quality factor  $Q$  along with mean relative tunability  $\tau$  at  $-50\text{ V}/\mu\text{m}$ , each extracted at 1 GHz. (b) Mean of the leakage current density at three different bias fields and the necessary bias field strength, i.e., offset to maximize the capacitance.

film strongly depends on the excimer laser energy level and has a decisive impact on the resulting RF properties of the film. Reading very high leakage currents in Figure 3.11c for both polarities<sup>11</sup> indicated a problem with the BST deposition. Therefore, the fluence was subject to one of the first studies with the results shown in Figure 3.12. It is noteworthy that each data point in these graphs contains information in a very condensed matter as it represents the complete sample with all varactors at once. Though this visualization requires restricting oneself to discrete pairs of bias field strength and frequency, the displayed results depict an expressive comparison. Again, the standard deviation of the data of the considered samples is sufficiently small such that the mean data is meaningful. Below a certain threshold of approximately  $4 \text{ mJ}/\text{mm}^2$ , the excitation energy is too low such that no functional, i.e., tunable layer with regular properties is obtained. Above that threshold, however, the permittivity, tunability and quality factor show no straight depen-

<sup>11</sup>Thus, a high leakage current was measured independent of whether the Schottky barrier to SMO was involved in the DC conduction or not.

dence on the laser energy. Note that a certain spread is typical for PLD processes, since the displayed properties depend on many parameters like stress, resulting stoichiometry and defect density. Hence, only trends can be considered in this evaluation.

Such a trend is certainly observed in Figure 3.12b where two more properties are displayed. Firstly, the leakage current density decreases by several orders of magnitude with decreased laser energy. As a simple measure for general asymmetry like the one observed in Figure 3.11, the leakage current is shown for three different bias field strengths. The similar dependence on the fluence of all three lines visualizes the generally similar symmetry in all samples. Solely the sample deposited with  $6.3 \text{ mJ/mm}^2$  shows a strongly reduced leakage current for negative bias fields, indicating the Schottky barrier at the TE-BST interface to be effectively limiting the leakage current. Since, furthermore, its zero-bias quality factor is reduced by almost one order of magnitude, this sample is rejected from this evaluation. On the one hand, this confirms the representative character of the other data shown in this figure. On the other hand, this clearly suggests an optimum fluence in the range  $4 \text{ mJ/mm}^2 - 6 \text{ mJ/mm}^2$ . Indeed, the low-performance BST films presented in section 3.4.1 were deposited with a fluence of about  $10 \text{ mJ/mm}^2$ , which agrees very well to the results here. This conclusion is underlined by the second graph in Figure 3.12b. Here, the bias field necessary to obtain the maximum capacitance, i.e., the offset of the bell-shaped capacitance versus bias field  $E_{DC,offset}$  is shown. A larger offset is connected to a stronger inherent polarization that must be compensated by the external bias field. Hence, it is interpreted as a degradation caused by defects and an possibly off-stoichiometric film. Note that the exact offset is not revealed in this study due to the large standard deviation and finite step size of the bias interval, i.e.,  $2.5 \text{ V}/\mu\text{m}$  and  $5 \text{ V}/\mu\text{m}$  for values smaller and greater than  $10 \text{ V}/\mu\text{m}$ . As a result of this study, a lower fluence was chosen for all following BST-film depositions.

Further studies were executed that are not discussed here. Among them, the oxygen background pressure during the BST deposition was optimized to minimize the number of oxygen vacancies while maintaining the reduced state of the SMO electrode. Furthermore, a decrease of the required substrate temperature during deposition was investigated to ensure compatibility with established industrial processes. The most important results are reported in [Sal20; Zei20].

## 4 Highly Accurate Analytic Models

Currently, there is a lack of analytic models with sufficient accuracy for thin-film MIM varactors. Hence, the only option to extract the material properties is the fitting of a fully-electromagnetic finite element method (FEM) model to the measurement results. However, this is very time-consuming. Furthermore, since biasing induces piezoelectricity, a respective modeling of biased states is not possible without multi-physics solvers. The corresponding FEM models are prohibitively complex. Their calculation requires vast computational resources, in particular for the high aspect ratio of the test structures in this work; the layer thickness and lateral extent are in the nm and  $\mu\text{m}$  range, respectively. The inter-dependence of the relevant material properties on shaping the overall characteristic constitutes an additional challenge. Considering the massive amount of data for the many samples with each carrying 36 test structures, which are in turn each measured at many bias states, FEM modeling is hardly feasible. This chapter derives a comprehensive model for both the electromagnetic and piezoelectric behavior of ferroelectric MIM varactors. The presented solution scheme allows a sophisticated and highly accurate identification of mechanic and electric properties with much lower computational effort.

The complexity of a model increases with the complexity of the analyzed behavior. Often, a multitude of input parameters is mapped onto a single or few model outputs. In the context of this work, typical input parameters are the geometry and material properties of a DUT. The output is usually the device impedance  $Z(f, E_{DC})$  that can be compared to independent information, i.e., measured characterization results. A central element of modeling is reversing this mapping for validation which allows studying materials and function principles. This common task in research is called an inverse problem. For example, at the end of this chapter, the mere microwave impedance is used to identify all relevant properties of ferroelectric varactors.

Two different kind of inverse problems are solved in this work, which are illustrated in Figure 4.1. The model inputs are grouped into sample properties and model parameters. The former contain all desired information about a DUT, while the latter are independent of a certain sample. The first kind is the model derivation which relies on trustworthy reference data to identify all model parameters. When

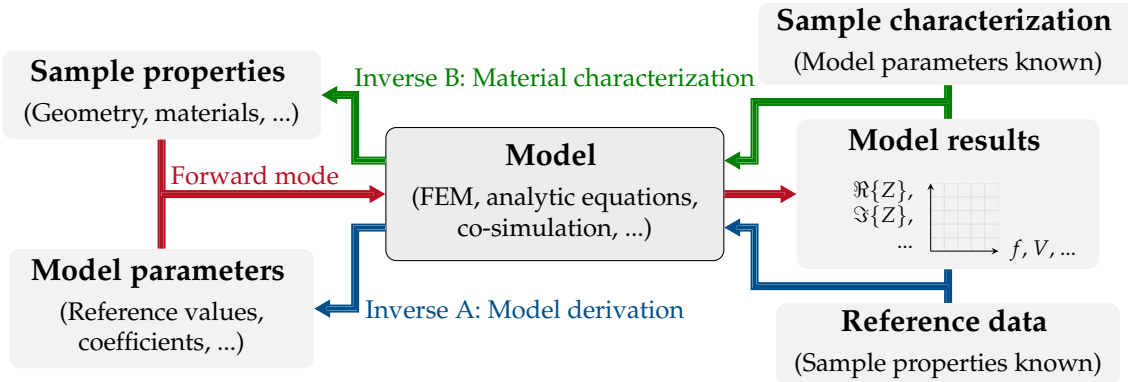


**Figure 4.1:** Schematic for the two kinds of inverse problems solved in this work.

deriving the coefficients of analytic models, using validated FEM simulation results as reference data is the beneficial choice. Alternatively, if available, measurement results of well-known materials can as well be used as reference data. Afterwards, the second kind uses the validated model parameters to characterize the contained materials of a DUT with as yet unknown properties.

Mathematically, inverse problems are a sub-group of optimization problems. They are solved by the parameter set  $\mathbf{p}$  that minimizes the difference between model output  $\mathbf{Z}_{\text{model}}(\mathbf{p})$  and true/reference data  $\mathbf{Z}_{\text{true}}$ , i.e.,

$$\mathbf{F}(\mathbf{p}) = \mathbf{Z}_{\text{model}}(\mathbf{p}) - \mathbf{Z}_{\text{true}} \rightarrow \mathbf{0}. \quad (4.1)$$

Theoretically, the naive approach of testing every possible combination of regularly swept parameters inside their expected range would yield the true result. However, this is generally unfeasible as it likely requires excessive computational resources and time even for small problems. Therefore, many optimization algorithms have been developed that, in a nutshell, trade correctness against speed.<sup>1</sup> There are gradient-based converging methods [Adb74; Ada96] and heuristics like the genetic [Sch07], evolutionary [Sim13] or particle swarm algorithm [WTL17]. For identification problems like in this work, accuracy in finding the global minimum is essential. This, however, generally challenges heuristic approaches that don't necessarily converge. During this work, several corresponding tests have failed to produce the optimum result in an acceptable time with varying initial values and parameter ranges. This leads to gradient-based methods that, on the downside, must be controlled carefully to not get stuck at local minima.

<sup>1</sup>There are additional quality measures like optimality, accuracy or completeness. Their discussion is, however, not required in this overview. Some examples of algorithms being compared in more detail can be found in [Sin93; CWD99; Has+05].

Among them, the iteratively regularized Gauss-Newton (IRGN) method provides a stable solution and avoids local minima that are far from the global one by a proper regularization [RI15]. Given a parameter set  $\mathbf{p}^i$ , the set for a subsequent run is defined as

$$\mathbf{p}^{i+1} = \mathbf{p}^i + \left[ \mathbf{J}(\mathbf{p}^i)^t \mathbf{J}(\mathbf{p}^i) + \beta^i \mathbf{I} \right]^{-1} \left[ \mathbf{J}(\mathbf{p}^i)^t \mathbf{F}(\mathbf{p}^i) \right] + \beta^i (\mathbf{p}^i - \mathbf{p}^0), \quad (4.2)$$

where  $\mathbf{J}(\mathbf{p})$  is the Jacobian matrix, i.e., the derivation of each row of  $\mathbf{F}(\mathbf{p})$  by each parameter in  $\mathbf{p}$

$$\mathbf{J}(\mathbf{p}) = \frac{\partial \mathbf{F}}{\partial \mathbf{p}} = \left[ \frac{\partial \mathbf{F}}{\partial p_1}, \frac{\partial \mathbf{F}}{\partial p_2}, \dots, \frac{\partial \mathbf{F}}{\partial p_P} \right]. \quad (4.3)$$

Since evaluated computationally, the derivation is executed numerically as difference quotient around  $\mathbf{p}^i$ . In (4.2),  $\mathbf{p}^{i+1}$  minimizes the Tikhonov functional, i.e., the summed squared error by linearizing  $\mathbf{F}(\mathbf{p}^i)$  around  $\mathbf{p}^i$  [KNS08]. The regularization parameter  $\beta^i$  enforces wider steps at the beginning as well as for badly chosen initial values. In this work, due to the normalization to respective average values as defined below,  $\beta^0 = 1$  can be used as a starting point which is halved in each iteration

$$\beta^i = \frac{1}{2^i}. \quad (4.4)$$

The inverse problems in this work deal with the microwave impedance of varactors. This allows to concretize the shape of the compared characteristic  $\mathbf{Z}_{\text{true}}$  and, equally,  $\mathbf{Z}_{\text{model}}$ . Generally, the sample properties are identified via measurement results over a wide range of frequencies and bias field strengths. Each data point carries two-fold information, i.e., real/imaginary part or magnitude/phase. Using the interpretation as capacitance and quality factor is reasonable due to a small variation over the observed frequency and bias range. The measurement data is normalized to its respective frequency-average value according to

$$\mathbf{C}_n = \frac{1}{\text{avg}_f[C_n]} [C_n(f_1), C_n(f_2), \dots, C_n(f_G)]^t, \quad (4.5)$$

where  $C_n(f_g)$  is the capacitance at the  $g$ -th observed frequency and  $n$ -th bias state and  $\text{avg}_f[C_n]$  describes the mean value across all observed frequencies.  $\mathbf{Q}_n$  is defined analogue. With that, the result-data vector is built depending on the considered inverse problem. If the sought parameters depend on the bias state or only one state is considered, one chooses

$$\mathbf{Z}_{\text{true},n} = [\mathbf{C}_n^t, \mathbf{Q}_n^t]^t. \quad (4.6)$$

When information for multiple, i.e.,  $N$  bias states is available and the sought parameters are bias-independent, the data is formatted as

$$\mathbf{Z}_{\text{true}} = [\mathbf{C}_1^t, \mathbf{Q}_1^t, \mathbf{C}_2^t, \mathbf{Q}_2^t, \dots, \mathbf{C}_N^t, \mathbf{Q}_N^t]^t. \quad (4.7)$$

Note that, besides varying bias states, other systematic changes can be incorporated analogously. For example, when deriving the analytic model for thin electrodes in the following section, the FEM simulated data for varied film thicknesses is used to obtain the respective model coefficients. Depending on the given problem, reference measurements of multiple samples can be used likewise, if their properties are well-known. Especially with an increasing number of parameters, a broader base of reference data enhances the optimization stability.

## 4.1 Unshielded Substrate Model (USM)

The established method for dielectric characterization does not exhibit the required accuracy for working with oxide electrodes with typical thicknesses of a few hundred nm up to a few  $\mu\text{m}$ . Although the method presented in section 3.2 extended the principally applicable frequency range up to the electrical SRF, it still exhibits only a limited accuracy for microwave frequencies. It merely provides a fair estimate of the dielectric constant and loss factor for known electrode properties (conductivity, surface roughness, effective thickness) and for lower frequencies up to approximately 1 GHz. It only approximates the BE electrode contribution by its sheet resistance, which causes two problems. Firstly, its sheet resistance needs to be known and is critically impacting the extracted dielectric properties. The thinner the BE, the stronger the sheet resistance is affected by surface roughness [Mor+18]. Secondly, any impact of the substrate is discarded in this model. It is well-known that electromagnetic fields decay exponentially inside a conductor. At a distance of one skin depth [Jac75]

$$\delta_{\text{skin}} = \sqrt{\frac{2}{\omega \mu \sigma}} \quad (4.8)$$

to the surface, the wave is damped only to  $1/e = 36.9\%$ . In the above expression,  $\omega$  is the circular frequency,  $\mu$  the magnetic permeability and  $\sigma$  the conductivity of the conductor. A comparison of skin depths for different conducting materials is shown in Figure 4.2a. As the film quality varies with fabrication parameters, three values for SMO are given. The conductivity of an average and rather good film quality

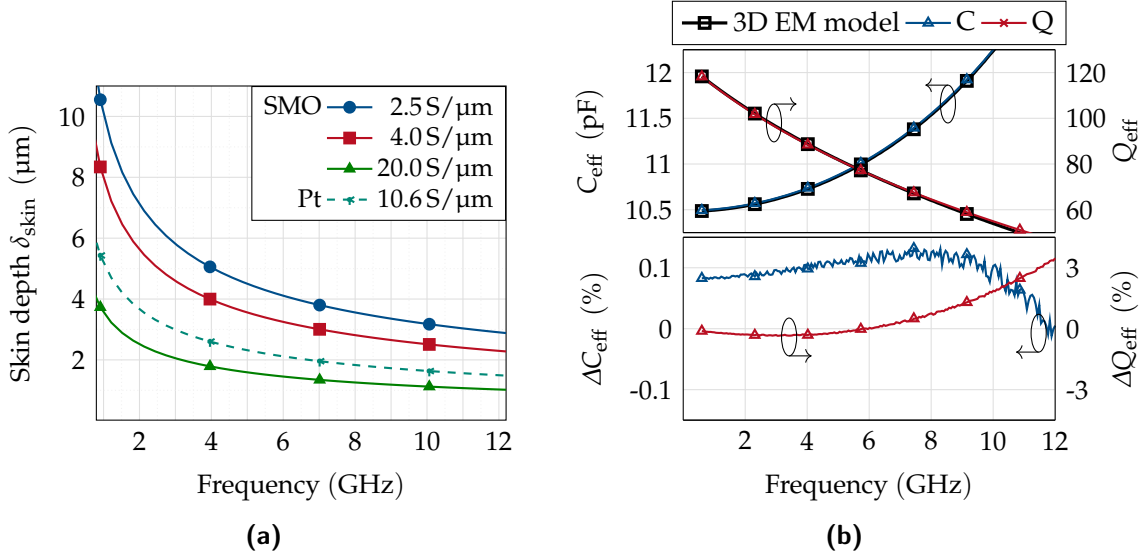


**Figure 4.2:** (a) Comparison of skin depths for SMO with average ( $2.5 \text{ S}/\mu\text{m}$ ), above average ( $4.0 \text{ S}/\mu\text{m}$ ) and single-crystal ( $20.0 \text{ S}/\mu\text{m}$ ) conductivity. Bulk platinum is added for comparison. (b) Capacitance and Q factor of the test structure with PEC BE versus frequency for the 3D EM model and the common RLC model, respectively, and their relative deviation.

have been characterized as  $2.5 \text{ S}/\mu\text{m}$  and  $4 \text{ S}/\mu\text{m}$ , respectively, compare Figure 2.10. However, even for platinum or the single-crystal SMO conductivity  $20.0 \text{ S}/\mu\text{m}$ , the skin depth still exceeds  $1 \mu\text{m}$  in the observed frequency range.

This allows to draw an important conclusion for the transfer on MIM structures. Since roughly 3–5 skin depths are required to yield the substrate negligible, even an electrode thickness of several  $\mu\text{m}$  still does not allow to discard the substrate impact [Jac75]. Hence, there is a strong need for developing another model that includes thin electrodes, where perfect shielding of the substrate is not possible anymore: The unshielded substrate model (USM). A schematic model is initially derived that matches accurately to the validated electromagnetically 3D-modeled data. Afterwards, the evaluation of the field energy in the substrate allows to link the schematic components with the material properties, i.e., dielectric thickness and permittivity and electrode thickness and conductivity. Finally, the USM is validated by a simulated multivariate deviation and characterization of several samples.

**Table 4.1:** Schematic Model fitting parameters for PEC and finite conductivity (FIN) BEs. For all models:  $C = 10.49 \text{ pF}$ ,  $Q_C = 1 / \tan \delta_{\text{diel}} = 125$

	$R_s$ ( $\Omega$ )	$L_s$ (pH)	$k$ (%)	$a_{\text{sub}}$ (ns/ $\Omega$ )	$\Delta C_{\text{max}}$ (%)	$\Delta Q_{\text{max}}$ (%)
PEC-RLC	0.012	2.17			0.11	3.53
FIN-RLC	0.227	1.97			0.61	6.05
FIN-USM	0.243	3.81	13.08	1.72	0.12	0.79

#### 4.1.1 Extended Schematic Model

This model is based on the electromagnetic 3D model that was validated in section 3.2. It is derived for the test structures with  $d_{\text{in}} = 20 \mu\text{m}$  and  $d_{\text{out}} = 80 \mu\text{m}$ . The same method can as well be applied to all other used electrode sizes, the respective model parameters are summarized in appendix B.1.

Firstly, the underlying assumption that the substrate is impacting the measured overall impedance significantly for thin BEs needs to be justified. However, providing impedance data from either characterization or a 3D electromagnetic model for samples with a sufficiently thick BE is impracticable due to limitations in fabrication or computational resources, respectively. As a proof of concept, a PEC BE is used instead as its infinite conductivity provides a vanishing skin depth. In Figure 4.2b, the input impedance data is plotted as overall effective capacitance and quality factor versus frequency. As can be seen, the common schematic RLC model fits the 3D model data very well with the parameters provided in Table 4.1. The capacitance from the TE outer ring to the BE is negligible for the overall capacitance due to its very large area. The very high quality factor arises from the PEC BE, since only the TE and the dielectric contribute losses. The remaining electrode resistance  $R_s$  is caused only by the TE and, therefore, very small, yielding the dielectric loss more prominent. The increasing error in  $Q_{\text{eff}}$  for higher frequencies can be explained by the distributed nature of the outer coupling capacitance, which is not accounted for in the lumped elements. However, for BEs with finite conductivity, the electrode loss dominates the overall quality factor, preventing this error from being significant. For a thick BE, the substrate is equally negligible as for PEC, since all fields decay inside the conductor and, hence, the substrate is shielded.

This changes for a decreasing BE thickness; the substrate needs to be taken into account for a correct modeling. In order to find a more sophisticated model, the field distribution in the substrate is shown in Figure 4.3. A large portion of field is observed only at the center, while a much weaker contribution is observed in the

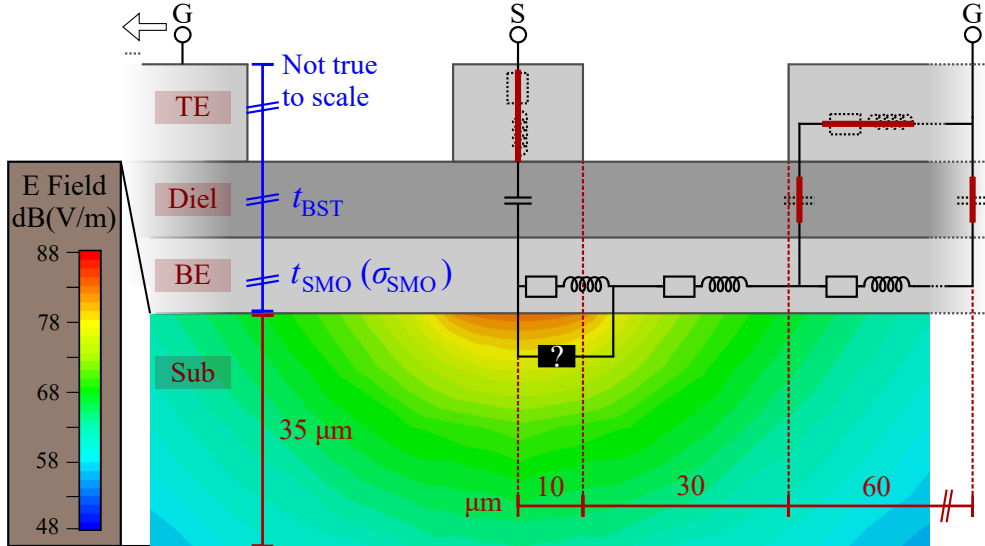


**Figure 4.3:** Distribution of the electric field in the substrate for  $t_{\text{SMO}} = 500 \text{ nm}$ ,  $\sigma_{\text{SMO}} = 3.33 \text{ S}/\mu\text{m}$  and  $t_{\text{BST}} = 80 \text{ nm}$ . In the substrate at the center, the fields are by orders stronger than in the outer region.

outer region. This concentration at the center is caused by the very strong fields in the dielectric of the main capacitance  $\underline{C} = C(1 - j \tan \delta_{\text{diel}})$ . This motivates the splitting of the BE's resistance and inductance into two; a high and low energy part representing the center and outer region, respectively. The resulting model is shown in Figure 4.4a. Generally, the TE inductance and resistance are assumed negligible due to a shorter conducting path length and the much higher conductivity. The splitting ratio is given by the factor

$$k = \frac{R_{\text{center}}}{R_s} = \frac{L_{\text{center}}}{L_s}. \quad (4.9)$$

The high energy portion  $R, L_{\text{center}}$  is in parallel to a complex impedance  $A_{\text{sub}} = 1/j\omega a_{\text{sub}}$ . Concluding from the frequency dependence of the latter, the interpretation as a capacitance seems natural. However, the resulting effective capacitance value in the nF range cannot be justified straightforwardly from the given geometry and materials. Surprisingly, a variation of the substrate permittivity and losses shows only a weak impact on the overall impedance. The detailed explanation of the physical origin of this parallel impedance is beyond the scope of thesis and, hence, left for future work. Generally, the weaker the field in the substrate, the smaller  $k$  and the weaker the influence of the substrate becomes;  $A_{\text{sub}}$  is shorted for  $k = 0$ .

Figure 4.4b compares the impedance data for a BE with finite conductivity  $\sigma_{\text{SMO}} =$

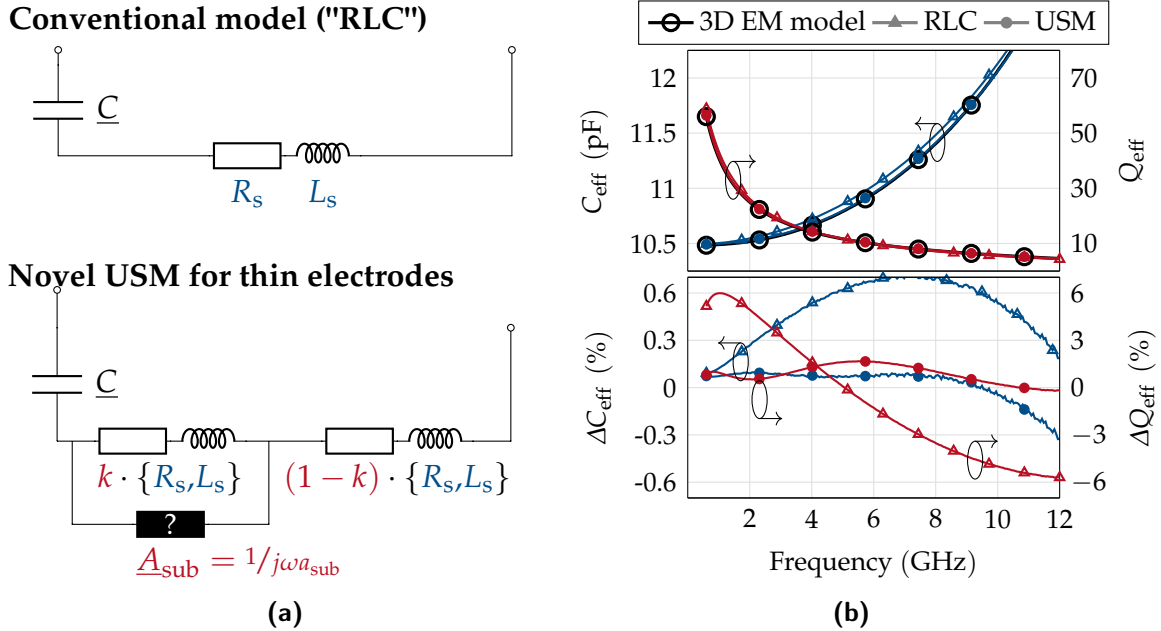


**Figure 4.4:** (a) Comparison of the standard RLC model and the novel USM. (b) Capacitance and quality factor versus frequency of all models for finite  $\sigma_{\text{SMO}} = 3.33 \cdot 10^6 \text{ S/m}$ , and their respective relative deviation.

3.33 S/ $\mu\text{m}$  and thickness  $t_{\text{SMO}} = 500 \text{ nm}$  for the RLC model and the USM. The RLC model is fitted by a matching low frequency capacitance and the smallest maximum relative deviation for  $Q_{\text{eff}}$ , see Table 4.1. However, it fails for this parameter set with a significant deviation. A too early increase of  $C_{\text{eff}}$  with frequency is predicted. The analytical description of the USM in Figure 4.4a is

$$Z_{\text{DUT,USM}} = \frac{1}{j\omega C} + k \frac{\underline{A}_{\text{sub}} Z_{\text{elec}}}{\underline{A}_{\text{sub}} + k Z_{\text{elec}}} + (1 - k) Z_{\text{elec}} \quad (4.10)$$

with  $Z_{\text{elec}} = R_s + j\omega L_s$ . It fits to the data of the EM model with a greatly increased accuracy. The corresponding model parameters in Table 4.1 yield the minimum RMSE over a broad range. They are obtained via IRGN optimization of this inverse problem as described at the beginning of this chapter. A broad variety of starting points with variation by up to 30 % confirms their validity. Note that particularly the starting point for  $k$  determines whether the optimizer converges or not. The other parameters can be varied in a wider range due to their unique impact on the  $C$ - $Q$ -frequency characteristic. Exact schematic modeling of the circular structure, i.e., perfect fitting is unfeasible due to the radial signal propagation and simultaneous

capacitive coupling of the inductive electrodes. This distributed nature requires the combination of an infinite number of lumped elements. However, the previously suggested splitting already provides a very accurate fitting of the 3D simulation result. This accurate, schematic fitting testifies a conclusive understanding of the dominant impacts and is a strong argument for reliable predictions based on this model.

#### 4.1.2 Parameterized Material Variations

In this section, the above model is parameterized by relating it with the set of major physical properties of the test structure

$$\mathcal{P} = \{t_{\text{SMO}}, \sigma_{\text{SMO}}, t_{\text{BST}}\}, \quad (4.11)$$

i.e., the thicknesses  $t_{\text{SMO}}$ ,  $t_{\text{BST}}$  and the conductivity  $\sigma_{\text{SMO}}$ .<sup>2</sup> Changes in the dielectric permittivity can be accounted for by scaling the thickness according to

$$t_{\text{BST}} := \frac{\varepsilon_{\text{ref}}}{\varepsilon_{\text{true}}} t_{\text{BST,true}} \quad (4.12)$$

with the respective permittivities used in the reference EM model  $\varepsilon_{\text{ref}}$  and the varied one  $\varepsilon_{\text{true}}$ , and the true, i.e., geometrical BST thickness  $t_{\text{BST,true}}$ . This is possible due to the predominantly vertical electric fields between the electrodes, which is confirmed by EM simulations with correspondingly scaled parameters. A change in the dielectric loss factor  $\tan \delta_{\text{diel}}$  mirrors in the loss factor of the main capacitor  $\underline{C} = C(1 - j \tan \delta_{\text{diel}})$ .

To estimate the impact of the parameters  $\mathcal{P}$ , the field energy in the substrate  $W_e$  is calculated and used as a comparative measure. Since the structure is electrically small with respect to the wavelength in all dimensions, the electrostatic field energy density  $w_e = \varepsilon |E|^2 / 2$  is used. Integration yields

$$\begin{aligned} W_e &= \int_V w_e dV \\ &= \int_{-15 \mu\text{m}}^{15 \mu\text{m}} \int_{-15 \mu\text{m}}^{15 \mu\text{m}} \int_{-30 \mu\text{m}}^{0 \mu\text{m}} \frac{\varepsilon |E|^2}{2} dz dy dx \\ &\approx \frac{\varepsilon}{2} \sum_{x_m} \sum_{y_n} \sum_{z_p} |E_{mnp}|^2 \Delta z_p \Delta y_n \Delta x_m \end{aligned} \quad (4.13)$$

---

<sup>2</sup>For parallel formalism to the electrode thickness, the conductivity is used here instead the commonly considered resistivity  $\rho = 1/\sigma$ . In the sub-skin-depth region, the resistance can well be approximated as proportional to both:  $R \propto \sigma t$ .

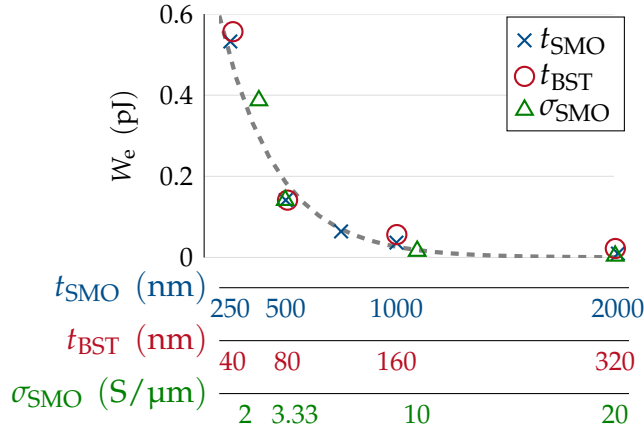


**Figure 4.5:** Simulated field energy in the substrate at the center versus thicknesses  $t_{\text{SMO}}$ ,  $t_{\text{BST}}$  and conductivity  $\sigma_{\text{SMO}}$  at 1 GHz and 1 V excitation amplitude.

For computational reasons, the integration is executed discretely and inside a limited volume  $V$ , which is a  $30 \times 30 \times 30 \mu\text{m}^3$  excerpt in the substrate directly below the BE and centered around the inner TE. However, this suffices to show a clear trend in Figure 4.5, where the resulting data is shown for frequency and excitation amplitude of 1 GHz and 1 V, respectively. A seemingly exponential increase of energy in the substrate for thinner layers and worse conductivity can clearly be observed. On the one hand, this demonstrates the necessity of taking the substrate into account. On the other hand, this suggests an exponential dependence of the model elements on the respective parameters. Therefore, the following expression for  $k$  is formulated:

$$k = k_{\text{ref}} \cdot \exp(N_{k,\mathcal{P}} \delta_{\mathcal{P}}) \quad (4.14)$$

with an exponential scaling coefficient  $N_{k,\mathcal{P}}$  and the relative parameter deviation

$$\delta_{\mathcal{P}} = \frac{\mathcal{P} - \mathcal{P}_{\text{ref}}}{\mathcal{P}_{\text{ref}}} \quad (4.15)$$

It was found that the assumption of an analogue dependence for the substrate contribution

$$a_{\text{sub}} = a_{\text{sub,ref}} \cdot \exp(N_{a,\mathcal{P}} \delta_{\mathcal{P}}). \quad (4.16)$$

with the scaling coefficient  $N_{a,\mathcal{P}}$  yields an accurate fitting of the overall impedance data. In this analysis, the reference values are

$$\begin{aligned} \mathcal{P}_{\text{ref}} &= \{t_{\text{SMO,ref}}, \sigma_{\text{SMO,ref}}, t_{\text{BST,ref}}\} \\ &= \{500 \text{ nm}, 3.33 \text{ S}/\mu\text{m}, 80 \text{ nm}\}. \end{aligned} \quad (4.17)$$

These values form a practical reference for the thin film varactors discussed in this work; the high accuracy for a broad range of parameters  $\mathcal{P}$  will be proven below. However, a too large  $\delta_{\mathcal{P}}$  will eventually lead to severe model errors. In this case, the reference values  $\mathcal{P}_{\text{ref}}$  can be chosen differently with an adjusted set of reference parameters for the schematic components. Besides (4.14) and (4.16), further intuitive variations of the other schematic elements will be introduced below.

The resulting model accuracy can be seen in Figure 4.6. In all subfigures, the overall capacitance and quality factor of the RLC and USM is plotted versus frequency in comparison to the 3D EM model, respectively. The error of the RLC model is plotted as colored background, which, as there is hardly any deviation for the USM, also describes the benefit of the latter. Firstly, the BE thickness  $t_{\text{SMO}}$  is varied from 250 nm to 1 000 nm. As in all cases  $t_{\text{SMO}} < \delta_{\text{skin}} = 2.76 \mu\text{m}$  (10 GHz), the BE resistance  $R_s$  is scaled linearly with the thickness. An additional scaling factor is introduced to account for the substrate loss, resulting in

$$R_s = R_{s,\text{ref}} \cdot \left( \frac{t_{\text{bot,ref}}}{t_{\text{SMO}}} \right) \cdot \exp(N_{R,t_{\text{SMO}}} \delta_{t_{\text{SMO}}}). \quad (4.18)$$

Since the substrate loss contributes in parallel to the conducting BE loss, the substrate contribution mitigates the linear scaling of  $R_s$  via a positive  $N_{R,t_{\text{SMO}}}$ . The BE inductance decreases only slightly for an increasing thickness according to

$$L_s = L_{s,\text{ref}} \cdot \exp(N_{L,t_{\text{SMO}}} \delta_{t_{\text{SMO}}}). \quad (4.19)$$

With these parameters, the data in Figure 4.6a is obtained. The RLC model with linearly scaled resistance deviates stronger for thin BEs. This is surprising, as the BE resistance should depend linearly on its thickness if  $t_{\text{SMO}} \ll \delta_{\text{skin}}$ . Furthermore, it's not able to display the characteristic slight drop of the capacitance in the lower GHz domain. The USM matches the RLC model for increasing  $t_{\text{SMO}}$  and also tracks the 3D EM model data for thin BEs. Secondly, the BE conductivity  $\sigma_{\text{SMO}}$  is varied from  $2 \text{ S}/\mu\text{m}$  to  $20 \text{ S}/\mu\text{m}$  in Figure 4.6b. As intuitively expected, the model components can be described analogously to (4.18) and (4.19). Finally, the dielectric thickness  $t_{\text{BST}}$  is varied from 40 nm to 320 nm. The capacitance naturally has a linear dependence on the thickness. A 3D model simulation sweep has shown that the asymmetric coupling of the circular TE to the planar BE can be modeled as exponentially decreasing, resulting in

$$C = C_{\text{ref}} \cdot \left( \frac{t_{\text{diel,ref}}}{t_{\text{BST}}} \right) \cdot \exp(N_{C,t_{\text{BST}}} \delta_{t_{\text{BST}}}). \quad (4.20)$$

The elements  $R, L_s$  are independent of  $t_{\text{BST}}$ , as they are dominated by the electrode contributions. With these parameters, the data in Figure 4.6c is obtained. The

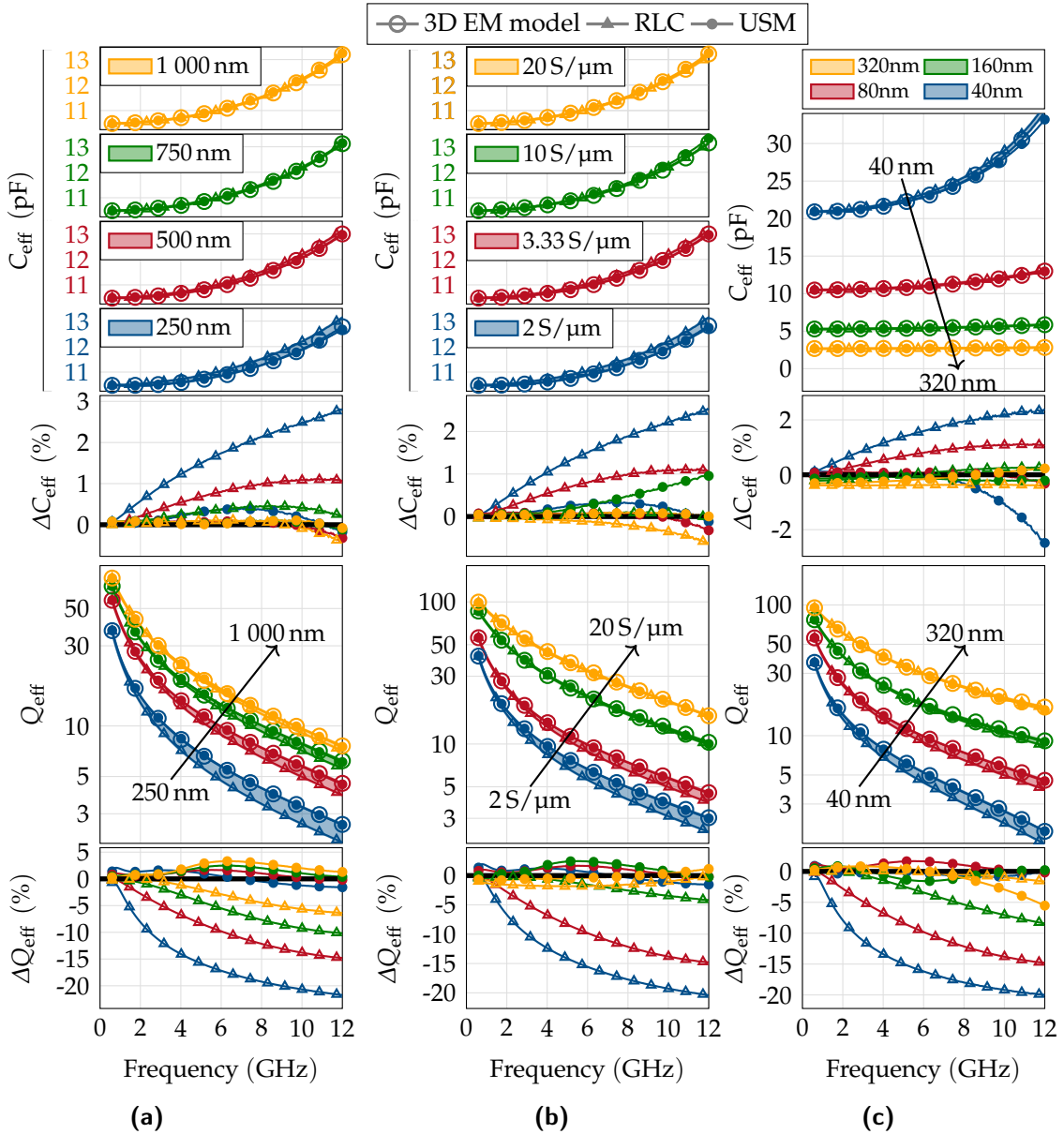


**Figure 4.6:** Capacitance and quality factor versus frequency for a varied (a)  $t_{\text{SMO}}$ , (b)  $\sigma_{\text{SMO}}$  and (c)  $t_{\text{BST}}$ . The highlighted area describes the error of the RLC model and, thus, the benefit of the USM model. For a fair comparison, the scaled resistance of the RLC data for varied BE thickness and conductivity was multiplied by the same exponential scaling as for the USM model.

**Table 4.2:** Input parameters for the USM, which is fitting variations of the varactor properties  $\sigma_{\text{SMO}}$ ,  $t_{\text{BST}}$ ,  $t_{\text{SMO}}$ .

	$N_{k,\mathcal{P}}$	$N_{a,\mathcal{P}}$	$N_R$	$N_L$	$N_C$
$\mathcal{P} = t_{\text{SMO}}$	-0.758	1.372	0.050	-0.016	
$\mathcal{P} = \sigma_{\text{SMO}}$	-0.758	1.372	0.050	-0.016	
$\mathcal{P} = t_{\text{BST}}$	-0.418	-0.419			0.005

electric field in the capacitor is stronger for a thinner dielectric, leading to a stronger penetration of the substrate. This leads to a stronger error if the substrate is neglected (RLC model). Again, the presented model accurately tracks the impedance characteristic for the full displayed frequency domain.

The resulting fixed parameters for the USM are shown in Table 4.2. They have also been obtained by IRGN optimization. The variation of  $t_{\text{SMO}}$  and  $\sigma_{\text{SMO}}$  should impact the substrate contribution equally due to the small BE thickness. Hence, their parameters can be fixed as equal during the optimization without missing the actual impedance characteristic. In overview on Figure 4.6, one observes a significant reduction of the maximum relative error of  $C_{\text{eff}}$  and  $Q_{\text{eff}}$  from up to 3 % and 20 % for the RLC model down to 1 % and 3 % for the USM, respectively.

### 4.1.3 Multivariate Model

For a wide applicability, a multivariate model is derived from the above. For this, the respective factors for each parameter  $\mathcal{P}$  are multiplied, leading to

$$k = k_{\text{ref}} \cdot \exp [N_{k,\text{bot}} (\delta_{t_{\text{SMO}}} + \delta_{\sigma_{\text{SMO}}}) + N_{k,t_{\text{BST}}} \delta_{t_{\text{BST}}}] , \quad (4.21)$$

$$a = a_{\text{sub,ref}} \cdot \exp [N_{a,\text{bot}} (\delta_{t_{\text{SMO}}} + \delta_{\sigma_{\text{SMO}}}) + N_{a,t_{\text{BST}}} \delta_{t_{\text{BST}}}] . \quad (4.22)$$

The electrode components are formed analogously by the respective exponential scaling and the quotients of BE conductivity and thickness to

$$R_s = R_{s,\text{ref}} \cdot \exp [N_R (\delta_{t_{\text{SMO}}} + \delta_{\sigma_{\text{SMO}}})] \cdot \left( \frac{t_{\text{bot,ref}}}{t_{\text{SMO}}} \right) \cdot \left( \frac{\sigma_{\text{bot,ref}}}{\sigma_{\text{SMO}}} \right) , \quad (4.23)$$

$$L_s = L_{s,\text{ref}} \cdot \exp [N_L (\delta_{t_{\text{SMO}}} + \delta_{\sigma_{\text{SMO}}})] . \quad (4.24)$$

In these expressions, the terms for the BE can be summarized due to the equality of the coefficients for  $\sigma_{\text{SMO}}$  and  $t_{\text{SMO}}$ . Since  $C$  is independent of the BE, (4.20) can be used also for the multivariate model. The impacts of varied varactor

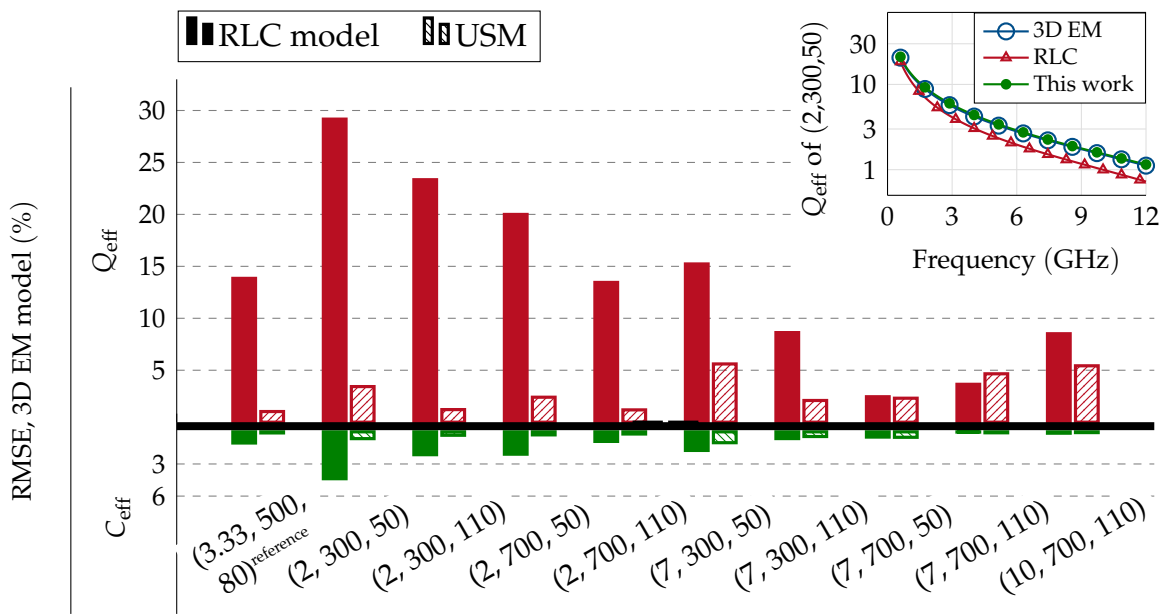


**Figure 4.7:** RMSE of effective  $Q$  factor (top) and capacitance (bottom) for both models for varactors with multivariate properties ( $\sigma_{\text{SMO}}/\text{S}\mu\text{m}^{-1}$ ,  $t_{\text{SMO}}/\text{nm}$ ,  $t_{\text{BST}}/\text{nm}$ ). The inset shows  $Q_{\text{eff}}$  versus frequency of the triple  $(2, 300, 50)$ .

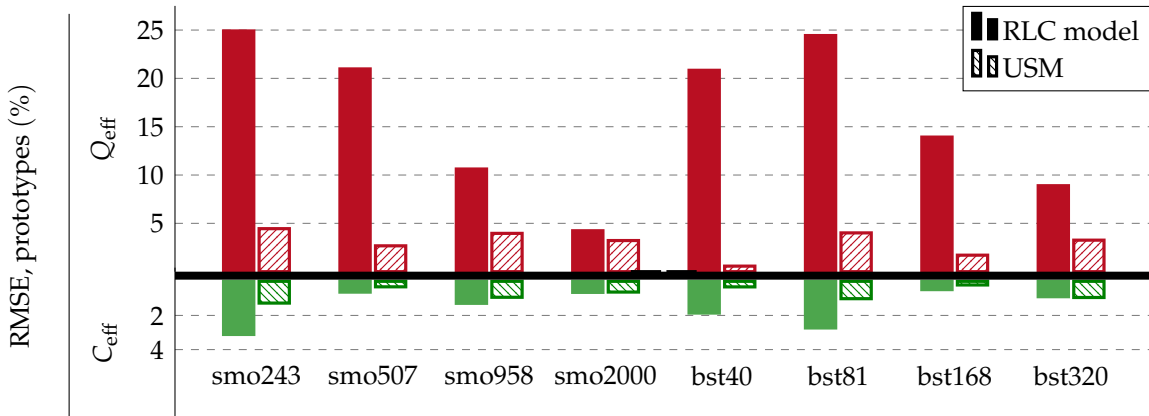
properties can cancel each other out by positive and negative relative deviations  $\delta_{\mathcal{P}}$ , with respect to the defined reference. Ideally, the limits of this model are found by a three-dimensional parameter sweep in fine steps. For this, however, a vast amount of simulation is necessary, which exceeds the available computational resources. Therefore, representative sets of multivariate varactor properties are selected. All permutations of the triples formed by  $\sigma_{\text{SMO}} = \{2,7\} \text{ S}/\mu\text{m}$ ,  $t_{\text{SMO}} = \{300,700\} \text{ nm}$  and  $t_{\text{BST}} = \{50,110\} \text{ nm}$  are analyzed. For comparison, the reference  $(\sigma_{\text{SMO}}/\mu\text{m}^{-1}, t_{\text{SMO}}/\text{nm}, t_{\text{BST}}/\text{nm}) = (3.33, 500, 80)$  is also shown. As a comparative measure, the RMSE is calculated across the observed frequency range and compared to the RLC model in Figure 4.7. For all samples, the USM yields an RMSE for  $C_{\text{eff}}$  and  $Q_{\text{eff}}$  below 1.0 % and 5.6 %, respectively. As described above, the resistance was scaled linearly with BE thickness and conductivity according to a negligible skin effect. For worse conductivity and thinner electrodes and, hence, less shielding of the substrate, the tremendous benefit of the USM can be clearly seen. The inset in Figure 4.7 shows the  $Q$  factor versus frequency of the sample (2, 300, 50). Again, enforcing a linear scaling of the resistance with varied  $t_{\text{SMO}}$  and  $\sigma_{\text{SMO}}$  in the RLC model does not yield the best-possible fit. This is surprising, as the skin effect does surely not extrude the fields for this triple of material properties. For the USM, the linear scaling of the BE contribution plausibly fits the EM model data for the shown triple, as well as for all other shown samples.<sup>3</sup> Despite the simplicity of this multivariate model, only a slight offset to the 3D EM data remains. A slightly increased error with respect to the RLC model is observed only for the sample (7, 700, 110). This can be explained by considering that this triple combines all parameters with the lowest substrate contribution. However, two aspects show that this is no principal limit of the model. Firstly, the error is still very similar to the one of the RLC model. Secondly, additional data for a further increased conductivity (10, 700, 110) shows a benefit of the USM. Hence, though  $A_{\text{sub}}$  is eventually shorted, (7, 700, 110) reveals a crossover flaw, where the phenomenological substrate has a too strong impact. This is due to the chosen reference parameters  $\mathcal{P}_{\text{ref}}$  that are impacted significantly by the unshielded substrate. This issue can be resolved by defining a second reference  $\mathcal{P}_{\text{ref2}}$  with correspondingly adjusted parameters for a more shielded case.

---

<sup>3</sup>The small value of  $N_R$  makes the exponential term in (4.23) much weaker than the linear scaling with thickness/conductivity.

**Table 4.3:** Properties of the measured sample varactors

Sample	$t_{\text{SMO}}$ (nm)	$t_{\text{BST}}$ (nm)	$\rho_{\text{SMO}}$ ( $\mu\Omega \text{ cm}$ )	$\epsilon_{r,\text{diel}}$	$\tan \delta_{\text{BST}}$ ( $10^{-3}$ )
smo243	243	91	37.7	366	4.6
smo507	507	91	67.4	92	4.1
smo958	958	86	61.6	420	11.0
smo2000	2 000	89	93.5	340	12.7
bst40	517	40	41.9	251	6.3
bst81	490	81	64.1	392	10.4
bst168	486	168	62.7	153	5.5
bst320	516	320	96.3	145	4.7


**Figure 4.8:** RMSE of  $C_{\text{eff}}$  and  $Q_{\text{eff}}$  of both models for measured test varactors. The material properties of the varactors are summarized in Table 4.3.

#### 4.1.4 Verification by Measurement

As the derivation of the USM was based on the comparison to 3D EM simulation data, it will be verified by test samples in this section. Several samples with varied thicknesses  $t_{\text{SMO}}$ ,  $t_{\text{BST}}$  and material properties  $\sigma_{\text{SMO}}$ ,  $\epsilon_{r,\text{diel}}$ ,  $\tan \delta_{\text{BST}}$  have been manufactured and characterized, the results are shown in Table 4.3. The sample names originate from the respective dielectric (bst) and BE (smo) thickness. The layer thicknesses are obtained with XRD measurements where possible<sup>4</sup> [Rad+14], allowing the determination of the material properties by fitting of the EM model as described in section 3.2. The corresponding RMSE of both schematic models is

<sup>4</sup>For smo958 and smo2000, RHEED was used instead due to the thick layers, see section 3.4.1.

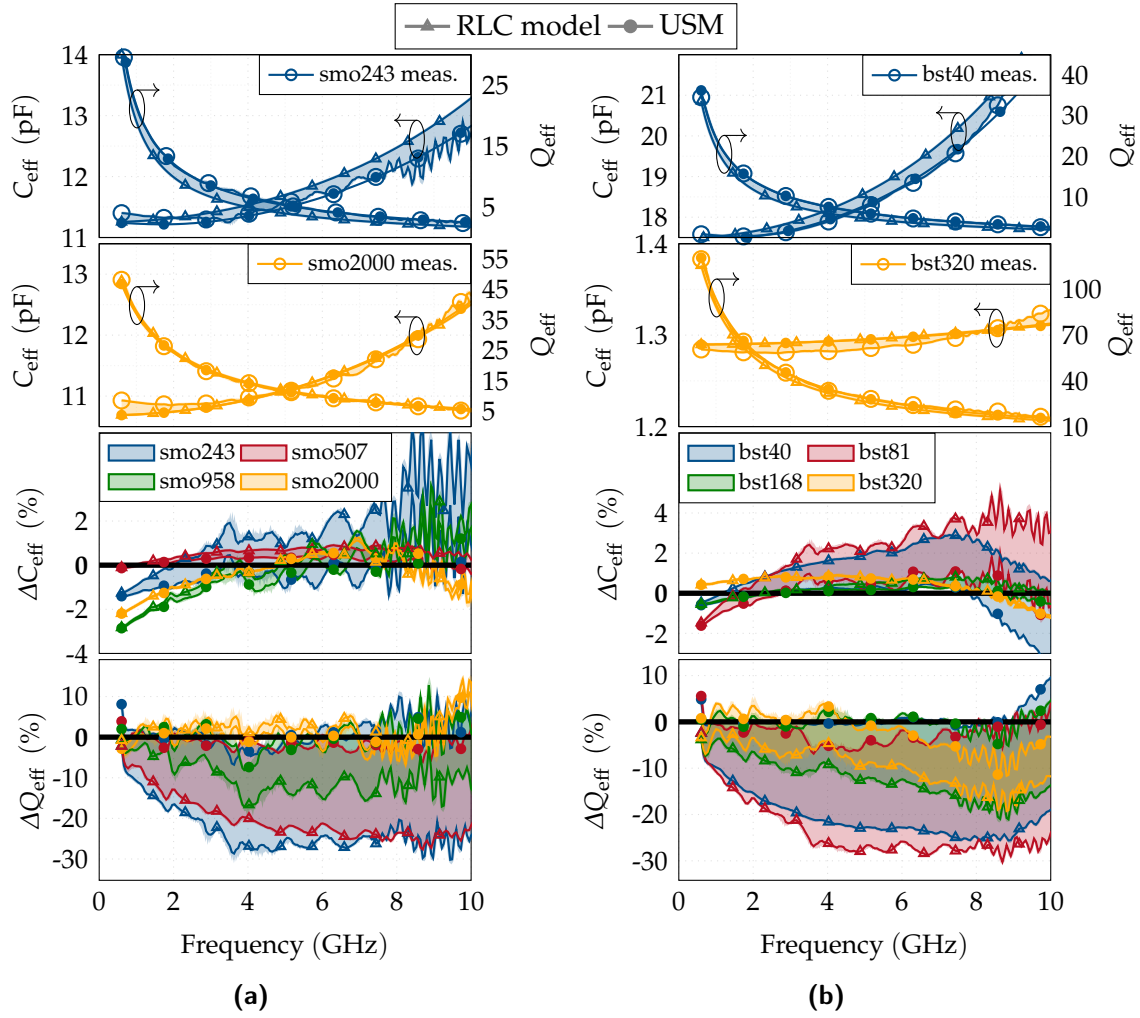


**Figure 4.9:** (a) Capacitance and quality factor versus frequency for the measured varactor smo243 and smo2000. Additionally, the relative deviation of both models in  $C$  and  $Q$  to the measurement data for smo243, smo507, smo958 and smo2000 is shown. The difference between the RLC and the USM has been highlighted. (b) Like (a) for bst40, bst81, bst168, bst320.

compared in Figure 4.8. The smaller error of the USM is confirmed by the measured samples. The maximum RMSE in  $Q_{\text{eff}}$  and  $C_{\text{eff}}$  is smaller than 4.5 % and 2.4 %, respectively, for the USM instead of 24.9 % and 3.1 % for the RLC model. Note that a larger error is obtained for samples with a larger resistivity, i.e., a greater difference to the used model reference  $\rho_{\text{SMO,ref}} = 30 \mu\Omega \text{ cm}$ .

The detailed results for the first four samples ("smo...") are shown in Figure 4.9a.

For smo243 and smo2000, the capacitance and quality factor are plotted in absolute values, respectively, and the error of the RLC model is highlighted. The comparison shows the particular benefit of the USM for thin electrodes. Nonetheless, even for smo2000, a better accuracy is achieved by the USM due to the low conductivity, i.e., worse substrate shielding. The same trend is confirmed by the relative deviation that is additionally shown for all four samples in the same plot. Detailed results for the latter four samples ("bst...") are shown in Figure 4.9b. For bst40, the capacitance is not exactly fitted by the USM, but approximated better than for the RLC model. This can be connected to the very strong fields in the dielectric, which lead to a very strong penetration of the substrate, challenging the model simplicity. The quality factor, however, is accurately fitted. As discussed above for the thicker SMO, the USM benefit is particularly strong for thinner BST. However, in this case, this still holds for the thicker BST layer of bst320, again due to limited shielding caused by the small SMO thickness and low conductivity. As the relative deviation for C and Q show, all varactors are accurately fitted by the USM.

## 4.2 Acoustic Unshielded Substrate Model (AUSM)

Section 2.1.3 has shown how acoustic waves are excited under an external bias field via induced piezoelectricity. In this section, the USM will be extended to the acoustic unshielded substrate model (AUSM), which incorporates these acoustic effects. Note that, for the all-oxide varactors in this work, acoustic activity will show an untypical impact on the impedance characteristic versus frequency. This is due to the partial resonance suppression caused by the adjacent oxide layers and the mechanical loading of the on-wafer probe. Nonetheless, the unambiguous identification of this effect being caused by acoustic waves is done at the end of this section via modeling.

### 4.2.1 Modeling Acoustic Resonances

The fundamental resonance frequency of an unloaded resonator corresponds to the wavelength equaling the double resonating length. It is referred to as  $\lambda/2$  resonator. When modeling acoustic resonances in BST varactors with that model, the acoustic resonance frequencies can be estimated as

$$f_{ac,res,n} = n \frac{2v_{ac,BST}}{t_{BST}} \quad (n = 1, 3, \dots), \quad (4.25)$$

with the acoustic velocity  $v_{\text{ac},\text{BST}}$  and the odd integer  $n$  describing all resonating path lengths causing constructive interference. However, a simple example calculation reveals this model to be unusable for this work on MIM varactors; even a very low acoustic velocity  $v_{\text{ac},\text{BST}} = 3 \text{ km/s}$  yields  $f_{\text{ac,res},1} = 75 \text{ GHz}$  for a film thickness of  $t_{\text{BST}} = 80 \text{ nm}$ . Since acoustic resonances are already observed in the lower GHz domain, this simple model is not applicable. Physically, the conflict arises from the assumption of ideal boundaries, i.e., of full reflection in the  $\lambda/2$  resonator. In reality, a significant portion of the acoustic wave is not reflected at the BST interfaces but transmitted into adjacent layers. This extends the effective resonator length, corresponding to a decrease of the recorded resonance frequency. For practical relevance of the AUSM, two more aspects are important. Firstly, not only the frequencies but also information about the amplitude is required. Secondly, the acoustic resonances must be linked to the microwave impedance since that impact is of primary interest.

Such a link was derived from the constitutional equations (2.37) by Lakin *et al.* who mapped the piezoelectric effect onto the microwave impedance of an MIM capacitance by [LKM93]

$$\underline{Z}_{C,\text{diel+ac}} = \frac{1}{j\omega C} \left[ 1 - K^2 \frac{\tanh \Phi}{\Phi} \frac{(z_t + z_b) \cosh^2 \Phi + \sinh 2\Phi}{(z_t + z_b) \cosh 2\Phi + (z_t z_b + 1) \sinh 2\Phi} \right] \quad (4.26)$$

with electromechanical coupling factor [Mas50]

$$K^2 = 1 - \frac{c_{\text{eff}}^E}{c_{\text{eff}}^D} = \frac{c_{\text{eff}}^D \varepsilon_{\text{eff}}^T g_{\text{ind}}^2}{1 + c_{\text{eff}}^D \varepsilon_{\text{eff}}^T g_{\text{ind}}^2}, \quad (4.27)$$

complex phase argument  $\Phi = \gamma_{\text{BST}} t_{\text{BST}} / 2$  and the complex propagation constant  $\gamma = \alpha + j\beta$  of the acoustic wave. The acoustic wave number and damping constant are given by  $\beta = \omega/v_{\text{ac}}$  and  $\alpha = \beta/(2Q)$ , respectively, with the acoustic quality factor  $Q$ . Further,  $z_t = Z_t/Z_{\text{BST}}$  and  $z_b = Z_b/Z_{\text{BST}}$  are the acoustic impedances of the top and bottom interface, respectively, normalized to the impedance of BST. The acoustic velocity and impedance are calculated by

$$\begin{aligned} v_{\text{ac}} &= \sqrt{c_{\text{eff}}^D / \rho} \\ Z &= \rho v_{\text{ac}}, \end{aligned} \quad (4.28)$$

with density  $\rho$ . The adjacent layers above and below BST are modeled as acoustic transmission lines (TLs) as shown in Figure 4.10 in red color. Analogue to electric transmission lines,  $Z_t$  and  $Z_b$  can be obtained from consecutively transforming the

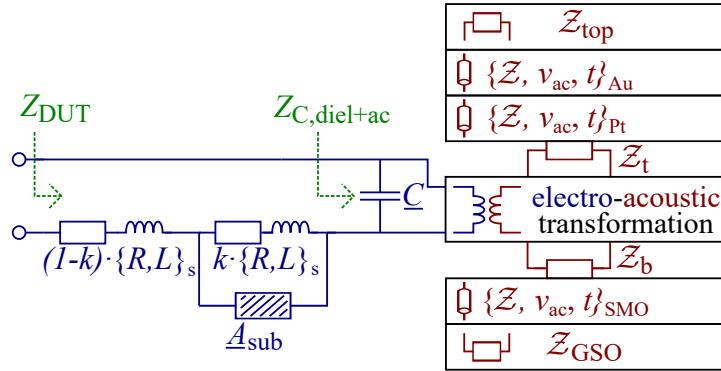


**Figure 4.10:** Schematic of combined electro-acoustic model for thin electrodes.

acoustic termination through all substrate and electrode layers towards the BST interface via [GVL06]

$$Z_{in} = Z_i \frac{Z_L + Z_i \tanh(\gamma_i t_i)}{Z_i + Z_L \tanh(\gamma_i t_i)}. \quad (4.29)$$

$Z_{in}$  is the TL input impedance,  $Z_L$  the load impedance at the opposite layer interface and  $Z_i, \gamma_i, t_i$  are the acoustic impedance, complex propagation constant and thickness of the layer, respectively.

However, this model just considers the acoustic impact of the sandwiching layers. On the electric side, (4.26) just contains the permittivity and dielectric loss factor of the ferroelectric. When dealing with real varactors at microwave frequencies, the electrode loss usually dominates the overall microwave loss. Hence, they must not be neglected when a highly accurate model is desired. For sufficiently thick BEs, simply adding  $Z_{elec} = R_s + j\omega L_s$  to the impedance can be expected to fit the measured characteristic well. However, as discussed in the previous section, this impedance does not fit for thin-film devices with a thinner BE as it neglects substrate effects. Instead, (4.26) should be extended by the model from section 4.1.1 to

$$Z_{DUT,AUSM} = Z_{C,diel+ac} + k \frac{A_{sub} Z_{elec}}{A_{sub} + k Z_{elec}} + (1 - k) Z_{elec}. \quad (4.30)$$

The resulting combined electro-acoustic model is shown in Figure 4.10. It relates the mere microwave impedance to the characteristic electric and acoustic properties of the contained materials. However, as the above derivation shows, plenty of parameters are contributing. Since most of these often vary significantly in fabricated samples, especially for thin films, this yields many degrees of freedom for the model inputs. As a result, the reliable extraction of material properties is impeded which, hinders a reasonable application of the model. The following section presents

how considering the bias dependence of the parameters allows an unambiguous identification nonetheless.

### 4.2.2 Solving the Inverse Problem

The as of yet only frequency-dependent model will be extended to a multivariate model by adding the dimension of the electric bias field. Well-known dependencies of the model parameters on the bias field can be exploited to reduce the degrees of freedom, consolidating the extracted material parameters. The formulae behind (4.30) are implemented as the model for the inverse problem of extracting the material parameters from the measured microwave impedance. The eight unknown parameters in the AUSM are the

- dielectric permittivity  $\epsilon(E_{DC})$  and loss factor  $\tan \delta_{\text{diel}}(E_{DC})$
- electromechanic coupling coefficient  $K^2(E_{DC})$
- BST stiffness  $c_{\text{BST}}^D(E_{DC})$
- BE resistivity  $\rho_{\text{SMO}}$
- SMO stiffness  $c_{\text{SMO}}$
- acoustic upper termination with impedance  $\mathcal{Z}_{\text{top}}^5$
- Acoustic-resonator-effective gold thickness  $t_{\text{Au,eff}}^6$

Some of them depend on the bias field as indicated by " $(E_{DC})$ " and must be allowed to vary correspondingly during optimization. For the other unknowns, the result must be constant for all bias states. Therefore, the iterative optimization is executed alternately for all bias-constant and bias-dependent parameters, respectively. The increased risk of missing out the global minimum due to this splitting is commented and disproved in the subsequent section after discussing the material properties, compare page 88.

The BE conductivity obviously does not change with bias field and can, hence, be extracted just once initially for the zero-bias impedance as shown in Section 4.1. The intuitive approach would be to start with the (stronger impacting) bias-dependent parameters  $K^2(E_{DC})$ ,  $c_{\text{BST}}^D(E_{DC})$ ,  $\epsilon^T(E_{DC})$  and  $\tan \delta_{\text{diel}}(E_{DC})$ , and continue with

---

<sup>5</sup>Though actually not part of the sample, this acoustic impedance must, nonetheless, be characterized as it can vary from one contact of the on-wafer probe to another. A curved surface of the probe tip, low probe overtravel [1] and varying varactor electrode quality prevent a sample-independent determination.

<sup>6</sup>The on-wafer probe is digging into the TE, reducing the path length for the acoustic wave in the resonator. Note that, in the electric domain (conductor losses), the TE is negligible due to a much higher conductivity than the BE [2].

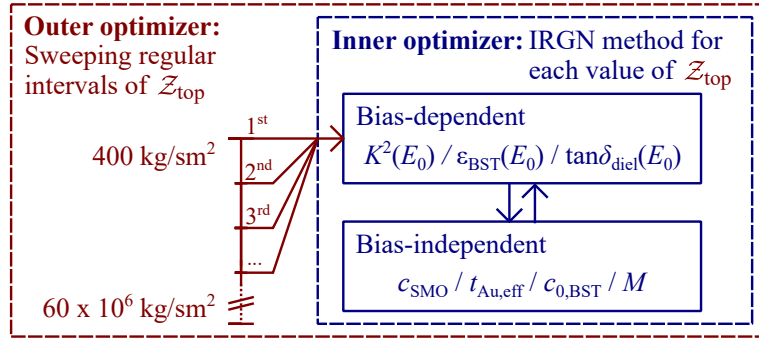


**Figure 4.11:** Flow chart of the convoluted optimizer of the model fitting for extracting the material properties.

the remaining bias-constant  $c_{\text{SMO}}$ ,  $Z_{\text{top}}$  and  $t_{\text{Au}}$ . However, two issues arise with this approach. Firstly, as the piezoelectric effect is induced by electrostriction, the impact of all mechanical parameters scales with the electric bias field, compare (2.36). Therefore, the optimizer converges only for bias fields stronger than approx.  $E_{\text{DC}} \geq 60 \text{ V}/\mu\text{m}$ . In the converging range, the BST stiffness varies only slightly and can be well-fitted to [Noe+07; Ven+08; Alz+14]

$$c_{\text{BST}}^D = c_{0,\text{BST}} + MD_0^2, \quad (4.31)$$

with the inherent stiffness  $c_{0,\text{BST}}$ , nonlinear electrostriction coefficient  $M$  and biasing displacement  $D_0 = \varepsilon^T E_{\text{DC}}$ . The optimizer will converge with reasonable results when propping up the stiffness by replacing the bias-dependent optimization parameter  $c_{\text{BST}}^D$  with bias-constant  $c_{0,\text{BST}}$  and  $M$ . Secondly, the three unknowns  $c_{\text{BST}}^D$ ,  $c_{\text{SMO}}$  and  $Z_{\text{top}}$  depend on each other in shaping the acoustic resonance effects in the measured microwave impedance, see (4.28). On the one hand, this causes many local minima that trap the optimizer and, on the other hand, this questions the confidence of the extracted parameters. Both issues are addressed by extending the previously described scheme to a convoluted optimization.  $Z_{\text{top}}$  is excluded from the IRGN method and is, instead, iteratively swept over regular intervals as an outer optimization. The choice of that parameter is motivated by the observation that its different initial values lead to a significantly differing fitting quality after convergence. Start and end of the initial interval is given by the two extreme cases "air" ( $400 \text{ kg}/\text{sm}^2$ ) and "metal" ( $60 \cdot 10^6 \text{ kg}/\text{sm}^2$ ), which estimates the material of the on-wafer probe. For each value of  $Z_{\text{top}}$ , the best-fitting other parameters are extracted by the inner optimizer. A flow chart for the optimization steps is shown in Figure 4.11. The quality of each result is rated by the outer target function

$$\text{ERR} = \frac{X(\tilde{C}, C) + X(\tilde{Q}, Q)}{2}, \quad (4.32)$$

**Table 4.4:** Initial values of inner parameters in the convoluted optimizer scheme. The dielectric permittivity starts with estimates from common parallel-plate capacitor calculation.

$K^2(E_{DC})$ (%)	$c_{0,BST}$ (GPa)	$M$ (Nm <sup>2</sup> /C <sup>2</sup> )	$c_{SMO}$ (GPa)	$t_{Au,eff}$	$\tan \delta_{dielectric}$
0 .. 5 [Cha+17]	245 [Ven+08]	3.3e12	336 [AR16]	{height meas.}	$10^{-3}$

which is based on the relative RMSE

$$X(\tilde{C}, C) = \sqrt{\text{avg}_n \text{avg}_g \left[ \left( \frac{\tilde{C}_n(f_g) - C_n(f_g)}{C_n(f_g)} \right)^2 \right]}, \quad (4.33)$$

where averaging is with respect to all of the observed  $G$  frequencies and  $N$  bias states and  $\tilde{C}$  is the modeled capacitance. The definition for  $X(\tilde{Q}, Q)$  is analogue. The sweeping interval for  $Z_{top}$  is iteratively refined around the value with lowest ERR. In conclusion, this convoluted optimization allows to rate the significance of the outer-swept parameter. Moreover, a strong variation of the inner parameters for results with similarly-low ERR warns against an unstable solution. Note that the impacts of the stiffness of SMO and BST are easily distinguishable due to the double-impact on resonance frequency and amplitude, compare (4.28), and the clearly differing layer thickness. The same holds for the effective gold thickness  $t_{Au}$ , which only affects the frequency and (almost) not the amplitude of acoustic resonances. Table 4.4 shows the initial values for the optimization of the "inner" parameters. The electromechanical coupling is initialized proportional to the relative tunability  $\tau(E_{DC}) = 1 - C(E_{DC})/C(0)$  with maximum value  $K_{max}^{2(0)} = 0.05$ . The starting point of  $t_{Au}$  is determined by profilometer measurements. Table 4.5 shows all remaining mechanical parameters. The densities for BST and SMO are estimated theoretically from dividing the unitcell atoms' weight by its volume [Sch44]. Furthermore, very large acoustic quality factors can be neglected for the thin layers in this work due to no observable impact on the microwave impedance; mechanical losses are negligible in these materials.

As a rule of thumb, a single run of the inner optimizer is completed within seconds in contrast a 3D multiphysics solver that can easily require many hours to complete.

**Table 4.5:** Mechanic properties of all layers. The acoustic velocity and impedance can be calculated by (4.28).

	$c$ (GPa)	$\rho$ (g/cm <sup>3</sup> )	$Q$	Source
Au	207	19.7	480	[GVL06; GTV13]
Pt	228	21.4	520	[GVL06; GTV13]
BST	{opt.}	5.5	$\geq 1000$	
SMO	{opt.}	6.1	$\geq 1000$	
GSO	295	6.7		[Pes+08]

#### 4.2.3 Verification by Measurement

For the model verification, four test structures with varying BST thicknesses {40, 81, 168, 320}nm ("VT40", "VT81", ...) are characterized. The electric bias field interval contains  $N = 24$  states between 0 V/ $\mu\text{m}$  and 100 V/ $\mu\text{m}$  with maximum step width 5 V/ $\mu\text{m}$  and smaller steps for low bias.

The quality of the model fitting can be judged from Figure 4.12 for VT81. On the top, surface plots of the capacitance and quality factor are overlayed with mesh plots of the model result. The maximum permittivity is reached at a small offset of 6 V/ $\mu\text{m}$ , but repeated cycling does not show the hysteresis with two peaks of the permittivity that would typically be connected to local ferroelectric domains. A permanent, maybe defect- or strain-induced inherent polarization is assumed [A13]. Hence, the bias field axis is offset such that the maximum permittivity lies at zero effective bias field. The bottom of Figure 4.12 shows more details of the same data, where 12 bias states are plotted solely versus frequency. For better readability, the respective lines have been shifted from each other and the capacitance was normalized to the mean value for each bias state. While the capacitance of all-oxide varactors has shown only weak affection by acoustic resonances [7], the normalization compensates the permittivity decrease under stronger biasing. Thereby, the relative increase of acoustic affection with increasing bias field strength can be observed and even the small capacitance variations can be used to stabilize the model fitting, compare (4.32). One can conclude that, despite the strong maximum biasing field and large frequency range, the model follows the measured data very closely.

Figure 4.13a allows to evaluate whether the reached minimum is global, i.e., the confidence of the extracted parameters that will be presented in the following section. The result of the outer optimizer, i.e., the relative error ERR is plotted versus the acoustic impedance of the top termination  $Z_{\text{top}}$ . Additionally, the interdependent inner parameters  $c_{\text{SMO}}$ ,  $c_{0,\text{BST}}$  and  $t_{\text{Au}}$  are plotted on the right axis. Since they

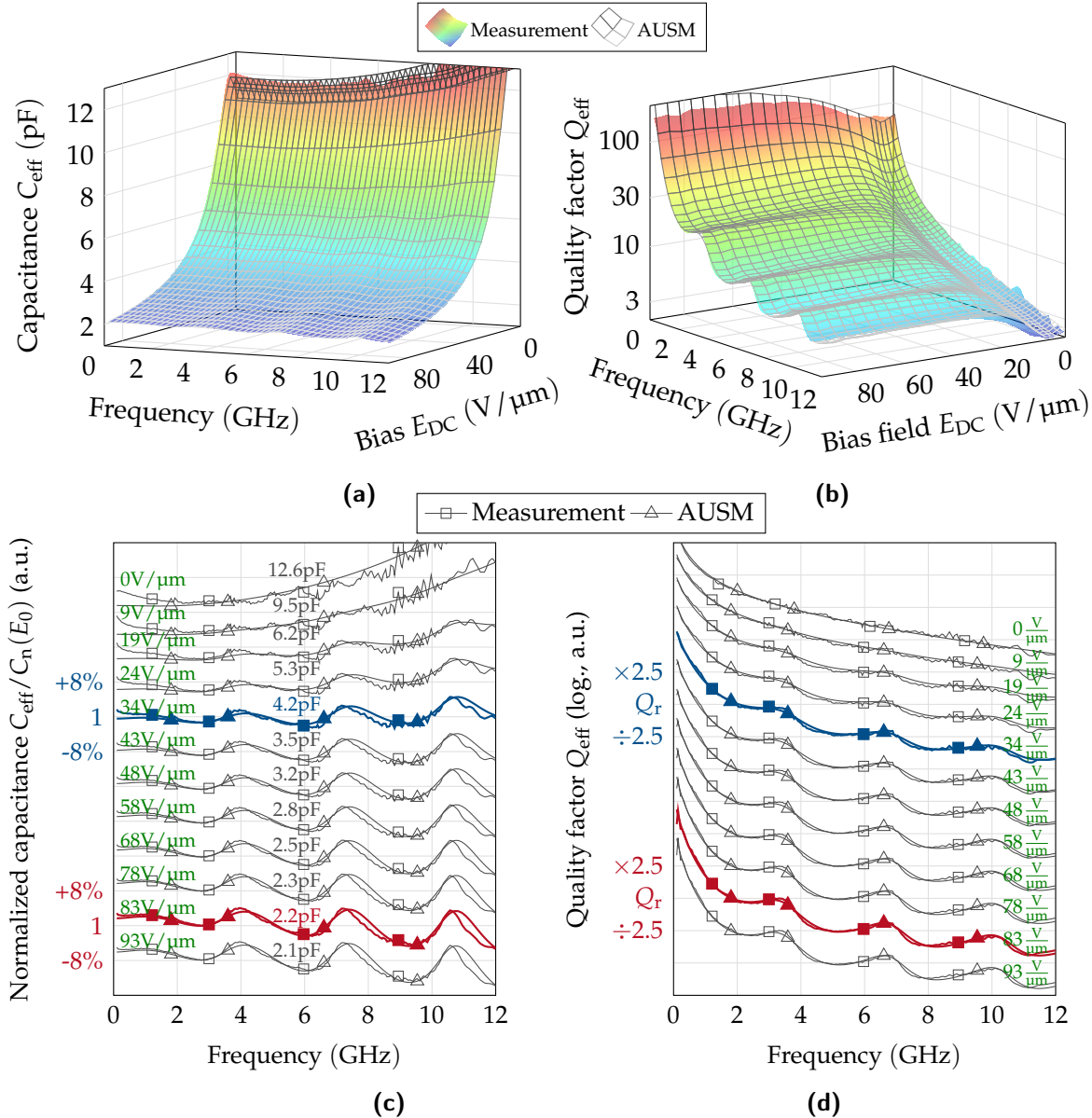


**Figure 4.12:** Measured and modeled (a) capacitance and (b)  $Q$  factor for VT81 with  $Z_{\text{top}} = 25 \cdot 10^6 \text{ kg/sm}^2$ , compare Figure 4.13a. Below, the normalized (c) capacitance and (d) quality factor are shown versus frequency for multiple electric bias fields  $E_{\text{DC}}$ . The capacitance and quality factor is normalized to its respective average value for the specific bias state  $C_n(E_{\text{DC}}) = \text{avg}_f\{C(E_{\text{DC}}, f)\}$  and  $Q_r = 20$ , respectively. The span of (c) and (d) is 1DIV  $\hat{=} 8\%$  and 1DIV  $\hat{=} 150\%$ , respectively. In both graphs, the data of each bias state has been shifted by 1DIV for readability.

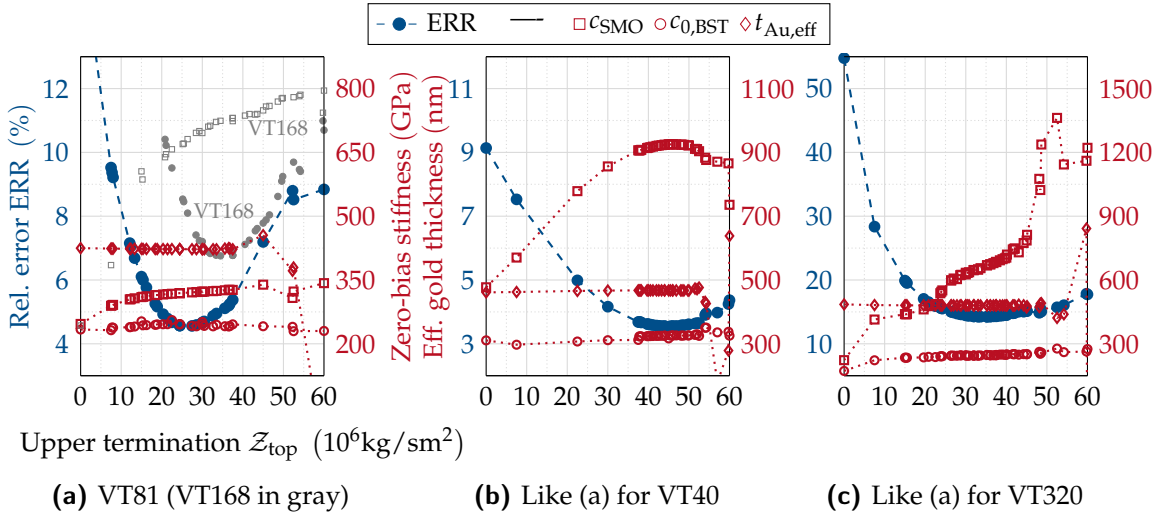


**Figure 4.13:** Result of outer optimizer to evaluate the globality of the obtained minimum. Namely, on the left axis (blue), target function ERR and on the right axis (red) SMO and zero-bias BST stiffness and effective gold thickness versus acoustic impedance of top termination are shown. In (a), ERR and  $c_{\text{SMO}}$  of VT168 are also shown for comparison with small gray and nonchained markers.

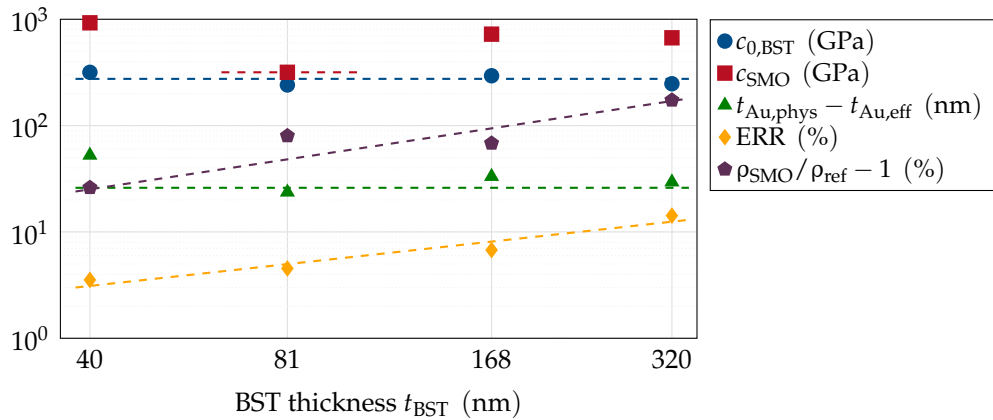
appear constant around the minimum (and even beyond), the separation of  $Z_{\text{top}}$  in the convoluted optimizer does not lead to a trapping in local minima despite the interdependence. With the profilometer result  $t_{\text{Au}}^0 = 446 \text{ nm}$ , the reduction to the effective gold thickness is 26 nm ( $t_{\text{Au}}^{\text{opt.}} = 420 \text{ nm}$ ). The data from Figure 4.12 corresponds to the minimum error at  $24 \cdot 10^6 \text{ kg/sm}^2$ .

Due to redundancy, the model results of the other three samples are not discussed in detail. Instead, only important aspects regarding the model accuracy are highlighted. The data, which is not shown here, can be found in appendix B.2. Table 4.6 compares the optimum ERR, which is interpreted as the true result, for all samples along with the extracted bias-independent parameters. No distinct plot is shown for VT168 as it shows a characteristic very similar to VT81. Instead, only ERR and  $c_{\text{SMO}}$  are added in Figure 4.13a as small, gray nonchained markers, since  $c_{0,\text{BST}}$  and  $t_{\text{Au},\text{eff}}$  are quasi-constant as for VT81. The width of the low-ERR valley with a slightly increased minimum is comparable. Therefore, in spite of the slightly increased slope, i.e., the uncertainty of  $c_{\text{SMO}}$  around the optimum, this does not degrade the parameter confidence. However, while the extracted SMO stiffness of VT81 matches well to expectations, comparable values as for VT168 have been predicted only for strong hydrostatic pressure [AR16]. Furthermore, the increased error indicates that the neglected oxygen barrier interlayer between BST and SMO might have

**Table 4.6:** Model inputs obtained by IRGN optimization and model error.

		VT40*	VT81	VT168	VT320#
$\rho_{\text{SMO}}$	( $\mu\Omega \text{ cm}$ )	42	60	56	91
$c_{\text{BST},0}$	(GPa)	317	242	294	247
$M$	( $\text{Nm}^2/\text{C}^2$ )	-2e+13	2e+12	5e+12	5e+13
$c_{\text{SMO}}$	(GPa)	926	321	724	669
$Z_{\text{top}}$	( $10^6 \text{ kg/sm}^2$ )	45.0	27.5	34.5	35.2
$t_{\text{Au,eff}}$	(nm)	467	422	467	481
	init.	520	446	500	510
ERR	(%)	3.5	4.6	6.8	14.2

\*Low acoustic resonance amplitude    #Low fitting quality


**Figure 4.14:** Comparison of the extracted data for the different samples.

significantly different properties [Rad17; A11]. In that case, the SMO stiffness would have to be understood as an effective value, wrapping up the interlayer impact. For VT40 and VT320, this is different as especially the optimum SMO stiffness varies significantly inside the range with only small increase from the lowest ERR. A generally lower error of the overall fitting for VT40 can be read from Figure 4.13b. Nonetheless, since lower acoustic resonance amplitudes are recorded for thinner BST layers, the confidence of the extracted mechanical parameters is reduced. A strongly increased relative error for VT320 follows from Figure 4.13c, reducing the reliability of all parameter extraction. The large step of  $c_{\text{SMO}}$  next to the optimum impedance and wide interval for impedances with similar error lets the extracted value be even more unsafe. However, the extracted zero-bias BST stiffness and

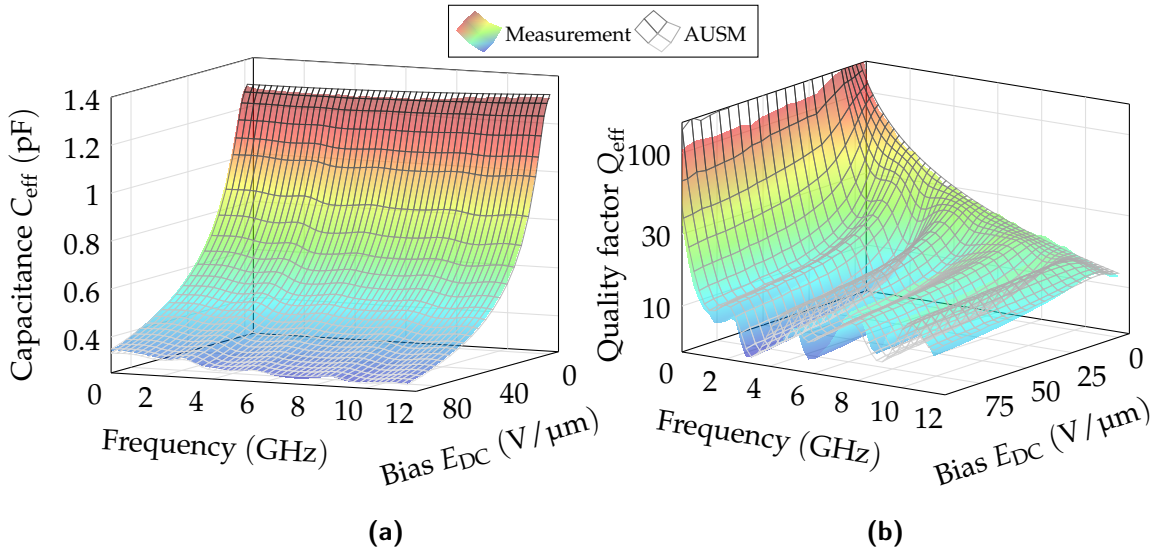


**Figure 4.15:** Measured and modeled (a) capacitance and (b) quality factor for VT320 with  $Z_{\text{top}} = 37.9 \cdot 10^6 \text{ kg/sm}^2$ , compare Figure 4.13c.

effective gold thickness are constant and within a reasonable range. The significant extracted properties are compared in Figure 4.14, each for the respective  $\mathcal{Z}$  with smallest ERR. The zero-bias stiffness of BST appears steady around 275 GPa for all samples in good agreement with reported values [BA02; Cha+17]. This does not hold for  $c_{\text{SMO}}$  for the previously discussed reasons. The largest confidence is put on VT81, which exhibits both a sufficient acoustic activity and small model error. The green markers depict the difference between deposited and effective gold thickness  $t_{\text{Au,phys}} - t_{\text{Au,eff}}$  due to the overtravel of the on-wafer probe. A similar reduction around 26 nm is generally observed with a larger value for VT40, which is connected to the low acoustic activity.

The strongly increased error of VT320 requires clarification and can be connected to an oxidization of the BE. During the longer deposition duration for thicker BST layers, the upper region of the  $\text{SrMoO}_3$  electrode is more likely to oxidize into insulating  $\text{SrMoO}_4$  due to a partial failure of the oxygen barrier interlayer, compare section 2.3. This oxidization is attributed to an increased SMO resistivity  $\rho_{\text{SMO}}$ , which also shows a weak trend with the model error in Table 4.6. Since neither the oxygen barrier nor the disturbing  $\text{SrMoO}_4$  interlayer is included in the model, the error increases. However, the impedance data for VT320 in Figure 4.15 shows that the increased error only affects details. The general characteristic, in particular the complicated double-dependence of the quality factor on bias field and frequency, is still tracked. While this does not improve the confidence of the extracted parameters,

it does confirm the general validity of the combined electroacoustic model.

#### 4.2.4 Identification of Bias-Dependent Properties

The bias-field dependent BST properties are shown in Figure 4.16. Note that all bias-independent properties have been presented and discussed in parallel to the model validation in the previous section. Note further for the following evaluation that the data for VT40 and VT320 are subject to the low measured acoustic activity and low fitting accuracy, respectively. For VT81 and VT168, however, a large confidence can be assumed from the previous section.

The pivotal parameter is the electromechanical coupling coefficient  $K^2$ , defining the robustness of all other extracted mechanical properties, see (4.26). Despite totally unforced by the optimizer, it develops similarly with bias field for all samples in spite of the low initial maximum value, see Table 4.4. VT81 exhibits a 5 % increase at maximum bias field strength. Note that the BE resistivity for VT81 is also increased stronger than the general trend with BST thickness, compare Table 4.6. Hence, the  $K^2$  increase might be connected to deposition process fluctuations like a higher oxygen partial pressure. In general, the high level of  $K^2$  is particularly significant for VT40 and VT81, where the very small BST thickness does not conflict with the functionality. Regarding a deployment in frequency-tunable thin-film bulk acoustic resonators (FBARs) for mobile applications [Ivi+08; Ven+08], the strong coupling would allow new devices with low-voltage switching. The maximum extracted  $K^2$  exceeds typically expected values which, in parts, is connected to the 2–4-fold increased maximum bias field strength. However, also for comparable field strengths, it's remarkably large when compared to reported values [Noe+07; Vol+08] for a similar film thickness but slightly smaller barium content. Similarly-large coupling coefficients under comparable field strengths have been reported only for much thicker films with an even increased barium content [Ivi+08].

The order of magnitude of the optimized stiffness  $c_{\text{BST}}^D$  generally agrees well with reported values [BA02; Cha+17]. Also, the nonlinear electrostriction coefficient  $M$  fits well to expectations for the samples VT81 and VT168, compare Table 4.6. A stronger variation with bias due to  $|M| \geq 10^{13} \text{Nm}^2/\text{C}^2$  is observed only for VT40 and VT320. The limited robustness of the mechanical properties for these two samples was discussed already in the previous section. Comparing all samples, the reliable extraction of the BST stiffness can be confirmed when the model error is sufficiently small. It is noteworthy that, despite the low fitting quality for VT320, a very similar BST stiffness is extracted for all samples. The negative coefficient  $M$  of VT40 might suffer from lower accuracy due to the lowest acoustic activity

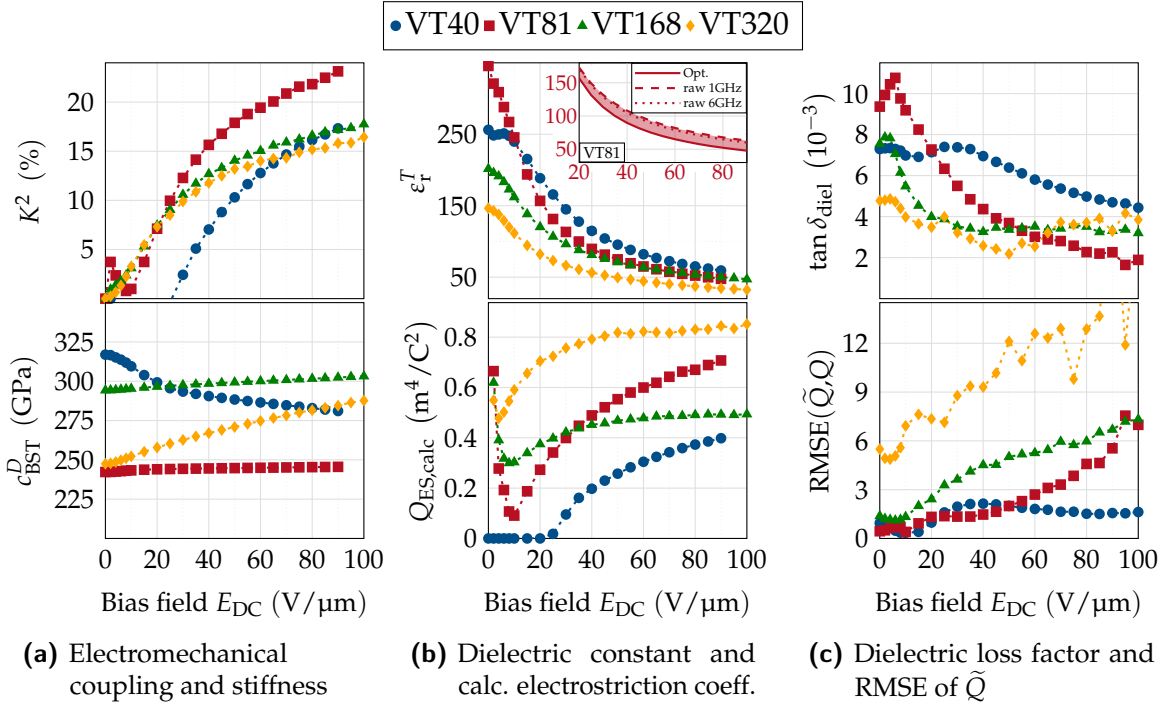


**Figure 4.16:** Extracted material properties of the BST layer versus effective bias field  $E_{DC}$ , which is offset such that  $0\text{ V}/\mu\text{m}$  corresponds to the permittivity maximum. The inset of (b, top) compares the modeled and raw relative permittivity for VT81. (b, bottom) shows the calculated effective electrostriction coefficient according to (4.27). In (c), the RMSE for the modeled varactor quality factor allows to rate the reliability of the extracted dielectric loss factor  $\tan \delta_{\text{diel}}$ . For all mechanical data, the data gains confidence with increasing bias strength due to the larger  $K^2$ .

excited by the thin layer. However, there is also a physical explanation for the observed different sign in  $M$ . The epitaxial BST layer is tensile-strained by only 0.5 % due to adapting for the slightly different lattice constant of the GSO substrate [4; A13]. This initial strain causes a decrease of the zero-bias permittivity of the BST films and might also contribute to the mechanical properties. It depends on the actual BST stoichiometry, i.e. on both the cation and oxygen distribution. As the strain value is rather small, a different stoichiometry might result in a different sign of the tetragonal distortion of the BST, namely, a transition from elongation to compression of the crystal structure along the c-axis.

Regarding the dielectric constant  $\epsilon_r^T$ , the plotted data is cleaned from the imprecision of acoustic effects. Without the model in this work, the straight-forward extraction is based on the equation of a PPC, see (3.12). However, as exemplarily shown for VT81

in the inset, this "raw" tunability depends on the chosen frequency and appears generally too pessimistic with, here, 4.2 % difference. The stronger reduction of  $\epsilon_r^T$  for VT320 and VT168 can well be connected to a stronger oxidization of the BE. Since a possibly insulating interlayer of SrMoO<sub>4</sub> is neglected in the model, its increasing impact on the microwave impedance will decrease the extracted permittivity.

With these fitted parameters, (4.27) can be used to calculate the effective electrostriction coefficient  $Q_{ES,calc}$ . Though expected to be constant with bias field [Mas50; VV07], a small bias dependence is observed. However, where multiple bias states have been reported for comparable structures in previous works, assuming a constant electrostriction coefficient has also led to a misfit for some of the bias states [Ivi+08; Ven+08]. Neglected transversal strain due to electric field at the circumference of the center electrode and unconsidered nonlinear effects, in particular, in regard of the very strong bias field might introduce a conflict with the model assumptions. Furthermore, the calculated values are higher than previously reported for BST [Mas50; VV07; Vol+08; Ivi+08]. This can well be explained by comprehending the permittivity  $\epsilon_{r,BST}$  as the effective value of BST, oxygen barrier and SrMoO<sub>4</sub>. As this is neglected in this comparison, the reduced indicated permittivity leads to an increased  $Q_{ES,calc}$ . By exemplarily scaling the permittivity of VT320 by the factor 2 and 3, the extracted electrostriction coefficient is reduced to  $Q_{ES,calc} = 0.25 \text{ m}^4/\text{C}^2$  and  $0.14 \text{ m}^4/\text{C}^2$ , respectively, which is very close to the reported values. Note, however, that the region of strongest deviation for weak bias fields suffers from low significance.

At this stage, the previously highlighted possibility of missing the global minimum can be excluded. A trapping in a local minimum could originate in the splitting of the mechanical parameters in sequential runs. However, when limiting the bias field range to the stronger values, the optimizer can be re-run with the unknown  $Q_{ES,calc}$  instead of  $K^2(E_0)$ . In this case, all mechanical parameters are optimized simultaneously. When restricting to bias fields, for which  $Q_{ES,calc}$  is quasi-constant in Figure 4.16b, the same results are obtained.

Finally, the strong dependence of acoustic effects on the geometry allows to distinguish acoustic losses from other mechanisms. This enables the study of dominant loss mechanisms as summarized in section 2.1.2. Figure 4.16c shows the "pure" dielectric contribution  $\tan \delta_{\text{diel}}$  versus the effective bias field  $E_{DC}$  because electrode contribution and acoustic resonance effects are separated by the model. The RMSE of  $\tilde{Q}$  towards the measured  $Q_m$  is also shown for each bias state. Generally, the increasing error with bias challenges the loss factor extraction. However, for VT40, VT81 and VT168, the extracted data shows a very small error, while, for VT320, an extraction is indicated as unfeasible under stronger bias in agreement with the discussion in the previous section. This mirrors the close tracking of  $Q$  in Figure 4.12b

in opposition to the coarser matching in Figure 4.15b. The asymptotic decrease of  $\tan \delta_{\text{diel}}$  to  $\approx 0.003$  with bias for VT81 and VT168 confirms the high quality of the deposited BST layers. While the loss tangent was assumed constant over the observed frequency range in this work, a dispersive characteristic can easily be implemented in the formulae to check for the dominance of a respective loss mechanism. Since this, however, reaches to the limits of the model accuracy, a corresponding analysis is reasonable only when interlayers, in particular the oxygen barrier for all-oxide varactors, are included.

#### 4.2.5 Suppression of Acoustic Resonances

An important expected property of all-oxide varactors is their inherent prevention of acoustic resonances. Both the oxide electrode and the ferroelectric are perovskites such that the structural similarity lengthens the acoustic resonating path. The oxide electrode is thereby not piezoelectric and, hence, damps acoustic waves instead enhancing them. Due to that, the strongest effect is expected for thin BST layers such that the largest portion of the perovskite stack consists of a non-ferroelectric oxide. The discussion of acoustic-resonance suppression in all-oxide varactors concludes this section. For that, the derived model is used for verification; arbitrary layers can be combined model-wise which overcomes limitations from manufacturability. Furthermore, important design aspects are given with suggestions for a material optimization via doping of BST.

The microwave impedance data of the previously presented samples is displayed in Figure 4.17a for the strongest applied bias ( $100 \text{ V}/\mu\text{m}$ ). Additionally, the characterization results of a commercial varactor (STPTIC-12, *STMicroelectronics*) are shown for comparison.<sup>7</sup> The sharp and narrow notch in  $Q$  of the commercial-varactor data reveals the larger acoustic-impedance steps, i.e., a weaker mechanical loading of the acoustic resonator. Since loading of a resonator generally widens and lowers the resonance amplitude, a higher loss in the surrounding frequencies is expected from loading. However, for the thinner BST films, the all-oxide-varactor  $Q$  factor nonetheless competes well, also for low frequencies without resonance activity in STPTIC-12. Furthermore, where acoustic resonances are active, a much weaker degradation of the  $Q$  factor is recorded. This is due to a lower acoustic activity

---

<sup>7</sup>Only a qualitative comparison is possible due to the very different varactor design and characterization setup. The commercial varactor is packaged and was mounted on a test network before characterization. The all-oxide test structures are unpackaged prototypes that have been probed directly on-wafer. For a clearer picture, the mechanic loading by the on-wafer probe must be removed as discussed in section 4.2.2. This is can only be done model-wise, which is made up for later in this section in agreement with this analysis.

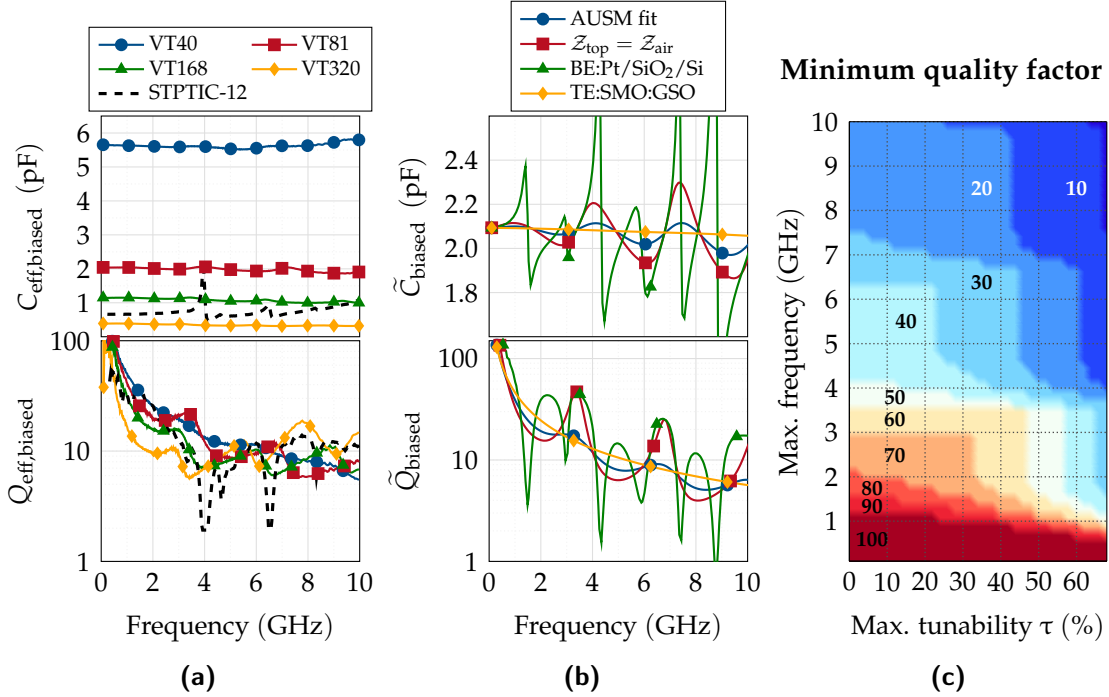


**Figure 4.17:** (a) Measured capacitance and  $Q$  factor of four samples with varying BST thickness from 40 to 320 nm. In all cases, a constant  $E_{\text{DC}} = 100 \text{ V}/\mu\text{m}$  was applied, i.e., bias voltages from 4 to 32 V. The data is compared to results for a commercial varactor biased with 10 V. (b) Model-wise comparison of various layer stacks based on the results for VT81. (c) Trade-off between maximum tunability  $\tau$  and minimum  $Q$  factor with maximum applicable frequency.

for thinner ferroelectric layers, as proven in Figure B.3. The capacitance shows no significant variation due to acoustic resonances. In summary, a great extension of the usable frequency range is demonstrated for the samples with thin BST.

The derived model will now be used to verify the benefit of the oxide electrode. Figure 4.17b shows modeled data based on the test structure with  $t_{\text{BST}} = 81 \text{ nm}$ . Firstly, the data is de-embedded from the mechanic loading by the on-wafer probe by replacing  $Z_{\text{top}}$  with  $Z_{\text{air}} = 400 \text{ kg}/\text{ms}^2$ . Due to the now larger step in the acoustic impedance, the resonant variation becomes stronger. However, comparing the order of magnitude, the qualitative statements based on the comparison to the commercial varactor in Figure 4.17a are still valid. This de-embedded model is now compared with two alternative layer stacks. In "BE:Pt/SiO<sub>2</sub>/Si", all layers below BST are replaced with a common alternative based on platinum and silicon, taken from [GVL06]. In detail, the BE is modeled as an equally thick (490 nm) platinum

layer and the substrate is comprised of a  $\text{SiO}_2$  surface on Si with 430 nm and 500  $\mu\text{m}$  thickness, respectively. Model-wise, this replacement can be done easily while being difficult experimentally, since thin-film growth strongly depend on the respective previous material. Hence, for the same BST layer with, in particular, equal electromechanic coupling  $K^2$ , the resonance-induced fluctuations are increased greatly. In "TE:SMO:GSO", the metal TE of the test structures is replaced with oxide materials, yielding a "true" all-oxide layer stack. As a result, all fluctuation vanishes, resulting in flat capacitance and loss factor characteristics. This confirms the strong impact of the oxide electrode and substrate. Note that, at frequencies without acoustic degradation in weakly-loaded resonators, the all-oxide varactor exhibits a lower  $Q$  factor. The lowest loss possible is obtained when reflected acoustic waves interfere destructively, i.e., cancel out each other.

To the end of this chapter, the high-performance potential and limits of this suppression technique will be discussed.<sup>8</sup> Considering that completely avoiding the reflection of acoustic waves is non-optimal, the microwave performance can be optimized by limiting the tunability. This, in turn, limits the acoustic degradation of the component quality factor. In applications where only a moderate tunability is required, this can greatly increase the usable frequency range. Figure 4.17c shows a corresponding contour plot for a modeled sample with  $\rho_{\text{SMO}} = 20 \mu\Omega \text{ cm}$ ,  $t_{\text{SMO}} = 5000 \text{ nm}$ ,  $t_{\text{BST}} = 40 \text{ nm}$ . This depicts the combination of the highest integrated conductivity, thickest SMO and thinnest BST layer that were up to now achieved in this work. The mechanic data is taken from sample VT40 as characterized in section 4.2.4. The axes depict the maximum tunability and frequency, respectively. For each data pair, the graph shows the minimum quality factor for all frequencies and tunabilities up to those values. Though  $Q$  naturally decreases with frequency, the effect of a lower maximum tunability can be clearly seen. Where no degradation with frequency is observed for a fixed tunability like, e.g., for  $2 \leq f/\text{GHz} \leq 4$ , acoustic waves interfere destructively, compare Figure 4.17b. Two exemplary sweet spots  $(f, \tau, Q)$  are  $(3.5 \text{ GHz}, 65\%, 40)$  and  $(6.6 \text{ GHz}, 44\%, 30)$ . In terms of the CQF defined in section 3.3.2, they correspond to  $\text{CQF} = 2900$  and  $363$  for 3.5 GHz and 6.6 GHz, respectively. In discussions with an industrial manufacturer, a benchmark of  $(4 \text{ GHz}, \geq 60\%, \geq 40)$  was identified as highly beneficial for application in modern RF frontends. This corresponds to  $\text{CQF} = 2160$ . Hence, this goal can be considered achieved by the former sweet spot in spite of the small frequency difference. The latter sweet spots covers all 5G-sub-6 GHz frequencies for mobile communications.

---

<sup>8</sup>This is based on the modeled layer stack with oxide BE and metal TE (" $\mathcal{Z}_{\text{top}} = \mathcal{Z}_{\text{air}}$ " in Figure 4.17b). As was shown, adjacent materials will have a strong impact on the acoustic effects. In this regard, the presented results might not yet be optimal; further studies are needed.

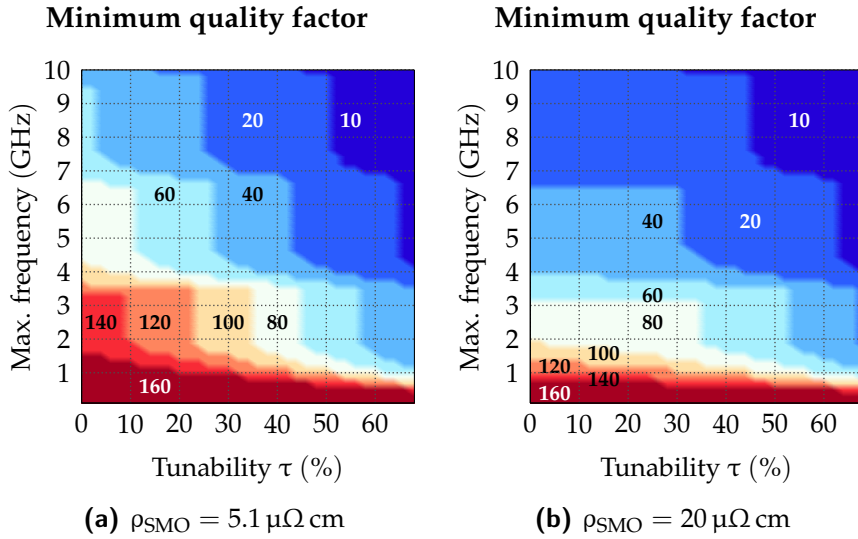


**Figure 4.18:** Modeled trade-off between maximum tunability  $\tau$  and minimum  $Q$  factor with maximum applicable frequency for decreased maximum dielectric loss  $\tan \delta_{\text{BST},\max} = 0.004$  to model a doped dielectric ( $t_{\text{SMO}} = 5\,000 \text{ nm}$ ,  $t_{\text{BST}} = 40 \text{ nm}$ ).

As an outlook, the expected theoretical limit of this stack is analyzed. Instead of externally limiting the tuning voltage, doping of BST can be used to trade tunability against decreased dielectric losses. Many works present promising experimental results on BST thin films, e.g., for the dopants manganese [Nad+15],  $\text{Al}_2\text{O}_3$  [Cho+04] or iron [YG09]. Furthermore, this will not only increase the  $Q$  factor but the device linearity will be additionally enhanced by the sacrificed tunability. Hence, this promises a great performance improvement for all-oxide varactors. Since their required tuning voltage level is generally uncritical, this improvement can be expected without sacrifice of another performance parameter.<sup>9</sup> The data in Figure 4.18a shows the model results for a scaled  $\tan \delta_{\text{BST},\max} = 0.004$  and the same relative decrease with bias as for VT40. This corresponds to a factor of 0.5 in agreement to [Cho+04; YG09]. Besides that, though not yet accomplished in this work, the lowest reported SMO resistivity  $\rho_{\text{SMO}} = 5.1 \mu\Omega \text{ cm}$  is used [Nag+05]. However, the impact of the electrode loss decreases with higher tunabilities, as can be seen by comparison to the data for  $\rho_{\text{SMO}} = 20 \mu\Omega \text{ cm}$  in Figure 4.18b.  $Q$  factors larger than 40 up to 6.5 GHz are conceivable with a high tunability of 44 %. When restricting oneself to frequencies smaller than 3.5 GHz that are commonly used for wide-range mobile

<sup>9</sup>Note that doping can cause a decrease of the maximum tunability which is not considered in this theoretical analysis.

communication,  $Q$  factors larger than 100 and 60 are provided for a maximum tunability of 35 % and 57 %, respectively. A general drawback is that the region for low acoustic activity naturally shows a strong bias field dependence due to the bell-shaped C-V curve. This makes cascading multiple varactors to reduce the RF voltage swing per varactor an important consideration for increased power levels. In conclusion to this section, the very thin BST layers that are feasible in the all-oxide technology enable a significant frequency range extension of ferroelectric varactors. The strongest benefit comes from the lower excitation of acoustic waves. As an outlook on future work and without inclusion in a systematic study, a proof of principle for this doping benefit is demonstrated in Figure 6.1. Though resonance effects can indeed be suppressed by exploiting stacks with very similar mechanic properties, this is not recommended as the sole engineering approach. If the energy in the excited acoustic waves is not reconverted to the electric domain, the quality factor degrades severely. However, all-oxide varactors can still be used in the presence of acoustic activity where conventional varactors with metal electrodes suffer from a disqualifying degradation. Hence, the smoothed  $Q - f$  curve due to lower impact of acoustic resonances helps to maximize the usable frequency range.

## 4.3 Summary on Presented Models

This chapter presented a novel highly accurate analytic model for ferroelectric thin-film MIM varactors with thin BEs. The common modeling approach of simply cascading a resistance and inductance to the main capacitance ("RLC model") fails to track the exact impedance characteristic over a wide frequency range. In the USM, the substrate contribution is modeled by extending impedance of the BE. In detail, it is split into a central and outer part, whereby an imaginary substrate impedance is added in parallel to the former. In difference to the common RLC model, the novel model follows expected trends like, e.g., a linear scaling of the electrode resistance with thickness in the below-skin-depth domain. As a result, the electric properties of both the dielectric and the BE can be identified simultaneously by a simple microwave characterization. In the AUSM, this model has been extended for the biased state where piezoelectricity is induced by electrostriction. All relevant mechanic properties and the bias-dependence of  $\epsilon_{r,BST}$ ,  $\tan \delta_{BST}$  are identified by including an TL-based acoustic resonator model. A highly accurate tracking of both the frequency- and bias-dependent impedance characteristic testifies a complete modeling of all dominant effects. Since FEM modeling is unfeasible when dealing with a multitude of samples, this analytic model is a key element to cope with large amount of characterization data. The material properties of a single varactor can be

characterized within seconds.

In the future, a few aspects of the suggested model can be improved. Firstly, the substrate representation as a capacitance in the nF range is surprising. Though the substrate scaling factor in the electrode resistance leads to well-matching results phenomenologically, a refined description can be found in future work. After a more physical representation is found, a coherent substrate loss description can be used to investigate the impact of greatly varying substrate properties. Secondly, if the dielectric thickness is very small, the oxygen barrier becomes more significant for the overall varactor impedance. For this case, a model should be derived that takes the oxygen barrier into account. Principally, adding a single layer into the modeled stack is simple. The challenge lies within the identification of its material properties, in particular due to its very small thickness. This will require systematic studies with varied thicknesses and barrier materials and possibly independent measurements.

# 5 Towards Industrial Realization

The far end of this project is to transfer the all-oxide technology to an industrial realization, i.e., a large-scale fabrication of discrete varactors or circuits. This work, however, can only prepare that transfer. The pivotal requirements to guarantee a sufficient yield of a large-scale fabrication are reproducibility and uniformity. Generally, PLD is known to be insufficient in that regard and will need to be replaced with another deposition process. Nonetheless, these two aspects are analyzed as a benchmark for future work. The compatibility to established substrates is likewise important for industrial processes; a functional all-oxide varactor deposited on silicon is demonstrated. The limited reproducibility of PLD processes impedes the demonstration of the superior circuit performance, which is expected from the material properties of high-quality test structures. Therefore, this discussion presents design concepts for the varactor integration in two configurations; firstly, as a surface-mount device and, secondly, by a fully integrated growth with the circuit.

## 5.1 Process Stability

For engineering materials in RF systems, reproducibility and uniformity is key. If the material properties can not be controlled in an established manufacturing process, this strongly impedes every further design of components or, even more, networks. For example, fundamental properties like the permittivity are defining for the device geometry and might be difficult to characterize in devices with a higher integration level. However, reproducibility generally is a challenge for thin-film components, especially if fabricated by PLD. To explain this issue, several samples fabricated throughout the work on this PhD project will be compared in this section. Note that many samples were part of systematic studies on the deposition parameters as discussed in section 3.4. These are excluded from this comparison such that the remaining ones ought to show similar performance.

This analysis is split into two parts; reproducibility and uniformity. For the former, several figure of merits are evaluated that are appropriate to compare samples

with different material properties and electrode sizes. The latter is discussed for two representative samples with low and high spread of the deposited material properties, respectively.

### Reproducibility

The compared samples have been fabricated in 2017 (samples #1-#3), during 2018 (#4-#13) and in 2019 (#14-#20). Four measures of comparison have been defined that should be, to a sufficient extent, independent of its respective film thicknesses. For each measure and sample, the values of mean, median and the respective sampled distribution are shown. Note that the distribution is scaled to a fixed maximum value for readability. Hence, its area does not integrate to unity but a smaller area generally reveals a smaller spread of the respective property. The general distinction of an approximately uniform distribution versus a distribution with a prominent expected value is possible nonetheless. Defect, i.e., either short-circuited or untunable varactors have been excluded before this evaluation. Note further that the quality factor  $Q_{\text{eff}}$  is not part of this comparison due to its strong dependence on the thickness of SMO and BST and on the effective capacitance due to the varying electrode size.

The first and most important measure is the zero-bias BST peak permittivity  $\epsilon_{r,\text{BST},\text{max}}$ , see Figure 5.1a. The data is calculated via the simple PPC model in (3.12) at 1 GHz. It has the strongest impact on the design of the eventual component, i.e., foremost its geometry and allows a direct insight into the material structure, i.e., the stoichiometry. A regularly large spread of up to 400 from smallest to largest permittivity is observed for the majority of the samples. However, an improvement due to the RF-characterization-based material optimization described in section 3.4 can be seen: The permittivity spread has been decreased towards the end of this work. The average relative permittivity lies generally between 250 and 350.

Secondly, the offset  $E_{\text{DC},\text{offset}}$  of the bell-shaped  $C-E_{\text{DC}}$  curve is compared in Figure 5.1b. It describes the bias field necessary to obtain the maximum permittivity. In our case, a small offset with small spread means no degradation of the material. This offset is natural, since BST exhibits inherent stress and, hence, spontaneous polarization due to the epitaxial growth inspite of slightly differing lattice constants. Nevertheless, while many samples lie inside the expected range, a significant number shows a larger spread. This large spread in particular reveals significantly varying film properties across the 5 mm  $\times$  5 mm substrate.

The third measure is the leakage current density at  $-50 \text{ V}/\mu\text{m}$  bias field strength shown in Figure 5.1c. It strongly varies for the presented set of samples, whereas the min/max spread is reduced in the recent samples. Note that the spread is

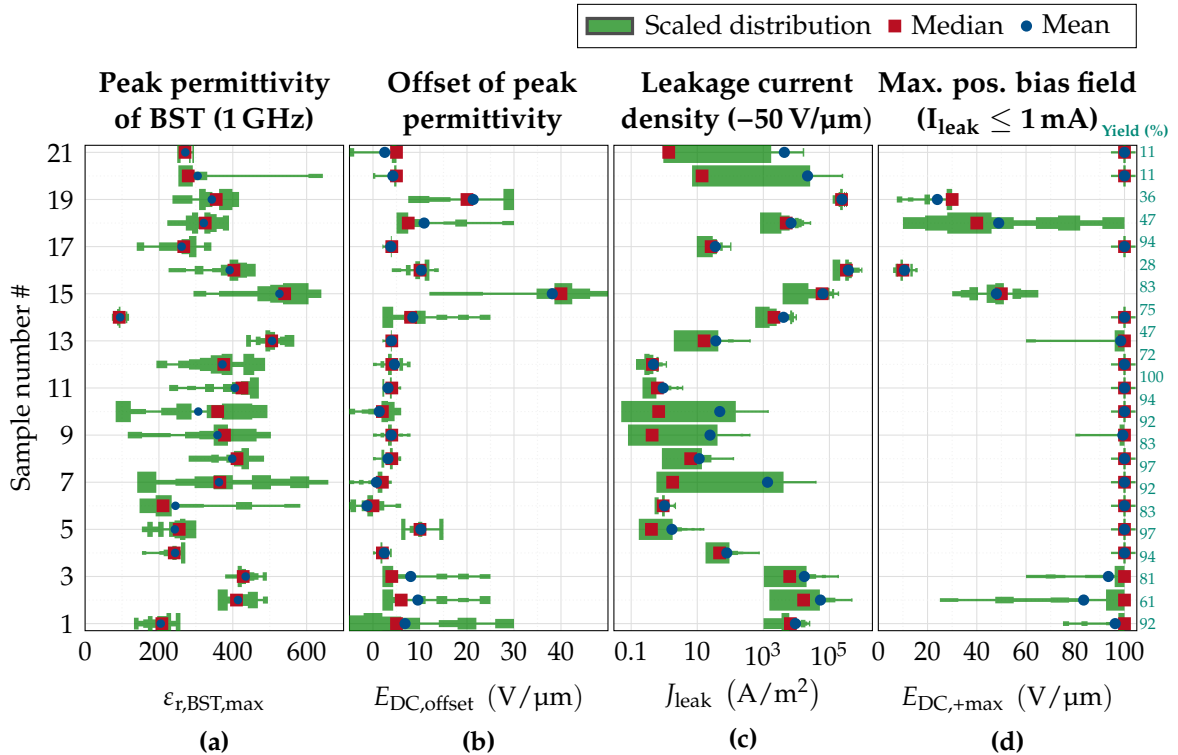


**Figure 5.1:** Comparison of samples that ought to be similar with respect to the four shown measures. The sampled distribution is scaled to a fixed maximum value for readability. More details on samples #4 and #10 are shown in Figure 5.2.

overemphasized for the samples #20 and #21 by the small yield. However, the remaining fluctuation of the mean and median values is surely of concern in regard to component design. A larger leakage current is attributed to a higher density of charged defects in BST, most often oxygen vacancies. A corresponding connection has been reported for both leakage current mechanisms that are commonly observed in BST thin films, namely SE [Sch+08] or Pool-Frenkel (PF) [Vor+04].

Finally, the maximum applied positive bias field is shown in Figure 5.1d. Regularly, it is  $100$  V/ $\mu$ m and gets reduced when the current exceeds  $1$  mA.<sup>1</sup> Note that all included dies were tunable down to  $-100$  V/ $\mu$ m without reaching that current limit, confirming the absence of short-circuits in the TE. In some respects, this measure mirrors the findings from the third one in Figure 5.1c as a generally higher leakage current facilitates an earlier exceeding of this limit. However, its discussion still brings two benefits. On the one hand, the data itself helps to rate the varactor

<sup>1</sup>For samples with  $d_{in} = 20$   $\mu$ m, the compliance level  $1$  mA corresponds to a current density of  $J_{leak} = 3.2 \cdot 10^6$  A/m $^2$ .

performance. On the other hand, biasing the center pad with positive and negative polarity relates to the Schottky barrier of the SMO-BST and BST-Pt interface, respectively, as has been discussed in section 3.3.1. Hence, this measure separates the impact of a possibly degrading oxygen diffusion at the SMO-BST interface. Despite the fact that the generally small BST film thickness indeed challenges this separation, this still is a useful indicator: Where a varactor cannot be biased to full strength, a degraded interface is revealed.

In overview, all four measures appear clearly correlated such that a distinction of high- and low-performance samples is possible. Comparing the samples, a certain change is natural as the optimization of both the deposition process and the materials was conducted in parallel to this work. However, while obvious trends of the material properties clearly suggested optimum process conditions, these did not yet ensure a stable deposition result. Hence, even the recent samples from 2019 do not document a high reproducibility.

## Uniformity

The following analysis addresses two aspects. Firstly, no loss criteria was considered in the previous section, since  $Q_{\text{eff}}$  is no fair comparison for varying electrode sizes. The alternative is comparing material properties, which is not possible without modeling. Hence, the USM is evaluated for selected samples to identify the SMO resistivity and BST loss factor. Secondly, in the above analysis, different samples have shown both a large and a small spread of material properties, respectively. The impact of this spread will be illustrated in the following discussion.

Figure 5.2 shows the loss-defining properties of the two samples #4 and #10, which are representative for a high and low uniformity, respectively. The BST permittivity is also plotted as it strongly impacts the dielectric loss factor. Red numbers depict extrapolated values for dysfunctional dies, i.e., these values are not validated by characterization. The layer thicknesses of #4 are  $t_{\text{SMO}} = 500 \text{ nm}$  and  $t_{\text{BST}} = 50 \text{ nm}$ . The SMO resistivity  $\rho_{\text{SMO}}$  is homogeneous with values between  $30 \mu\Omega \text{ cm}$  and  $36 \mu\Omega \text{ cm}$ . From comparison with Figure 2.10, these resistivity values  $\rho_{\text{SMO}} \approx 3\rho_{\text{Pt}}$  appear up to now as a good standard for integrated layers. The BST permittivity  $\epsilon_{r,\text{BST}}$  is highly homogeneous compared to all functional layers. Neglecting die F2, it ranges between 210 and 285, where the rather small values are typical for very thin layers due to the neglected oxygen barrier.<sup>2</sup> The dielectric loss factor  $\tan \delta_{\text{BST}}$  is likewise homogeneous with most values around 0.005. Note that,

---

<sup>2</sup>The oxygen barrier is neglected in this model and, hence, affects the extracted BST properties, compare Figure 2.11b. This impacts especially for thin BST layers where the fixed thickness of the oxygen barrier contributes stronger.

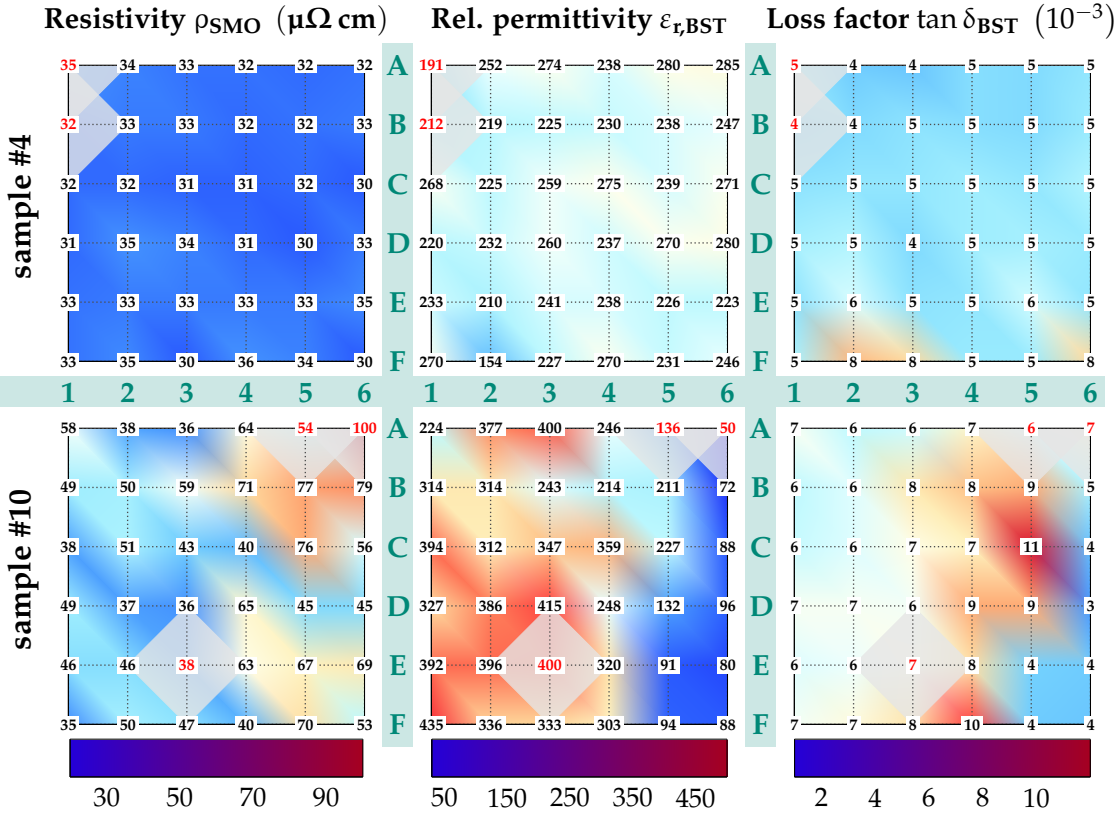


**Figure 5.2:** Detailed zero-bias material properties of two samples from Figure 5.1, extracted by the model presented in Section 4.1. The upper and the lower data is representative for samples with small (#4) and large spread (#10), respectively. Red numbers depict extrapolated values for dysfunctional dies.

like the permittivity, the loss factor is stronger affected by the oxygen barrier for thinner layers. However, even when the corresponding non-ferroelectric lower loss improves the extracted value, a very high quality of the dielectric is documented. The layer thicknesses of sample #10 are  $t_{\text{SMO}} = 507 \text{ nm}$  and  $t_{\text{BST}} = 91 \text{ nm}$ . Generally, a weak trend from good to bad varactors from left to right (columns 1 to 6) is observed. The resistivity shows a wide spread between  $35 \mu\Omega \text{ cm}$  and  $79 \mu\Omega \text{ cm}$ .<sup>3</sup> Hence, it is degraded in comparison to sample #4 which might be connected to the longer deposition time of thicker BST layers or other process fluctuations. The high values of the BST permittivity are significantly larger than for #4. However, the degradation with increasing column number is clearly visible. The parallel

<sup>3</sup>Note that this wide spread possibly decreases the accuracy of the model with a fixed reference, which is  $30 \mu\Omega \text{ cm}$  in this case.

**Table 5.1:** Bias-independent properties and model error of SrTiO<sub>3</sub>/Si varactor.

$t_{\text{SMO}}$ (nm)	$t_{\text{BST}}$ (nm)	$\rho_{\text{SMO}}$ ( $\mu\Omega \text{ cm}$ )	$c_{\text{SMO}}$ (GPa)	$c_{0,\text{BST}}$ (GPa)	$M$ (Nm <sup>2</sup> /C <sup>2</sup> )	$Z_{\text{ac,top}}$ (kgs/m <sup>2</sup> )	ERR (%)
700	95	45.9	334.3	288.0	4.12e+11	3.30e+07	6.1

decreasing  $\epsilon_{r,\text{BST}}$  and increasing  $\rho_{\text{SMO}}$  can be explained by a failure of the oxygen barrier, adding a layer of insulating SrMoO<sub>4</sub> in-between. The dielectric loss factor for the good varactors is still small with values between 0.006 and 0.008. The local peak loss factors for dies C5 and F4 indicate defect dies.

## 5.2 Transfer to Silicon Substrate

The original substrate GdScO<sub>3</sub> was chosen due to its matching lattice constant and interface to the deposited oxide thin films. However, high material costs even for only small substrate sizes promote the search for alternatives, in particular when addressing an industrial realization. The most widely used substrate for semiconductor processes is silicon. An easy integrability with established fabrication processes motivates the experimental transfer that is presented in this section.

The GdScO<sub>3</sub> substrate is replaced with a silicon substrate that was previously covered with a 97 nm SrTiO<sub>3</sub> layer ("SrTiO<sub>3</sub>/Si"). To evaluate the success of the transfer, a detailed view only on selected properties suffices. For this, the model presented in Section 4.2 is used on this sample to identify its material properties. Note that the change of substrate from GdScO<sub>3</sub> to SrTiO<sub>3</sub>/Si is not considered and might degrade the model accuracy. However, the model can still be deployed as a good estimate because a variation of the substrate properties has shown a low impact on the phenomenological substrate impedance, compare section 4.1.1. The summarized characterization results are shown in Figure 5.3. The close tracking of the measured data by the model documents the high confidence of the extracted properties. A significant difference in the acoustic resonance frequencies is observed in comparison to the results for the GdScO<sub>3</sub> varactors, compare Figure 4.12. This reveals the impact of the structural similarity of the GdScO<sub>3</sub> substrate to the deposited oxide thin films. Further validation, i.e., the graph on result stability of the nested optimizer and a comparison of the individual bias states can be found in the appendix in Figure B.4 and Figure B.5, respectively. The film thicknesses, bias-independent model results and fitting error ERR are shown in Table 5.1. The low ERR yields the resulted fitting properties to be reliable. Their similarity to the reported values and the results in

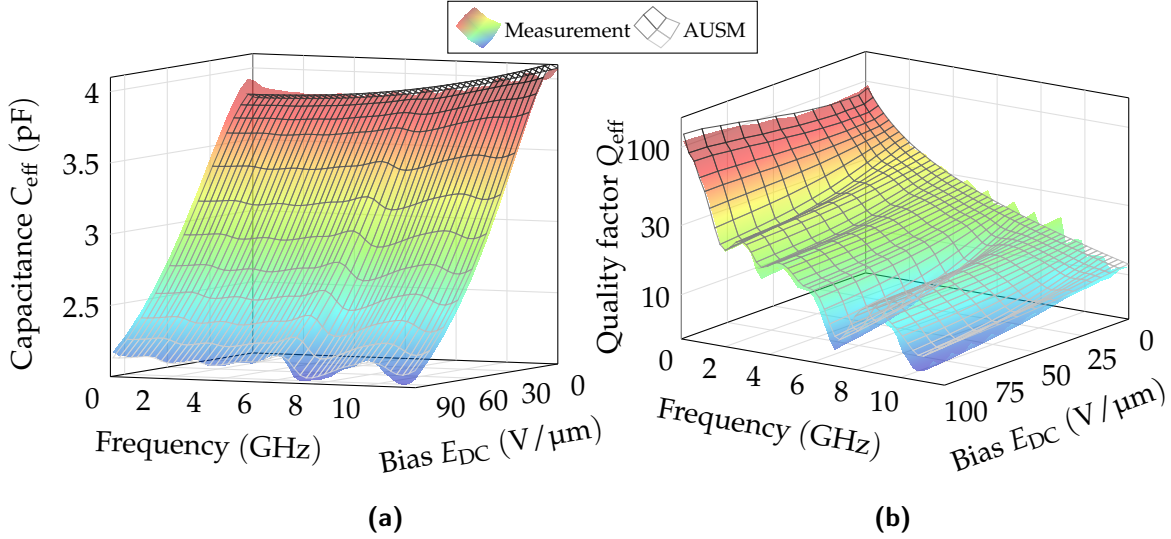


**Figure 5.3:** Measured and modeled capacitance and quality factor versus frequency and electric bias field. A detailed evaluation reporting the low model error can be found in the appendix in Figure B.4 and Figure B.5.

Table 4.6 confirms regular mechanic film properties and the applicability of the model.

This allows to validly analyze selected results of the  $\text{SrTiO}_3/\text{Si}$  varactor in Figure 5.4. For an easier comparison of the modeled data, the respective data for VT81 is added as gray dashed lines. The measured quality factor  $Q_{\text{eff}}$  is high despite the thin BE. This is due to two reasons. The first requirement is the functional SMO layer with extracted  $\rho = 45.9 \mu\Omega \text{ cm}$  despite the non-optimal growth conditions [Sal20]. Secondly, the BST permittivity is decreased significantly to  $\epsilon_{r,\text{BST},\text{max}} = 130$  compared to the  $\text{GdScO}_3$  samples in section 4.2.4. The corresponding capacitance decrease further lifts the measured  $Q_{\text{eff}}$ . Note that this comparison does not consider the possibly significant fluctuation of properties between the deposition of different samples. Furthermore, a decreased tunability  $\tau$ , a rather large dielectric loss factor  $\tan \delta_{\text{diel}}$  and the decreased electromechanic coupling coefficient  $K^2$  further indicate a lower film quality. However, the latter leads to a reduced degradation by acoustic waves, which is another reason for the higher  $Q_{\text{eff}}$  under bias.

In conclusion, the transfer of the integrated oxide thin films to the industrially established silicon substrate was successful. Systematic studies on the optimization of deposition on  $\text{SrTiO}_3/\text{Si}$  will follow in the future. Nonetheless, the presented results are very promising and clearly document the feasibility of the transfer to other substrates.

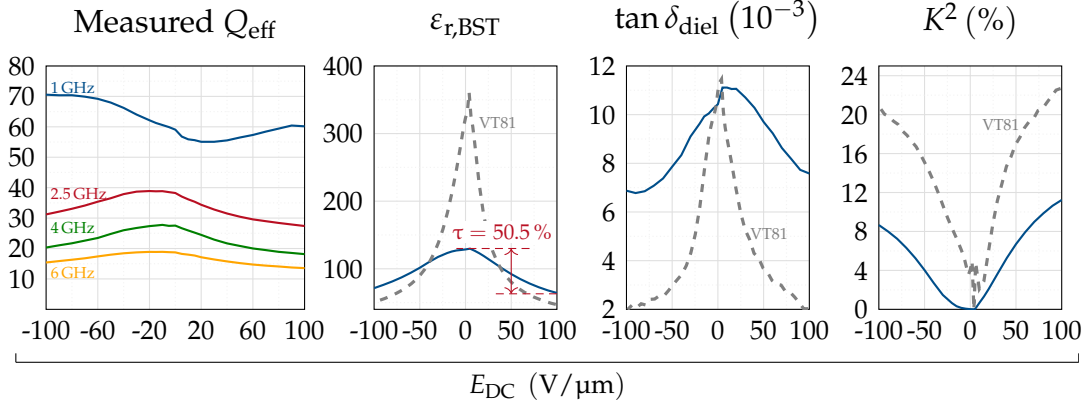


**Figure 5.4:** Selected results of varactor on SrTiO<sub>3</sub>/Si substrate. The measured  $Q_{eff}$  depicts the varactor quality factor. The other data, i.e., the BST relative permittivity  $\epsilon_{r,BST}$ , loss factor  $\tan \delta_{dielectric}$  and electromechanical coupling coefficient  $K^2$  is obtained by modeling. The modeled data of VT81 is shown as a dashed line for comparison.

### 5.3 Surface-Mount Device

Despite the issue of low reproducibility, first steps have been taken towards the system integration of all-oxide varactors. In this section, a varactor design in surface-mount device (SMD) configuration is proposed that can be as well used for circuit-integrated deposition concepts.

The design of an SMD is not straightforward due to conflicting area requirements of bonding surface and desired capacitance range. Filters and matching networks in mobile communications typically deploy capacitances in the lower pF domain. To obtain the required values, the electrode area needs to be small ( $< 300 \mu m^2$ ) due to the very thin, high permittivity BST layer. As this is much too small for stable bonding processes, separate contact areas must be added that do not contribute to the capacitance of the MIM stack. Hence, an experimental fabrication process was developed in this work that solves the conflict between both area requirements.

The component is designed for flip-chip bonding and provides low-inductance integration into circuits. The process steps of the design flow are shown in Figure 5.5. In the first step, the planar deposited SMO and BST layers are structured laterally. The desired regions are covered with photoresist, and the remaining parts are dry-etched with ion beam etching (IBE) using argon ions with energy 500 eV. The etching avoids the capacitive coupling of the contact pads to the BE, which would increase the varactor capacitance. Secondly, an insulation layer is added and structured on either side of the BST/SMO bar that can consist of several materials.

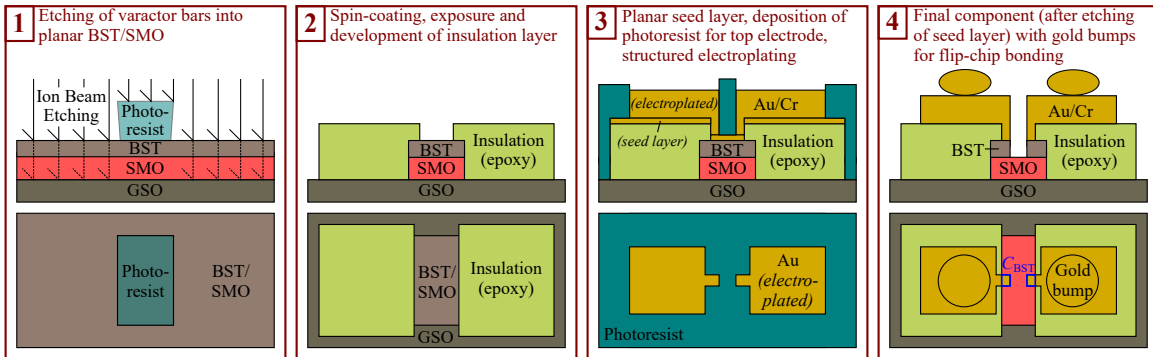


**Figure 5.5:** Processing steps of the SMD varactor in profile (top) and top view (bottom). Geometric ratios are not true to scale.

In this work, either the epoxy-based negative photoresist SU-8 (*Microchem Corp.*) or the amorphous silicon compounds  $\text{SiO}_x$  or  $\text{SiN}_x$ , deposited via plasma-enhanced chemical vapour deposition (PECVD), were used. The former is fast but will often result in rather thick insulation layers while the latter allows an easier control of the resulting film thickness, down to a few 100 nm. This layer overlaps the BST area on all edges to ensure electric insulation between the contact pads and the BE. For the TE, 20 nm chromium and 80 nm gold are deposited by physical vapor deposition (PVD), i.e., thermal evaporation as a seed layer. Then, the unwanted regions are covered with photoresist for electroplating the TE. In the final step, the sample is cleaned from the photoresist and exposed to another short IBE step for removing the seed layer. While, for the test structure, platinum was deposited for adhesion in isotropic sputtering, a directed deposition process like evaporation must be used here. In test samples with sputtered top electrodes, the varactors were shorted after the final step due to remaining metal on the vertical edges.

The final device is shown in step 4 of Figure 5.5. The resulting varactor consists of a twofold cascaded MIM stack, the effective varactor area of each is marked in blue in the top view. The varactor top electrode area on top of BST is  $A_{\text{elec}} = 15.4 \mu\text{m} \times 13 \mu\text{m} = 200 \mu\text{m}^2$  for both capacitances, with a spacing of  $d_{\text{TE}} = 50 \mu\text{m}$ . A microscope photo of the fabricated oxide varactor with epoxy insulation is shown in Figure 5.6a. The thicknesses of the respective layers are as follows:  $t_{\text{SMO}} = 2.1 \mu\text{m}$ ,  $t_{\text{BST}} = 59 \text{ nm}$ ,  $t_{\text{epoxy}} = 7.6 \mu\text{m}$  and  $t_{\text{TE}} = 1.5 \mu\text{m}$ . Length/width of the contact pad and epoxy insulation are  $150 \mu\text{m}/100 \mu\text{m}$  and  $200 \mu\text{m}/200 \mu\text{m}$ , respectively, with  $30 \mu\text{m}$  overlap of the epoxy on the oxide.

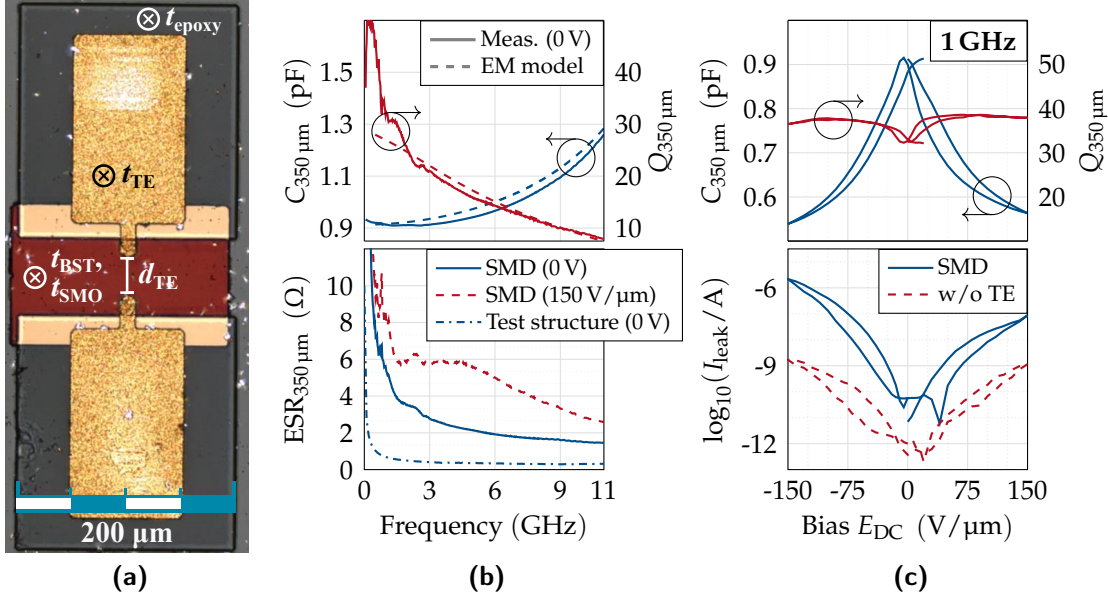


**Figure 5.6:** Fabricated SMD varactor. (a) Microscope photo. (b,c) Embedded data vs frequency and electric bias field, respectively. The ESR of a test structure is also shown for comparison. The leakage current is compared to a sample without TE, where the sole top metalization is provided by the on-wafer probe.

## Characterization

Like the test structures, the SMD varactor is characterized on-wafer but with a SG-probe with  $350\text{ }\mu\text{m}$  pitch. It probes the device at the far ends of the contact pads, the skate traces are visible in Figure 5.6a. As the bias voltage is again applied in-line with the RF test signal, the double voltage is applied and divides equally on both of the cascaded varactors.<sup>4</sup> In a real application, this setup can easily be biased through a decoupled, third port connected to the bottom electrode. This provides an inherent one-sided decoupling of the bias and the RF signal, which greatly simplifies the required bias network.

The capacitance, quality factor and ESR are plotted versus frequency in Figure 5.6b. The reduced maximum frequency of  $11\text{ GHz}$  is due to the wider pitch of the on-wafer probe. Due to the wide pitch and small pin surface of the on-wafer probe, an additional series resistance is measured. When deployed in circuits, that resistance is much smaller due to an areal contact of bumps that are, additionally, closer to the actual capacitances at the center. The data can be de-embedded from the

<sup>4</sup>Equal capacitances are assumed for both pads, i.e., equal electrode size and BST permittivity.

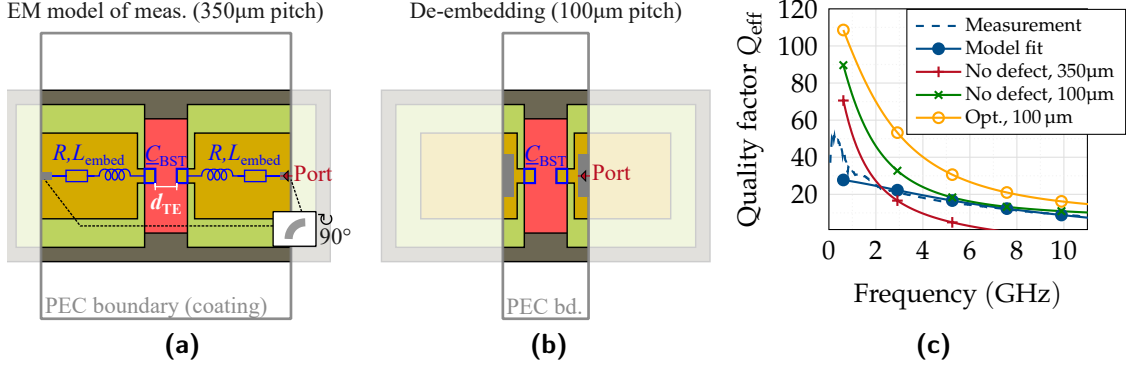
increased resistance in a subsequent modeling step. At 1 GHz and with no bias voltage applied,  $C_{350\text{ }\mu\text{m}} = 0.91 \text{ pF}$  and  $Q_{350\text{ }\mu\text{m}} = 33$  are recorded. Even when taking its embedded nature into account, the quality factor is still smaller than expected. This is more clear to see in the  $\text{ESR}_{350\text{ }\mu\text{m}}$ . The zero-bias resistance is increased by approximately one order of magnitude in comparison to the reference test structure from section 3.3.1. This large increase reveals unexpected defects when considering that a comparable BE resistance can be assessed from the geometry of the SMO conduction path. The bias-induced increase of the ESR is inherent to ferroelectric varactors and has been discussed elsewhere, see sections 2.1.2 and 3.3.1.

Figure 5.6c (top) shows  $C_{350\text{ }\mu\text{m}}$  and  $Q_{350\text{ }\mu\text{m}}$  at 1 GHz versus the electric bias field  $E_{\text{DC}}$ . For a BST film thickness of 59 nm, a common ion battery voltage level of 3.7 V corresponds to  $63 \text{ V}/\mu\text{m}$  electric bias field. While, for this layer stack and bias field strength, a tunability of 66 % was measured in the reference test structure, this prototype only shows 28.6 %. This will be discussed further together with the increased zero-bias ESR in the following section. The general characteristic of the quality factor is as expected from the reference test structure. For weak bias fields, the quality factor increases with bias up to 38 until it decreases for stronger bias, presumably due to acoustic activity.

The leakage current is shown at the bottom of Figure 5.6c. For the test structure, the interface to the top electrode caused a SE-dominated leakage current  $I_{\text{leak}} < 1 \text{ nA}$ . Due to the symmetric design used in this work, the weaker Schottky barrier between BST and SMO should not be effective. Hence, a symmetrical and equally small leakage current was expected for both negative and positive polarity. However, the leakage current is by orders larger and the I-V characteristic does not clearly indicate a dominant mechanism. By probing another sample before adding the top electrode, i.e., after step 2 in Figure 5.5, the epoxy-based insulation layer is found responsible. Although in this case, the only metalization is provided by the pins of the on-wafer probe, a significant leakage current is measured. Additionally, considering the smaller contact surface, its I-V characteristic is in good agreement with the characteristic of the DUT. Hence, the leakage current through the SU-8 pads and the SMO bottom electrode appears to dominate the measured leakage current and overshadows the one of the actual varactor.

## Discussion and Integration

In this section, the de-embedding is explained and the extracted results are discussed, as the RF performance does not meet the expectations. The effective relative permittivity can be calculated as  $\epsilon_{r,\text{eff}} = 57$  from a simple PPC model as in (3.12) but with a factor 2 for the twofold cascade. Both the permittivity and tunability are



**Figure 5.7:** EM model of SMD varactor (a) as measured and (b) for de-embedding of the contact pads. (b) Quality factor for several SMD varactors. The characterized data and fitting model is compared to results for defect-free BST and the potential performance for an optimized geometry.

much smaller than in the reference test structure or other reported values of BST thin films [Vor+04]. As the 350 µm pitch of the SG on-wafer probes is larger than the effective distance of the bonded bumps, a higher series resistance is measured. This probing resistance needs to be compensated before evaluating the losses of the device. The above geometric parameters are entered into the corresponding 3D EM model, shown in Figure 5.7a. It is excited via pins and a barrel port to a PEC boundary. The excitation and compensation of its additional inductance is implemented analogue to section 3.2.<sup>5</sup> However, note that a negative calibration inductance  $L_{\text{neg}}$  is not effective in this design due to the much different structure, i.e., the similarity of the SMD varactor to the calibration structure. The coarse fitting of the EM model and the measurement data is shown in Figure 5.6b.

With the above effective permittivity and an average BE conductivity of  $4 \cdot 10^6$  S/m taken from Figure 2.10, the effective dielectric loss factor of  $\tan \delta_{\text{BST}} = 0.035$  is determined by the EM model. The vastly increased dielectric loss factor requires clarification. Two effects are conceivable. Firstly, a fine layer of epoxy or photoresist could have remained on top of the BST layer before the evaporation of the TE seed layer. This, indeed, was observed for earlier samples. However, this error source was excluded by a reactive-oxygen-ion etching step that was inserted prior to the evaporation of the seed layer. More probably, the degradation is connected to the deposition of the TE, i.e., step 3 in Figure 5.5. The chromium adhesion layer may

<sup>5</sup>Instead of the top boundary, the coating boundary is used in this case. If the top boundary was used, a huge capacitive coupling between the contact pads and the boundary would distort the electromagnetic fields in the simulation that could not be easily compensated.

have partly oxidized into chromium (III) oxide. The consequence would be an interlayer with higher resistance and an oxygen-deficient BST with less tunability and an increased loss tangent [Kim+00]. The absence of acoustic resonances in the measured ESR also indicates a deficient BST lattice. Although chromium was already combined with BST before as, e.g., in thick films devices, the particularly thin BST layer is more likely to suffer from the oxygen drain. Unfortunately, an accurate modeling of a possible semiconducting chromium (III) oxide interlayer or residual photoresist on top of the BST layer is not possible. Due to the very high aspect ratio, a EM simulation is feasible only with a single effective dielectric block between the electrodes. Hence, a relation to chromium must be clarified in future work experimentally by replacing chromium with another adhesion layer, e.g. platinum. This is not possible in the currently used PVD, while the otherwise used sputtering is disqualified by being isotropic.

However, the EM model can be used to predict the RF properties without degraded BST and to de-embed the on-wafer measurement. The de-embedding, i.e., the modeling of a contact via gold bumps is done by narrowing the pitch and increasing the cross section of the excitation pins to 100 µm, respectively, as shown in Figure 5.7a-b. The modeled device quality factors are shown in Figure 5.7c with "No defect" depicting a varactor with non-degraded BST. For the following evaluation, all SMD varactors exhibit an effective low-frequency capacitance of 6.1 pF, i.e., the same BST properties and electrode size. By comparison to "No defect, 100 µm", the EM model predicts a Q factor decrease by up to 15 from the embedding by the 350 µm measurement pitch.<sup>6</sup> Hence, when the complete contact pad is used for integration into circuits, the corresponding resistance will decrease drastically. Note that the presented varactor merely depicts a first prototype with not yet optimized SMO thickness and a geometry with increased spacing of electrodes for simpler handling. The potential performance of this varactor design is assessed by the model with optimized geometry, "Opt., 100 µm" in Figure 5.7c. It uses a TE and BE thickness of  $t_{TE} = t_{SMO} = 5 \mu m$ , respectively, and a smaller TE spacing of  $d_{TE} = 30 \mu m$ . With that, a quality factor of  $Q = 40$  is modeled for 4 GHz. This fulfills a requirement on this technology to be of general industrial interest that was defined by a large European manufacturer of semiconductor components in bilateral discussions.

In conclusion on this discussion, three main tasks remain for future work. Firstly, the deposition process should be stabilized to yield predictable dielectric and conduction properties of the films. Secondly, the epoxy-based negative photoresist SU-8 enabled a significant leakage current; its exchange with other insulating materials

---

<sup>6</sup>For the fitting model with reduced permittivity and increased dielectric loss factor, the de-embedding does not increase the overall quality factor significantly. This is due to the dielectric loss dominating the electrode loss up to about 5 GHz.

like, e.g.,  $\text{SiN}_x$  or  $\text{SiO}_x$  deposited by PECVD should be attempted to decrease the leakage current. Thirdly and most importantly, the dielectric layer was severely degraded after the top electrode processing. Hence, the chromium adhesion layer must be replaced. First lab prototypes can be, e.g., realized with platinum deposited via MBE. After optimizing the manufacturing process, the integrable varactor will be built with thick electrodes and optimized geometry to realize the predicted performance.

The final step regarding the SMD varactor is its integration into circuits. Principally, two concepts are conceivable. On the one hand, the varactor can be flip-chipped as an independent device and bonded into a circuit with a corresponding footprint. On the other hand, the varactor can be grown as an integrated component with the complete circuit on the same substrate. The sophisticated deposition process of the oxide thin films recommends the former concept since the fabrication of varactor and circuit can be split and conducted independently from each other. Furthermore, varactor testing is simplified and substrate size limitations for the varactor deposition do not limit the size of the total circuit. The benefits of the latter concept are the absence of any increased inductance and contact resistance of the integration step itself. Both concepts have been investigated within this project. Additional steps required for bonding the independent component contain deposition of the ball bumps, flip-chipping and bonding via thermocompression. Two main challenges impeded the successful demonstration of a complete bonding process. Firstly, the stable adhesion via the gold bumps is sensitive to temperature, pressure and surface quality. Secondly, a certain minimum temperature is required for placing the gold bumps and, more severely, for thermocompression bonding. However, heating up the all-oxide varactor under oxygen atmosphere increases the risk to oxidize the BE. Hence, a careful control and optimization of all process parameters is necessary. Within this work, the deposition of gold bumps could be accomplished with a maximum heating-plate temperature of 125 °C. However, during first experiments for thermocompression<sup>7</sup>, a stable adhesion of the TE with the substrate could not yet be established. After replacing the epoxy insulation with a silicon compound, the next step will be finding the optimum temperature transiency for thermocompression, i.e., the trade-off between a stable adhesion and the non-oxidization of SMO. Note that a certain minimum cross section of the sample should be satisfied for easy handling and especially precise flip-chipping. The second concept of growing circuit-integrated varactors does not require additional steps, i.e., the recipe from section 5.3 can be used. The surrounding circuit

---

<sup>7</sup>Different temperature-time curves with up to 190 °C over up to 2 min have been evaluated without success yet. However, a limited sample quality impeded reliable tests as, e.g., the TE occasionally loosened from the insulating epoxy.

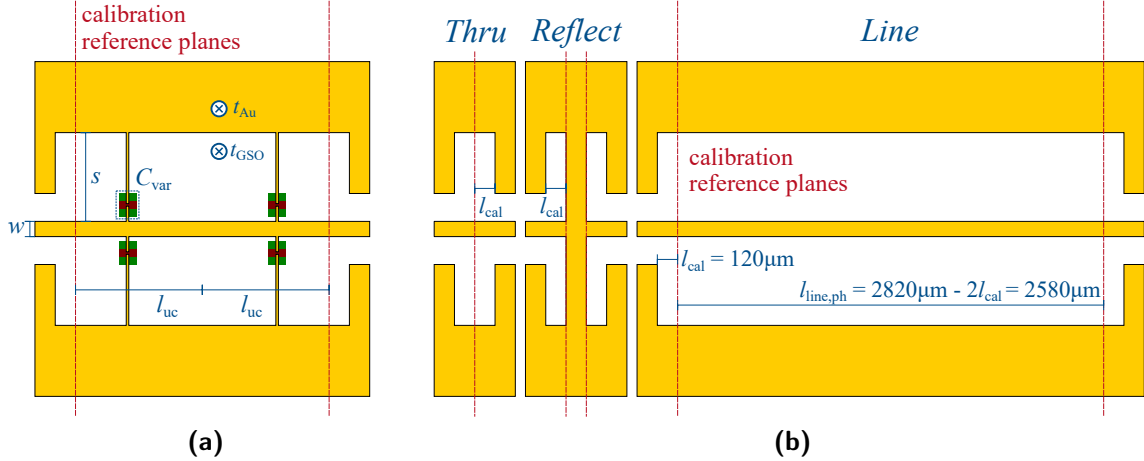


**Figure 5.8:** (a) Design of loaded CPW with geometric parameters. (b) Design of TRL calibration scheme with shifted reference plane to exclude the contact pads.

can be grown simultaneously with the TE deposition in the same step. However, in the currently established PLD process, this yields a limitation of the substrate size to  $\approx 4 \times 4 \text{ mm}^2$ , excluding a non-processable region at the substrate edge. After transferring the deposition to, e.g., sputtering, larger substrate sizes are conceivable. An example realization of a phase shifter based on all-oxide varactors will be presented in the following section.

## 5.4 Fully Integrated Tunable Circuits

A phase shifter built as a loaded CPW is adequate to firstly demonstrate the performance of varactors in networks. The design of the independent SMD can be easily adapted for the integrated component. The lithography mask of the TE is simply extended by the phase shifter network, see section 5.3. Hence, the substrate for the CPW is the same as for the SMD component, i.e.,  $\text{GdScO}_3$  for the scope of this section. The design of the loaded CPW containing the definition of all geometric parameters is shown in Figure 5.8a.

Note that the contact pads are not part of the analyzed phase shifter. They are excluded by the thru-reflect-line (TRL) calibration structure shown in Figure 5.8b. At a distance of  $l_{cal} = 120 \mu m$ , all transition effects in the EM fields due to the change in gap width are decayed. The remaining electrical length of the line is  $l_{line,ph} = 2580 \mu m$ . Since  $l_{line,el} = \lambda_c/4$  with center frequency wavelength  $\lambda_c$ , the

**Table 5.2:** Geometric and electric properties of the loaded PS design.

$w$ (mm)	$s$ (mm)	$t_{\text{GSO}}$ (mm)	$t_{\text{Au}}$ ( $\mu\text{m}$ )	$l_{\text{uc}}$ (mm)	$C_{\text{var}}$ (pF)	$C'$ (pF/mm)	$Z_0$ ( $\Omega$ )
0.1	0.5	1	5	0.73	Unloaded	0.15	71.2
					Unbiased	3	8.2
					Biased	1	2.7
							16.3

corresponding frequency is [Ag851]

$$f_c = \frac{c_0}{4l_{\text{line},\text{el}}} = \frac{c_0}{4l_{\text{line},\text{ph}}\sqrt{\epsilon_{r,\text{eff}}}} = 8.6 \text{ GHz}, \quad (5.1)$$

with effective relative permittivity  $\epsilon_{r,\text{eff}} = (\epsilon_{r,\text{GSO}} + 1)/2 \approx 11.4$  [ZB00]. As  $f_{\max}/f_{\min} = 8/1$  for a single line length, the lower frequency limit is obtained as

$$f_{\min} = \frac{2}{9}f_c = 1.9 \text{ GHz}. \quad (5.2)$$

A lower minimum frequency would require a larger substrate or the termination by a well-defined impedance matching to the characteristic line impedance. For this demonstration, the phase shifter will be evaluated at frequencies above that limit such that the given line length suffices.

Neglecting the finite conductor thickness, the impedance of an unloaded CPW is calculated by [ZB00]

$$Z_0 = \frac{30\pi}{\sqrt{\epsilon_{r,\text{eff}}}} \frac{K'(k)}{K(k)}, \quad (5.3)$$

with elliptic integral of the first kind  $K(k)$ <sup>8</sup> and geometric ratio  $k = w/(w + 2s)$ . An unloaded impedance of  $Z_0 = 71.9 \Omega$  is obtained for the dimensions given in Table 5.2. Neglecting losses, the impedance of any TL supporting a quasi-transverse electromagnetic (TEM) mode like CPW can be described by

$$Z_0 = \sqrt{\frac{L'}{C'}}. \quad (5.4)$$

<sup>8</sup>Note that  $K'(k) = K(k')$  with  $k' = \sqrt{1 - k^2}$ .

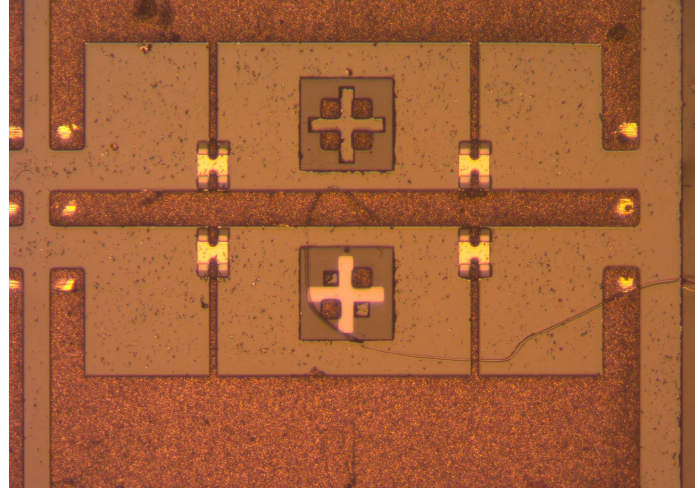


**Figure 5.9:** Microscope photo of a fabricated PS (with lithography alignment marks). Contacting with GSG on-wafer probes leave white scratches in the metalization.

with  $L'$  and  $C'$  being the inductance and capacitance per unit length, respectively. These can be approximated analytically with an error less than 1 % by a Schwarz-Christoffel conformal mapping as described in [Hei93]. With that, the characteristic impedance of the loaded CPW is approximated with sufficient accuracy by

$$Z_{0,\text{var}} = \sqrt{\frac{L'}{C' + C'_{\text{var}}}}, \quad (5.5)$$

with the specific loading capacitance  $C'_{\text{var}} = 2C_{\text{var}}/l_{\text{uc}}$ , a single varactor's capacitance  $C_{\text{var}}$  and the length of a loading unit cell  $l_{\text{uc}}$ .<sup>9</sup> The impedance of loaded CPW are generally small due to the necessary significance of the specific loading capacitance  $C'_{\text{var}} \gg C'$ . This can be partly compensated by increasing the TL specific inductance with, e.g., slits in the ground lines. Table 5.2 shows the impedance data of the loaded CPW for the two capacitance values 3 pF and 1 pF for the zero-bias and biased case, respectively. With  $t_{\text{BST}} = 80 \text{ nm}$  and varactor TE overlapping area  $A_{\text{var}} = 12 \times 12 \mu\text{m}^2$ , this corresponds to  $\epsilon_{r,\text{BST}}(0 \text{ V}) = 376$  and a tunability of  $\tau = 67 \%$ . Due to the reported permittivity fluctuations, a more detailed modeling is obsolete prior to the characterization. In this case, the expected characteristic impedance of the loaded CPW lies between  $9.6 \Omega$  and  $16.3 \Omega$ .

Figure 5.9 shows a microscope photo of the fabricated phase shifter. The characterization results are shown in Figure 5.10 for a reference impedance of  $Z_{\text{ref}} = 10.1 \Omega$ .

<sup>9</sup>This approximation is most accurate for a long line with many shunt varactors. Then,  $l_{\text{uc}}$  approximates the spacing between two varactor stubs.

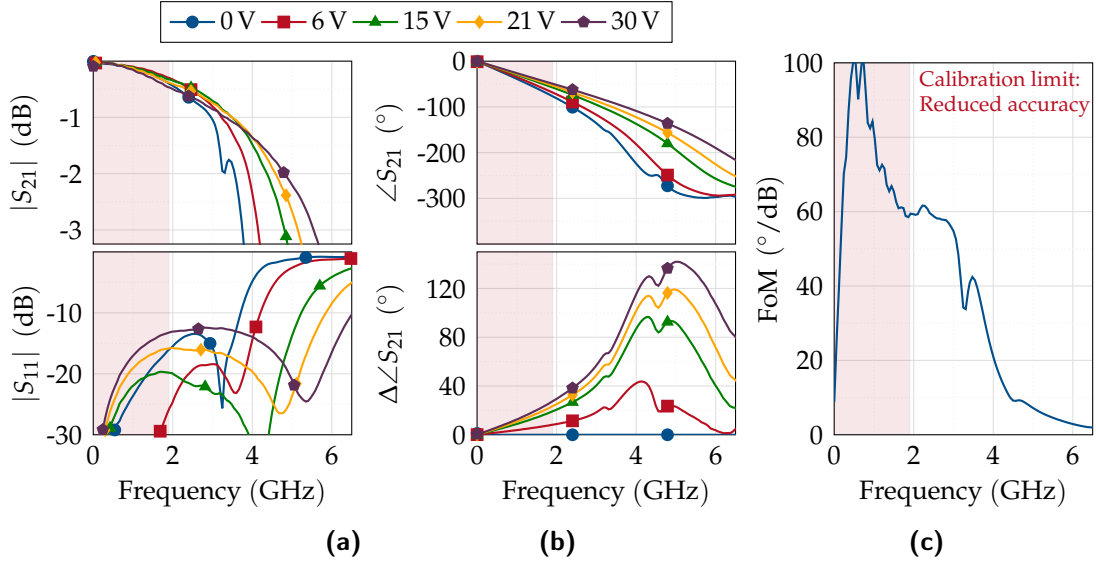


**Figure 5.10:** Characterization results of the PS for different bias states and  $Z_{\text{ref}} = 10.1 \Omega$  as (a) insertion loss  $|S_{21}|$  and return loss  $|S_{11}|$ , (b) transmission phase  $\angle S_{21}$  and its difference to the zero-bias phase and (c) figure of merit.

The insertion loss is smaller than 1 dB up to 3 GHz, while the return loss is better than 10 dB up to 3.7 GHz for all bias states. In a co-simulation of an EM model with discrete capacitors, a zero-bias and full-bias capacitance of 2.2 pF and 0.9 pF, respectively, leads to coarse fitting of the measured data. Assuming equal material properties for all varactors, this corresponds to a zero-bias relative permittivity of  $\varepsilon_{r,BST} = 276$  and a tunability  $\tau = 59\%$ . Note that a limited fitting accuracy allows no statement on the varactor quality factor. Though the overall differential phase shift is small due to the limited phase shifter length, it rises up to  $57^\circ$  at 3 GHz. Phase shifters with different lengths are commonly compared by a FoM relating the differential phase shift to the insertion loss as

$$\text{FoM} = \frac{\max(\angle S_{21}) - \min(\angle S_{21})}{\max(|S_{21,\text{dB}}|)}. \quad (5.6)$$

As shown in Figure 5.10c, it is steadily larger than  $54^\circ/\text{dB}$  up to 3 GHz and peaks, within the calibration range, in  $62^\circ/\text{dB}$  at 2.2 GHz.

A fair comparison to competing phase shifter technologies is impeded by the limited number of unit cells due to the small substrate size. The length of reported phase shifters usually spans across a few cm. For a given differential phase shift, a smaller phase shifter length requires a larger capacitance change per unit cell. This degrades the matching condition over the full tuning range and, hence, the FoM

**Table 5.3:** Comparison with other reported ferroelectric phase shifters.

Frequency (GHz)	FoM (°/dB)	Bias voltage (V)	Length (mm)	Width (mm)	
Thin-film technology					
2	40	160	2.6	2.4	[Kim+04]
2.2	62	30	1.9	1.9	This work
2.4	62	160	2.2	2.6	[Kim+04]
2.4	42	(sim.)	6.61	10.2	[Ma+14]
2.5	56	160	5.4	6.5	[Kim+02]
4.2	47	12	0.8	0.8	[Che+07]
10	80	17.5	17.5	3.5	[Aci+02]
12	26	20	7.25	1.5	[Mer+17]
15	50	19	3.06	0.8	[Par+06]
30	27	20	3.06	0.7	[Erk+00]
Thick-film technology					
1.72	70	200	36	1.6	[Nik+14]
4	36	140	2.31	1.64	[Saz+11]
7.7	46	50	10	4.5	[Nik+15]
10	29	140	2.31	1.64	[Saz+11]
Varactor diodes					
2.5	113	13	3	2	[ACJ18]
3.5	48	15	10	10	[Urb+20]

[Erk+00]. Furthermore, the required biasing voltage is increased. Despite the simple design and non-optimal deposition, the comparison in Table 5.3 reveals a good performance of the all-oxide phase shifter. In comparison to the reported thick-film phase shifters, a slightly higher FoM is indicated despite the smaller required size and reduced bias voltage. In future work, the frequency range can be extended with a more sophisticated design including, e.g., a tapering of the shunt stubs. When the available substrate size is increased, an even better performance, i.e., a higher FoM is expected. Furthermore, a well-performing concept of reflection-type phase shifter has been reported, where varactor diodes are used for demonstration and which can be adopted to ferroelectric varactors [ACJ18].

## 6 Conclusion & Outlook

For the first time, this work investigates the novel all-oxide technology for microwave varactors. They belong to the group of ferroelectric thin-film varactors, which deploy the strong electric-field dependence of the polarization to tune the capacitance with a direct current (DC) bias voltage. The most prominent ferroelectric material is barium strontium titanate  $\text{Ba}_x\text{Sr}_{1-x}\text{TiO}_3$  (BST), which is also used in this work. The state of the art is based on metal-, e.g., platinum electrodes and impaired by a low BST crystal quality close to the metal interface. This degradation originates in the strong crystallographic mismatch between metals and the oxide ceramics. It inflicts an untunable deadlayer between the electrode and the BST layer that, additionally, grows polycrystalline. As a result, the varactor requires higher tuning voltage levels and suffers from an increased dielectric loss. Both of these drawbacks can be overcome by the all-oxide technology. The term "all-oxide" refers to the replacement of metals as electrode material with a conducting oxide. After the concept of radio frequency (RF) varactors with oxide electrodes was generally discarded already decades ago due to too high conduction loss, it could be revived by novel findings on the highly conducting strontium molybdate  $\text{SrMoO}_3$  (SMO). It structurally matches very neatly to BST. Hence, when using SMO as bottom electrode (BE), the ferroelectric can grow monocrystalline from the first atomic layer on. Instead of the minimum BST thickness of about  $t_{\text{BST}} \approx 300 \text{ nm}$  for state-of-the-art varactors, highly functional all-oxide varactors with thicknesses down to  $t_{\text{BST}} = 40 \text{ nm}$  have been demonstrated. This greatly reduces the required tuning voltage level down to ion battery voltage level, making the use of DC-DC converters for biasing obsolete.

Since this work depicts the pioneer steps in this novel research field, a comprehensive RF characterization and modeling is required for the optimal design of devices. An automated setup is developed that allows to characterize all varactors on a sample at all bias states in a row. Powerful post-processing Matlab scripts quickly yield a statistic evaluation and an easy comparison of multiple samples of any evaluated property. However, prior to the actual characterization, a major contribution of this work is the significant extension of the applicable frequency range of the deployed on-wafer test structures. Due to the particular shape of this standard test structure,

the electromagnetic (EM) field distribution in the test structures is very different from the one during calibration. This introduces a systematic error that affects the recorded data for increasing frequencies in the GHz range. The impact of this systematic error is identified; it can be compensated by subtracting a small negative inductance. Furthermore, systematic studies based on this improved RF characterization are a key element for the optimization of the deposition process. Finally, they allow for the deposition of high-performance varactors with unprecedented SMO and BST thicknesses greater than 5  $\mu\text{m}$  and smaller than 50 nm, respectively.

The most significant progress of this work is achieved in the field of analytic RF modeling. Prior to this work, only a rudimentary interpretation of the varactor is available: The RLC model. It comprises a complex capacitance in series with a resistance and inductance, modeling the dielectric and electrodes, respectively. In particular, there is no mean to consider the substrate. However, simple evaluations of the skin depth reveal that the substrate often contributes significantly, especially for the thin BEs usually used in such thin-film devices. This conflict is resolved during this work by extending the RLC model with a phenomenological substrate impedance  $A_{\text{sub}}$ , resulting in a reasonably exact fitting of the true impedance. This novel unshielded substrate model (USM) depends on the five major material parameters, i.e., BE and dielectric thicknesses, BE conductivity as well as dielectric permittivity and loss factor. The variation of the former four impacts the EM energy in the substrate exponentially, leading to a likewise exponentially scaled contribution of  $A_{\text{sub}}$ . The greatly increased accuracy of the USM is proven over a wide parameter range via extensive EM modeling and validation by several samples. In particular, and in contrast to the RLC model, intuitive expectations like a linear dependence of the sub-skin-depth-BE resistance on its thickness are very well fulfilled by the USM. In a second phase, this model is extended by the dimension of the electric bias field to the acoustic unshielded substrate model (AUSM). For this, the electromechanical excitation of acoustic waves must be considered due to the electrostriction-induced piezoelectricity. A convoluted optimizer scheme for the identification of the material properties is derived and validated that yields a very high accuracy of the AUSM. It enables an unprecedentedly close impedance tracking in both bias field and frequency up to 100 V/ $\mu\text{m}$  and 12 GHz, respectively. Two significant benefits are obtained. Firstly, the high accuracy makes the AUSM a powerful tool for the design of circuits based on the all-oxide technology. Secondly, both electric and mechanic properties of the analyzed materials can be identified by a mere on-wafer RF characterization within a very short time. Finally, the AUSM is used to predict the possible suppression of acoustic resonances in all-oxide varactors, which are the dominant cause of the frequency limitation in conventional thin-film varactors. A significant extension of the applicable frequency range is predicted for optimized acoustic properties of the thin films.

The last part of this work investigates the required steps for an industrial realization of the all-oxide technology. Reproducibility and uniformity are evaluated as a key precondition for the design of RF circuits. Both cannot be sufficiently guaranteed with the hitherto used pulsed laser deposition (PLD), such that this work can not pursue the demonstration of the expected excellling performance. Nonetheless, some further steps are investigated. The feasibility of the transfer to the industrially established silicon substrate is demonstrated, which is important for the later integrability of the all-oxide technology with industrial fabrication processes. Furthermore, design concepts for the circuit integration are demonstrated in two configurations. Firstly, the layout and experimental fabrication process of a standalone surface-mount device (SMD) is presented and characterized. Secondly, the varactor is grown fully integrated into an all-oxide phase shifter that shows good performance despite the fluctuating deposition condition and PLD-inflicted limited substrate size. In the future and with another deposition method, high-performing varactors can be tailored to fabricate significantly improved phase shifters and other circuits.

In the following, two approaches for future work are presented that can significantly improve the device performance in the complete 5G sub-6 GHz range and beyond.

**The first approach** is using doping BST, which evolves in recent years as a highly promising approach to optimize the material tunability and loss. Note, however, that the modeled assessment of the performance of doped BST in Figure 4.18 can only be understood as a rough estimate. Its accuracy is particularly strained by the order-of-magnitude estimate of material properties and the neglected impact on the electromechanical coupling. Hence, systematic studies with samples of varying doping material and concentration are necessary. A first example varactor with doped BST having 3 % manganese content was fabricated and characterized as an outlook to demonstrate the potential. Figure 6.1 compares the results of the doped varactors with those of an original all-oxide varactor with undoped BST.<sup>1</sup> The respective relative tunability  $\tau$  and quality factor at 1 GHz in Figure 6.1a react on the doping as expected: The quality factor increases and the tunability decreases. The important information, however, comes from Figure 6.1b. The  $Q_{\text{eff}}$  factor of both samples is plotted versus frequency for a fixed tunability of 25 %.<sup>2</sup> In spite of the equal evaluated tunability in both samples, a remarkable improvement in the

<sup>1</sup>The varactor with undoped BST ( $t_{\text{BST}} = 85 \text{ nm}$ ,  $t_{\text{SMO}} = 800 \text{ nm}$ ,  $\sigma_{\text{SMO}} = 51.1 \mu\Omega \text{ cm}$ ) is chosen with similar properties to the doped one ( $t_{\text{BST}} = 100 \text{ nm}$ ,  $t_{\text{SMO}} = 750 \text{ nm}$ ,  $\sigma_{\text{SMO}} = 56.9 \mu\Omega \text{ cm}$ ).

<sup>2</sup>Hence, the electric bias fields of the doped and undoped varactor are different, i.e., 66 V/ $\mu\text{m}$  vs. 31 V/ $\mu\text{m}$  for 25 % tunability.

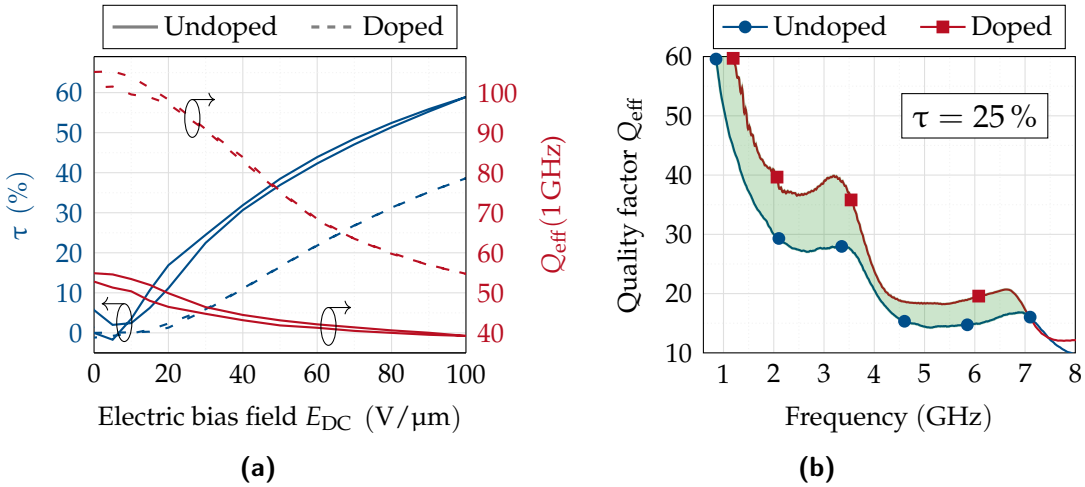


**Figure 6.1:** Comparison of varactors with 3 %-manganese-doped and pure BST, respectively. (a) Tunability  $\tau$  and  $Q_{\text{eff}}$  factor versus electric bias field and (b)  $Q_{\text{eff}}$  factor at 25 % tunability, obtained at a bias field of 66 V/ $\mu\text{m}$  and 31 V/ $\mu\text{m}$ , respectively.

doped varactor is observed, depicted as the green area in the plot. Due to the very similar BE conductivity and thickness, this difference is attributed to the dielectric. However, as this is just a single sample with non-optimized properties, more detailed studies will reveal the exact benefit and potential of doping BST. When targeting ultra-thin BST layers for lowest acoustic activity, the incorporation of the oxygen barrier layer between BST and SMO in the model becomes increasingly important, see section 4.2.4.

The second approach improves the integration of the all-oxide technology in RF circuits. An important precondition for this will be to stabilize the deposition process as was shown in section 5.1. However, a precise control of the material properties is commonly difficult for the used method, i.e., PLD [Sub+13]. Furthermore, the usable substrate size is limited. With the current substrate size of 5 mm  $\times$  5 mm, the realization of circuits is obstructed as was shown in section 5.4. Both issues might be solved by a transfer to another deposition method like, e.g., sputtering as in [Miz+00]. With precise control of the deposited material properties and larger substrate sizes, the design of high-performance circuits can be pursued with high confidence. Besides that, a related topic is the exchange of the rather expensive gadolinium scandate (GSO) substrate with the widely used silicon. The general feasibility was also demonstrated already in section 5.2 and this topic will be further investigated in the future.

Beyond the scope of this thesis on microwave varactors, the all-oxide technology might as well provide valuable benefits in other fields.

Firstly, the application in thin-film bulk acoustic resonators (FBARs) introduces a large degree of freedom for design engineers: The structural similarity can be exploited to chose the capacitance independent of the acoustic resonator length. Hence, the input impedance is no longer strictly connected to the chosen resonance frequency. Furthermore, a low-voltage use case is favored by the large demonstrated coupling coefficient even for very thin BST layers.

Secondly, thinking beyond RF scenarios, another application as memory cells in DRAM might be promising. Ferroelectric memories are valued due to clear advantages like non-volatility, low power consumption, high endurance and high speed writing [Tak00]. Ferroelectric-memory-based reconfigurable devices can also be used as dynamic programmable gate array (DPGA) [Tak00]. A particular benefit of the all-oxide technology in these applications would be replacing platinum with SMO. Hence, the issue of platinum contamination of the ferroelectric layer during annealing processes can be avoided [Bou+02].

# Appendix

# A De-Embedding of Excitation Bridge in EM Simulation

This chapter refers to section 3.2. It explains the calculation of self-inductance values by magnetostatic (MS) simulations in detail, i.e., how to remove the impact of the excitation bridge from the simulation results for the complete varactor. As no external magnetic flux is present, the apparent<sup>1</sup> inductance can be calculated as

$$L = \frac{\Phi}{I}, \quad (\text{A.1})$$

where  $\Phi$  and  $I$  is the magnetic flux and the current, respectively. The latter is an input parameter for the MS simulation and the former is obtained by

$$\Phi = \int_A \vec{B} \cdot d\vec{A}, \quad (\text{A.2})$$

where  $\vec{B}$  is the magnetic flux density and  $A$  depicts any open surface framed by the current loop of the MS simulation. For computational calculations, the domain gets discretized and the above integral is replaced by a summation across all contained mesh cells.

The excitation bridge is copied from the EM simulation, where the circular electrodes and all material below are removed. Instead, a perfect electrically conducting (PEC) boundary is added which closes the current loop. The corresponding MS model is shown in Figure A.1a. As excitation, the cylindrical RF port in the center can be replaced by a coil segment with a single winding of the same size and shape. However, the RF port is treated as PEC during the EM simulation, whereas the coil segment allows magnetic fields inside its body in the MS simulation. To achieve the most similar excitation compared to the EM simulation, the RF port is split up. The length of the coil segment is defined very small, i.e., 0.1  $\mu\text{m}$  and the remaining gap

---

<sup>1</sup>Anyways, since no magnetically nonlinear materials are contained, a distinction between incremental and apparent inductance is obsolete.

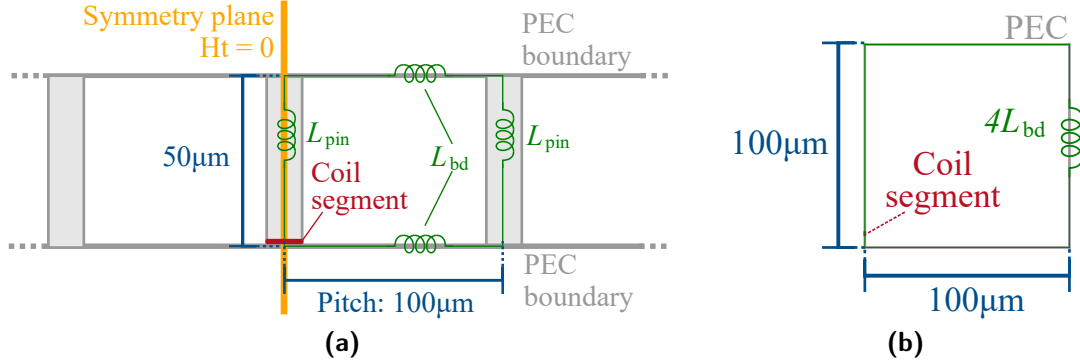


**Figure A.1:** Simulation setup to obtain the self inductance of (a) the excitation bridge, where mutual inductances are not shown in the schematic, and (b) of the PEC boundary.

is filled with another PEC cylinder.<sup>2</sup> The matching distribution of magnetic fields in the MS and EM simulations confirms a valid representation in the MS model. From the field distribution shown in Figure 3.6b the inductance

$$L_{\text{exBridge-MS}} = 41.6 \text{ pH} \quad (\text{A.3})$$

is extracted. However, this is not yet the final result since the additional inductance of the previously introduced lower PEC boundary must be removed. This is done in a second step, after the inductance  $L_{\text{bd}}$  has been determined. However, MS simulations require a closed current loop for convergence, which impedes a simple simulation of the conductor strip. Due to that,  $L_{\text{bd}}$  is extracted indirectly with a simulation setup as shown in Figure A.1b. A square is formed of four equal PEC bricks and with side length equal to the pitch of the on-wafer probe, i.e., 100 μm. As in the MS model for the full excitation bridge, only a very short coil segment is defined to exclude fields inside the metal, whereby its thickness is negligible.<sup>3</sup> The determination of the accurate effective width of the PEC boundary is, however, not straightforward. The current will not use the full width of the bounding box and will instead distribute differently for different distances from the center. This is shown in Figure A.2a by means of the magnetic field close to the boundary, which induces the surface current in the conductor. The effective conducting width  $w$  is defined as the width, where the inducing magnetic field decreases to  $-40 \text{ dB} \triangleq 1\%$  with respect to

<sup>2</sup>The fields inside the center cylinder were falsely included in the calculations for [1], leading to slightly increased inductance values in the referenced paper. This, however, remains without impact on the central results of that work.

<sup>3</sup>No significant difference in the resulting inductance was observed below a coil thickness of 1 μm. Hence, 0.1 μm was chosen for this analysis.

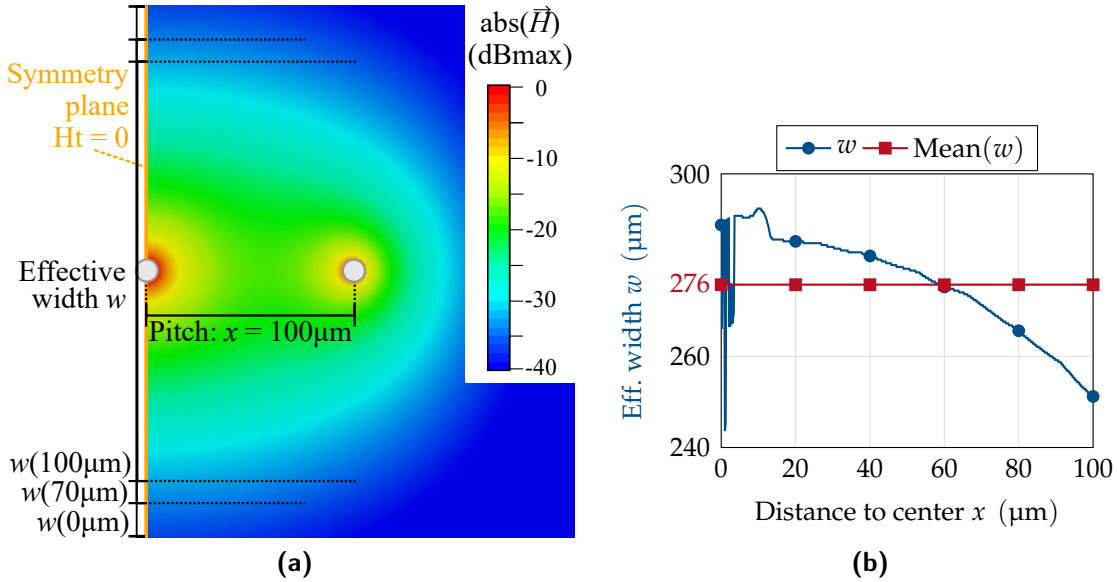


**Figure A.2:** (a) Top view of Figure A.1a with magnetic field and definition of the effective boundary width. (b) Width  $w$ , at which the magnetic field decays to  $-40$  dB (1 %) with respect to the plane maximum versus distance  $x$  to center pin. Both refer to a height close to the PEC boundary of Figure A.1a, i.e., at  $z = 49$   $\mu\text{m}$ .

the plane maximum. The resulting width is plotted over the distance to the center  $x$  in Figure A.2b. Using its mean value as an approximation for the overall effective boundary width, the self inductance of one boundary strip is obtained as [RG17, p. 155]

$$L_{\text{bd}} = \frac{1}{4} L_{\text{bd,sq}} = 6.3 \text{ pH.} \quad (\text{A.4})$$

Of course, an intuitive approach to avoid the uncertainty provided by the PEC boundary, would be to use a rectangular bar with known inductance instead. However, independent of the chosen conductor geometry, its close proximity to the test structure (EM) or the opposite PEC boundary (MS), respectively, causes a significant mutual inductance. Hence, as this cannot be avoided, it is important to choose a geometry which provides a similar mutual inductance as the test structure. Due to the planar BE with only thin layers on top, a large similarity is expected from replacing it with a PEC boundary. This is likewise confirmed by the matching magnetic field distribution in both simulations. Due to that geometric similarity, it can also be expected that the self inductance of the test structure is of the order of  $L_{\text{bd}}$ . Note that possibly differing mutual inductances can affect the precision of the extracted self inductance.

In conclusion, the resulting inductance of the excitation bridge obtained from this MS simulation is

$$L_{p/p} = L_{\text{exBridge-MS}} - \frac{L_{bd}}{2} = 41.55 \text{ pH} - \frac{6.26 \text{ pH}}{2} = 38.4 \text{ pH}. \quad (\text{A.5})$$

The obtained result can be validated by comparison to the values obtained by analytic approximations which exist for many simple conductor geometries. The port and pins can be approximated as cylindrical wires. Since no field is confined inside the PEC wire, their inductance in nH can be approximated by [RG17, p.151]

$$L_{RFport} = L_{pin} = 2l \left[ \log \frac{2l}{r} - 1 \right] \approx 19.96 \text{ pH}, \quad (\text{A.6})$$

where  $l$  and  $r$  is the length and radius of the pin in cm, respectively. With the same unit scaling, the approximation for the boundary inductance can be calculated from the formula for a square with rectangular section. One obtains [RG17, p.155]

$$L_{bd,alt} = \frac{1}{4} L_{\text{square,loop}} = \frac{1}{4} \left( 8l \left[ \log \frac{l}{\alpha + \beta} + 0.2235 \frac{\alpha + \beta}{l} + 0.726 \right] \right) \approx 6.55 \text{ pH} \quad (\text{A.7})$$

with side length  $l = 100 \mu\text{m}$ , width  $\alpha = 276 \mu\text{m}$  and breadth  $\beta = 0$  for the infinitely flat boundary, which strongly agrees with (A.4). The overall analytic result

$$L_{p/p,alt} = L_{RFport} + \frac{L_{pin} + L_{bd,alt}}{2} = 33.2 \text{ pH} \quad (\text{A.8})$$

is of the order of (A.5), the value from the full MS simulation. The decrease with respect to the MS result is explained by the negligence of mutual inductances of parallel conductors in the analytic consideration. The MS result from (A.5) will be used as it inherently takes the weak inductive coupling into account.

## B Additional Data to the Analytic Models

### B.1 USM

This section contains additional data to the USM.

**Table B.1:** Extension to section 4.1.1 and section 4.1.2: Model parameters for all pairs of used electrode sizes.

	A1/B1/C2	B2	B3	C3	A2	C1	A3
$d_{\text{in}} (\mu\text{m})$	20	20	20	30	40	40	60
$d_{\text{out}} (\mu\text{m})$	40	60	80	60	60	80	80
$C_{\text{ref}} (\text{pF})$	10.506	10.494	10.488	23.414	41.348	41.314	91.004
$R_{\text{ref}} (\Omega)$	0.243	0.247	0.246	0.212	0.187	0.192	0.157
$L_{\text{ref}} (\text{pH})$	3.913	3.873	3.811	3.980	3.870	3.769	3.786
$k_{\text{ref}}$	0.218	0.171	0.131	0.194	0.205	0.157	0.180
$a_{\text{ref}} (\text{ns}/\Omega)$	1.217	1.466	1.723	1.638	1.959	2.330	2.733
$N_C$	0.003	0.002	0.006	-0.002	-0.003	0.000	-0.001
$N_R$	0.057	0.055	0.051	0.070	0.085	0.083	0.111
$N_L$	-0.032	-0.025	-0.017	-0.032	-0.030	-0.022	-0.025
$N_{k,\text{bot}}$	-0.667	-0.651	-0.594	-0.625	-0.739	-0.765	-0.898
$N_{k,\text{BST}}$	-0.441	-0.423	-0.317	-0.046	-0.095	-0.083	-0.307
$N_{a,\text{bot}}$	1.281	1.192	1.056	1.082	1.238	1.184	1.325
$N_{a,\text{BST}}$	-0.051	-0.333	-0.510	-1.047	-0.913	-0.941	-0.556

## B.2 AUSM

This section contains additional data to the AUSM.

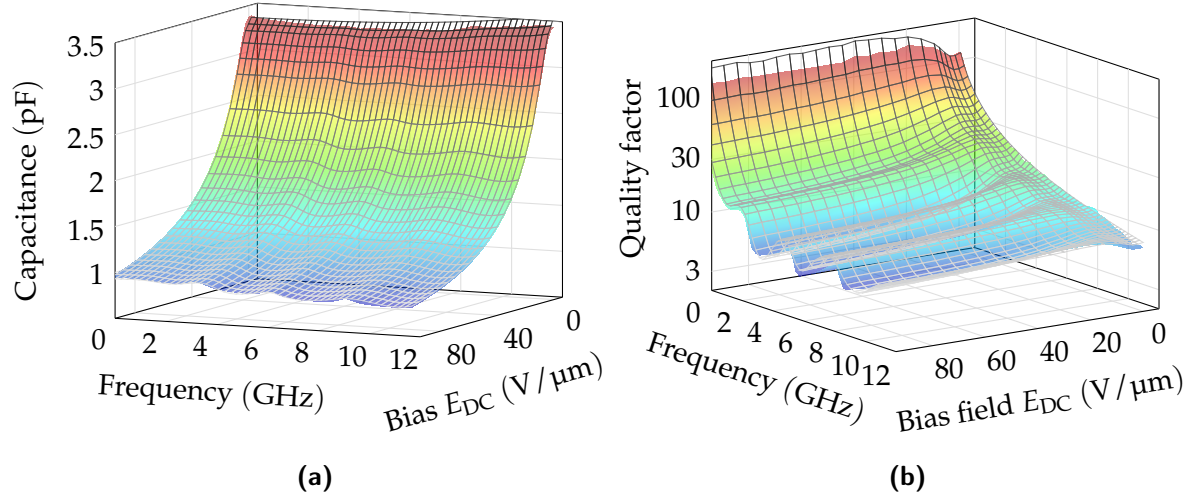


**Figure B.1:** Extension to section 4.2.3. Measured and modeled impedance data for VT168 with  $\mathcal{Z}_{\text{top}} = 35 \cdot 10^6 \text{ kg/sm}^2$ , compare Figure 4.13a. Semi-transparent colored surface plots of the measured (a) capacitance and (b) quality factor along with gray-scaled mesh plots for the model result.

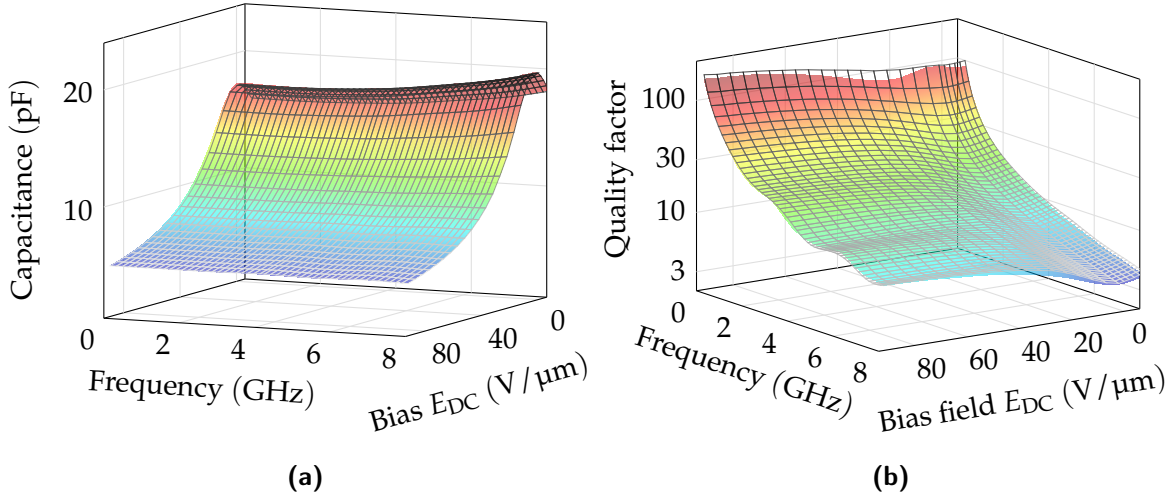


**Figure B.2:** Extension to section 4.2.3. Measured and modeled impedance data for VT40 with  $Z_{\text{top}} = 45 \cdot 10^6 \text{ kg/sm}^2$ , compare Figure 4.13b. Semi-transparent colored surface plots of the measured (a) capacitance and (b) quality factor along with gray-scaled mesh plots for the model result.

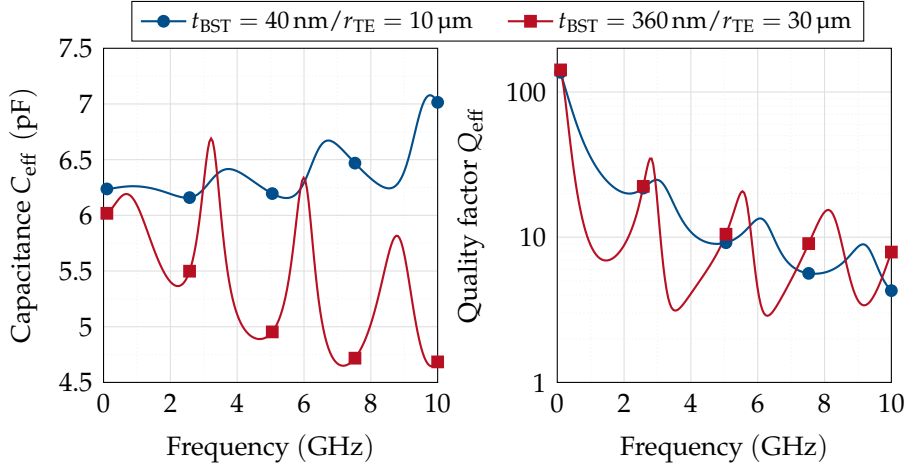


**Figure B.3:** Extension to section 4.2.5, showing the impact of acoustic activity depending on the film thickness. The data shows capacitance and  $Q$  factor for two different modeled stacks "air/Au/Pt/BST/SMO/GSO". Since  $t_{\text{BST}}/r_{\text{TE}}^2$  is equal in both cases, there is no change in the microwave characteristic (constant nominal capacitance), only in the acoustic domain.

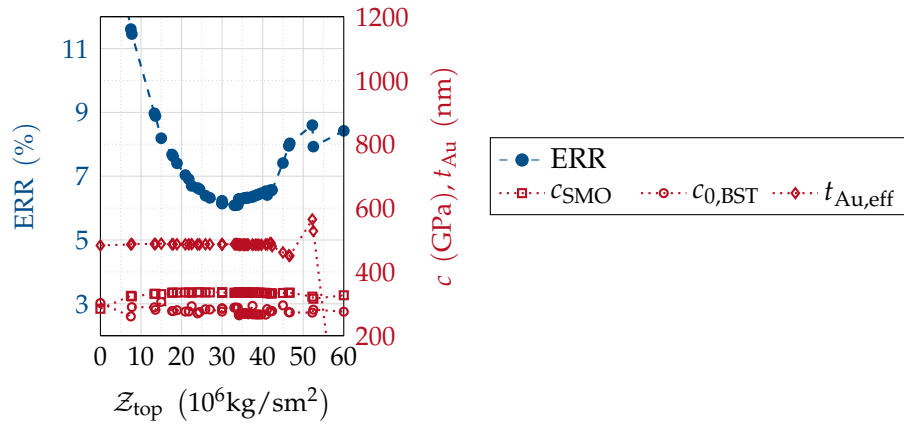


**Figure B.4:** Extension to section 5.2. Result of outer optimizer to evaluate the globality of the obtained minimum for the  $\text{SrTiO}_3/\text{Si}$  sample. The left axis (blue) shows the target function ERR. On the right one (red), SMO and zero-bias BST stiffness and effective gold thickness versus acoustic impedance of top termination are shown. See section 4.2.3 for a more detailed explanation.

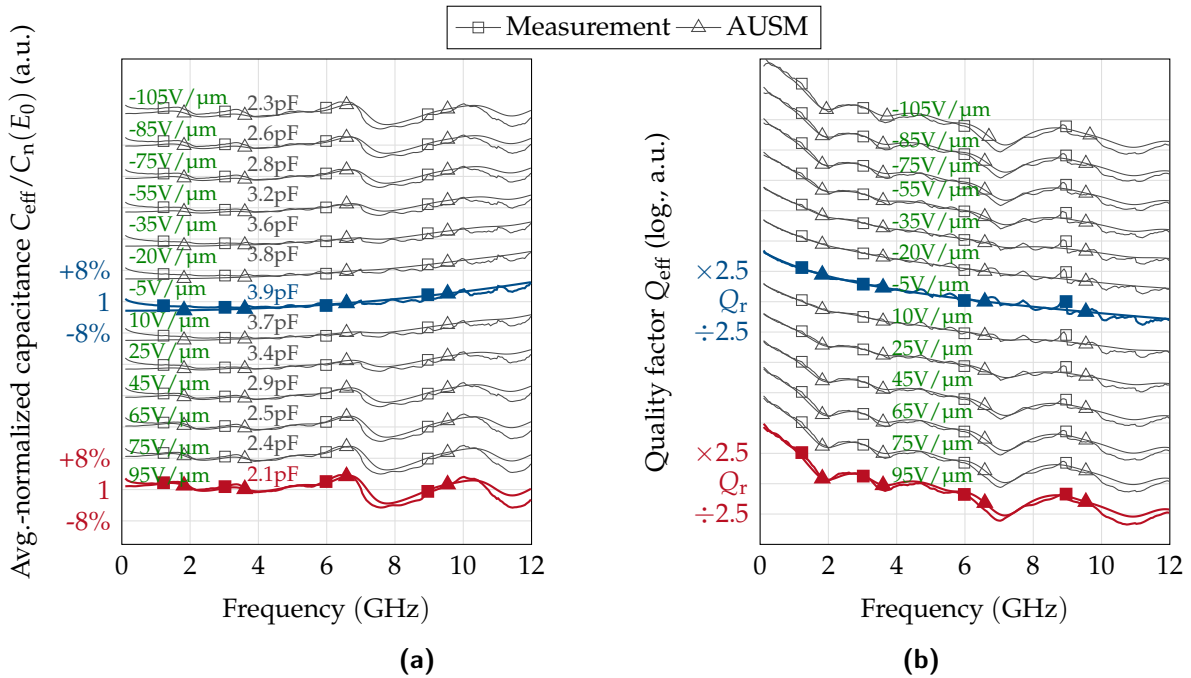


**Figure B.5:** Extension to Figure 5.3. Measured and modeled impedance data for the SrTiO<sub>3</sub>/Si sample with  $Z_{\text{ac,top}} = 33 \cdot 10^6 \text{ kg/sm}^2$  (see Figure B.4). The (a) normalized capacitance and (b) quality factor are shown versus frequency for multiple electric bias fields  $E_{\text{DC}}$ . The normalization value for the capacitance (its average value  $C_n(E_{\text{DC}}) = \text{avg}_f\{C(E_{\text{DC}}, f)\}$ ) labels each data line. The quality factor reference value is  $Q_r = 20$ . In both graphs, the data of each bias state has been shifted by one line of the grid for readability.

# Acronyms

**ADC** analog-to-digital converter.

**ATFT** Advanced Thin-Film Technology group.

**AUSM** acoustic unshielded substrate model.

**BAW/SAW** bulk/surface acoustic wave.

**BE** bottom electrode.

**BST** barium strontium titanate  $\text{Ba}_x\text{Sr}_{1-x}\text{TiO}_3$ .

**CPW** coplanar waveguide.

**CQF** commutation quality factor.

**CSD** chemical solution deposition.

**DC** direct current.

**DPGA** dynamic programmable gate array.

**DUT** device under test.

**EM** electromagnetic.

**ESR** equivalent series resistance.

**FBAR** thin-film bulk acoustic resonator.

**fcc** face-centered cubic.

**FEM** finite element method.

**FoM** figure of merit.

**FWHM** full width at half maximum.

**GSG** ground-signal-ground.

**GSO** gadolinium scandate.

**IBE** ion beam etching.

**IDC** interdigitated capacitor.

**ImpA** impedance analyzer.

**IoT** Internet of Things.

**IRGN** iteratively regularized Gauss-Newton.

**ISS** impedance standard substrate.

**LNA** low-noise amplifier.

**MBE** molecular beam epitaxy.

**MEMS** micro-electromechanic systems.

**MIM** metal-insulator-metal.

**MIMO** multiple-input multiple-output.

**MOCVD** metalorganic chemical vapour deposition.

**MS** magnetostatic.

**OSL** open-short-load.

**OT** over-travel.

**PCB** printed circuit board.

**PEC** perfect electrically conducting.

**PECVD** plasma-enhanced chemical vapour deposition.

**PF** Pool-Frenkel.

**PLD** pulsed laser deposition.

**PPC** parallel-plate capacitor.

**PS** phase shifter.

**PVD** physical vapor deposition.

**RF** radio frequency.

**RFFE** RF frontend.

**RHEED** reflection high-energy electron diffraction.

**RMSE** root-mean-squared error.

**RSM** reciprocal space map.

**SDR** software-defined radio.

**SE** Schottky emission.

**SMD** surface-mount device.

**SMO** strontium molybdate  $\text{SrMoO}_3$ .

**SRF** self-resonant frequency.

**TE** top electrode.

**TEM** transmission electron microscopy.

**TEM** transverse electromagnetic.

**TF** thin-film.

**TL** transmission line.

**TRL** thru-reflect-line.

**USM** unshielded substrate model.

**VCO** voltage controlled oscillator.

**VNA** vector network analyzer.

**VPF** voltage performance factor.

**XRD** X-ray diffraction.

# Symbols and Abbreviations

$(\cdot)^t$	$\mathbf{A}^t$ depicts the transposition of a matrix $\mathbf{A}$ .
$\beta^T$	Dielectric impermittivity for a constant stress $T$
$\chi$	Electric susceptibility
$\delta_{\text{skin}}$	Skin depth: An EM field that enters a conductor will decay to $1/e \approx 37\%$ at a distance of $1\delta_{\text{skin}}$
$\varepsilon_0$	Electric constant; $\varepsilon_0 \approx 8.854\ 187\ 817\ 62 \cdot 10^{-12}\ \text{As/Vm}$
$\varepsilon_r$	Relative permittivity ( $\varepsilon_r = \varepsilon/\varepsilon_0$ )
$\mathcal{Z}$	Acoustic impedance $\mathcal{Z} = \rho v_{\text{ac}}$
ERR	Combined error criteria for the relative deviation of modeled capacitance and quality factor to the respective measured data
$\omega$	Angular frequency ( $\omega = 2\pi f$ )
$\sigma_{\text{SMO}}$	SMO conductivity ( $\sigma_{\text{SMO}} = 1/\rho_{\text{SMO}}$ )
$\tan \delta_{\text{diel}}$	Pure dielectric loss factor (cleaned from impact of acoustic waves)
$\underline{A}_{\text{sub}}$	Phenomenological substrate impedance
$\rho_{\text{SMO}}$	SMO resistivity ( $\rho_{\text{SMO}} = 1/\sigma_{\text{SMO}}$ )
$\varrho$	Material density
$\hat{=}$	The sign $\hat{=}$ in an equation depicts the equaling of the former expression to the <i>order of magnitude</i> of the latter one.
$c^E$	Elastic stiffness for a constant electric field $E$

$C_{\text{eff}}$	Effective varactor capacitance (after de-embedding via subtracting negative inductance)
$C_{\text{meas}}$	Raw effective varactor capacitance (as measured)
$D$	Electric displacement
$E$	Electric field
$E_{\text{DC}}$	Electric bias field in varactors to tune the BST permittivity
$g_{\text{ind}}$	Electrostriction-induced piezoelectricity coefficient of the strain-voltage form
$j$	Imaginary unit ( $j = \sqrt{-1}$ )
$k$	Proportionality factor that weights the high-energy portion with significant substrate contribution at the center of the test structure against the total electrode impedance
$K^2$	Electromechanical coupling coefficient
$M$	Electrostrictive nonlinearity of stiffness
$Q_{\text{eff}}$	Effective varactor quality factor (after de-embedding via subtracting negative inductance)
$Q_{\text{ES}}$	Electrostriction coefficient
$Q_{\text{meas}}$	Raw varactor quality factor (as measured)
$S$	Mechanic strain
$s^D$	Elastic compliance for a constant electric displacement $D$
$T$	Mechanic stress
$T_c$	Curie temperature: Phase transition between ferro- and paraelectric phase in a ferroelectric material
$v_{\text{ac}}$	Acoustic velocity

# Bibliography

- [Abb+17] B. Abbott, A. Chen, T. Daniel, K. Gamble, T. Kook, M. Solal, K. Steiner, R. Aigner, S. Malocha, C. Hella, M. Gallagher, and J. Kuypers. "Temperature compensated saw with high quality factor". In: *IEEE International Ultrasonics Symposium (IUS)*. Sept. 2017. DOI: [10.1109/ultsym.2017.8092294](https://doi.org/10.1109/ultsym.2017.8092294).
- [Aci+02] B. Acikel, T. R. Taylor, P. J. Hansen, J. S. Speck, and R. A. York. "A new high performance phase shifter using  $\text{Ba}_x\text{Sr}_{1-x}\text{TiO}_3$  thin films". In: *IEEE Microwave and Wireless Components Letters* 12.7 (July 2002), pages 237–239. DOI: [10.1109/1mwc.2002.801129](https://doi.org/10.1109/1mwc.2002.801129).
- [ACJ18] B. An, G. Chaudhary, and Y. Jeong. "Wideband Tunable Phase Shifter With Low In-Band Phase Deviation Using Coupled Line". In: *IEEE Microwave and Wireless Components Letters* 28.8 (Aug. 2018), pages 678–680. DOI: [10.1109/1mwc.2018.2847025](https://doi.org/10.1109/1mwc.2018.2847025).
- [Ada96] L. Adams. *Linear and nonlinear conjugate gradient-related methods*. Philadelphia: Society for Industrial and Applied Mathematics, 1996. ISBN: 9780898713763.
- [Adb74] P. R. Adby. *Introduction to Optimization Methods*. Dordrecht: Springer Netherlands, 1974. ISBN: 9789400957053.
- [Ag851] Product Note 8510-8A. *Applying the 8510 TRL Calibration for Non-Coaxial Measurements*. Technical report. Agilent Technologies, 2000.
- [AGK15] A. Ahmed, I. A. Goldthorpe, and A. K. Khandani. "Electrically tunable materials for microwave applications". In: *Applied Physics Reviews* 2.1 (Mar. 2015), page 011302. DOI: [10.1063/1.4906255](https://doi.org/10.1063/1.4906255).
- [Alt+19] A. G. Altynnikov, A. G. Gagarin, A. V. Tumarkin, and I. V. Kotel'nikov. "Characterization of the Properties of Barium–Strontium Titanate Films and Controlled Elements Based on Them in the Frequency Range of 1–60 GHz". In: *Technical Physics Letters* 45.6 (June 2019), pages 540–543. DOI: [10.1134/s1063785019060026](https://doi.org/10.1134/s1063785019060026).

- [Alz+14] S. Alzuaga, W. Daniau, R. Salut, T. Baron, S. Ballandras, and E. Defay. "Tunable and High Quality Factor SrTiO<sub>3</sub> Surface Acoustic Wave Resonator". In: *Applied Physics Letters* 105.6 (Aug. 2014), page 062901. DOI: 10.1063/1.4892659.
- [AR16] L. Ali and Z. Rahaman. *Variation of the Physical Properties of Four Transition Metal Oxides SrTMO<sub>3</sub> (TM = Rh, Ti, Mo, Zr) under Pressure: An ab-initio Study*. 2016. arXiv: 1607.02592 [cond-mat.mtrl-sci].
- [Arb97] J. W. Arblaster. "Crystallographic Properties of Platinum". In: *Platinum Metals Review* 41.1 (1997), pages 12–21.
- [Ass17] GSM Association. *5G, the Internet of Things (IoT) and Wearable Devices: What do the new uses of wireless technologies mean for radio frequency exposure?* 2017. URL: [https://www.gsma.com/latinamerica/wp-content/uploads/2019/04/5g\\_iot\\_web\\_FINAL.pdf](https://www.gsma.com/latinamerica/wp-content/uploads/2019/04/5g_iot_web_FINAL.pdf).
- [ATS05] K. F. Astafiev, A. K. Tagantsev, and N. Setter. "Quasi-Debye microwave loss as an intrinsic limitation of microwave performance of tunable components based on SrTiO<sub>3</sub> and Ba<sub>x</sub>Sr<sub>1-x</sub>TiO<sub>3</sub> ferroelectrics". In: *Journal of Applied Physics* 97.1 (Jan. 2005), page 014106. DOI: 10.1063/1.1829149.
- [BA02] Z.-G. Ban and S. P. Alpay. "Phase Diagrams and Dielectric Response of Epitaxial Barium Strontium Titanate Films: A Theoretical Analysis". In: *Journal of Applied Physics* 91.11 (June 2002), pages 9288–9296. DOI: 10.1063/1.1473675.
- [Ban+98] J. D. Baniecki, R. B. Laibowitz, T. M. Shaw, P. R. Duncombe, D. A. Neumayer, D. E. Kotecki, H. Shen, and Q. Y. Ma. "Dielectric relaxation of Ba<sub>0.7</sub>Sr<sub>0.3</sub>TiO<sub>3</sub> thin films from 1 mHz to 20 GHz". In: *Applied Physics Letters* 72.4 (Jan. 1998), pages 498–500. DOI: 10.1063/1.120796.
- [Bao+08] P. Bao, T. J. Jackson, X. Wang, and M. J. Lancaster. "Barium strontium titanate thin film varactors for room-temperature microwave device applications". In: *Journal of Physics D: Applied Physics* 41.6 (Feb. 2008), page 063001. DOI: 10.1088/0022-3727/41/6/063001.
- [BB13] W. H. Bragg and W. L. Bragg. "The reflection of X-rays by crystals". In: *Proceedings of the Royal Society of London. Series A, Containing Papers of a Mathematical and Physical Character* 88.605 (July 1, 1913), pages 428–438. DOI: 10.1098/rspa.1913.0040.

- [Ber+08] J. Berge, M. Norling, A. Vorobiev, and S. Gevorgian. “Field and temperature dependent parameters of the dc field induced resonances in  $\text{Ba}_x\text{Sr}_{1-x}\text{TiO}_3$ -based tunable thin film bulk acoustic resonators”. In: *Journal of Applied Physics* 103.6 (Mar. 2008), page 064508. DOI: 10.1063/1.2896585.
- [Bet69] K. Bethe. “Über das Mikrowellenverhalten nichtlinearer Dielektrika”. RWTH Aachen, 1969. URL: <https://publications.rwth-aachen.de/record/76972>.
- [Bou+02] H. Boubekeur, T. Mikolajick, W. Pamler, J. Höpfner, L. Frey, and H. Ryssel. “Platinum contamination issues in ferroelectric memories”. In: *Journal of Applied Physics* 92.6 (Sept. 2002), pages 3257–3265. DOI: 10.1063/1.1500414.
- [BT20] A. De Bonis and R. Teghil. “Ultra-Short Pulsed Laser Deposition of Oxides, Borides and Carbides of Transition Elements”. In: *Coatings* 10.5 (May 2020), page 501. DOI: 10.3390/coatings10050501.
- [Bub+04] D. M. Bubb, J. S. Horwitz, S. B. Qadri, S. W. Kirchoefer, C. Hubert, and J. Levy. “(Ba, Sr)TiO<sub>3</sub> thin films grown by pulsed laser deposition with low dielectric loss at microwave frequencies”. In: *Applied Physics A* 79.1 (June 2004), pages 99–101. DOI: 10.1007/s00339-003-2396-x.
- [BZ74] R. Blinc and B. Zeks. *Soft Modes in Ferroelectrics and Antiferroelectrics*. North-Holland Pub. Co., 1974. ISBN: 9780444105820.
- [CC73] G. J. Coombs and R. A. Cowley. “Paraelectric, piezoelectric and pyroelectric crystals: I. Dielectric properties”. In: *Journal of Physics C: Solid State Physics* 6.1 (Jan. 1973), pages 121–142. DOI: 10.1088/0022-3719/6/1/024.
- [CCY05] D. R. Chase, L.-Y. Chen, and R. A. York. “Modeling the capacitive nonlinearity in thin-film BST varactors”. In: *IEEE Transactions on Microwave Theory and Techniques* 53.10 (Oct. 2005), pages 3215–3220. DOI: 10.1109/tmtt.2005.855141.
- [Cha+17] A. Chaabani, A. Njeh, W. Donner, A. Klein, and M. H. B. Ghozlen. “Elasticity Study of Textured Barium Strontium Titanate Thin Films by X-Ray Diffraction and Laser Acoustic Waves”. In: *Japanese Journal of Applied Physics* 56.5 (Mar. 2017), page 055501. DOI: 10.7567/jjap.56.055501.

- [Che+07] L.-Y. V. Chen, R. Forse, A. H. Cardona, T. C. Watson, and R. York. "Compact Analog Phase Shifters using Thin-Film (Ba,Sr)TiO<sub>3</sub> Varactors". In: *IEEE/MTT-S International Microwave Symposium*. June 2007. DOI: [10.1109/mwsym.2007.380008](https://doi.org/10.1109/mwsym.2007.380008).
- [Cho+04] K. B. Chong, L. B. Kong, L. Chen, L. Yan, C. Y. Tan, T. Yang, C. K. Ong, and T. Osipowicz. "Improvement of dielectric loss tangent of Al<sub>2</sub>O<sub>3</sub> doped Ba<sub>0.5</sub>Sr<sub>0.5</sub>TiO<sub>3</sub> thin films for tunable microwave devices". In: *Journal of Applied Physics* 95.3 (Feb. 2004), pages 1416–1419. DOI: [10.1063/1.1638615](https://doi.org/10.1063/1.1638615).
- [CKP11] K. Chaudhary, B. K. Kaushik, and K. Pal. "Design of High Speed Optimized Flash ADC". In: *Computer Networks and Information Technologies*. Springer-Verlag GmbH, Mar. 7, 2011. ISBN: 978-3-642-19542-6.
- [CWD99] C.-H. Chen, S. D. Wu, and L. Dai. "Ordinal comparison of heuristic algorithms using stochastic optimization". In: *IEEE Transactions on Robotics and Automation* 15.1 (1999), pages 44–56. DOI: [10.1109/70.744601](https://doi.org/10.1109/70.744601).
- [Del+03] S. Delprat, M. Ouaddari, F. Vidal, M. Chaker, and K. Wu. "Voltage and frequency dependent dielectric properties of BST-0.5 thin films on alumina substrates". In: *IEEE Microwave and Wireless Components Letters* 13.6 (June 2003), pages 211–213. DOI: [10.1109/lmwc.2003.814091](https://doi.org/10.1109/lmwc.2003.814091).
- [Erk+00] E. G. Erker, A. S. Nagra, Y. Liu, P. Periaswamy, T. R. Taylor, J. Speck, and R. A. York. "Monolithic Ka-band phase shifter using voltage tunable BaSrTiO<sub>3</sub>/parallel plate capacitors". In: *IEEE Microwave and Guided Wave Letters* 10.1 (2000), pages 10–12. DOI: [10.1109/75.842071](https://doi.org/10.1109/75.842071).
- [FS16] C. R. Freeze and S. Stemmer. "Role of film stoichiometry and interface quality in the performance of (Ba,Sr)TiO<sub>3</sub> tunable capacitors with high figures of merit". In: *Applied Physics Letters* 109.19 (Nov. 2016), page 192904. DOI: [10.1063/1.4967374](https://doi.org/10.1063/1.4967374).
- [Fu14] J. Y. Fu. "On the theory of the universal dielectric relaxation". In: *Philosophical Magazine* 94.16 (Apr. 2014), pages 1788–1815. DOI: [10.1080/14786435.2014.897037](https://doi.org/10.1080/14786435.2014.897037).
- [Fuk+96] Y. Fukuda, K. Numata, K. Aoki, and A. Nishimura. "Origin of Dielectric Relaxation Observed for Ba<sub>0.5</sub>Sr<sub>0.5</sub>TiO<sub>3</sub> Thin-Film Capacitor". In: *Japanese Journal of Applied Physics* 35.Part 1, No. 9B (Sept. 1996), pages 5178–5180. DOI: [10.1143/jjap.35.5178](https://doi.org/10.1143/jjap.35.5178).
- [Gar90] B. M. Garin. "One-phonon dielectric losses by excitation of sound". In: *Sov. Phys. Solid State* 32.11 (Nov. 1990), pages 1917–1920.

- [Gev+09] S. Gevorgian, A. Deleniv, A. Vorobiev, H. Jacobsson, and T. Lewin. "CAD oriented frequency, temperature, and DC bias dependent small-signal, scalable circuit model of parallel-plate paraelectric varactors". In: *International Journal of RF and Microwave Computer-Aided Engineering* 19.2 (Mar. 2009), pages 243–257. DOI: 10.1002/mmce.20345.
- [Gie09] A. Giere. "Material- und Bauteiloptimierung steuerbarer Mikrowellenkomponenten mit nichtlinearen Ferroelektrika". PhD thesis. Technical University of Darmstadt, 2009.
- [Gou+18] J. P. Goud, M. S. Alkathy, K. Sandeep, S. Ramakanth, and K. C. J. Raju. "Influence of laser fluence on structural, optical and microwave dielectric properties of pulsed laser deposited Ba<sub>0.6</sub>Sr<sub>0.4</sub>TiO<sub>3</sub> thin films". In: *Journal of Materials Science: Materials in Electronics* 29.18 (July 2018), pages 15973–15982. DOI: 10.1007/s10854-018-9683-y.
- [Gra13] Eugene Grayver. *Implementing Software Defined Radio*. Springer New York, 2013. DOI: 10.1007/978-1-4419-9332-8.
- [Gro09] F. W. Grover. *Inductance Calculations*. Dover Publications Inc., Oct. 22, 2009. 304 pages. ISBN: 9780486474403.
- [GS03] J. I. Gersten and F. W. Smith. *The physics and chemistry of materials*. Wiley, 2003. DOI: 10.1021/ed080p387.2.
- [GT86] V. L. Gurevich and A. K. Tagantsev. "Intrinsic Dielectric Losses in Crystals - Low-Temperatures". In: *Zhurnal Eksperimentalnoi I Teoreticheskoi Fiziki* 91.1 (1986), pages 245–261.
- [GT91] V. L. Gurevich and A. K. Tagantsev. "Intrinsic dielectric loss in crystals". In: *Advances in Physics* 40.6 (Dec. 1991), pages 719–767. DOI: 10.1080/00018739100101552.
- [GTV13] S. S. Gevorgian, A. K. Tagantsev, and A. K. Vorobiev. *Tunable Film Bulk Acoustic Wave Resonators*. Springer London, 2013. DOI: 10.1007/978-1-4471-4944-6.
- [GVL06] S. Gevorgian, A. Vorobiev, and T. Lewin. "DC Field and Temperature Dependent Acoustic Resonances in Parallel-Plate Capacitors Based on SrTiO<sub>3</sub> and Ba<sub>0.25</sub>Sr<sub>0.75</sub>TiO<sub>3</sub> Films: Experiment and Modeling". In: *Journal of Applied Physics* 99.12 (June 2006), page 124112. DOI: 10.1063/1.2209727.
- [Has+05] R. Hassan, B. Cohan, O. de Weck, and G. Venter. "A Comparison of Particle Swarm Optimization and the Genetic Algorithm". In: *AIAA/ASME/ASCE/AHS/ASC Structures, Structural Dynamics and Materials Conference*. Apr. 2005. DOI: 10.2514/6.2005-1897.

- [Hei93] W. Heinrich. "Quasi-TEM description of MMIC coplanar lines including conductor-loss effects". In: *IEEE Transactions on Microwave Theory and Techniques* 41.1 (1993), pages 45–52. DOI: 10.1109/22.210228.
- [Hor+95] T. Horikawa, T. Makita, T. Kuroiwa, and N. Mikami. "Dielectric Relaxation of (Ba, Sr)TiO<sub>3</sub> Thin Films". In: *Japanese Journal of Applied Physics* 34.9B (1995).
- [Ina08] K. Inaba. "X-ray thin-film measurement techniques". In: *The Rigaku Journal* 24 (2008).
- [Inc18] Skyworks Inc. "White Paper: 5G New Radio Solutions: Revolutionary Applications Here Sooner Than You Think". 2018.
- [Ito+16] M. Ito, M. Uchida, Y. Kozuka, K. S. Takahashi, and M. Kawasaki. "Effective carrier doping and metallization in LaxSr<sub>2-x-y</sub>BayIrO<sub>4-δ</sub> thin films". In: *Physical Review B* 93.4 (Jan. 2016). DOI: 10.1103/physrevb.93.045139.
- [Ivi+08] B. Ivira, A. Reinhardt, E. Defay, and M. Aid. "Integration of Electrostrictive Ba<sub>0.7</sub>Sr<sub>0.3</sub>TiO<sub>3</sub> Thin Films into Bulk Acoustic Wave Resonator for RF-Frequency Tuning under DC Bias". In: *IEEE International Frequency Control Symposium*. May 2008. DOI: 10.1109/freq.2008.4623000.
- [Jac75] John Jackson. *Classical electrodynamics*. New York: Wiley, 1975. ISBN: 9780471431329.
- [Jaf58] H. Jaffe. "Piezoelectric Ceramics". In: *Journal of the American Ceramic Society* 41.11 (Nov. 1958), pages 494–498. DOI: 10.1111/j.1151-2916.1958.tb12903.x.
- [Jeo04] J.-H. Jeon. "Effect of SrTiO<sub>3</sub> concentration and sintering temperature on microstructure and dielectric constant of Ba<sub>1-x</sub>Sr<sub>x</sub>TiO<sub>3</sub>". In: *Journal of the European Ceramic Society* 24.6 (Jan. 2004), pages 1045–1048. DOI: 10.1016/s0955-2219(03)00385-6.
- [Jon83] A. K. Jonscher. *Dielectric relaxation in solids*. Chelsea Dielectrics Press, 1983. ISBN: 978-0950871103.
- [JPH05] D. S. Jeong, H. B. Park, and C. S. Hwang. "Reasons for obtaining an optical dielectric constant from the Poole–Frenkel conduction behavior of atomic-layer-deposited HfO<sub>2</sub> films". In: *Applied Physics Letters* 86.7 (2005), page 072903. DOI: 10.1063/1.1865326.
- [Kao04] K. C. Kao. "Electric Polarization and Relaxation". In: *Dielectric Phenomena in Solids*. Elsevier, 2004, pages 41–114. DOI: 10.1016/b978-012396561-5/50012-8.

- [Kas+73] S. Kashida, I. Hatta, A. Ikushima, and Y. Yamada. "Ultrasonic Velocities in BaTiO<sub>3</sub>". In: *Journal of the Physical Society of Japan* 34.4 (Apr. 1973), pages 997–1001. DOI: 10.1143/jpsj.34.997.
- [KDO07] A. Kletsov, Y. Dahnovsky, and J. V. Ortiz. "Surface Green's function calculations: A nonrecursive scheme with an infinite number of principal layers". In: *The Journal of Chemical Physics* 126.13 (Apr. 2007), page 134105. DOI: 10.1063/1.2713743.
- [Kie19] D. Kienemund. "High-Power Varactors for Fast Adaptive Impedance Matching at 13.56 MHz". PhD thesis. Technical University of Darmstadt, July 9, 2019.
- [Kim+00] W. J. Kim, W. Chang, S. B. Qadri, J. M. Pond, S. W. Kirchoefer, D. B. Chrisey, and J. S. Horwitz. "Microwave properties of tetragonally distorted (Ba<sub>0.5</sub>Sr<sub>0.5</sub>)TiO<sub>3</sub> thin films". In: *Applied Physics Letters* 76.9 (Feb. 2000), pages 1185–1187. DOI: 10.1063/1.125977.
- [Kim+02] D. Kim, Y. Choi, M. G. Allen, J. S. Kenney, and D. Kiesling. "A wide-band reflection-type phase shifter at S-band using BST coated substrate". In: *IEEE Transactions on Microwave Theory and Techniques* 50.12 (Dec. 2002), pages 2903–2909. DOI: 10.1109/tmtt.2002.805293.
- [Kim+04] D. Kim, S.-S. Je, J. S. Kenney, and P. Marry. "Design of ferroelectric phase shifters for minimum performance variation over temperature". In: *IEEE MTT-S International Microwave Symposium Digest (IEEE Cat. No.04CH37535)*. 2004. DOI: 10.1109/mwsym.2004.1335861.
- [Kit05] C. Kittel. *Introduction to Solid State Physics*. 8th edition. John Wiley & Sons, 2005. ISBN: 0-471-68057-5.
- [KNS08] B. Kaltenbacher, A. Neubauer, and O. Scherzer. *Iterative Regularization Methods for Nonlinear Ill-Posed Problems*. Walter de Gruyter, Jan. 2008. DOI: 10.1515/9783110208276.
- [Kos+12] G. Koster, L. Klein, W. Siemons, G. Rijnders, J. S. Dodge, C.-B. Eom, D. H. A. Blank, and M. R. Beasley. "Structure, physical properties, and applications of SrRuO<sub>3</sub> thin films". In: *Reviews of Modern Physics* 84.1 (Mar. 2012), pages 253–298. DOI: 10.1103/revmodphys.84.253.
- [Koz+12] Y. Kozuka, H. Seki, T. C. Fujita, S. Chakraverty, K. Yoshimatsu, H. Kumigashira, M. Oshima, M. S. Bahramy, R. Arita, and M. Kawasaki. "Epitaxially Stabilized EuMoO<sub>3</sub>: A New Itinerant Ferromagnet". In: *Chemistry of Materials* 24.19 (2012), pages 3746–3750. DOI: 10.1021/cm302231k.

- [Lee+03] Y. S. Lee, J. S. Lee, T. W. Noh, D. Y. Byun, K. S. Yoo, K. Yamaura, and E. Takayama-Muromachi. "Systematic trends in the electronic structure parameters of the 4d transition-metal oxides SrMO<sub>3</sub> (M=Zr, Mo, Ru, and Rh)". In: *Physical Review B* 67.11 (Mar. 2003). DOI: 10.1103/physrevb.67.113101.
- [Lew09] R. A. Lewis. "A terahertz system of units". In: *International Conference on Infrared, Millimeter, and Terahertz Waves*. Sept. 2009. DOI: 10.1109/icimw.2009.5324759.
- [Lin+05] G. Linker, R. Smithey, J. Geerk, F. Ratzel, R. Schneider, and A. Zaitsev. "The growth of ultra-thin epitaxial CeO<sub>2</sub> films on r-plane sapphire". In: *Thin Solid Films* 471.1-2 (Jan. 2005), pages 320–327. DOI: 10.1016/j.tsf.2004.05.126.
- [Liu+00] Y. Liu, A. S. Nagra, E. G. Erker, P. Periaswamy, T. R. Taylor, J. Speck, and R. A. York. "BaSrTiO<sub>3</sub> / interdigitated capacitors for distributed phase shifter applications". In: *IEEE Microwave and Guided Wave Letters* 10.11 (2000), pages 448–450. DOI: 10.1109/75.888828.
- [Liu+15] G. Liu, S. Zhang, W. Jiang, and W. Cao. "Losses in ferroelectric materials". In: *Materials Science and Engineering: R: Reports* 89 (Mar. 2015), pages 1–48. DOI: 10.1016/j.mser.2015.01.002.
- [LKM93] K. M. Lakin, G. R. Kline, and K. T. McCarron. "High-Q microwave acoustic resonators and filters". In: *IEEE Transactions on Microwave Theory and Techniques* 41.12 (1993), pages 2139–2146. DOI: 10.1109/22.260698.
- [LLK90] H. Ledbetter, M. Lei, and S. Kim. "Elastic constants, Debye temperatures, and electron-phonon parameters of superconducting cuprates and related oxides". In: *Phase Transitions* 23.1 (July 1990), pages 61–70. DOI: 10.1080/01411599008241819.
- [Ma+14] L.-Q. Ma, F.-Y. Meng, X.-X. Liu, and P.-Y. Wang. "An S-band left-handed tunable phase shifter based on BST thin film". In: *Proceedings of 2014 3rd Asia-Pacific Conference on Antennas and Propagation*. 2014. DOI: 10.1109/apcap.2014.6992784.
- [Ma+98] Z. Ma, A. J. Becker, P. Polakos, H. Huggins, J. Pastalan, H. Wu, K. Watts, Y. H. Wong, and P. Mankiewich. "RF measurement technique for characterizing thin dielectric films". In: *IEEE Transactions on Electron Devices* 45.8 (1998), pages 1811–1816. DOI: 10.1109/16.704383.
- [Mar64] H.-J. Martin. *Die Ferroelektrika*. Leipzig : Geest & Portig, 1964.

- [Mas50] W. P. Mason. *Piezoelectric Crystals and Their Application to Ultrasonics*. Bell Telephone Laboratories series. Van Nostrand, 1950. DOI: 10.1063/1.3067231.
- [Mau11] H. Maune. "Design und Optimierung hochlinearer ferroelektrischer Varaktoren für steuerbare Hochfrequenz-Leistungsverstärker". PhD thesis. Technical University of Darmstadt, Sept. 27, 2011.
- [Mau20] H. Maune. "Reconfigurable Microwave Systems based on Functional Materials". Postdoctoral Thesis. May 12, 2020. DOI: 10.25534/TUDATALIB-98.
- [Men+11] W. Meneskou, F. Paul, X. Zhou, H. Elsenheimer, J. R. Binder, and E. Ivers-Tiffée. "Nonlinear ceramics for tunable microwave devices part I: materials properties and processing". In: *Microsystem Technologies* 17.2 (Feb. 2011), pages 203–211. DOI: 10.1007/s00542-011-1277-z.
- [Mer+17] D. Mercier, A. Niembro-Martin, H. Sibuet, C. Baret, J. Chautagnat, C. Dieppedale, C. Bonnard, J. Guillaume, G. Le Rhun, C. Billard, P. Gardes, and P. Poveda. "X band distributed phase shifter based on sol-gel BCTZ varactors". In: *European Microwave Conference (EuMC)*. Oct. 2017. DOI: 10.23919/eumc.2017.8231072.
- [Mey+16a] C. J. G. Meyers, C. R. Freeze, S. Stemmer, and R. A. York. "(Ba,Sr)TiO<sub>3</sub> tunable capacitors with RF commutation quality factors exceeding 6000". In: *Applied Physics Letters* 109.11 (Sept. 2016), page 112902. DOI: 10.1063/1.4961626.
- [Mey+16b] C. J. G. Meyers, C. Freeze, S. Stemmer, X. Lan, L. Chau, and R. A. York. "Two-port tunable interdigital capacitors fabricated on low-loss MBE-grown Ba<sub>0.29</sub>Sr<sub>0.71</sub>TiO<sub>3</sub>". In: *IEEE MTT-S International Microwave Symposium (IMS)*. May 2016. DOI: 10.1109/mwsym.2016.7540112.
- [Mey+17] C. J. G. Meyers, C. R. Freeze, S. Stemmer, and R. A. York. "Effect of BST film thickness on the performance of tunable interdigital capacitors grown by MBE". In: *Applied Physics Letters* 111.26 (Dec. 2017), page 262903. DOI: 10.1063/1.5004566.
- [Mik+12] E. Mikheev, A. P. Kajdos, A. J. Hauser, and S. Stemmer. "Electric field-tunable BaxSr<sub>1-x</sub>TiO<sub>3</sub> films with high figures of merit grown by molecular beam epitaxy". In: *Applied Physics Letters* 101.25 (Dec. 2012), page 252906. DOI: 10.1063/1.4773034.
- [Mit95] J. Mitola. "The software radio architecture". In: *IEEE Communications Magazine* 33.5 (May 1995), pages 26–38. DOI: 10.1109/35.393001.

- [Miz+00] H. Mizoguchi, N. Kitamura, K. Fukumi, T. Mihara, J. Nishii, M. Nakamura, N. Kikuchi, H. Hosono, and H. Kawazoe. “Optical properties of  $\text{SrMoO}_3$  thin film”. In: *Journal of Applied Physics* 87.9 (May 2000), pages 4617–4619. DOI: [10.1063/1.373111](https://doi.org/10.1063/1.373111).
- [MMK85] G. Mader, H. Meixner, and P. Kleinschmidt. “Temperature and stress dependence of Young’s modulus in semiconducting barium titanate ceramics”. In: *Journal of Applied Physics* 58.2 (July 1985), pages 702–704. DOI: [10.1063/1.336185](https://doi.org/10.1063/1.336185).
- [Mor+18] R. M. Morais, M. S. Klem, M. S. Ozório, T. C. Gomes, and N. Alves. “Roughness influence on the sheet resistance of the PEDOT:PSS printed on paper”. In: *Current Applied Physics* 18.2 (Feb. 2018), pages 254–260. DOI: [10.1016/j.cap.2017.11.008](https://doi.org/10.1016/j.cap.2017.11.008).
- [Mot36] N. F. Mott. “The electrical conductivity of transition metals”. In: *Proceedings of the Royal Society of London. Series A - Mathematical and Physical Sciences* 153.880 (Feb. 1936), pages 699–717. DOI: [10.1098/rspa.1936.0031](https://doi.org/10.1098/rspa.1936.0031).
- [Nad+15] K. Nadaud, C. Borderon, R. Renoud, and H. W. Gundel. “Effect of manganese doping of  $\text{BaSrTiO}_3$  on diffusion and domain wall pinning”. In: *Journal of Applied Physics* 117.8 (Feb. 2015), page 084104. DOI: [10.1063/1.4913694](https://doi.org/10.1063/1.4913694).
- [Nag+05] I. Nagai, N. Shirakawa, S.-I. Ikeda, R. Iwasaki, H. Nishimura, and M. Kosaka. “Highest conductivity oxide  $\text{SrMoO}_3$  grown by a floating-zone method under ultralow oxygen partial pressure”. In: *Applied Physics Letters* 87.2 (July 2005), page 024105. DOI: [10.1063/1.1992671](https://doi.org/10.1063/1.1992671).
- [NHM72] R. Neville, B. Hoeneisen, and C. A. Mead. “Anomalous resonance of strontium titanate”. In: *Journal of Applied Physics* 43.10 (Oct. 1972), pages 3903–3905. DOI: [10.1063/1.1660845](https://doi.org/10.1063/1.1660845).
- [Nik+14] M. Nikfalazar, C. Kohler, A. Friederich, M. Sazegar, Y. Zheng, A. Wiens, J. R. Binder, and R. Jakoby. “Fully printed tunable phase shifter for L/S-band phased array application”. In: *IEEE MTT-S International Microwave Symposium*. IEEE, June 2014. DOI: [10.1109/mwsym.2014.6848295](https://doi.org/10.1109/mwsym.2014.6848295).
- [Nik+15] M. Nikfalazar, A. Mehmood, M. Sohrabi, A. Wiens, Y. Zheng, H. Maune, R. Jakoby, M. Mikolajek, A. Friederich, C. Kohler, and J. R. Binder. “Low bias voltage tunable phase shifter based on inkjet-printed BST MIM varactors for C/X-band phased arrays”. In: *European Mi-*

- crowave Integrated Circuits Conference (EuMIC)*. IEEE, Sept. 2015. DOI: 10.1109/eumic.2015.7345157.
- [Nin+06] N. Ning, X. P. Li, J. Fan, W. C. Ng, Y. P. Xu, X. Qian, and H. L. Seet. “A tunable magnetic inductor”. In: *IEEE Transactions on Magnetics* 42 (June 24, 2006), pages 1585–1590. DOI: 10.1109/TMAG.2006.870651.
- [Noe+07] A. Noeth, T. Yamada, V. Sherman, P. Muralt, A. Tagantsev, and N. Setter. “DC Bias-Dependent Shift of the Resonance Frequencies in BST Thin-Film Membranes”. In: *IEEE Transactions on Ultrasonics, Ferroelectrics and Frequency Control* 54.12 (Dec. 2007), pages 2487–2492. DOI: 10.1109/tuffc.2007.565.
- [Nor04] D. P. Norton. “Synthesis and properties of epitaxial electronic oxide thin-film materials”. In: *Materials Science and Engineering: R: Reports* 43.5-6 (Mar. 2004), pages 139–247. DOI: 10.1016/j.mser.2003.12.002.
- [Oua+05] M. Ouaddari, S. Delprat, F. Vidal, M. Chaker, and K. Wu. “Microwave characterization of ferroelectric thin-film materials”. In: *IEEE Transactions on Microwave Theory and Techniques* 53.4 (Apr. 2005), pages 1390–1397. DOI: 10.1109/tmtt.2005.845759.
- [Par+06] J. Park, J. W. Lu, D. S. Boesch, S. Stemmer, and R. A. York. “Distributed phase shifter with pyrochlore bismuth zinc niobate thin films”. In: *IEEE Microwave and Wireless Components Letters* 16.5 (May 2006), pages 264–266. DOI: 10.1109/lmwc.2006.873528.
- [Pes+08] K. A. Pestka, J. D. Maynard, A. Soukiassian, X. X. Xi, D. G. Schlom, Y. Le Page, M. Bernhagen, P. Reiche, and R. Uecker. “Experimental Measurement of the Elastic Constants of  $\text{GdScO}_3$  via Resonant Ultrasound Spectroscopy Utilizing ab-initio Calculations”. In: *Applied Physics Letters* 92.11 (Mar. 2008), page 111915. DOI: 10.1063/1.2901881.
- [PLC19] Omdia (Informa PLC). “White paper: In 5G smartphone designs, RF Front-End graduates from traditional supporting role to co-star with modem”. Aug. 28, 2019.
- [Pop+78] J. M. Poplavko, A. S. Knjazev, V. G. Tsykalov, and L. P. Pereverzeva. “Temperature dependence of soft mode frequency and its damping in various ferroelectrics”. In: *Ferroelectrics* 21.1 (Jan. 1978), pages 399–401. DOI: 10.1080/00150197808237277.
- [Poz11] D. M. Pozar. *Microwave Engineering*. John Wiley & Sons Inc, Nov. 4, 2011. 752 pages. ISBN: 9780470631553.

---

## Bibliography

- [Pre+17] Sebastian Preis, Daniel Kienemund, Nikolai Wolff, Holger Maune, Rolf Jakoby, Wolfgang Heinrich, and Olof Bengtsson. "Thick-film MIM BST varactors for GaN power amplifiers with discrete dynamic load modulation". In: *IEEE MTT-S International Microwave Symposium (IMS)*. June 2017. DOI: 10.1109/mwsym.2017.8059097.
- [Qua20] Inc. Qualcomm Technologies. *Global update on spectrum for 4G & 5G*. 2020. URL: <https://www.qualcomm.com/media/documents/files/spectrum-for-4g-and-5g.pdf>.
- [Rad+14] A. Radetinac, A. Mani, S. Melnyk, M. Nikfalazar, J. Ziegler, Y. Zheng, R. Jakoby, L. Alff, and P. Komissinskiy. "Highly conducting SrMoO<sub>3</sub> thin films for microwave applications". In: *Applied Physics Letters* 105.11 (Sept. 2014), page 114108. DOI: 10.1063/1.4896339.
- [Rad17] A. Radetinac. "Hochleitfähiges SrMoO<sub>3</sub>: Vom Schichtwachstum zur Anwendungseignung". PhD thesis. Technical University of Darmstadt, 2017.
- [RC99] J. Robertson and C. W. Chen. "Schottky barrier heights of tantalum oxide, barium strontium titanate, lead titanate, and strontium bismuth tantalate". In: *Applied Physics Letters* 74.8 (Feb. 1999), pages 1168–1170. DOI: 10.1063/1.123476.
- [Res16] Inc. Resonant. "White Paper: RF Innovation and the Transition to 5G Wireless Technology". Oct. 20, 2016.
- [Res20] ABI Research. "White Paper: 5G Teardowns Reveal Qualcomm's RF Leadership Due To Growing Design Complexity". 2020.
- [RG17] E. B. Rosa and F. W. Grover. *Formulas and Tables for the Calculation of Mutual and Self-Inductance*. Volume 8. 1. Feb. 7, 2017. ISBN: 978-1334016967.
- [RI15] S. J. Rupitsch and J. Ilg. "Complete Characterization of Piezoceramic Materials by Means of Two Block-Shaped Test Samples". In: *IEEE Transactions on Ultrasonics, Ferroelectrics, and Frequency Control* 62.7 (July 2015), pages 1403–1413. DOI: 10.1109/tuffc.2015.006997.
- [Sal20] P. Salg. "Interfaces in all-oxide thin-film varactors with highly-conducting SrMoO<sub>3</sub> electrodes for microwave applications". PhD thesis. Technical University of Darmstadt, Oct. 14, 2020. DOI: 10.25534/TUPRINTS-00013239.
- [Saz+11] M. Sazegar, A. Mehmood, Y. Zheng, H. Maune, X. Zhou, J. Binder, and R. Jakoby. "Compact tunable loaded line phase shifter based on screen printed BST thick film". In: *2011 German Microwave Conference*. 2011.

- [SC12] N. Setter and E. L. Colla. *Ferroelectric Ceramics: Tutorial reviews, theory, processing, and applications (Monte Verita)*. Birkhaeuser, 2012. ISBN: 9783034875516.
- [Sch+08] R. Schafranek, S. Payan, M. Maglione, and A. Klein. "Barrier height at (Ba,Sr)TiO<sub>3</sub>/Pt interfaces studied by photoemission". In: *Physical Review B* 77.19 (May 2008). DOI: 10.1103/physrevb.77.195310.
- [Sch07] R. Schaefer. *Foundations of Global Genetic Optimization*. Springer-Verlag GmbH, July 7, 2007. ISBN: 9783540731924.
- [Sch08] M. Schmidt. "Abstimmbare Anpassnetzwerke auf Basis ferroelektrischer Varaktoren für Mobilfunkanwendungen". PhD thesis. Friedrich-Alexander-Universität Erlangen-Nürnberg (FAU), 2008.
- [Sch44] W. G. Schlecht. "Calculation of density from x-ray data". In: *American Mineralogist* 29.3-4 (1944), pages 108–110.
- [She+10] S. Sheng, X.-Y. Zhang, P. Wang, and C. K. Ong. "Effect of bottom electrodes on dielectric properties of high frequency Ba<sub>0.5</sub>Sr<sub>0.5</sub>TiO<sub>3</sub> parallel plate varactor". In: *Thin Solid Films* 518.10 (Mar. 2010), pages 2864–2866. DOI: 10.1016/j.tsf.2009.09.063.
- [Sim13] D. Simon. *Evolutionary Optimization Algorithms*. John Wiley & Sons, June 13, 2013. 784 pages. ISBN: 9781118659502.
- [Sim67] J. G. Simmons. "Poole-Frenkel Effect and Schottky Effect in Metal-Insulator-Metal Systems". In: *Physical Review* 155.3 (Mar. 1967), pages 657–660. DOI: 10.1103/physrev.155.657.
- [Sin93] M. Sinclair. "Comparison of the performance of modern heuristics for combinatorial optimization on real data". In: *Computers & Operations Research* 20.7 (Sept. 1993), pages 687–695. DOI: 10.1016/0305-0548(93)90056-o.
- [Smi+03] R. C. Smith, S. Seelecke, Z. Ounaies, and J. Smith. "A Free Energy Model for Hysteresis in Ferroelectric Materials". In: *Journal of Intelligent Material Systems and Structures* 14.11 (Nov. 2003), pages 719–739. DOI: 10.1177/1045389x03038841.
- [Smi+08] M. B. Smith, K. Page, T. Siegrist, P. L. Redmond, E. C. Walter, R. Se-shadri, L. E. Brus, and M. L. Steigerwald. "Crystal Structure and the Paraelectric-to-Ferroelectric Phase Transition of Nanoscale BaTiO<sub>3</sub>". In: *Journal of the American Chemical Society* 130.22 (June 2008), pages 6955–6963. DOI: 10.1021/ja0758436.

- [Sub+13] G. Subramanyam, M. W. Cole, N. X. Sun, T. S. Kalkur, N. M. Sbrockey, G. S. Tompa, X. Guo, C. Chen, S. P. Alpay, G. A. Rossetti, K. Dayal, L.-Q. Chen, and D. G. Schlom. "Challenges and opportunities for multi-functional oxide thin films for voltage tunable radio frequency / microwave components". In: *Journal of Applied Physics* 114.19 (Nov. 2013), page 191301. DOI: 10.1063/1.4827019.
- [Tag+03] A. K. Tagantsev, V. O. Sherman, T. F. Astafiev, J. Venkatesh, and N. Setter. "Ferroelectric Materials for Microwave Tunable Applications". In: *Journal of Electroceramics* 11 (1-2 2003), pages 5–66. DOI: 10.1023/B: JECR.0000015661.81386.e6.
- [Tag79] A. K. Tagantsev. "Effect of a weak electric field on the dielectric losses in centrosymmetric ferroelectrics of the displacement type". In: *Journal of Experimental and Theoretical Physics* 50 (Nov. 1979), page 948.
- [Tag81] A. K. Tagantsev. "Low-frequency dielectric relaxation in centrosymmetric crystals". In: *Journal of Experimental and Theoretical Physics* (1981).
- [Tak00] H. Takasu. "The Ferroelectric Memory and its Applications". In: *Journal of Electroceramics* 4.2/3 (2000), pages 327–338. DOI: 10.1023/a:1009910525462.
- [Tel21] Telefonaktiebolaget LM Ericsson. *Ericsson Mobility Report November 2020*. Jan. 6, 2021. URL: <https://www.ericsson.com/en/mobility-report>.
- [Tom+02] A. Tombak, J.-P. Maria, F. Ayguavives, Z. Jin, G. T. Stauf, A. I. Kingon, and A. Mortazawi. "Tunable barium strontium titanate thin film capacitors for RF and microwave applications". In: *IEEE Microwave and Wireless Components Letters* 12.1 (Jan. 2002), pages 3–5. DOI: 10.1109/7260.975716.
- [TPS93] A. K. Tagantsev, J. Petzelt, and N. Setter. "Relation between intrinsic microwave and submillimeter losses and permitivity in dielectrics". In: *Solid State Communications* 87.12 (Sept. 1993), pages 1117–1120. DOI: 10.1016/0038-1098(93)90812-2.
- [Uch10] K. Uchino. *Ferroelectric Devices*. New York: CRC Press, 2010. DOI: 10.1201/b15852-11.
- [Urb+20] Maciej Urbanski, Bartłomiej Kola, Krzysztof Czuba, Heinrich Pryszecki, and Frank Ludwig. "Voltage Driven Phase Shifters for Phase Reference Distribution System in SINBAD". In: *International Microwave and Radar Conference (MIKON)*. IEEE, Oct. 2020. DOI: 10.23919/mikon48703.2020.9253786.

- [Ven+08] I. B. Vendik, P. A. Turalchuk, O. G. Vendik, and J. Berge. "Modeling Tunable Bulk Acoustic Resonators Based on Induced Piezoelectric Effect in BaTiO<sub>3</sub> and Ba<sub>0.25</sub>Sr<sub>0.75</sub>TiO<sub>3</sub> Films". In: *Journal of Applied Physics* 103.1 (Jan. 2008), page 014107. DOI: 10.1063/1.2830866.
- [Ven+77] O. G. Vendik, A. Y. Zaionchkovskii, V. V. Konovalenko, A. S. Ruban, T. B. Samoilova., and D. V. Shpanskii. "Central Peak in the Spectrum of Fluctuations of the Ferroelectric Mode and Dielectric Losses in SrTiO<sub>3</sub> at 4.2 K". In: *Sov. Phys. Solid State* 19.5 (May 1977).
- [Ven+99] O. G. Vendik, E. K. Hollmann, A. B. Kozyrev, and A. M. Prudan. "Ferroelectric Tuning of Planar and Bulk Microwave Devices". In: *Journal of Superconductivity* 12.2 (1999), pages 325–338. DOI: 10.1023/a:1007797131173.
- [Vid+12] S. Vidya, A. John, S. Solomon, and J. K. Thomas. "Optical and dielectric properties of SrMoO<sub>4</sub> powders prepared by the combustion synthesis method". In: *Advances in materials Research* 1.3 (Sept. 2012), pages 191–204. DOI: 10.12989/amr.2012.1.3.191.
- [Vol+08] A. Volatier, E. Defaÿ, M. Aïd, A. N'hari, P. Ancey, and B. Dubus. "Switchable and Tunable Strontium Titanate Electrostrictive Bulk Acoustic Wave Resonator Integrated with a Bragg Mirror". In: *Applied Physics Letters* 92.3 (Jan. 2008), page 032906. DOI: 10.1063/1.2837616.
- [Vor+03] A. Vorobiev, P. Rundqvist, K. Khamchane, and S. Gevorgian. "Silicon substrate integrated high Q-factor parallel-plate ferroelectric varactors for microwave/millimeterwave applications". In: *Applied Physics Letters* 83.15 (Oct. 2003), pages 3144–3146. DOI: 10.1063/1.1619213.
- [Vor+04] A. Vorobiev, P. Rundqvist, K. Khamchane, and S. Gevorgian. "Microwave loss mechanisms in Ba<sub>0.25</sub>Sr<sub>0.75</sub>TiO<sub>3</sub> thin film varactors". In: *Journal of Applied Physics* 96.8 (Oct. 2004), pages 4642–4649. DOI: 10.1063/1.1789631.
- [VP71] O. G. Vendik and L. M. Platonova. "Effects of Charged Lattice Imperfections on the Dielectric Properties of Materials". In: *Sov. Phys. Solid State* 13 (1971), pages 1353–1359.
- [VTZ98] O. G. Vendik, L. T. Ter-Martirosyan, and S. P. Zubko. "Microwave losses in incipient ferroelectrics as functions of the temperature and the biasing field". In: *Journal of Applied Physics* 84.2 (July 1998), pages 993–998. DOI: 10.1063/1.368166.

- [VV07] O. Vendik and I. Vendik. "Electromechanical Coupling Coefficient of Isotropic Sample with a Marked Electrostriction". In: *Journal of the European Ceramic Society* 27.8-9 (Jan. 2007), pages 2949–2952. DOI: 10.1016/j.jeurceramsoc.2006.11.068.
- [VVK00] I. B. Vendik, O. G. Vendik, and E. L. Kollberg. "Commutation quality factor of two-state switchable devices". In: *IEEE Transactions on Microwave Theory and Techniques* 48.5 (May 2000), pages 802–808. DOI: 10.1109/22.841874.
- [VZ00] O. G. Vendik and S. P. Zubko. "Ferroelectric phase transition and maximum dielectric permittivity of displacement type ferroelectrics ( $\text{Ba}_x\text{Sr}_{1-x}\text{TiO}_3$ )". In: *Journal of Applied Physics* 88.9 (Nov. 2000), pages 5343–5350. DOI: 10.1063/1.1317243.
- [VZ97] O. G. Vendik and S. P. Zubko. "Modeling the dielectric response of incipient ferroelectrics". In: *Journal of Applied Physics* 82.9 (Nov. 1997), pages 4475–4483. DOI: 10.1063/1.366180.
- [VZN02] O. G. Vendik, S. P. Zubko, and M. A. Nikol'ski. "Microwave loss-factor of  $\text{Ba}_x\text{Sr}_{1-x}\text{TiO}_3$  as a function of temperature, biasing field, barium concentration, and frequency". In: *Journal of Applied Physics* 92.12 (Dec. 2002), pages 7448–7452. DOI: 10.1063/1.1524314.
- [Wal08] R. H. Walden. *Analog-to-Digital Conversion in the Early Twenty-First Century*. In: *Wiley Encyclopedia of Computer Science and Engineering*. American Cancer Society, 2008, pages 1–14. DOI: 10.1002/9780470050118.ecse014.
- [Was05] R. Waser. *Nanoelectronics and Information Technology*. corr. ed. Volume 2. Wiley-VCH, 2005. ISBN: 9783527405428.
- [Was95] R. Waser. *Science and Technology of Electroceramic Thin Films*. Kluwer Academic Publishers, 1995. ISBN: 0792333322.
- [Wei+13] C. Weickmann, R. Jakoby, E. Constable, and R. A. Lewis. "Time-domain spectroscopy of novel nematic liquid crystals in the terahertz range". In: *International Conference on Infrared, Millimeter, and Terahertz Waves (IRMMW-THz)*. Sept. 2013. DOI: 10.1109/irmmw-thz.2013.6665423.
- [Wei03] C. Weil. "Passiv steuerbare Mikrowellenphasenschieber auf der Basis nichtlinearer Dielektrika". PhD thesis. Technical University of Darmstadt, 2003.

---

## Bibliography

- [Wei17] C. Weickmann. "Liquid Crystals Towards Terahertz: Characterisation and Tunable Waveguide Phase Shifters for Millimetre-Wave and Terahertz Beamsteering Antennas". PhD thesis. Technical University of Darmstadt, 2017.
- [Wie17] A. Wiens. "Tunable Ferroelectric Matching Networks implemented into High Power RF Amplifiers for High Dynamic and Wideband Efficiency". PhD thesis. Technical University of Darmstadt, 2017.
- [WTL17] D. Wang, D. Tan, and L. Liu. "Particle swarm optimization algorithm: an overview". In: *Soft Computing* 22.2 (Jan. 2017), pages 387–408. DOI: 10.1007/s00500-016-2474-6.
- [YG09] Y. Ye and T. Guo. "Dielectric properties of Fe-doped Ba<sub>0.65</sub>Sr<sub>0.35</sub>TiO<sub>3</sub> thin films fabricated by the sol-gel method". In: *Ceramics International* 35.7 (Sept. 2009), pages 2761–2765. DOI: 10.1016/j.ceramint.2009.03.023.
- [ZB00] O. Zinke and H. Brunswig. *Hochfrequenztechnik 1*. Edited by Anton Vlcek, Hans Ludwig Hartnagel, and Konrad Mayer. Springer Berlin Heidelberg, 2000. DOI: 10.1007/978-3-642-57131-2.
- [ZCT13] P. Zubko, G. Catalan, and A. K. Tagantsev. "Flexoelectric Effect in Solids". In: *Annual Review of Materials Research* 43.1 (July 2013), pages 387–421. DOI: 10.1146/annurev-matsci-071312-121634.
- [Zei20] L. Zeinar. "Dielektrika in epitaktischen Volloxid-Varaktoren für Mikrowellen-Anwendungen". PhD thesis. Technical University of Darmstadt, 2020.

# Own Contributions

## First-Author Publications

- [1] **D. Walk**, D. Kienemund, L. Zeinar, P. Salg, A. Radetinac, P. Komissinskiy, L. Alff, R. Jakoby, and H. Maune. "Characterization and Deembedding of Negative Series Inductance in On-Wafer Measurements of Thin-Film All-Oxide Varactors". In: *IEEE Microwave and Wireless Components Letters* 29.3 (Mar. 2019), pages 213–215. DOI: 10.1109/lmwc.2019.2897901.
- [2] **D. Walk**, D. Kienemund, P. Salg, L. Zeinar, A. Radetinac, L. Molina-Luna, P. Komissinskiy, L. Alff, R. Jakoby, and H. Maune. "Highly Accurate Analytic Modeling of Dispersive Field Distributions in MIM Capacitances With Electrodes Thinner Than Skin Depth". In: *IEEE Transactions on Microwave Theory and Techniques* 67.12 (Dec. 2019), pages 4665–4673. DOI: 10.1109/tmtt.2019.2944622.
- [3] **D. Walk**, P. Agrawal, L. Zeinar, P. Salg, A. Arzumanov, P. Komissinskiy, L. Alff, R. Jakoby, S. J. Rupitsch, and H. Maune. "All-Oxide Varactor Electromechanical Properties Extracted by Highly Accurate Modeling Over a Broad Frequency and Electric Bias Range". In: *IEEE Transactions on Ultrasonics, Ferroelectrics, and Frequency Control (Accepted with minor revisions on 10th Feb. 2021, resubmitted on 1st Mar. 2021)* (2021).

*Pari-passu first author*

- [4] P. Salg, **D. Walk**, L. Zeinar, A. Radetinac, L. Molina-Luna, A. Zintler, R. Jakoby, H. Maune, P. Komissinskiy, and L. Alff. "Atomically interface engineered micrometer-thick SrMoO<sub>3</sub> oxide electrodes for thin-film Ba<sub>x</sub>Sr<sub>1-x</sub>TiO<sub>3</sub> ferroelectric varactors tunable at low voltages". In: *APL Materials* 7.5 (May 2019), page 051107. DOI: 10.1063/1.5094855.

## Conference Contributions

- [5] **D. Walk**, P. Salg, D. Kienemund, A. Radetinac, L. Zeinar, C. Schuster, P. Komissinskiy, L. Alff, R. Jakoby, and H. Maune. "Characterization and Modeling of Epitaxially Grown BST on a Conducting Oxide Electrode". In: *European Microwave Conference (EuMC)*. Sept. 2018. DOI: 10.23919/eumc.2018.8541771.
- [6] **D. Walk**, D. Kienemund, P. Salg, L. Zeinar, A. Radetinac, P. Komissinskiy, L. Alff, R. Jakoby, and H. Maune. "All-Oxide Thin Film Varactor: From Test Structure to SMD Component". In: *European Microwave Conference (EuMC)*. Oct. 2019. DOI: 10.23919/eumc.2019.8910758.
- [7] **D. Walk**, D. Kienemund, P. Agrawal, P. Salg, L. Zeinar, P. Komissinskiy, L. Alff, R. Jakoby, and H. Maune. "Suppression of Acoustic Resonances in All-Oxide Varactors". In: *IEEE/MTT-S International Microwave Symposium (IMS)*. Aug. 2020. DOI: 10.1109/ims30576.2020.9224035.
- [8] **D. Walk**, P. Salg, P. Komissinskiy, L. Alff, R. Jakoby, and H. Maune. "**Invited:** Advanced RF Modeling of Varactors with Thin Oxide Electrodes". In: *Electronic Materials and Applications*. The American Ceramic Society, Jan. 2021.

## Additional Publications and Contributions

- [A01] P. Salg, A. Radetinac, **D. Walk**, L. Molina-Luna, R. Egoavil, P. Komissinskiy, H. Maune, R. Jakoby, and L. Alff. "Interface engineering in all-oxide  $\text{Ba}_x\text{Sr}_{1-x}\text{TiO}_3$  thin-film varactors with highly conducting  $\text{SrMoO}_3$  electrodes". In: *DFG Spring meeting*. DFG, 2017.
- [A02] P. Salg, A. Radetinac, L. Zeinar, **D. Walk**, H. Maune, R. Jakoby, P. Komissinskiy, and L. Alff. "All-oxide epitaxial ferroelectric varactors for low-voltage microwave applications". In: *International Workshop on Oxide Electronics*. 2017.
- [A03] L. Zeinar, P. Salg, A. Radetinac, **D. Walk**, H. Maune, R. Jakoby, P. Komissinskiy, and L. Alff. "Effect of cation stoichiometry on electric properties of thin-film varactors with  $\text{Ba}_x\text{Sr}_{(1-x)}\text{TiO}_3$  tunable dielectric and highly conducting  $\text{SrMoO}_3$  electrodes". In: *DFG Spring meeting*. DFG, 2018.

- [A04] H. Maune, D. Kienemund, A. Wiens, S. Preis, C. Schuster, **D. Walk**, O. Bengtsson, and R. Jakoby. "Ferroelectrics for Tunable High-Power Applications". In: *IEEE MTT-S International Microwave Workshop Series on Advanced Materials and Processes for RF and THz Applications (IMWS-AMP)*. July 2018. DOI: 10.1109/imws-amp.2018.8457141.
- [A05] P. Salg, L. Zeinar, **D. Walk**, A. Radetinac, H. Maune, R. Jakoby, P. Komissinskiy, and L. Alff. "Oxygen diffusion in epitaxial oxide heterostructures with SrMoO<sub>3</sub> thin films". In: *International Workshop on Oxide Electronics*. 2018.
- [A06] L. Zeinar, P. Salg, **D. Walk**, A. Radetinac, H. Maune, R. Jakoby, P. Komissinskiy, and L. Alff. "Influence of Ti-stoichiometry on electrical and crystal propertoes of BST Varactors". In: *International Workshop on Oxide Electronics*. 2018.
- [A07] P. Salg, L. Zeinar, **D. Walk**, H. Maune, R. Jakoby, P. Komissinskiy, and L. Alff. "Oxygen diffusion in epitaxial oxide heterostructures with SrMoO<sub>3</sub> thin films". In: *DFG Fall meeting*. European Materials Research Society, 2018.
- [A08] D. Kienemund, **D. Walk**, N. Bohn, J. R. Binder, R. Jakoby, and H. Maune. "Proceedings of the 48th European Microwave Conference Suppression of Acoustic Resonances in Fully-Printed, BST Thick Film Varactors Utilizing Double MIM Structures". In: *European Microwave Conference (EuMC)*. Sept. 2018. DOI: 10.23919/eumc.2018.8541497.
- [A09] H. Maune, **D. Walk**, P. Salg, L. Zeinar, D. Kienemund, C. Schuster, A. Radetinac, P. Komissinskiy, L. Alff, and R. Jakoby. "Invited: All-Oxide BST-Components for Reconfigurable Communication Systems". In: *Electronic Materials and Applications*. The American Ceramic Society, 2019.
- [A10] H. Maune, **D. Walk**, P. Komissinskiy, L. Alff, and R. Jakoby. "Invited: RF Modeling of Tunable Varactors with Thin Oxide Electrodes". In: *Electronic Materials and Applications*. The American Ceramic Society, 2020.
- [A11] P. Salg, L. Zeinar, A. Radetinac, **D. Walk**, H. Maune, R. Jakoby, L. Alff, and P. Komissinskiy. "Oxygen diffusion barriers for epitaxial thin-film heterostructures with highly conducting SrMoO<sub>3</sub> electrodes". In: *Journal of Applied Physics* 127.6 (Feb. 2020), page 065302. DOI: 10.1063/1.5129767.

- [A12] D. Wang, M. Nickel, **D. Walk**, A. Jimenez, E. Polat, R. Reese, G. P. Rehder, A. L. C. Serrano, L. G. Gomes, P. Ferrari, R. Jakoby, and H. Maune. "Slow Wave Inverted Microstrip Line Based on Metallic Nanowire Filled Alumina Membrane". In: *German Microwave Conference (GeMiC)*. 2020, pages 160–163.
- [A13] L. Zeinar, P. Salg, **D. Walk**, S. Petzold, A. Arzumanov, R. Jakoby, H. Maune, L. Alff, and P. Komissinskiy. "Matching conflicting oxidation conditions and strain accommodation in perovskite epitaxial thin-film ferroelectric varactors". In: *Journal of Applied Physics* 128.21 (Dec. 4, 2020), page 214104. DOI: 10.1063/5.0021097.

## Awards

- *APL Materials* Excellence in Research Award 2019 as pari-passu first author in [4]

## Supervised Work

- „Suppression Techniques for Acoustic Resonances in Ferroelectric Multilayer Varactors for High-Power Matching Circuits“, *Master Thesis*, Sanjay Shankaranarayana Sastry, 2017
- „Potential Investigation of All-Oxide Varactors in Phase Shifters“, *Master Thesis*, Jonas Bley, 2020

# **Curriculum Vitae**

## **Personal Information**

Name: Dominik Walk

Date of birth: 12.06.1989

Place of birth: Diez, Germany

## **Academic Education and Employment**

- |                 |  |
|-----------------|--|
| 2016'12–2021'03 | Research Associate at Institute for Microwave Engineering and Photonics (TU Darmstadt) |
| 2008'10–2016'10 | Study of Electrical Engineering at TU Darmstadt (B.Sc., M.Sc.)                         |
| 1999'08–2008'03 | Sophie-Hedwig Gymnasium Diez, secondary school (Degree: Abitur)                        |